

THE  
M...  
C...

Ages and distribution of ignimbrites in the Mogollon-Datil  
volcanic field, southwest New Mexico: a stratigraphic  
framework using  $^{40}\text{Ar}/^{39}\text{Ar}$  dating and paleomagnetism

Geotechnical  
Information Center

William C. McIntosh

N.M.I.M.T.  
LIBRARY  
SOCORRO, N.M.

Submitted in Partial Fulfillment  
of the Requirements for the Degree of  
Doctor of Philosophy in Geology

September, 1989

## Table of Contents

Table of Contents .....	i
List of Figures .....	iv
List of Tables .....	vi
Acknowledgements .....	vii
Abstract .....	ix
Introduction .....	xii
References .....	xviii
<b>Chapter A: Paleomagnetism .....</b>	<b>A 1</b>
Evaluation of paleomagnetism as a correlation criterion for Mogollon-Datil ignimbrites, southwestern New Mexico	
ABSTRACT .....	A 1
INTRODUCTION .....	A 4
GEOLOGIC SETTING .....	A 7
FIELD AND LABORATORY PROCEDURES .....	A 10
NATURE OF REMANENCE .....	A 17
Simple TRM (Type 1) .....	A 17
TRM accompanied by lightning-induced IRM (Type 2) .....	A 39
TRM plus CRM (Type 3) .....	A 41
TRM plus random lithic-hosted magnetizations (Type 4) .....	A 48
Acceptance/Rejection criteria .....	A 50
REMANENCE DIRECTIONS .....	A 51
Well-studied units (n≥4) .....	A 51
Poorly studied units (n=1-3) .....	A 59
DISCUSSION .....	A 62
Evaluation of remanence quality .....	A 62
Attitude control and tectonic rotations .....	A 69
Paleomagnetic effects of flowage in outflow sheets .....	A 76
Outflow vs. intracaldera facies .....	A 78
Utility of paleomagnetism as a correlation criterion .....	A 82
Paleomagnetic pole positions and assessment of non-dipole field behavior .....	A 91
CONCLUSIONS .....	A 99
REFERENCES .....	A 102
<b>Chapter B: <sup>40</sup>Ar/<sup>39</sup>Ar Dating .....</b>	<b>B 1</b>
High-Precision <sup>40</sup> Ar/ <sup>39</sup> Ar sanidine geochronology of ignimbrites in the Mogollon-Datil volcanic field, southwestern New Mexico	
ABSTRACT .....	B 1
INTRODUCTION .....	B 2
MOGOLLON-DATIL VOLCANIC FIELD .....	B 4
METHODS .....	B 7

SANIDINE MINERALOGY .....	B 10
AGE SPECTRA RESULTS .....	B 16
DISCUSSION .....	B 25
Precision and resolution .....	B 25
Accuracy .....	B 30
Cryptoperthitic exsolution .....	B 33
Alteration .....	B 34
Contamination .....	B 35
History of Mogollon-Datil ignimbrite activity ..	B 37
CONCLUSIONS .....	B 41
REFERENCES .....	B 43
<b>Chapter C: Stratigraphy .....</b>	<b>C 1</b>
Ages and distribution of ignimbrites in the Mogollon-Datil volcanic field, southwest New Mexico: a stratigraphic framework using $^{40}\text{Ar}/^{39}\text{Ar}$ dating and paleomagnetism	
ABSTRACT .....	C 1
INTRODUCTION .....	C 3
GEOLOGIC SETTING AND PREVIOUSLY ESTABLISHED STRATIGRAPHY .....	C 7
METHODS: $^{40}\text{Ar}/^{39}\text{Ar}$ DATING AND PALEOMAGNETISM ..... C 13	
HISTORY OF IGNIMBRITE ACTIVITY .....	C 20
Episode 1 (36.2 Ma-33.5) .....	C 22
Organ cauldron activity - 36.2 to 35.5 Ma .....	C 24
Smaller volume ignimbrites - 35.7 to 35.0 Ma .....	C 27
Kneeling Nun Tuff - 34.9 Ma .....	C 33
Smaller volume ignimbrites - 34.9 to 33.7 Ma .....	C 35
"Box Canyon" Tuff - 33.5 Ma .....	C 42
Episode 2 - 32.1 to 31.4 Ma .....	C 44
Hells Mesa Tuff - 32.1 Ma .....	C 44
Caballo Blanco Tuff - 31.7 Ma .....	C 46
Tadpole Ridge Tuff - 31.4 Ma .....	C 49
Episode 3 - 29.0 to 27.4 Ma .....	C 52
Davis Canyon Tuff - 29.0 Ma .....	C 52
La Jencia Tuff - 28.9 Ma .....	C 54
Vicks Peak Tuff - 28.6 Ma .....	C 57
Smaller volume tuffs of the Black Range - 29.0 to 28.1 Ma .....	C 59
Shelly Peak Tuff - 28.1 Ma .....	C 62
Bloodgood Canyon Tuff and related units- 28.1 Ma .....	C 64
Lemitar and Caronita tuffs - 28.0 Ma .....	C 67
South Canyon Tuff - 27.4 Ma .....	C 72
Slash Ranch/Jordan Canyon Tuff - 26 Ma? ..	C 74
Episode 4 - 24.3 Ma .....	C 75
tuff of Turkey Springs - 24.3 Ma .....	C 75

DISCUSSION .....	C 77
Utility of $^{40}\text{Ar}/^{39}\text{Ar}$ and paleomagnetism as correlation criteria Mogollon-Datil time- stratigraphic framework .....	C 77
Mogollon-Datil time-stratigraphic framework ..	C 80
Summary of Mogollon-Datil ignimbrite activity .	C 83
REFERENCES .....	C 85
<b>Chapter D: Polarity Record .....</b>	<b>D 1</b>
Calibration of the latest Eocene-Oligocene Magnetic Polarity Time Scale using $^{40}\text{Ar}/^{39}\text{Ar}$ dated ignimbrites	
ABSTRACT .....	D 1
INTRODUCTION .....	D 1
METHODS .....	D 5
MOGOLLON-DATIL POLARITY RECORD .....	D 7
CORRELATION WITH THE MARINE ANOMALY RECORD .....	D 10
DISCUSSION .....	D 11
REFERENCES .....	D 15
<b>Appendices: .....</b>	<b>E 1</b>
Appendix 1 - Paleomagnetic data from ignimbrites ...	E 1
Appendix 2 - Paleomagnetic data from lavas .....	E 9
Appendix 3 - $^{40}\text{Ar}/^{39}\text{Ar}$ data .....	E 11



## List of Figures

## Chapter A: Paleomagnetism

A-1. Map of Mogollon-Datil volcanic field .....	A 8
A-2. NRM intensity (J <sub>nrm</sub> ) versus low-field bulk susceptibility .....	A 18
A-3. Simple, univectoral demagnetization behavior .	A 19
A-4. Low-coercivity, high-temperature magnetizations .....	A 22
A-5. Thermomagnetic analyses .....	A 30
A-6. IRM acquisition, backfield, and demagnetization curves .....	A 33
A-7. Paleo- and rock-magnetism of stratigraphic sequences of samples .....	A 37
A-8. Removal of lightning-induced IRM components ...	A 40
A-9. CRM components apparently carried by SD magnetite .....	A 43
A-10. Combination of IRM and CRM components .....	A 45
A-11. CRM carried by hematite and TRM carried by magnetite .....	A 47
A-12. Randomly directed magnetizations carried by lithic fragments .....	A 49
A-13. Site-mean remanence data for well-studied ignimbrites .....	A 52
A-14. Site-mean remanence data from three facies of the South Canyon Tuff .....	A 56
A-15. Unit-mean remanence directions .....	A 57
A-16. Site-mean remanence data for moderately well-constrained ignimbrites .....	A 60
A-17. Site-mean data for single-site ignimbrites ..	A 61
A-18. Structural dip versus deviation from unit-mean direction .....	A 72
A-19. Evidence for 25° rotation of Turututu Butte .	A 74
A-20. Paleomagnetic fold test indicating high-temperature rheomorphic flowage .....	A 77
A-21. Distinctive paleomagnetic directions of four younger ignimbrites .....	A 88
A-22. Overlapping paleomagnetic directions of four older ignimbrites .....	A 89
A-23. Mean paleomagnetic directions for Mogollon-Datil ignimbrites and lavas .....	A 93

Chapter B: <sup>40</sup>Ar/<sup>39</sup>Ar dating

B-1. Location map for <sup>40</sup> Ar/ <sup>39</sup> Ar dating samples .....	B 5
B-2. Sanidine compositions .....	B 11
B-3. X-ray diffraction spectra .....	B 15
B-4. Contour diagram of strain index and d-spacing .	B 17
B-5. Representative age spectra .....	B 20
B-6. Comparison of <sup>40</sup> Ar/ <sup>39</sup> Ar, K-Ar, and fission-track data .....	B 24
B-7. Agreement of <sup>40</sup> Ar/ <sup>39</sup> Ar ages and stratigraphic order .....	B 31
B-8. Composite stratigraphic section and polarity record .....	B 39

**Chapter C: Stratigraphy**

C-1. Silicic volcanic fields of southwestern North America .....	C 4
C-2. Map of the Mogollon-Datil volcanic field .....	C 5
C-3. Evolution of Mogollon-Datil stratigraphic concepts .....	C 12
C-4. Unit-mean paleomagnetic directions of ignimbrites .....	C 17
C-5. Composite stratigraphic column .....	C 21
C-6. Stratigraphic framework for Mogollon-Datil ignimbrites .....	C 23
C-7. Organ/Doña Ana intracauldron sequence and adjacent outflow ignimbrites .....	C 26
C-8. Datil Well Tuff .....	C 30
C-9. Tuff of Farr Ranch .....	C 31
C-10. Bell Top 4 Tuff .....	C 32
C-11. Kneeling Nun Tuff .....	C 34
C-12. Overlapping paleomagnetic data from 4 older ignimbrites .....	C 36
C-13. Tuff of Lebya Well .....	C 38
C-14. Rockhouse Canyon Tuff .....	C 39
C-15. Cooney Tuff .....	C 40
C-16. Blue Canyon Tuff .....	C 41
C-17. Box Canyon Tuff .....	C 43
C-18. Hells Mesa Tuff .....	C 45
C-19. Caballo Blanco Tuff .....	C 47
C-20. Tadpole Ridge Tuff .....	C 50
C-21. Davis Canyon Tuff .....	C 53
C-22. Paleomagnetic data from three 29.0-28.6 Ma crystal-poor ignimbrites .....	C 55
C-23. La Jencia Tuff .....	C 56
C-24. Vicks Peak Tuff .....	C 58
C-25. Poorly studied Episode 3 ignimbrites .....	C 60
C-26. Tuff of Garcia Camp .....	C 61
C-27. Shelly Peak Tuff .....	C 63
C-28. Bloodgood Canyon Tuff .....	C 65
C-29. Distinctive paleomagnetic data from 4 younger ignimbrites .....	C 68
C-30. Tuff of Triangle C Ranch .....	C 69
C-31. Caronita Canyon Tuff .....	C 70
C-32. Lemitar Tuff .....	C 71
C-33. South Canyon Tuff .....	C 73
C-34. Tuff of Turkey Springs .....	C 76

**Chapter D: Polarity Record**

D-1. Proposed calibration of Magnetic Polarity Time Scale .....	D 3
D-2. Location map of study area .....	D 6
D-3. Composite stratigraphic section and magnetic polarity record .....	D 8
D-4. Comparison of Mogollon-Datil and other MPTS calibrations .....	D 12

## List of Tables

**Chapter A: Paleomagnetism**

A-1. Unit-mean data from well-studied ignimbrites ..	A 11
A-2. Comparison of different analyses of demagnetization data .....	A 15
A-3. Site-mean paleomagnetic data for ignimbrites ..	A 23
A-4. Differences between unit-mean directions of ignimbrites .....	A 86
A-5. Mean directions and paleopoles for Mogollon-Datil volcanic field .....	A 92
A-6. Site-mean paleomagnetic data for lavas .....	A 95

**Chapter B:  $^{40}\text{Ar}/^{39}\text{Ar}$  dating**

B-1. $^{40}\text{Ar}/^{39}\text{Ar}$ plateau ages and mineralogical data ...	B 12
B-2. $^{40}\text{Ar}/^{39}\text{Ar}$ analytical data .....	B 18
B-3. Precision of $^{40}\text{Ar}/^{39}\text{Ar}$ plateau ages and other dating techniques .....	B 27

**Chapter C: Stratigraphy**

C-1. Summary of $^{40}\text{Ar}/^{39}\text{Ar}$ , paleomagnetic, and stratigraphic data for ignimbrites .....	C 10
--	------

**Chapter D: Polarity Record**

D-1. Comparison of precision of $^{40}\text{Ar}/^{39}\text{Ar}$ and other dating methods .....	D 9
---	-----

## ACKNOWLEDGEMENTS

I gratefully acknowledge the continued generous help of my advisors: Chuck Chapin, Phil Kyle, John Sutter, and John Geissman. This project was conceived in conspiracy between Chuck and Phil, and during its course they provided continuing help, ideas, advice, support, discussions, reviews, humor, and friendship. John Geissman's arrival in Albuquerque greatly improved paleomagnetic aspects of this study, he is thanked for advice, guidance, reviews, and access the cryogenic magnetometer at UNM. John Sutter and Mick Kunk of the U.S. Geological Survey in Reston provided knowledge and laboratory facilities which made possible the  $^{40}\text{Ar}/^{39}\text{Ar}$  dating vital to this project.

Jim Ratté has been my fifth unsung advisor. He has enthusiastically shared his knowledge of stratigraphy, geology, and outcrop locations in the greater Mogollon area, and on many occasions we have worked together in the field. Several other New Mexico geologists have also provided abundant important information, including Wolf Elston, Bill Seager, Russ Clemons, Tommy Finnell, Sheila Seaman, Mike Hermann, and Rich Abbitz.

The New Mexico Bureau of Mines and Mineral Resources and Director Frank Kottowski are gratefully acknowledged for financial and material support throughout the duration of this study. Many others at the Bureau, especially Bob Osburn, Charles Ferguson, Rich Harrison, and Steve Cather, have provided abundant interest and help.

This project could not have been accomplished without the generous field assistance of friends and coworkers, especially Nelia Dunbar and her dog Ophie. Nelia Dunbar is furthermore thanked for her untold patience and attention in many things.

## ABSTRACT

The combination of high-precision  $^{40}\text{Ar}/^{39}\text{Ar}$  sanidine plateau ages and paleomagnetic data provides reliable long-distance correlation criteria for 25 discontinuously exposed regional ignimbrites in the 40,000 km<sup>2</sup>, Eocene-Oligocene Mogollon-Datil volcanic field of southwestern New Mexico.

$^{40}\text{Ar}/^{39}\text{Ar}$  age spectra from sanidine separates (97 spectra, 85 samples, 36 units) are characteristically flat and, with few exceptions, yield plateau ages showing within-sample and within-unit precision less than  $\pm 0.5\%$ . Precise relative  $^{40}\text{Ar}/^{39}\text{Ar}$  ages, which agree closely with independently established stratigraphic order, have been determined for 7 ignimbrites (3-8 samples/unit) and preliminary ages have been determined for another 26 units (1-2 samples/unit).

Regional and local ignimbrite outflow sheets show stable paleomagnetic remanence directions which are uniform over most of their extents, including facies ranging from thick, densely welded proximal ignimbrites to unwelded distal fringes as thin as 1.5 m. The largest sources of dispersion in the paleomagnetic data set (404 sites in 25 regional and 54 local ignimbrites) are uncertainties in determinations of the paleohorizontal, and local, fault-related tectonic rotations, particularly in strongly extended areas.

$^{40}\text{Ar}/^{39}\text{Ar}$  and paleomagnetic correlation criteria are complementary:  $^{40}\text{Ar}/^{39}\text{Ar}$  data serve to resolve age

differences between paleomagnetically similar units, and paleomagnetism helps distinguish between units that are altered, lack sanidine, or are too close in age to be resolved even by the  $^{40}\text{Ar}/^{39}\text{Ar}$  method.

Used in concert with lithologic and stratigraphic position data,  $^{40}\text{Ar}/^{39}\text{Ar}$  ages and paleomagnetic directions allow accurate long-range ignimbrite correlations which provide reliable ties between previously established subregional stratigraphic sequences. Regional stratigraphic markers now shown to be more extensive than previously believed include Kneeling Nun Tuff (34.9 Ma), Box Canyon Tuff (33.5 Ma), Caballo Blanco Tuff (31.7 Ma), Vicks Peak Tuff (28.6 Ma), and Bloodgood Canyon Tuff (28.1 Ma).

A precise, comprehensive, ignimbrite-based, time-stratigraphic framework has been developed for the Mogollon-Datil volcanic field. This framework provides significant age constraints for sequences of lavas and sedimentary rocks which cannot themselves be precisely dated.

Mogollon-Datil ignimbrite activity ranged from 36.2 to 24.3 Ma and was highly episodic, being confined to 4 brief (<2.6 m.y.) eruptive intervals separated by 1.5 to 3 m.y. long hiatuses. Cauldron-forming activity originated in the 36.1-35.4 Organ/Doña cauldron area and subsequently migrated north and west. Rhyolitic activity was most intense between 29 and 27.4 Ma; this interval is characterized by alternating ignimbrite eruptions from the Mogollon and Socorro cauldron complexes, punctuated by 2 brief intervals

(29.0-28.7 Ma and 28.1 Ma) of extensive rhyolitic dome and flow eruptions in the central Black Range area between the two complexes.

The Mogollon-Datil ignimbrite sequence also provides a precisely dated but inherently discontinuous record of Late Eocene-Oligocene geomagnetic polarity. This polarity record includes 7 polarity reversals and tightly constrains the age and length of 4 polarity intervals: 27.4-28.0 Ma normal, 28.0-28.9 Ma reversed, 34.6-34.9 Ma reversed, and 34.9-35.9 Ma normal. Mogollon-Datil data best fit the marine magnetic anomaly record if these 4 polarity intervals are correlated with marine anomalies 10, 10r, 15r, and 16. This correlation supports an Eocene-Oligocene boundary age near 33.6 Ma.

The mean paleomagnetic pole position for Mogollon-Datil ignimbrites (n=68 unit-mean VGPs) is located at (78.8°N, 166.6°W,  $K=19.8$ ,  $A_{95}=4.0$ ,  $\sigma=18.2^\circ$ ). In contrast to earlier findings (Diehl et al., 1988), mean directions of normal and reversed polarity Mogollon-Datil ignimbrites are nearly antipodal (176.4° apart), and show no evidence of long term differences in the zonal harmonics of opposite geomagnetic polarity states.



## INTRODUCTION

The Mogollon-Datil volcanic field is the northern tip of a once contiguous Late Eocene-Oligocene volcanic field which extended from southwestern New Mexico into central Mexico. Because it is readily accessible and generally well exposed, the Mogollon-Datil volcanic field has been the subject of a large amount of professional and student geological research. Much progress has been made toward precisely understanding the regional volcanic history of the entire field, but this work has been hampered by the lack of a comprehensive regional time-stratigraphic framework.

The ignimbrites (ash-flow tuffs) of the Mogollon-Datil volcanic field provide ideal time-stratigraphic markers for use in a regional stratigraphic framework. The Mogollon-Datil volcanic sequence includes about 30 distinct widespread ( $>1000 \text{ km}^2$ ), voluminous ( $100\text{-}1300 \text{ km}^3$ ) ignimbrites which were erupted episodically throughout the latest Eocene and Oligocene epochs. Knowledge of the stratigraphy in various sub-regions of the volcanic field has been greatly advanced by detailed mapping studies of these ignimbrites (e.g. Osburn and Chapin, 1983a and 1983b; Ratté et al., 1984; Elston, 1984; Seager et al., 1982). However, because of the discontinuous pattern of outcrops produced by basin and range extension, accurate correlation of ignimbrites between well-mapped subregions has proven difficult.

Many previous long-distance correlations of Mogollon-Datil ignimbrites have been based upon lithology, a criterion which is undependable when used alone. Lithologies of most individual ignimbrite units show lateral, vertical, and sectoral variations (Hildreth and Mahood, 1985). In addition, several distinct Mogollon-Datil ignimbrites are lithologically identical. Some of these ignimbrites have been dated by conventional K-Ar and fission track techniques, but in many cases these methods have proven too imprecise to resolve correlation problems (e.g. Ratté et al, 1984). Also, attempts to geochemically "fingerprint" individual ignimbrites have shown only limited success (Bornhorst, 1980).

The primary goal of this project has been to develop a detailed, accurate, time-stratigraphic framework for the Mogollon-Datil volcanic field. The study has focussed on ignimbrites, using a combination of paleomagnetic analysis and high-precision  $^{40}\text{Ar}/^{39}\text{Ar}$  dating to assemble established stratigraphic sequences from well-mapped sub-regions into an integrated regional framework.

Paleomagnetic analysis has been applied to many of the long standing stratigraphic problems in the Mogollon-Datil volcanic field. Paleomagnetic analysis is a well-established method for correlation of ignimbrites (Grommé et al. 1972; Best et al, 1973; Hildreth and Mahood, 1985). Individual ignimbrite units, both welded and non-welded, commonly show uniform thermoremanent magnetizations (TRM) representing an

accurate record of the geomagnetic field direction during rapid post-emplacement cooling (Grommé et al. 1972; Best et al., 1973; Reynolds, 1977; Hoblitt et al., 1985). Because of reversals and secular variation of the geomagnetic field, the probability is low that any two different ignimbrites will have recorded identical field directions (Grommé et al. 1972; Bogue and Coe, 1981). Unique or distinctive paleomagnetic directions have proven invaluable in this study in distinguishing between lithologically similar Mogollon-Datil ignimbrites. Paleomagnetic identification of thin, unwelded, distal fringes of ignimbrites has helped establish previously unknown overlap relationships between units from different eruptive centers.

High-precision  $^{40}\text{Ar}/^{39}\text{Ar}$  age determinations of sanidine separates have also been applied to stratigraphic problems in the Mogollon-Datil volcanic field. This study and an initial study of Kedzie (1984; Kedzie et al., 1985) have shown that the  $^{40}\text{Ar}/^{39}\text{Ar}$  age spectrum dating method is significantly more precise than conventional K-Ar and fission-track dating techniques. Data from Mogollon-Datil ignimbrites indicates a precision of  $\pm 0.02$  to 0.2 Ma, in sharp contrast to the precision of  $\pm 1.3$  Ma or worse shown by conventional K-Ar and fission-track ages on the same units (Marvin et al., 1987). A further indication of the high precision of these  $^{40}\text{Ar}/^{39}\text{Ar}$  age determinations is shown by their close agreement with established stratigraphic order in rapidly erupted sequences of ignimbrites.

In addition to the primary goal of development of an integrated time-stratigraphic framework, this study addresses three additional objectives: 1) evaluation of local and regional tectonic rotations within the Mogollon-Datil volcanic field, 2) correlation of the Mogollon-Datil magnetic polarity record with those of other mid-Tertiary volcanic fields, and 3) calibration of the worldwide geomagnetic polarity time scale using Mogollon-Datil data.

Paleomagnetic analysis is a proven technique for constraining tectonic rotations about non-horizontal axes, a common feature in regions that have undergone basin and range extension (Hagstrum and Gans, 1989; Hudson and Geissman, 1987; Golembek and Brown, 1988). In cases where rotated domains are smaller than entire ignimbrite sheets, paleomagnetic data from individual fault blocks provide very sensitive records of rotations about non-horizontal axes (Hagstrum and Gans, 1989; Hillhouse and Wells, 1986; Geissman and Harlan, in press ). Larger scale regional tectonic rotations can be identified by averaging data from many igneous units and noting deviations of the mean from expected directions derived from apparent polar wander paths (Hudson and Geissman, 1987; Golembek and Brown, 1988). Both techniques can be applied to stratigraphic sequences to constrain the timing of rotational events.

The problem of precisely correlating the geologic history of the Mogollon-Datil volcanic field with other North American mid-Tertiary volcanic fields is greatly

facilitated by the determination of a precisely dated Mogollon-Datil magnetic polarity record. Considerable paleomagnetic data are available for the San Juan field (Diehl et al., 1974; Beck et al., 1977; Ellwood, 1982), and extensive  $^{40}\text{Ar}/^{39}\text{Ar}$  dating work is presently underway (Lipman, 1987; Lanphere, 1988). Eventually, it will be possible to extend polarity- and age-based correlations to the Trans-Pecos field of west Texas and southward into Mexico. Such correlations will provide precise constraints on the volcanic history of the entire region, which will in turn constrain models of regional stress history and help distinguish among competing plate tectonic models for mid-Tertiary North America.

Finally, the aspect of this study with the most far-reaching consequences is the use of the precisely dated Mogollon-Datil magnetic polarity record to refine the ages of geomagnetic polarity chrons inferred from marine magnetic anomalies. Radiometric calibration of the mid-Tertiary geomagnetic polarity record is a long-standing controversy, and published calibration points vary in age by as much as 20% (Berggren et al., 1985). This variation results largely from lack of fresh, datable seafloor materials and from the imprecision of conventional K-Ar age determinations. Accurate one-to-one correlations between the precisely dated Mogollon-Datil polarity record and the seafloor anomaly sequence would reduce the uncertainty in polarity chron ages to 1%. Such accurate calibration would tightly constrain

Tertiary sea floor spreading rates and improve correlations between marine and terrestrial biostratigraphic records.

The Ph.D dissertation which follows has been divided into four individual manuscripts for publication, which separately present: A) paleomagnetic work, B)  $^{40}\text{Ar}/^{39}\text{Ar}$  dating work, C) Mogollon-Datil stratigraphy, and D) calibration of the mid-Tertiary geomagnetic polarity record. Some repetition is involved in this form of presentation. The four manuscripts are followed by appendices containing detailed paleomagnetic and  $^{40}\text{Ar}/^{39}\text{Ar}$  data.

Two of the manuscripts (B and C) include other authors in addition to myself. Laura Kedzie was included in the dating manuscript because 12 age determinations from her M.S. thesis (Kedzie, 1984) were integrated into the  $^{40}\text{Ar}/^{39}\text{Ar}$  data set. Chuck Chapin, John Sutter, and Jim Ratté were included as authors because of their participation in the planning, direction, and support of this project. However, I was primarily responsible for the field work, laboratory analysis, data interpretation, and preparation of the manuscripts, and therefore feel justified in including these manuscript in this thesis.

## REFERENCES

- Beck, M.E., Sheriff, S.D., Diehl, J.F., and Hailwood, E.A., 1977, Further paleomagnetic results for the San Juan volcanic field of southern Colorado: *Earth and Planetary Science Letters*, v. 37, p. 124-130.
- Berggren, W.A., Kent, D.V., and Flynn, J.J., 1985, Jurassic to Paleogene: Part 2, Paleogene geochronology and chronostratigraphy, in Snelling, N.J. (ed.), *The Chronology of the Geological Record: Geological Society of London Memoir 10*, p. 141-195.
- Best, M.G., Shuey, R.T., Caskey, C.R., and Grant, S.K., 1973, Stratigraphic relations of members of the Needles Range Formation at type localities in southwestern Utah: *Geological Society of America Bulletin*, v. 84, p. 3269-3278.
- Bogue, S.W., and Coe, R.S., 1981, Paleomagnetic correlation of Columbia River basalt flows using secular variation: *Journal of Geophysical Research*, v. 86, p. 11883-11897.
- Bornhorst, T.J., 1980, Major- and trace-element geochemistry and mineralogy of Upper Eocene to Quaternary volcanic rocks of the Mogollon-Datil volcanic field, southwestern New Mexico: unpublished Ph.D. dissertation, University of New Mexico, Albuquerque, 1104 p.
- Diehl, J.F., Beck, M.E., and Lipman, P.W., 1974, Paleomagnetism and magnetic-polarity zonation in some Oligocene volcanic rocks of the San Juan Mountains, south-western Colorado: *Geophysical Journal*, v. 37, p. 323-332.
- Ellwood, B.B., 1982, Estimates of flow direction of calc-alkaline welded tuffs and paleomagnetic data reliability from anisotropy of magnetic susceptibility measurements: central San Juan Mountains, southwest Colorado: *Earth and Planetary Science Letters*, v. 59, p. 303-314.
- Elston, W.E., 1984, Mid-Tertiary ash flow tuff cauldrons, southwestern New Mexico: *Journal of Geophysical Research*, v. 89, p. 8733-8750.
- Geissman, J.W. and Harlan, S., in press, Paleomagnetic evidence for tectonic rotations in the Hoover Dam area, Nevada: *Geology*.
- Golembek, M.P., and Brown L.L., 1988, Clockwise rotation of the Mojave Desert: *Geology*, v. 16, p. 126-130.

- Grommé, C.S., McKee, E.H., and Blake, M.C., 1972, Paleomagnetic correlations and potassium-argon dating of middle Tertiary ash-flow sheets in eastern Great Basin, Nevada and Utah: Geological Society of America Bulletin, v. 83, p. 1619-1638.
- Hagstrum, J.T., and Gans, P.B., 1989, Paleomagnetism of the Oligocene Kalamazoo Tuff: Implications for Middle Tertiary extension in east central Nevada: Journal of Geophysical Research, v. 94, p. 1827-1842.
- Hildreth, W. and Mahood, G., 1985, Correlation of ash-flow tuffs: Geological Society of America Bulletin, v. 96, p. 968-974.
- Hillhouse, J.W., and Wells, R.E., 1986, Assessment of rotations in the eastern Mojave Desert, California and Arizona, from paleomagnetism of the Peach Springs Tuff: EOS Transactions AGU, v. 67, p. 922.
- Hoblitt, R.P., Reynolds, R.R., and Larson, E.E., 1985, Suitability of non-welded pyroclastic-flow deposits for studies of magnetic secular variation. A test based on deposits emplaced on Mount St. Helens, Washington, in 1980: Geology, v. 13, p. 242-245.
- Hudson, M.R., and Geissman, J.W., 1987, Paleomagnetic and structural evidence for middle Tertiary counter-clockwise block rotation in the Dixie Valley region, west-central Nevada: Geology, v. 15, p. 638-642.
- Kedzie, L.L., 1984, High-precision  $^{40}\text{Ar}/^{39}\text{Ar}$  dating of major ash-flow tuff sheets, Socorro, New Mexico: unpublished M.S. thesis, New Mexico Institute of Mining and Technology, Socorro, New Mexico, 197 p.
- Lanphere, M.A., 1988, High-resolution  $^{40}\text{Ar}/^{39}\text{Ar}$  geochronology of Oligocene volcanic rocks, San Juan Mountains, Colorado: Geochimica Cosmochimica Acta, v. 52, p. 1425-1434.
- Lipman, P.W., 1987, Oligocene central San Juan caldera cluster, Colorado: Geological Society of America Abstracts with Programs, v. 19, p. 315.
- Marvin, R.F., Naeser, C.W., Bikerman, M., Mehnert, H.H., and Ratté, J.C., 1987, Isotopic ages post-Paleocene igneous rocks within and bordering the Clifton  $1^\circ \times 2^\circ$  quadrangle, Arizona-New Mexico: New Mexico Bureau of Mines and Mineral Resources Bulletin 118, 63 p.



- Osburn, G.R., and Chapin, C.E., 1983a, Nomenclature for Cenozoic rocks of the northeast Mogollon-Datil volcanic field, New Mexico: New Mexico Bureau of Mines and Mineral Resources Stratigraphic Chart 1.
- Osburn, G.R., and Chapin, C.E., 1983b, Ash-flow tuffs and cauldrons in the northeast Mogollon-Datil volcanic field: a summary: New Mexico Geological Society Guidebook 34, p. 197-204.
- Ratté, J.C., Marvin, R.F., and Naeser, C.W., 1984, Calderas and ash-flow tuffs of the Mogollon Mountains: Journal of Geophysical Research, v. 89, p. 8713-8732.
- Reynolds, R.L., 1977, Paleomagnetism of welded tuffs of the Yellowstone Group: Journal of Geophysical Research, v. 82, p. 3677-3693.
- Seager, W.R., Clemons, R.E., Hawley, J.W., and Kelley, R.E., 1982, Geology of the northwest part of Las Cruces 1° x 2° sheet, New Mexico: New Mexico Bureau of Mines and Mineral Resources Geological Map 53, scale 1:125,000.

Evaluation of paleomagnetism as a correlation criterion  
for Mogollon-Datil ignimbrites, southwestern New Mexico

McIntosh, W.C., New Mexico Bureau of Mines and Mineral  
Resources, New Mexico Institute of Mining and Technology,  
Socorro, NM 87801

ABSTRACT

Paleomagnetic and rock-magnetic data show that 36-24 Ma ignimbrite outflow sheets in the Mogollon-Datil volcanic field carry well-behaved remanent magnetizations (RMs) that provide useful, reliable correlation criteria. Over 90% of 404 sites in 47 regional and 36 local ignimbrites exhibit well-grouped ( $\alpha_{95} < 10^\circ$ ) RMs carried by finely dispersed, high-temperature-oxidation assemblages of magnetite, hematite, and maghemite. These RMs, interpreted as thermoremanent magnetization (TRM), are readily separated by alternating field demagnetization from lightning-induced isothermal components. Chemical remanence or randomly directed, lithic-hosted RMs obscure the TRM in a few sites in altered or poorly welded, lithic-rich tuff.

Within individual ignimbrite outflow sheets, TRM directions are generally laterally and vertically consistent in both densely welded proximal and poorly welded distal facies. Discordancies in individual site-mean directions principally reflect uncertainties in structural corrections, particularly in areas of locally strong tectonic extension. The magnetizations of these outflow sheets show no evidence

of syn-cooling secular variation or sub-blocking-temperature flowage.

The unit mean TRM directions of 22 well-constrained (n=4 to 24 sites per unit) ignimbrite outflow sheets lie within 30° of the time averaged Eocene-Oligocene field. Distinctive to unique unit-mean TRM directions, differing 15-30° from the time-averaged field, provide strong correlation criteria for 9 of these units. Less distinctive unit-mean TRM directions of other units are also useful for correlation, particularly when combined with  $^{40}\text{Ar}/^{39}\text{Ar}$  ages and lithologic, stratigraphic, and geochemical data.

TRMs of thick (>500 m) intracaldera ignimbrite sequences agree in polarity with associated outflow sheets, but show less consistent directions, which may reflect secular variation during protracted cooling or large discrepancies between eutaxitic foliations and the syn-cooling paleohorizontal.

In contrast to earlier findings (Diehl et al., 1988), mean directions of normal and reversed polarity Mogollon-Datil ignimbrites are nearly antipodal (176.4° apart), and yield mean virtual geomagnetic poles (VGPs) that are statistically indistinguishable at the 1  $\sigma$  level. These results show no evidence of long term differences in the zonal harmonics of the normal and reversed polarity states. Normal and reversed polarity lavas show non-antipodal mean directions (165.6° apart) which apparently reflect defects in the data set. The mean paleomagnetic pole position for

Mogollon-Datil ignimbrites (n=68 unit-mean VGPs) is located at (78.8°N, 166.6°W, K=19.8,  $A_{95}$ =4.0,  $\sigma$ =18.2°).

## INTRODUCTION

Paleomagnetic analysis and  $^{40}\text{Ar}/^{39}\text{Ar}$  dating are a tremendously effective combination of techniques for correlating ignimbrites (ash-flow tuffs) in the Mogollon-Datil volcanic field (McIntosh et al., 1986; McIntosh, dissertation, Chapter C) and elsewhere (Deino and Best, 1988). Regional correlations of ignimbrites in the Mogollon-Datil field and Great Basin have been problematic, chiefly because the extensive, originally continuous ignimbrite sheets have been tectonically disrupted by basin-and-range extensional faulting (Chapin and Seager, 1975).

Stratigraphic sequences of ignimbrites in various subregions of the Mogollon-Datil field have been established by detailed mapping (Osburn and Chapin, 1983a and 1983b; Ratté et al., 1984; Elston, 1984; Seager et al., 1982), but correlations between discontinuously exposed subregions have been problematic. Although lithologic and geochemical data provide important basic correlation criteria, they have in many cases proven unreliable, because of similarities between different ignimbrites, and because individual ignimbrites show lateral, vertical, and sectoral variations (Hildreth and Mahood, 1985; Bornhorst, 1980). In addition, conventional K-Ar and fission-track dating methods have proven too imprecise to resolve many ignimbrite correlation problems (e.g. Marvin et al., 1987).

Most sanidine-bearing Mogollon-Datil regional ignimbrites have now been precisely ( $\pm 0.15$  Ma) dated by the

$^{40}\text{Ar}/^{39}\text{Ar}$  method (McIntosh et al., 1986; McIntosh, 1989; McIntosh, dissertation, Chapter B). This approach has demonstrated new correlations, revealed previously unknown units, and shown ignimbrite activity in the field to be highly episodic (McIntosh et al., 1986; McIntosh, dissertation, Chapter C).  $^{40}\text{Ar}/^{39}\text{Ar}$  dating alone, however, will not solve all Mogollon-Datil correlation problems. Ages of some units are too similar to be resolved, some units lack sanidine, and the technique is presently too expensive and time-consuming to use on an outcrop-by-outcrop basis. Many of these deficiencies, however, can be overcome by supplemental paleomagnetic analysis.

Paleomagnetic analysis is a well-established, inexpensive method for correlation of ignimbrites (Grommé et al. 1972; Best et al., 1973; Hildreth and Mahood, 1985). Many ignimbrites, both welded and non-welded, possess uniform thermoremanent magnetization (TRM) directions representing an accurate record of the geomagnetic field direction during rapid post-emplacement cooling (Dalrymple et al., 1965; Grommé et al. 1972; Best et al., 1973; Reynolds, 1977; Hoblitt et al., 1985; Weiss et al., 1989). Because of reversals and secular variation of the geomagnetic field, paleomagnetic analysis can potentially distinguish between individual volcanic units differing in age by as little as centuries (Grommé et al., 1972; Bogue and Coe, 1981). Paleomagnetic analysis offers the further potential of placing precisely dated units within the

established magnetic polarity time scale (McIntosh, dissertation, Chapter D).

Not all ignimbrites, however, carry simple, uniform, single-component TRMs; some exhibit complex, non-uniform remanent magnetization (RM) which is unsuitable for stratigraphic correlation. Some complicating factors include: 1) multicomponent TRMs reflecting sub-Curie-temperature compaction (Rosenbaum, 1986) or flowage (Ellwood, 1982), 2) non-uniform TRM directions due to secular variation of the geomagnetic field during initial cooling of the unit (Hagstrum and Gans, 1989), 3) chemical remanent magnetizations (CRMs) acquired during cooling, hydrothermal alteration, or weathering (Gose, 1970; Reynolds, 1977; Geissman et al., 1982), and 4) tectonic rotations (Hudson and Geissman, 1987; Wells and Hillhouse, 1989; Hagstrum and Gans, 1989; Geissman and Harlan, in review).

This paper examines the paleomagnetism of Mogollon-Datil ignimbrites and evaluates the utility of paleomagnetic correlation as an approach to solving some of the volcanic field's long-standing stratigraphic problems. The data presented represent part of a comprehensive effort in which paleomagnetic analyses and  $^{40}\text{Ar}/^{39}\text{Ar}$  dating have been combined to develop a time-stratigraphic framework for the Mogollon-Datil volcanic field. Other papers present the  $^{40}\text{Ar}/^{39}\text{Ar}$  dating work and time-stratigraphic framework (McIntosh et al., 1986; McIntosh, dissertation, Chapters B

and C), and implications for radiometric calibration of the mid-Tertiary geomagnetic polarity time scale (McIntosh, 1988; McIntosh, dissertation, Chapter D).

Previously published paleomagnetic studies of the Mogollon-Datil volcanic field include: 1) initial field-magnetometer polarity determinations for some of the units (Strangway et al., 1976), 2) a reconnaissance-scale determination of a mean paleomagnetic pole for older Mogollon-Datil units (Diehl et al., 1988) and associated progress reports (Diehl et al., 1982; McClannahan et al., 1983; McClannahan, 1984), and 3) progress reports for the present study (McIntosh, 1983; McIntosh et al., 1986).

#### GEOLOGIC SETTING

The Mogollon-Datil volcanic field (Fig. 1) is the northern tip of a once contiguous late Eocene-Oligocene volcanic field which extended from southwestern New Mexico into central Mexico. Mogollon-Datil volcanism commenced in the late Eocene with the eruption of voluminous intermediate composition stratovolcanoes. This activity was followed throughout the Oligocene by additional basaltic-andesite eruptions accompanied by episodic rhyodacitic to rhyolitic caldera volcanism. Between 36.2 and 24.3 Ma, about 30 major rhyolitic ignimbrite sheets were erupted, totalling some 8,000 km<sup>3</sup> in volume and covering at least 40,000 km<sup>2</sup> (McIntosh et al., 1986; Ratté et al., 1984; Osburn and Chapin, 1983b; Elston, 1984; McIntosh, dissertation, Chapter C).



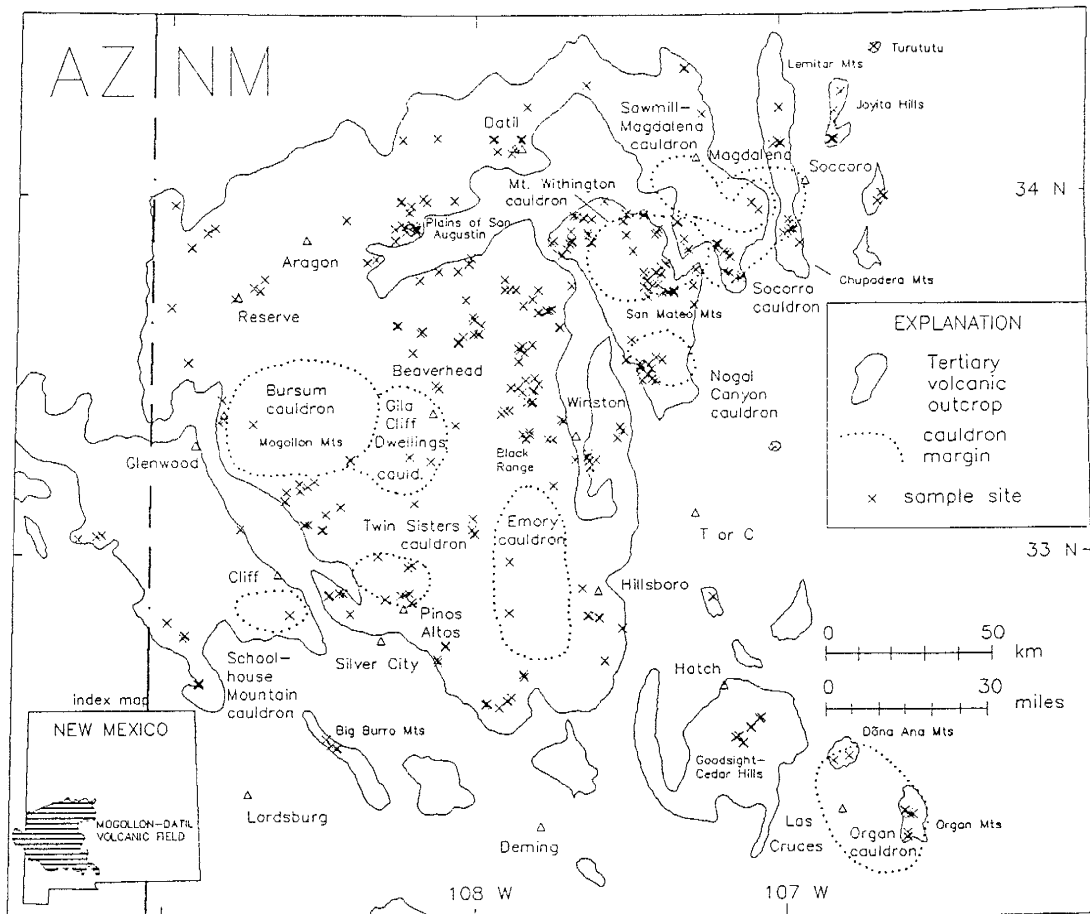


Figure 1. Map of Mogollon-Datil volcanic field showing paleomagnetic sampling sites, calderas, extent of Tertiary volcanic outcrops, and place names referred to in text.

These ignimbrites provide potentially ideal time-stratigraphic markers for use in a regional stratigraphic framework. Ignimbrite outflow sheets (Table 1) extend as far as 140 km from their source cauldrons, and overlap relations between distal fringes of outflow sheets record the relative age relationships of widely separated eruptive centers. Mogollon-Datil ignimbrite outcrops are generally fresh, although some areas have been affected by K-metasomatism or hydrothermal alteration (Chapin et al., 1978).

From the mid-Oligocene to the present, southwestern New Mexico has experienced basin-and-range and Rio Grande rift extensional tectonism, which has broken the region into fault-block mountain ranges separated by infilled basins. The degree of structural complexity varies widely within the volcanic field. In some ranges, volcanic units are nearly flat-lying (Ratté et al., 1984), whereas steep dips ( $45-70^\circ$ ) and low-angle faults in other areas indicate tectonic extension in excess of 100% (Chamberlin, 1983).

The structural complexity of the Mogollon-Datil volcanic field has proven a major obstacle to the development of an accurate, ignimbrite-based, regional stratigraphic framework. Discontinuous exposure patterns preclude the use of detailed mapping alone to correlate established stratigraphic sequences at widely separated localities. Two major correlation problems involve distinguishing among 5 younger (28.1-24.3 Ma) high-silica

rhyolitic ignimbrites and among 4 older (34.9-31.7 Ma) low-silica rhyolitic ignimbrites. In both cases, lithology and geochemistry are insufficient to uniquely identify the units. Identification is particularly problematic for the distal fringes of these units, where thin, unwelded facies of regional ignimbrites can easily be confused with locally derived, dome-related units.

An additional problem is the correlation of ignimbrite outflow sheets with their source cauldrons. Cauldrons have not yet been confidently located for many of the regional ignimbrites (Table 1; Ratté et al., 1984; Osburn and Chapin, 1983b) and outflow facies have not yet been recognized for the some of the established cauldron complexes (Seager and McCurry, 1988; Elston, 1984).

As will be presented below, many of the long standing Mogollon-Datil ignimbrite correlation problems have now been resolved using paleomagnetic analysis in concert with high-precision  $^{40}\text{Ar}/^{39}\text{Ar}$  dating.

#### FIELD AND LABORATORY PROCEDURES

In this study, a total of 3055 oriented samples were collected from 404 sites in ignimbrites in the Mogollon-Datil volcanic field (Fig. 1, Appendix 1). Initially, several geographically widespread sites were sampled from major ignimbrite outflow sheets in order to determine their mean remanence directions and assess within-unit directional variations. Later, sites were chosen to address specific

Table 1. Unit-mean paleomagnetic direction, VGP, extent, volume, source cauldron, and reference for Mogollon-Datil ignimbrites with 4 or more sampled sites.

Unit	$^{40}\text{Ar}/^{39}\text{Ar}$		volume ( $\text{km}^3$ )	n/na/nr polarity	mean direction				VGP				Caldera	Reference
	age (Ma)	extent (km)			inc	dec	k	$\alpha_{95}$	plat °N	plong °E	k	$\alpha_{95}$		
* Turkey Springs	24.3	62		R 15/2/2	-51.8	175.9	112.1	3.6	86.5	143.5	71.1	4.6		5
South Canyon	27.4	135	700	R 22/17/4	-29.8	202.6	75.6	3.6	63.1	198.1	90.1	3.3	Withington	7
Lemitar	28.0	78	450	N 10/8/3	36.6	358.9	128.3	4.3	76.4	264.9	156.9	3.9		7
Caronita Canyon	28.0	30	50	N 4/1/0	41.5	354.2	70.8	11.0	79.0	100.4	55.7	12.4		7
* Triangle C Ranch	28.1	58		N 5/0/1	49.2	357.3	304.4	4.4	85.9	105.7	275.3	4.6		10
Bloodgood Canyon	28.1	155	1000	R 22/1/0	-27.1	165.3	99.7	3.1	66.9	110.4	140.2	2.6	Bursum	8
Shelly Peak	(28.1)	96	100-200	R 8/2/0	-32.7	174.8	75.6	6.4	73.9	269.0	100.8	5.5	Gila Cliff Dwellings?	8
Garcia Camp	28.1	25		R 7/0/0	-48.8	185.4	137.2	5.2	84.1	198.3	135.7	5.2	dome	4
Vicks Peak	28.6	200	1050	R 24/7/1	-27.9	182.8	83.6	3.3	71.1	243.9	107.5	2.9	Nogal	7
La Jencia	28.9	158	1250	R 15/1/8	-49.3	168.2	111.6	3.6	79.4	147.5	115.3	3.6	Sawmill/Magdalena	7
Davis Canyon	29.0	125	200-400	R 6/0/1	-53.5	159.6	80.9	7.5	73.3	164.4	46.1	10.0	Gila Cliff Dwellings?	8
lower Tadpole Ridge	31.4	45		R 6/0/0	-71.1	203.8	38.2	11.0	61.8	100.3	13.9	18.6	Tadpole Ridge	6
Caballo Blanco	31.7	143		R 6/2/0	-46.0	171.4	228.9	4.4	80.7	126.8	190.2	4.9	Emory?	3
Hells Mesa	32.1	152	1200	R 10/7/1	-60.2	166.0	103.0	4.8	76.8	202.2	57.8	6.4	Socorro	7
Box Canyon	33.5	25	>100	R 12/2/3	-56.0	141.3	87.0	4.7	59.3	175.2	40.8	6.9		8
Blue Canyon	33.7	135		R 6/3/0	-37.3	144.4	139.3	5.7	56.0	148.8	117.1	6.2		7
Rockhouse Canyon	34.4	142		R 8/1/2	-55.6	144.8	104.5	5.4	61.6	173.2	46.1	8.2		7
* Lebya Well	34.7	72		R 4/0/0	-61.7	171.2	72.8	10.8	77.8	218.3	44.9	13.9		9
Kneeling Nun	34.9	213	>900	R 21/3/4	-43.7	167.1	70.6	3.8	76.5	132.8	63.6	4.0	Emory	2
Bell Top tuff 4	35.0	112		N 5/0/0	56.1	2.7	457.2	3.6	85.5	101.8	331.9	4.2		1
* Farr Ranch	35.6	143		N 9/2/2	50.4	345.5	122.8	4.7	77.8	156.0	122.0	4.7		9
Datil Well	35.5	140		N 5/0/0	53.3	19.9	143.9	6.4	73.3	155.7	111.4	7.3		7

Explanation: \* denotes informal unit name; ages in parentheses are based on stratigraphic constraints; lateral extent is maximum exposed width of outflow sheet; volume estimates are after McIntosh et al., 1986a; n=number of sites used in mean; na=number of sites rejected because of anomalous directions ( $>15^\circ$  from unit mean); nr=number of sites rejected because  $\alpha_{95} > 10^\circ$ ; inc and dec are unit-mean inclination and declination; plat and plong are position of VGP; k is Fishers (1953) precision parameter;  $\alpha_{95}$  is radius of cone of 95% confidence. References: 1. Clemons, 1976; 2. Elston et al., 1975; 3) Elston, 1957; 4. Duffield, 1988; 5. Ferguson, 1988; 6. Finneil, 1976; 7. Osburn and Chapin, 1983a; 8. Ratté et al., 1984; 9. Ratté and McIntosh, 1989; 10. J. Ratté, pers. com., 1988.

stratigraphic and tectonic questions. Finally, local tuff units and lavas were sampled, primarily to fill in gaps in the magnetic polarity record of the volcanic field. Results from the lavas are only briefly considered in this paper, specifically for calculations of paleomagnetic pole positions.

Wherever possible, sampling sites were selected in well-exposed and minimally weathered outcrops. Hydrothermally altered, metasomatized, and structurally complex areas were generally avoided, although some were sampled for comparison with fresh or structurally undisturbed rocks. Wherever possible, topographically exposed ridges and slopes were avoided, in order to minimize lightning-induced isothermal remanent magnetizations (IRMs). In practice, however, it was necessary to collect almost half of the sites from topographically exposed outcrops.

Oriented cores were field-drilled at 386 sites and oriented hand samples were collected from 18 sites within designated wilderness areas. For most of the sites in regional ignimbrites, 6 to 9 samples were collected at 1 to 10 m intervals at an inferred common stratigraphic level. At 5 sites, stratigraphic sequences of 12 to 20 samples were collected, in order to assess within-unit vertical magnetic variations. At 15 sites in local tuff units, where mainly the magnetic polarity was of interest, only 4 samples were collected. Ninety percent of all field-drilled and hand samples were oriented by suncompass to an accuracy of about

2°; the remainder were oriented by magnetic compass to an accuracy of about 4°.

Much care was taken in assessment of structural attitude at each site, because attitude is commonly the largest uncertainty in paleomagnetic studies of ignimbrites (Grommé et al., 1972, Geissman et al., 1982; Hagstrum and Gans, 1989; Wells and Hillhouse, 1989). Map-scale attitudes of sedimentary units, ignimbrite sheets, or ignimbrite cooling units were determined wherever possible, otherwise the attitudes of local stratigraphic contacts, pumice foliations, or welding breaks were measured.

In the laboratory, standard-sized specimens (2.35 cm diameter by 2.1 cm long) were prepared and natural remanent magnetizations (NRMs) were measured using the modified, microcomputer-interfaced Schonstedt SSM-1 spinner magnetometer at the New Mexico Bureau of Mines and Mineral Resources. Two pilot samples from each site were then subjected to stepwise alternating field (AF) demagnetization in peak fields of 2 to 50 mT using a home-built single-axis demagnetization unit. Results were analyzed using modified orthogonal demagnetization diagrams (Zijderveld, 1967; Roy and Park, 1974) and the remaining samples were demagnetized to peak fields required to produce univectoral decay. Selected samples were also subjected to stepwise thermal demagnetization to temperatures of 100-750°C using a Schonstedt TSD-1. The 2-G Model 760R cryogenic magnetometer and Schonstedt GSD-1 AF demagnetization unit at the

University of New Mexico were used to analyze samples which were weakly magnetized ( $<10^4$  A/m) or required AF demagnetization to inductions exceeding 50 mT.

Principle component analysis (PCA) (Kirschvink, 1980) was used to determine the direction of characteristic RM of samples showing complex demagnetization behavior. Individual sample data with maximum angular deviations (MAD) (Kirschvink, 1980) in excess of  $18^\circ$  were excluded from these calculations. For the majority of samples, which exhibited demagnetization segments showing simple univectoral decay toward the origin, the RM at the demagnetization step which minimized dispersion was accepted as characteristic. For these well-behaved samples, this approach yields site-mean results statistically indistinguishable from those of PCA or vector-subtraction techniques (Table 2).

Site-mean directions and cones of 95% confidence ( $\alpha_{95}$ ) were determined using Fisher (1953) statistics. Individual samples showing strongly divergent directions or lacking univectoral AF demagnetization decay segments were excluded from site-mean calculations. In order to maximize the precision of the data set, remagnetization circle techniques were avoided. All site-mean data less precise than an arbitrary cutoff value ( $\alpha_{95} > 10^\circ$ ) were considered unsuitable for detailed stratigraphic correlations and were excluded from unit-mean calculations. Except where otherwise noted, all site-mean directions reported in this paper have been corrected for structural attitude. Because the study area

Table 2. Comparison of site-mean directions for representative Type 1, 2 and 3 sites using different methods for determining characteristic RM.

site	type	n	uniform AF demagnetization level					PCA					$\delta$
			dm	inc	dec	k	$\alpha_{95}$	n	inc	dec	k	$\alpha_{95}$	
141	1	8	30	48.7	359.0	175	4.2	8	47.7	355.1	173	4.2	2.8
431	1	9	10	-19.1	158.2	611	2.1	9	-18.5	158.2	638.5	2.2	0.6
16	2	7	40	-45.6	167.0	358	3.2	7	-44.5	166.3	287.0	3.6	1.2
140	2	8	40	49.1	2.9	340	3.0	8	48.0	0.2	171.0	4.3	2.1
210	3	8	40	-20.0	284.8	17	13.8	8	-43.5	148.8	88.0	5.9	104.8
314	3	8	40	-59.1	228.8	7	22.5	7	-45.5	155.4	78.0	6.9	44.4

Explanation: type denotes demagnetization behavior: 1=TRM, 2=TRM+IRM, 3=TRM+CRM; PCA is principle component analysis (Kirschvink, 1980); n is number of samples used in mean; dm is AF demagnetization level (mT); inc and dec are site mean inclination and declination; k is Fishers (1953) precision parameter;  $\alpha_{95}$  is radius of cone of 95% confidence;  $\delta$  is angular difference between mean directions of the 2 methods.



extends over only  $1.5^\circ$  of latitude, paleomagnetic directions have been compared directly instead of converting them to virtual geomagnetic poles (VGPs). Site-mean VGPs have been calculated for well-constrained ignimbrites, and these values show precision parameters similar to those of mean RM directions. In the discussions below, the North American reference pole ( $81.5^\circ\text{N}$ ,  $138.5^\circ\text{E}$ ) of Diehl et al. (1988) has been used to estimate the time-averaged Oligocene geomagnetic field direction for the field area ( $D=350.5^\circ$ ,  $I=50^\circ$ ).

In addition to paleomagnetic analyses, a variety of rock magnetic properties were investigated. Magnetic mineralogy of selected samples was assessed by examining polished sections with an oil-immersion, reflected light microscope capable of magnifications of 1250X. Thermomagnetic analyses were performed using a vertical Curie balance at the University of Colorado. For selected samples, a pulsed, direct-current (DC) induction coil capable of 1.3 Tesla peak fields was employed to determine IRM acquisition curves, and AF and DC backfield demagnetization techniques were applied to samples given saturation IRMs. Also studied in selected samples was the AF demagnetization behavior of anhysteretic remanent magnetization (ARM) components acquired using 100 mT peak AF fields in an applied field of 0.06 mT. A Sapphire SI-2 computer-interfaced induction coil was used to measure low-field bulk susceptibility and anisotropy of susceptibility,

and to monitor mineralogical changes during thermal demagnetization. The anisotropy of magnetic susceptibility (AMS) of several Mogollon-Datil ignimbrites was also studied in detail; these results will be reported elsewhere.

#### NATURE OF REMANENCE

The nature of the paleomagnetic remanence in the 404 ignimbrite sites studied can be divided into 4 categories, primarily on the basis of AF and thermal demagnetization behavior. The following sections present demagnetization behavior, rock-magnetic data, and oxide mineralogy for each of these categories, here informally designated Types 1 to 4.

##### Simple TRM (Type 1)

Samples from 48% of the 404 ignimbrite sites exhibited strong ( $10^{-2}$  to  $10^1$  A/m, Fig. 2), well-grouped ( $\alpha_{95}=2$  to  $10^\circ$ ) NRM vectors which decayed univectorally toward the origin in response to both AF and thermal demagnetization (Figs. 3,4). Characteristic RMs isolated from these Type 1 samples by AF demagnetization at 15-50 mT generally showed modest improvements in grouping ( $\alpha_{95}=1$  to  $8^\circ$ ) relative to NRM directions (Table 3; Appendix 1).

Demagnetization behavior, rock-magnetic analyses, and petrographic observations together indicate that the NRMs of Type I samples consist of various combinations of three different parallel-directed RM components believed to be carried by finely dispersed single-domain (SD) and pseudo-single-domain (PSD) magnetite, hematite, and maghemite. The

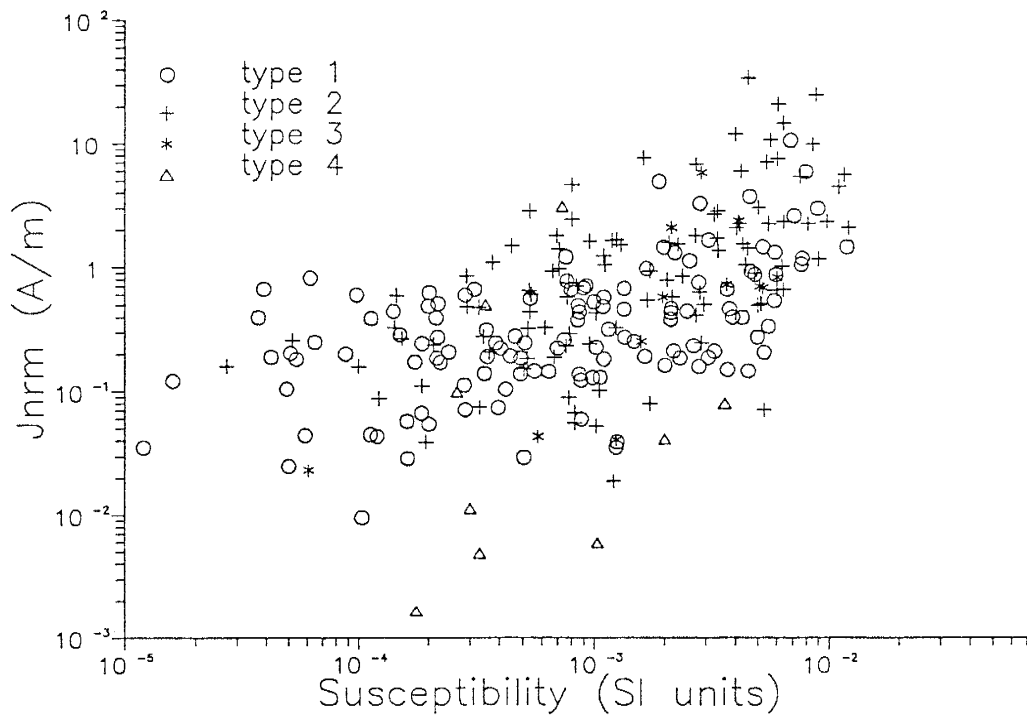


Figure 2. Site-mean NRM intensity ( $J_{nrm}$ ) versus low-field bulk susceptibility. Site types 1 to 4 are defined by demagnetization behavior as explained in text.

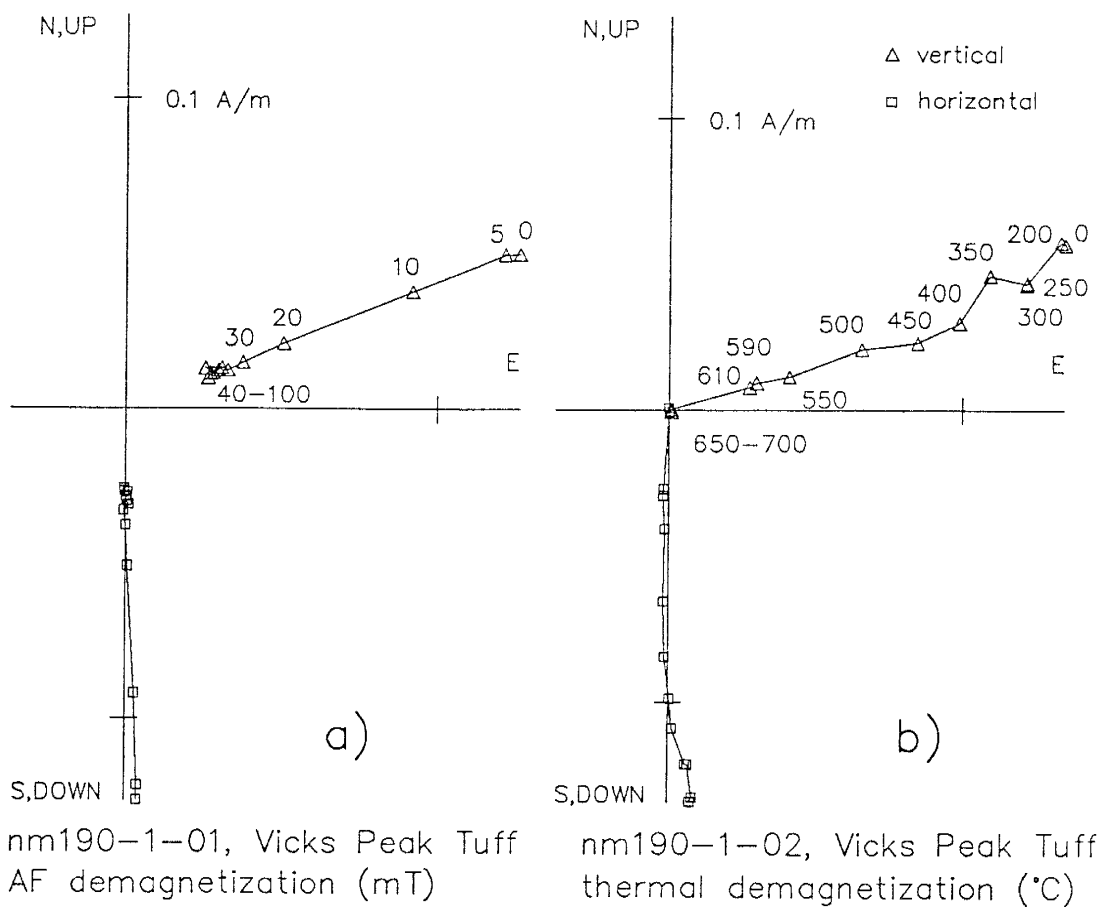


Figure 3. Orthogonal demagnetization diagrams demonstrating simple, univectoral, AF and thermal demagnetization behavior characteristic of TRM bearing samples from 48% of studied sites: a,b) Samples from site 190 show remanence dominantly carried by magnetite. (Figure continued on following page.)

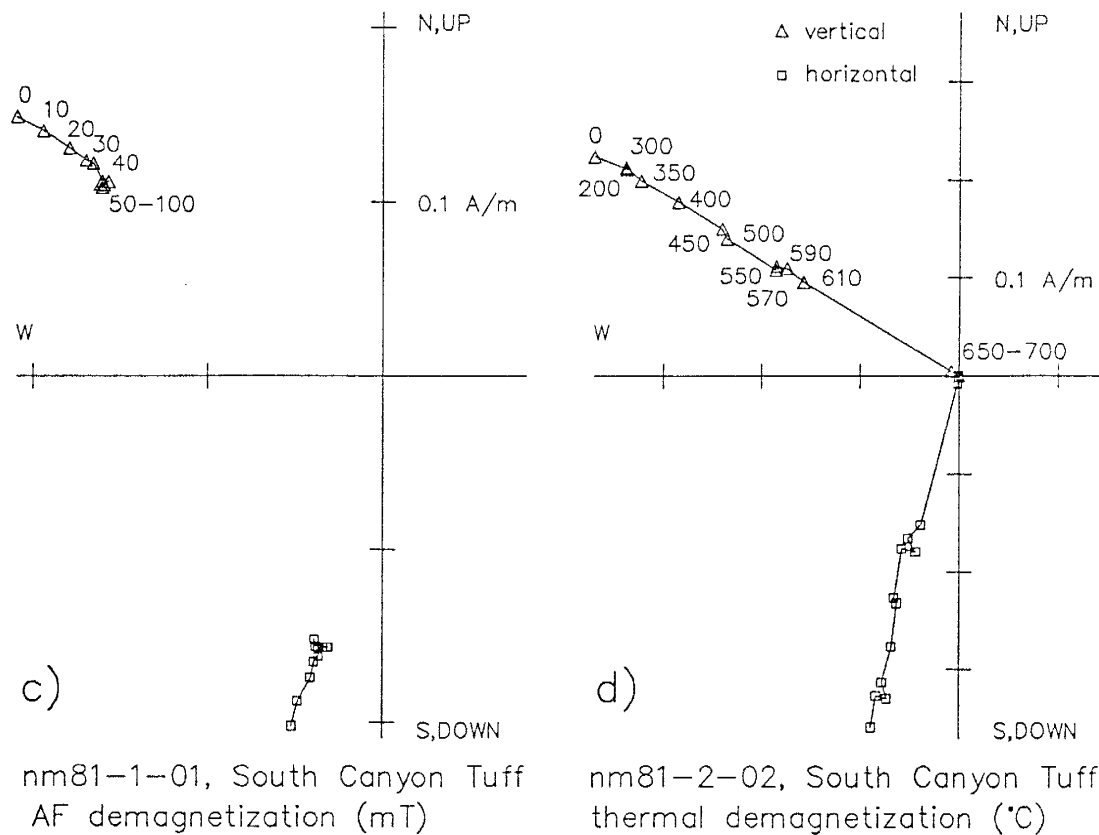


Figure 3 (continued). Orthogonal demagnetization diagrams demonstrating simple, univectoral AF and thermal demagnetization behavior characteristic of TRM bearing samples from 48% of studied sites: c,d) Samples from site 81 show remanence carried by a combination of magnetite and hematite. (Figure continued on following page.)

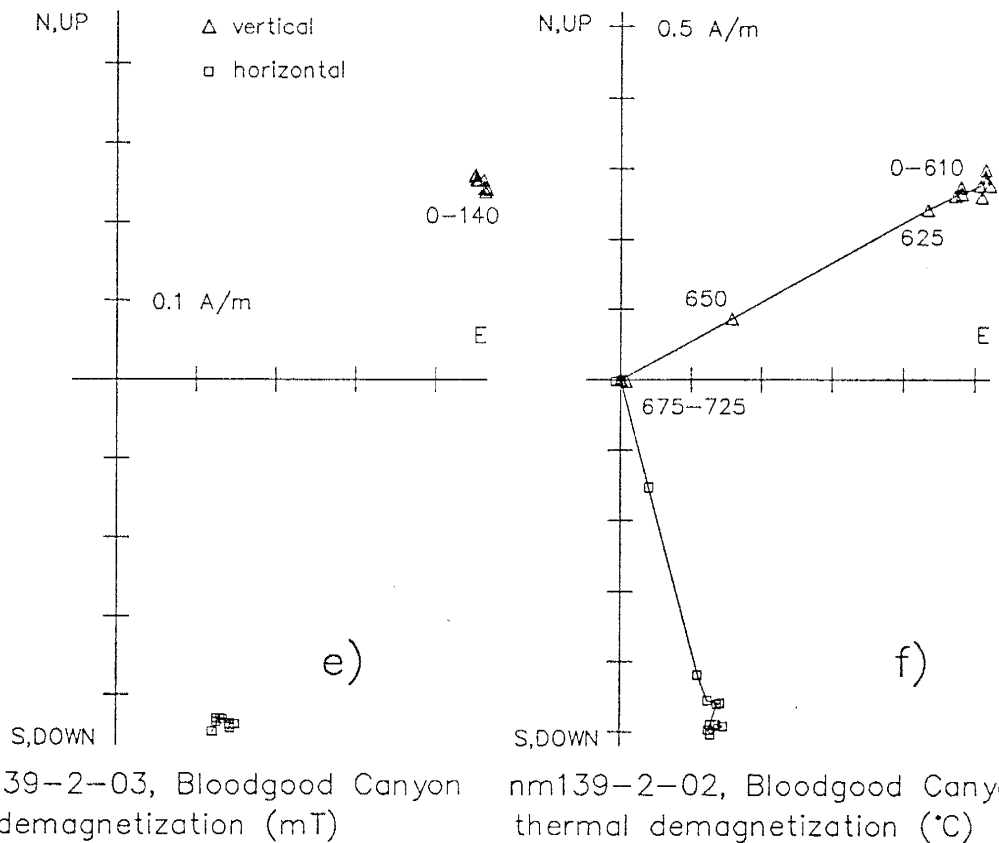
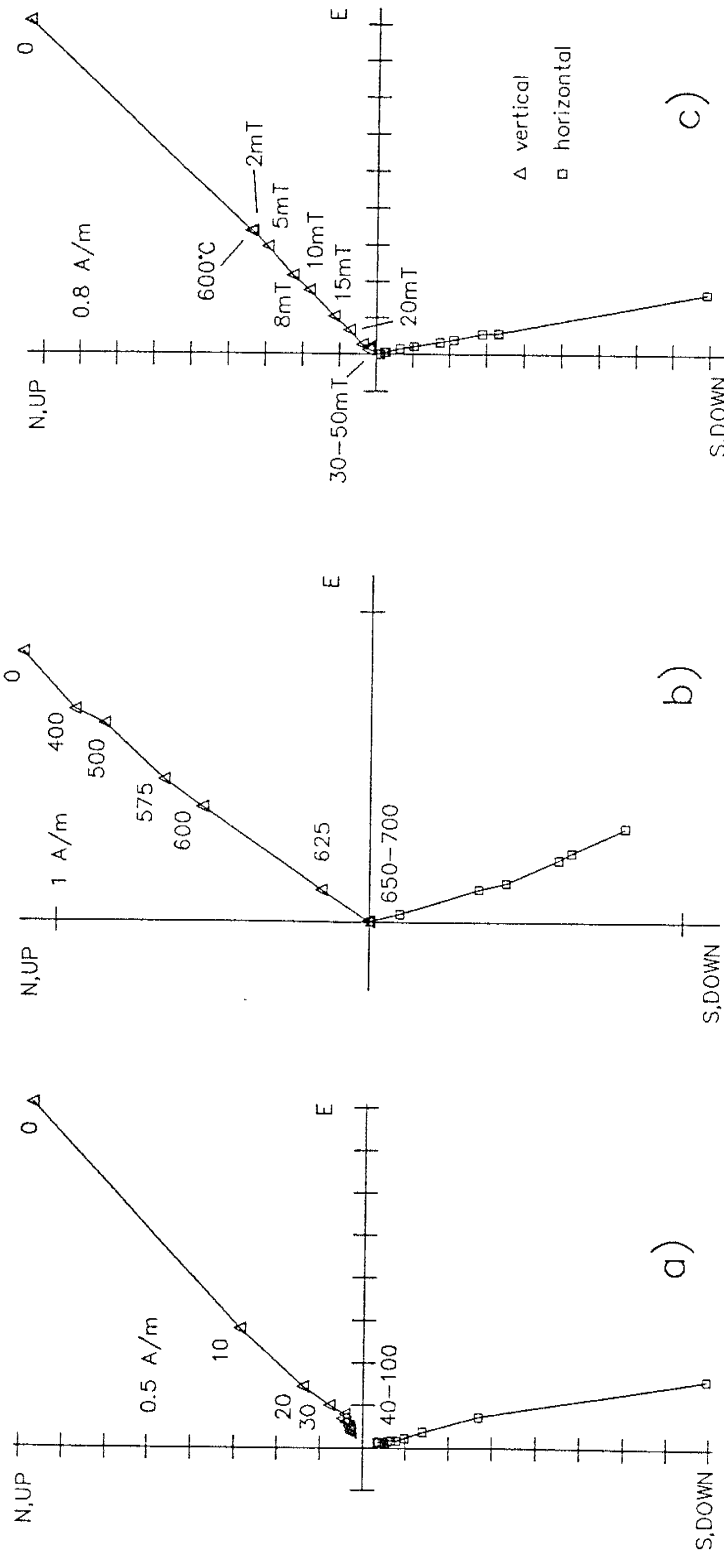


Figure 3 (continued). Orthogonal demagnetization diagrams demonstrating simple, univectoral AF and thermal demagnetization behavior characteristic of TRM bearing samples from 48% of studied sites: e, f) Samples from site 139 show remanence carried dominantly by hematite. Orthogonal projection in this and following figures is after Roy and Park (1967).



nm103-1-01, Kneeling Nun  
AF demagnetization (mT)

nm103-3-02, Kneeling Nun  
thermal demagnetization (°C)

nm103-5-02, Kneeling Nun Tuff  
thermal then AF

Figure 4. Orthogonal demagnetization diagrams of samples from site 103 show significant low-coercivity, high-temperature magnetizations apparently carried by magnetite which is stable to unusually high temperatures. This magnetization is best shown by c), where AF demagnetization was employed following thermal demagnetization to 600°C.









Table 3. (continued) Site-mean paleomagnetic data from Mogollon-Datil ignimbrites.

site	lat (°N)	long (°W)	dip	str	dm	inc	dec	k	$\alpha_{95}$	n	type	site	lat (°N)	long (°W)	dip	str	dm	inc	dec	k	$\alpha_{95}$	n/T	type	
<u>tuff of Table Mountain (33.9 Ma)</u>																								
296	32.60	107.96	0	0	40	-36.9	181.5	43	9.3	7	3	unit-mean direction: -46.7 168.6 21 28.0 3/0/0												
<u>Cooney Tuff (approx. 34 Ma)</u>																								
079	33.38	108.82	13	115	40	-51.4	145.5	160	4.4	8	2	305	33.38	108.83	0	0	30	-31.4	175.3	750	2.0	8	1	
229	33.06	109.23	8	317	40	-54.1	182.8	190	4.0	8	1	unit-mean direction: -46.7 168.6 21 28.0 3/0/0												
<u>Blue Canyon Tuff (33.7 Ma)</u>																								
084	34.25	107.83	2	90	30	-38.5	152.4	111	5.8	7	2	375	33.92	108.23	4	320	40	-33.0	149.4	747	2.5	6	2	
093	33.92	108.25	3	135	40	-36.7	145.1	262	3.7	7	2	042	34.16	106.81	52	207	30	-41.7	171.7	232	3.6	8	2	Ad
240	33.99	108.07	5	195	40	-32.7	140.8	71	6.6	8	2	321	33.53	107.42	24	295	40	-24.9	117.6	277	3.6	7	1	Acg
328	33.90	108.23	2	90	40	-40.5	146.7	109	5.3	8	2	516	33.94	107.62	21	202	50	-59.5	179.2	115	5.7	7	2	Acg
354	33.53	107.46	28	317	30	-41.1	131.4	360	2.9	8	1	unit-mean direction: -37.3 144.4 139 5.7 6/3/0												
<u>Rockhouse Canyon Tuff (approx. 34.6)</u>																								
070	34.00	106.66	43	175	40	-55.6	162.9	155	4.9	7	2	439	33.90	108.20	3	120	30	-50.8	135.7	279	3.3	8	2	
086	34.16	107.85	7	152	40	-50.1	144.2	338	3.6	6	2	468	34.31	107.63	15	135	30	-61.4	130.0	201	3.9	8	1	
089	33.91	108.20	6	180	80	-54.5	145.8	113	5.7	7	2	517	33.94	107.62	21	202	30	-49.7	173.9	606	2.7	6	2	Ac
239	33.99	108.07	5	195	30	-56.8	145.7	2067	1.2	8	1	145	33.82	108.02	0	0	30	28.6	45.0	2	69.1	8	3	R
371	33.80	108.06	0	0	40	-55.5	163.7	491	2.7	7	1	405	33.43	107.81	13	160	30	-35.4	151.8	2	53.7	8	1	R
403	33.46	107.81	13	140	40	-55.6	133.4	823	1.9	8	1	unit-mean direction: -55.6 144.8 105 5.4 8/1/2												
<u>tuff of Lebya Well (34.7 Ma)</u>																								
088	33.91	108.19	6	145	40	-63.6	163.1	234	3.6	8	2	436	33.96	108.22	0	0	40	-59.9	180.0	79	8.7	5	2	
231	33.97	108.98	4	274	40	-50.9	174.4	397	2.8	8	1	404	33.43	107.81	13	160	40	-46.5	144.8	102	6.0	7	1	
438	33.90	108.20	3	120	30	-71.7	162.1	101	5.5	8	2	unit-mean direction: -61.7 171.2 73 10.8 4/0/0												
<u>Kneeling Nun Tuff (34.9 Ma)</u>																								
092	33.92	108.20	3	122	40	-47.5	165.3	96	5.7	8	2	324	33.92	108.21	9	110	40	-31.4	171.8	43	9.3	7	2	
103	32.85	107.89	40	152	30	-44.6	163.2	113	5.2	8	1	374	33.90	108.20	2	300	30	-41.5	161.1	401	2.8	8	2	
110	33.47	107.81	12	180	20	-47.7	170.5	299	3.9	6	1	383	33.98	108.16	0	0	30	-33.6	178.6	290	5.4	4	2	
118	33.33	107.75	0	0	20	-45.5	166.3	259	3.5	8	1	416	32.89	107.23	10	0	40	-38.8	181.3	515	2.4	8	1	
123	32.49	107.13	5	250	30	-35.9	162.0	168	4.3	8	1	420	33.27	107.60	11	111	PCA	-32.1	177.6	550	3.3	5	3	
126	32.83	107.59	13	322	30	-54.3	164.5	47	8.2	8	2	456	32.68	107.84	8	42	30	-44.6	146.6	246	3.5	8	2	
179	33.39	107.72	0	0	30	-43.2	176.3	869	1.9	8	1	465	34.16	108.24	2	135	40	-55.2	162.6	142	4.7	8	2	
202	32.76	108.09	0	0	30	-52.7	179.5	171	4.2	8	1	127	32.81	107.52	15	175	30	-36.8	140.1	177	4.2	8	1	Ac
208	32.56	107.08	7	225	40	-44.6	158.0	42	8.7	6	3	376	33.92	108.23	0	0	30	-31.5	153.7	168	4.3	8	1	Ac
210	33.29	107.63	18	25	PCA	-43.5	148.8	88	5.9	8	3	498	32.89	108.29	30	204	30	-18.2	150.2	464	2.6	8	1	Ac
256	33.34	107.82	8	195	30	-41.6	169.7	488	2.5	8	1	311	33.53	107.46	34	332	40	-75.7	138.9	15	14.7	8	4	R
294	32.59	107.92	0	0	10	-39.0	175.0	515	2.4	8	1	384	33.99	108.17	0	0	30	41.3	297.7	2	65.0	8	2	R
295	32.60	107.97	0	0	40	-46.5	168.5	850	1.9	8	1	412	33.27	107.63	8	194	40	66.5	29.3	11	29.0	4	4	R
314	33.35	107.52	24	0	PCA	-45.5	155.4	78	6.9	7	3	413	33.27	107.63	8	194	40	-10.6	107.7	2	36.3	4	2	R
<u>tuff of Stone House Ranch (approx 35.0 Ma)</u>																								
177	33.38	107.71	10	130	30	52.2	325.1	349	3.0	8	1	213	33.28	107.63	8	240	30	48.1	326.2	116	5.6	7	1	
212	33.28	107.63	8	240	30	30.1	321.3	64	7.0	8	1	411	33.27	107.63	8	194	40	45.3	53.6	12	28.1	4	2	R
<u>Bell Top 4 Tuff (35.0 Ma)</u>																								
125	32.51	107.15	8	285	40	54.4	5.9	636	2.2	8	1	211	33.28	107.63	8	240	PCA	55.4	1.8	401	3.0	7	9	3
206	32.53	107.11	3	280	100	58.9	5.3	125	6.8	5	2	317	33.37	107.52	30	330	30	51.5	0.5	618	2.2	8	2	
209	32.55	107.08	7	225	30	60.1	0.1	970	1.8	8	1	unit-mean direction: 56.1 2.7 457 3.6 5/0/0												
<u>tuff of Farr Ranch (35.6 Ma)</u>																								
065	33.77	107.44	15	162	30	50.0	347.7	331	3.7	6	2	390	33.50	107.42	16	0	30	51.6	347.1	410	2.7	8	1	
066	33.98	106.68	15	162	40	51.5	348.9	492	2.8	7	2	437	33.97	108.21	0	0	40	41.1	344.7	109	5.8	7	2	
071	34.00	106.65	43	175	40	52.8	354.0	965	1.8	8	1	238	33.99	108.07	5	195	100	33.3	2.7	39	8.9	8	2	Ae
091	33.92	108.20	3	122	40	57.7	345.7	423	2.7	8	2	313	33.34	107.53	26	347	40	27.1	351.0	157	4.8	7	1	Acg
308	33.50	107.42	19	293	30	43.7	337.9	310	3.1	8	1	178	33.38	107.71	9	5	PCA	22.2	43.4	28	12.8	6	3	R
316	33.38	107.52	30	330	30	43.5	339.3	302	3.2	8	1	385	33.99	108.17	0	0	100	52.8	14.1	11	24.3	5	2	R
388	33.49	107.41	10	0	30	60.7	347.6	206	3.9	8	1	unit-mean direction: 50.4 345.5 123 4.7 9/2/2												
<u>Datil Well Tuff (35.5 Ma)</u>																								
085	34.16	107.85	7	152	40	49.4	15.5	156	4.8	7	2	466	34.16	108.13	2	135	40	55.0	19.8	488	3.5	5	2	
090	33.92	108.20	3	122	40	56.3	20.8	647	2.2	8	2	481	33.31	107.02	9	272	100	59.6	31.3	70	6.6	8	2	
237	33.99	108.07	5	195	35	45.6	15.1	65	7.5	7	2	unit-mean direction: 53.3 19.9 144 6.4 5/0/0												

Table 3. (continued) Site-mean paleomagnetic data from Mogollon-Datil ignimbrites.

site	lat (°N)	long (°W)	dip	str	dm	inc	dec	k	$\alpha_{95}$	n	type	site	lat (°N)	long (°W)	dip	str	dm	inc	dec	k	$\alpha_{95}$	n/t	type	
<u>Sugarlump/Rubio Peak Tuff sequence (approx 36-35 Ma)</u>																								
<u>upper Sugarlump Tuff member (35.2 Ma)</u>												unit-mean direction:												
455	32.84	107.60	15	340	30	41.4	346.0	338	3.0	8/8	1	461	32.72	108.12	6	4	7	30	44.0	347.3	426	12.1	2/0/0	
<u>lower Sugarlump Tuff member</u>												unit-mean direction:												
460	32.71	108.12	7	32	40	63.7	340.4	166	5.2	6/8	2	509	32.48	108.46	2	8	31	5	30	62.3	337.7	961	8.1	2/0/0
<u>basal Sugarlump Tuff member</u>																								
462	32.61	107.90	8	125	30	49.2	271.1	250	3.5	8/8	2 E													
<u>upper Rubio Peak tuff member</u>																								
347	33.76	107.68	30	270	30	-34.4	175.1	150	4.5	8/8	1													
<u>lower Rubio Peak tuff member</u>												unit-mean direction:												
463	32.61	107.89	7	110	20	-63.8	152.6	154	5.4	6/8	2	458	32.62	107.88	7	165	10	-40.1	166.1	129	4.9	8/8	1	
<u>older Steeple Rock tuffs (approx. 35 Ma)</u>																								
512	32.78	108.94	33	298	40	-60.8	158.7	81	6.2	8/8	2	513	32.78	108.94	27	296	50	50.8	26.7	141	4.7	8/8	2	
<u>Bell Top 3 Tuff (35.7 Ma)</u>												unit-mean direction:												
122	32.49	107.13	5	250	30	70.2	329.2	123	5.0	8/8	2	205	32.53	107.11	3	280	30	69.9	329.9	9000	1.6	2/0/0		
<u>Bell Top Tuff 2 (&gt;35.7 Ma)</u>												unit-mean direction:												
121	32.49	107.13	5	250	30	42.5	348.4	61	8.6	6/8	2	204	32.53	107.10	3	280	30	39.7	350.0	210	17.3	2/0/0		
<u>Organ Mountain Intracaldera Sequence (36.2-35.5 Ma)</u>																								
<u>Dona Ana Tuff (35.5 Ma)</u>												unit-mean direction:												
130	32.45	106.79	15	260	30	64.2	344.4	146	6.3	5/8	1	203	32.44	106.84	19	165	30	54.4	329.7	109	5.3	8/8	1	
<u>Squaw Mountain Tuff (35.8 Ma)</u>												unit-mean direction:												
417	32.29	106.60	46	158	30	66.9	10.5	43	9.3	7/8	2	529	32.29	106.61	44	162	30	49.9	350.4	230	3.4	9/9	2	
<u>Achenback Park Tuff (approx. 36 Ma)</u>												unit-mean direction:												
418	32.28	106.59	44	170	30	47.0	321.6	83	6.7	7/9	1	484	32.24	106.60	26	215	40	42.1	26.1	736	2.0	8/8	2	
419	32.29	106.58	43	162	30	51.3	0.1	150	4.2	9/9	1													
<u>Cueva Tuff (36.2 Ma)</u>												unit-mean direction:												
482	32.22	106.60	26	215	30	-67.1	208.4	121	5.5	7/8	2	483	32.22	106.60	26	215	40	-53.4	220.3	4	67.8	2/0/1		
485	32.22	106.60	26	215	30	-65.4	167.4	99	5.6	8/8	1													
<u>local dome-related ignimbrites (35 - 28 Ma)</u>																								
150	32.89	108.48	15	330	40	-43.1	134.8	1	75.7	8/8	4 R	330	33.99	108.24	3	157	0	-68.2	50.1	2	47.9	8/8	4 R	
151	32.90	108.47	15	330	30	-62.8	152.4	538	2.4	8/8	2	340	33.87	107.20	43	342	35	-38.0	168.5	121	8.5	4/4	2	
152	32.90	108.47	15	330	30	-37.2	158.3	148	4.6	8/8	2	341	33.87	107.20	43	342	100	-53.2	52.6	1	180.0	4/4	4 R	
174	33.95	107.68	14	197	40	28.2	320.8	84	7.4	6/9	2	342	33.87	107.20	43	342	60	-47.1	182.4	8	35.4	4/4	4 R	
214	33.27	107.67	14	155	30	-1.5	245.8	1	76.9	8/8	4 R	360	33.56	107.41	0	0	40	-39.8	157.3	17	13.7	8/8	2 R	
220	33.59	107.81	0	0	30	-55.4	146.6	471	2.6	8/8	2	362	33.55	107.39	16	42	40	-34.9	153.1	32	9.9	8/8	2	
221	33.59	107.85	0	0	30	-49.5	207.0	1004	1.8	8/8	2	365	33.94	107.64	18	260	35	-21.8	192.7	7	27.3	6/4	4 R	
222	33.57	107.84	15	182	30	-62.7	120.9	417	2.7	8/8	1	378	34.12	107.88	5	82	40	-47.9	182.3	11	19.1	7/8	4 R	
223	33.58	107.85	10	167	30	-52.5	184.0	200	3.9	8/8	1	382	34.13	107.93	4	40	40	-59.1	192.2	23	55.4	2/8	4 R	
224	33.58	107.86	10	187	30	-56.2	197.0	238	4.3	6/8	1	396	33.51	107.43	41	310	30	-59.5	69.6	3	61.7	4/4	4 R	
225	33.55	107.86	15	207	30	-44.8	177.5	590	2.3	8/8	1	398	33.51	107.44	41	310	40	56.7	328.2	379	3.5	6/8	1	
264	32.65	108.89	18	320	40	-30.7	193.7	221	3.7	8/8	2	425	33.86	107.30	13	42	30	19.0	200.6	4	56.2	4/4	4 R	
265	32.65	108.89	18	320	2	60.3	26.9	52	9.4	6/8	1	427	33.85	107.30	13	42	2	-8.7	117.9	15	24.8	4/4	4 R	
307	32.90	108.44	18	307	40	-67.9	155.3	48	8.8	7/8	2	445	33.90	106.97	8	0	40	-4.5	302.1	2	57.4	4/4	4 R	
309	33.51	107.46	20	208	30	33.8	20.5	23	54.3	2/4	4 R	448	33.91	106.96	0	0	40	-37.2	182.8	8	34.5	4/4	4 R	
320	33.52	107.42	18	305	40	-44.3	159.5	70	8.1	6/8	2	454	32.84	107.63	18	340	30	58.7	353.0	1078	2.8	4/4	1	
323	33.53	107.42	24	295	30	-30.8	160.3	69	6.7	8/8	2	457	32.67	107.84	5	343	30	40.6	67.8	2	46.7	8/8	4 R	
327	33.90	108.23	2	90	40	-37.5	181.4	334	3.0	8/8	2	475	33.14	108.44	24	276	50	-24.8	200.3	494	4.1	4/4	2	

Explanation: Site mean paleomagnetic data AF demagnetization level (dm); PCA=principal component analysis used to identify TRM; inc and dec are site-mean inclination and declination; k is Fishers (1953) precision parameter; n - for sites: denotes number of samples used in mean/total, for unit-means: denotes number of sites used in mean/number of sites rejected because of anomalous directions (>15° from unit mean)/number of sites rejected because  $\alpha_{95} > 10^\circ$ ; type denotes demagnetization behavior: 1=TRM, 2=TRM+IRM, 3=TRM+CRM, 4=TRM+lithic hosted components; R=rejected site ( $\alpha_{95} > 10^\circ$ ); A=anomalous site, differs from unit-mean by >15°, following letter gives probable reason: Aa=poor attitude control, Ab=basal site in area of pre-eruptive topographic relief, Ac=local structural complexity, Ad=tectonically extended area, Ae=unremoved CRM or IRM components, AF=secular variation recorded in thick intracaldera facies, Ag=possible incorrect unit ID, E=excluded from pole calculations because of anomalous VGP.

relative contributions of these three magnetizations to the NRM tend to be consistent within sites, but vary widely among different sites.

The NRM of the majority of ignimbrite sites is dominated by RMs which show low unblocking-temperatures ( $<580^{\circ}\text{C}$ ) and moderate coercivities (median destructive induction (MDI)=10-50 mT) characteristic of fine-grained magnetite (or low-Ti titanomagnetite) (Geissman et al., 1983). These magnetite-carried RMs are in many cases accompanied by lower intensity magnetizations with higher unblocking-temperatures ( $>580^{\circ}\text{C}$ ) and high coercivities (MDI $>100$  mT) characteristic of hematite. The RM intensities of these samples decreased by 50 to 99% during AF demagnetization to 30-50 mT, but showed little change at higher peak inductions (Figs. 3a). Similar intensity decreases resulted from thermal demagnetization to 550-600 $^{\circ}\text{C}$ , and most of the remaining remanence was unblocked in the 600-650 $^{\circ}\text{C}$  temperature range (Figs. 3b). Remaining small fractions of remanence, parallel to the NRM but typically  $<1\%$  of NRM intensity, were unblocked between 650 and 720 $^{\circ}\text{C}$ .

For the remaining minority of samples, the NRM is dominated by RMs showing higher unblocking temperatures ( $>580^{\circ}\text{C}$ ) and varying coercivities. In most cases, these high-unblocking-temperature magnetizations show high coercivities (MDI  $>140$  mT) characteristic of hematite and are accompanied by subordinate magnetite-carried RMs (Fig. 3c,d). Hematite-carried RMs entirely dominate the NRM of

some samples from flow tops or areas of hydrothermal alteration (Fig. 3e,f). In these cases the NRM is completely unaffected by AF demagnetization to 140 mT (Fig. 3e) and shows unblocking temperatures between 610 and 675°C (Fig. 3f).

Portions of the high-unblocking-temperature magnetizations in some samples show coercivities ( $MDI < 50$  mT) which are far too low for hematite. As will be discussed in a following section, the carrier of these magnetizations is interpreted to be finely dispersed maghemite. In these samples, the fraction of remanence remaining after heating to 600°C was considerably larger than that remaining after AF demagnetization to 20-100 mT (Figs. 4a,b). The behavior of this maghemite-carried RM component is best recognized by applying AF demagnetization following thermal demagnetization to 600°C (Fig. 4c).

The presence of both magnetite and higher Curie-temperature phases in most Type 1 samples is supported by strong-field induced magnetization versus temperature (JsT) experiments. JsT curves all display a convex-downward segment with a primary Curie temperature between 540 and 590°C (Fig. 5b-d). In some cases (Fig. 5b), this primary Curie temperature is well-defined, similar to JsT curves of pure magnetite (Fig. 5a). More commonly, this lower Curie temperature is indistinct, and accompanied by an approximately linear, higher temperature segment with an even less distinct secondary Curie temperature between 610

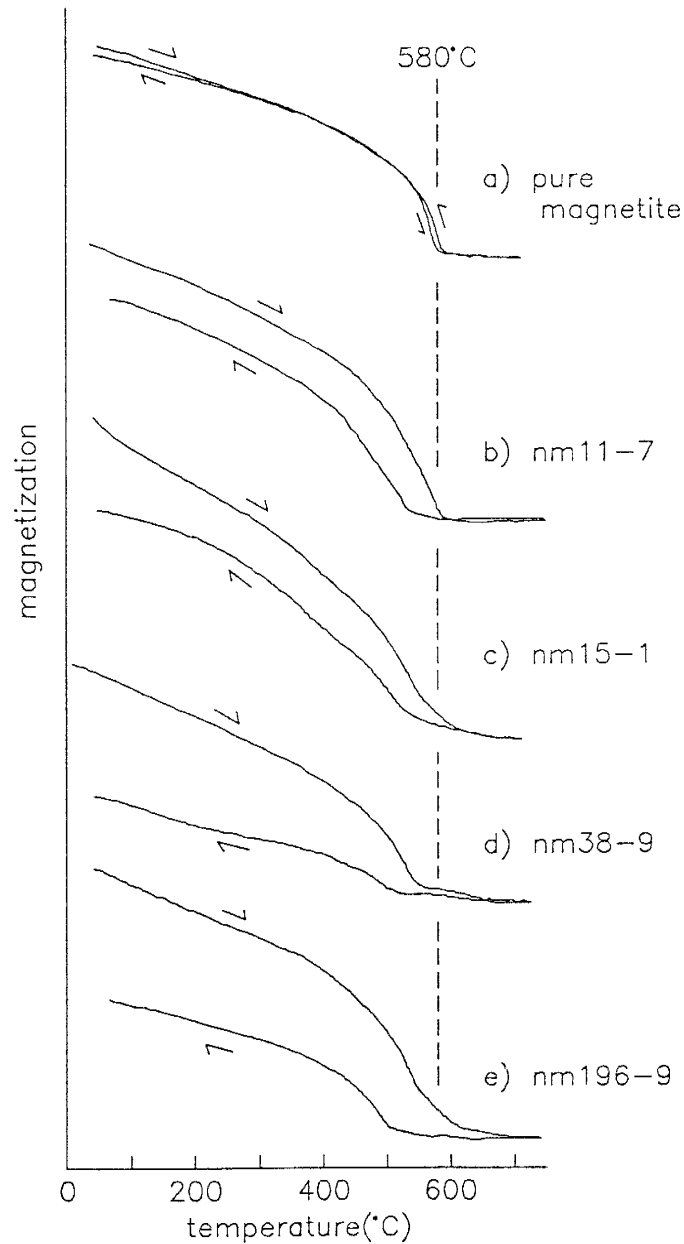


Figure 5. Thermomagnetic analyses of selected whole-rock samples, run in air. Vertical scale shows saturation magnetization in arbitrary units. Samples show primary Curie temperatures near that of pure magnetite, but behavior is in all cases somewhat irreversible.

and 700°C (Fig. 5). This higher-temperature JsT segment apparently represents at least some of the carriers of the high-unblocking-temperature, variable-coercivity RMs observed during demagnetization.

The lower temperature segments of the JsT curves of all samples are irreversible, showing reduced saturation magnetizations after heating due to laboratory oxidation of magnetite to hematite (Fig. 5). Analogous laboratory oxidation of magnetite also occurred during thermal demagnetization, producing regular, moderate reductions in bulk susceptibility and RM intensity of samples.

The reversibility of the higher temperature JsT curve segments is variable. Some of the 620-700°C segments (Fig. 5c) are reversible, as might be expected for hematite, a completely oxidized Fe-Ti oxide. Most high-temperature segments, however, show reduced post-heating magnetizations (Fig. 5d,e), indicating that the high-Curie temperature phase has undergone oxidation or some other mineralogical change. This irreversible behavior is uncharacteristic of hematite, which is stable under such conditions.

None of the JsT heating curves show either increases or abrupt decreases in magnetization, such as might be associated, respectively, with exsolution of titanomaghemite to form magnetite and ilmenite or collapse of maghemite to hematite. Likewise, no increases or abrupt decreases in bulk susceptibility were observed during thermal demagnetization.



IRM acquisition curves of Type 1 samples with magnetite-dominated remanence show steep initial curve segments which flatten abruptly with the saturation of magnetite at inductions of 100-200 mT (Fig. 6a). The high inductions of the inflection points indicate that much of the magnetite is in the SD or PSD size range, and the broad range of saturation magnetizations (5 to 80 A/m) indicate widely ranging magnetite concentrations (Dankers, 1978). At inductions higher than the magnetite inflection points, most of these samples show a gentle, linear increase in IRM (Fig. 6a), which indicate that magnetite is accompanied by substantial fractions of hematite (Dankers, 1978).

IRM acquisition curves confirm the predominance of hematite in samples with dominantly high-unblocking-temperature, high-coercivity IRMs. Abundant hematite is demonstrated by significantly increasing IRM at inductions of 0.2 to 1.3 T (Fig. 6c,d), but initial steep IRM curve segments with 100-200 mT inflections (Fig. 6c,d) show that some magnetite is also present, although in some cases it clearly carries little or no remanence (Fig. 3 e,f). Some of the higher induction curve segments show distinct changes in slope (Fig. 6d), suggesting bimodal populations in the grain size or composition of hematite.

Partial removal of induced IRMs by DC backfield and AF demagnetization further confirm the magnetic mineralogy suggested by acquisition curves. The IRMs of magnetite dominated samples are entirely neutralized by backfields of

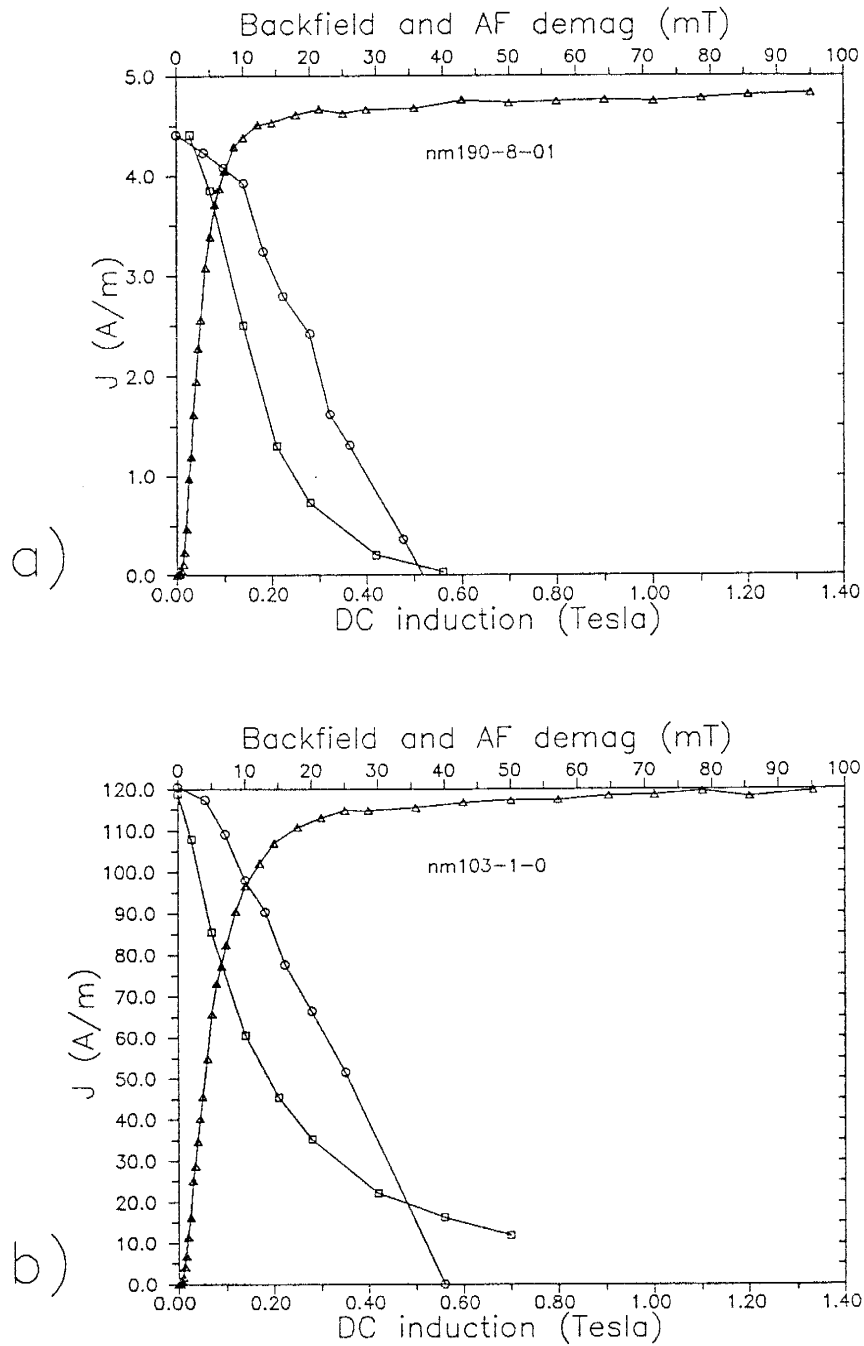


Figure 6 (a-b). Caption on following page.

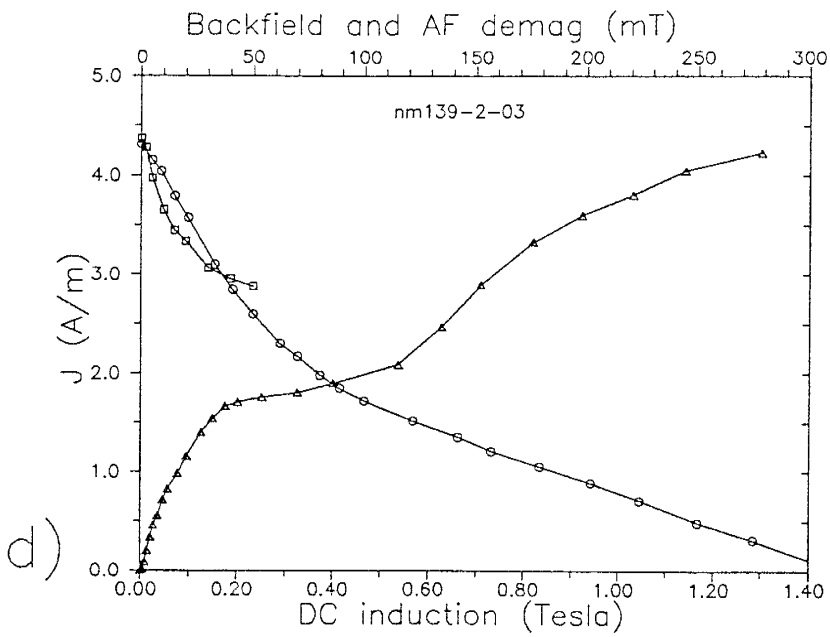
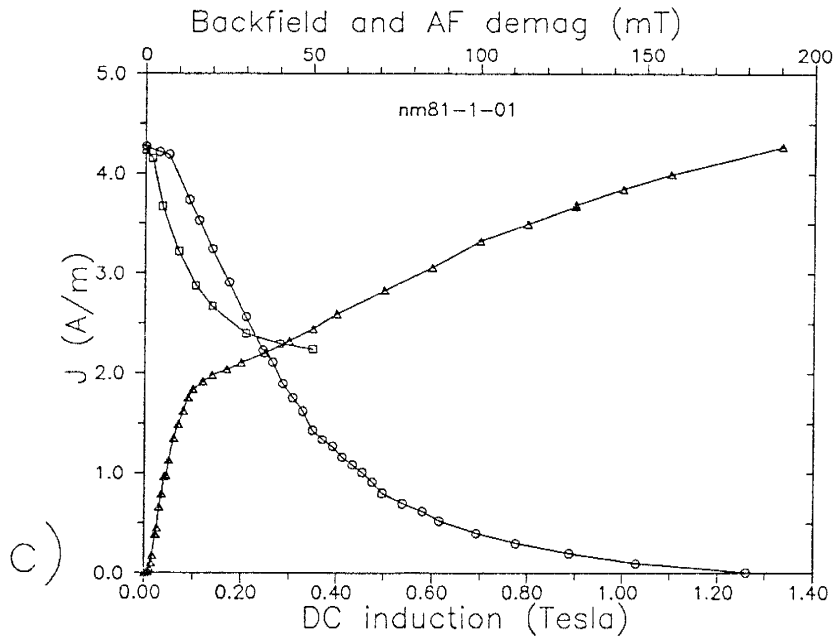


Figure 6 (c-d). Caption on following page.

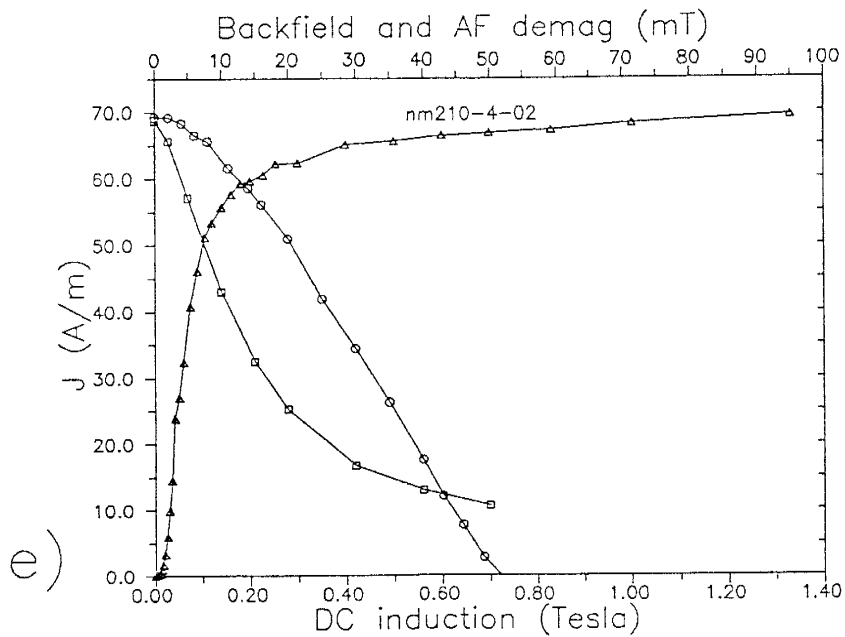


Figure 6. Laboratory IRM acquisition, backfield, and demagnetization curves of selected samples originally carrying a variety of types of NRM components: a) magnetite-dominated TRM, b) magnetite plus maghemite TRM, c) magnetite plus hematite TRM, d) hematite-dominated TRM, e) TRM plus CRM carried by SD magnetite.  $J$  is intensity of laboratory-induced remanent magnetization.

50-80 mT, and reduced by 90% by AF demagnetization to 50 mT (Fig. 6a). The IRMs of hematite dominated samples require backfields of 200-300 mT for neutralization, and are reduced by only 30-50% by AF demagnetization to 50 mT (Figs. 6c,d).

In samples where the RM is dominated by high-unblocking-temperature, low-coercivity RM components believed to be carried by maghemite, IRM acquisition curves have steep initial segments (Fig. 6b) similar to those of magnetite-dominated samples (Fig. 6a). Above the magnetite-saturation inflection point the curves are nearly flat, indicating little contribution to the IRM by hematite (Fig. 6b).

Low-field susceptibilities of Type 1 ignimbrite samples range from  $10^{-5}$  to  $10^{-2}$  (dimensionless SI units), averaging about  $10^{-3}$ , and are crudely proportional to NRM intensities (Fig. 2). In stratigraphic sections through individual ignimbrites, susceptibilities are generally lowest in the oxidized tops of units, and highest in densely welded zones toward the bases (Fig. 7). Susceptibilities tend to decrease with increasing potassium metasomatism or propylitic alteration, and are lowest in areas of zeolitization or strong hydrothermal alteration.

It was not possible to petrographically determine the principal carriers of remanence in Mogollon-Datil ignimbrites. All samples contain significant quantities of disseminated opaque oxide grains which are too fine to identify optically ( $<2\mu\text{m}$ ). Many of these tiny grains show

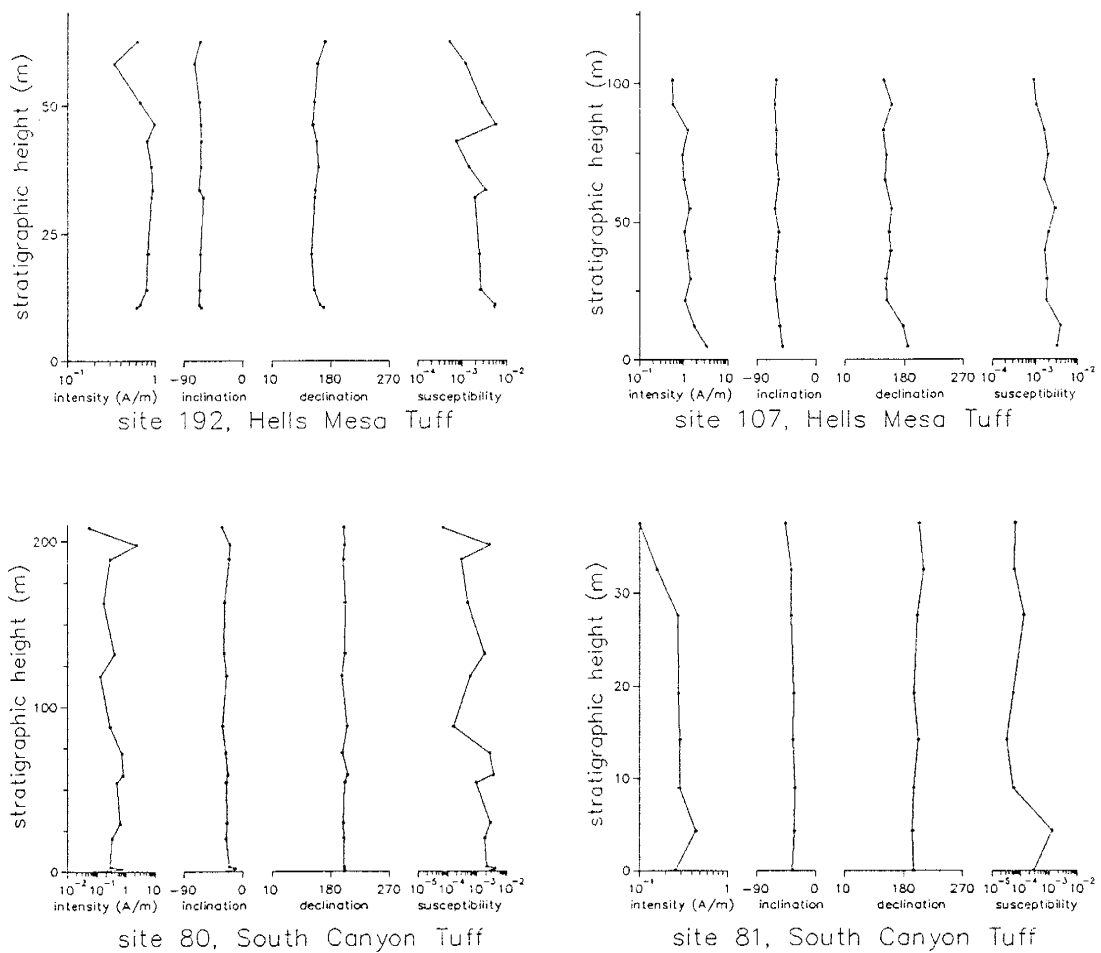


Figure 7. Paleo- and rock-magnetic properties of stratigraphically collected sequences of samples from 4 sites in 2 different ignimbrites, showing systematic variations in intensity and bulk susceptibility, but relatively consistent remanence directions (NRM).

red internal reflections characteristic of microcrystalline hematite. Fe-Ti oxides crystals, 10-600 $\mu$ m in diameter, comprise 0.1 to 5% of the modal volume of Type 1 samples, and consist primarily of hematite, plus subordinate magnetite and titanium oxides. These phases apparently were produced by high-temperature oxidation of original titanomagnetite and ilmenohematite. The original titanomagnetite crystals now consist of hematite-rich martite containing 0-25% relict magnetite and 2 to 40% Ti-rich lamellae consisting of ilmenite, fine intergrowths of hematite and rutile, and/or pseudobrookite. Original ilmenohematite crystals now consist of monocrystalline hematite containing tabular to irregular lamellae of ilmenite or intergrown rutile and hematite. No significant maghemite was observed in these samples. In moderately hydrothermally altered and potassium metasomatized Type 1 samples, however, many crystals show the effects of slight to advanced dissolution. Although petrographic observations and demagnetization behavior both demonstrate the presence of magnetite and hematite, the relative concentrations indicated by the two methods generally show poor agreement, implying that ultrafine disseminated oxides dominate the remanence.

As will be discussed below, the conclusion that the NRM of Type 1 samples is carried by magnetite and high-temperature deuteritic hematite is in accord with studies of many other ignimbrites (e.g. Geissman et al., 1983; Geissman

and Van der Voo, 1980; Weiss et al., 1989). Less conventional is the interpretation of maghemite as a significant carrier of low-unblocking-temperature, low to moderate coercivity RM. In any case, the parallel nature of magnetite, hematite, and apparent maghemite components, their univectoral demagnetization behavior, and tight grouping of remanence directions within sites all support the interpretation that Type 1 samples possess a stable TRM acquired during rapid post-emplacement cooling.

#### **TRM accompanied by lightning-induced IRM (Type 2)**

Samples from 43% of the ignimbrite sites showed multivectoral Type 2 demagnetization behavior reflecting removal of high-intensity, scattered, low-coercivity RMs which are interpreted as lightning-induced IRMs. For many of these sites, some samples showed multivectoral behavior and the remainder were well-grouped and behaved univectorally. All Type 2 sites were collected from ridges or slopes exposed to lightning in areas where topographically protected outcrops were not available.

The NRMs of samples from Type 2 sites showed scattered directions ( $\alpha_{95}=10$  to  $180^\circ$ ) and generally strong but highly variable intensities ( $10^{-1}$  to  $10^2$  A/m). AF demagnetization of samples from Type 2 sites produced large initial changes in RM direction and reductions in intensity, generally followed by univectoral decay toward the origin (Fig. 8). These segments where univectoral decay occurs exhibit a



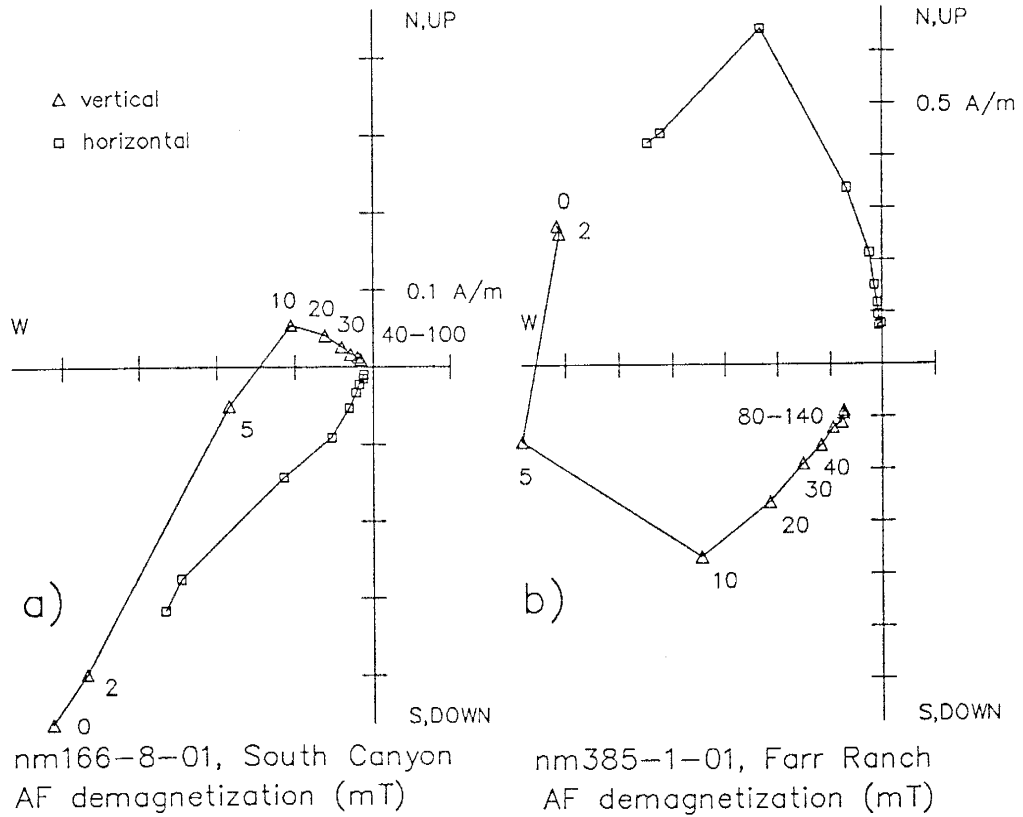


Figure 8. Orthogonal demagnetization diagrams of samples from sites 166 and 385 showing removal of lightning-induced IRM components. IRM components of this nature were observed in samples from about 40% of the sites in this study.

range of decay rates similar to those shown by samples from Type 1 sites.

For most Type 2 sites, AF demagnetization to 20-100 mT significantly reduced within-site dispersion, yielding  $\alpha_{95} < 10^\circ$  (Table 3, Appendix 1). For 6 sites, however, AF inductions as large as 140mT were insufficient to produce univectoral decay or reduce  $\alpha_{95}$  values to less than  $10^\circ$ . Use of thermal demagnetization to remove high-intensity scattered RM components from representative Type 2 samples proved unsuccessful.

Petrographic and rock magnetic observations show no significant differences in mineralogy between samples from Type 1 and Type 2 sites. The only systematic difference in rock magnetic properties is that the ratio of NRM intensity to bulk susceptibility is in many cases higher in Type 2 samples (Fig. 2).

Type 2 behavior apparently indicates remanence composed of two components: 1) a last-removed TRM analogous to that associated with Type 1 behavior, and 2) lightning-induced IRM. In all but a few cases it was possible to randomize IRMs and resolve the TRM using AF demagnetization.

#### **TRM plus CRM (Type 3)**

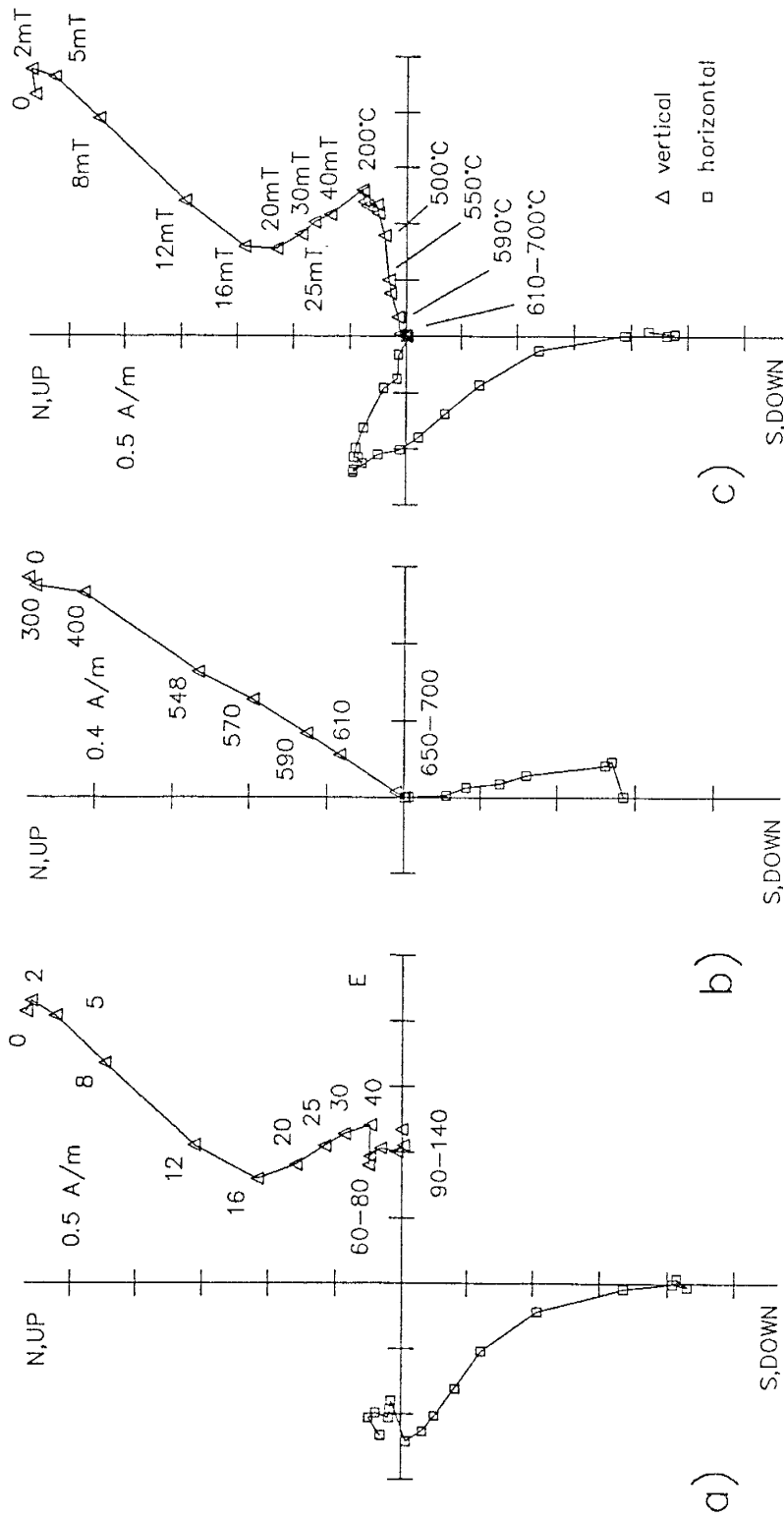
A total of 4% of the ignimbrite sites showed multivectoral AF demagnetization behavior which was consistent from sample to sample. The majority of these sites were collected in areas of slight to moderate potassium metasomatism or hydrothermal alteration. Two

varieties of this atypical demagnetization behavior were observed.

First, samples from 12 sites showed behavior suggestive of a CRM carried by fine-grained magnetite. In 6 of these sites, NRM vectors were well-grouped within sites ( $\alpha_{95}=4-7^\circ$ ), and AF demagnetization produced systematic changes in RM direction which generally increased dispersion (Fig. 9a). PCA of the RM removed in AF demagnetization resolved two distinct components: a larger, low-coercivity (MDI=10-30 mT) component and smaller, high-coercivity (MDI>140 mT). The low-coercivity component is well-grouped within sites ( $\alpha_{95}<10^\circ$ ) and is similar in direction to the expected time-averaged Oligocene geomagnetic field. The high-coercivity component is less well-grouped within sites and generally differs strongly from expected field directions.

Thermal demagnetization was unable to separate these two components. Unblocking of RM in both untreated samples and samples previously AF demagnetized to 140 mT produced only univectoral decay toward the origin, and indicated maximum unblocking temperatures near  $580^\circ\text{C}$  (Figs. 9b,c).

Samples from these five sites apparently contain non-parallel CRM and TRM components, both carried by low-titanium magnetite. The unblocking temperature spectra of these two magnetizations apparently overlap completely, whereas their coercivity spectra show only partial overlap. The higher coercivity CRM components apparently reside



nm210-4-02, Kneeling Nun AF demagnetization (mT) S,DOWN  
 nm210-3-03, Kneeling Nun thermal demagnetization (°C) S,DOWN  
 nm210-1-02, Kneeling Nun AF then thermal S,DOWN

Figure 9. Orthogonal demagnetization diagrams of samples from site 210 demonstrate CRM components apparently carried by SD magnetite: a) AF demagnetization yields high-coercivity, low-inclination, westerly component, b) univectoral thermal demagnetization behavior, c) AF followed by thermal demagnetization reveals low blocking temperature of CRM component. CRM components of this nature were observed only in a few sites in this study.

principally in SD grains, whereas the lower coercivity TRM components are carried by a wider spectrum of magnetite grains sizes. PCA allows accurate resolution of the first-removed TRM components in most of these samples.

Similar consistent multicomponent AF demagnetization behavior was shown by samples from an additional 6 sites, but only after removal of scattered low-coercivity components interpreted as lightning induced IRM (Fig. 10). Using PCA, some sites yielded moderate-coercivity magnetizations interpreted as TRM because they were well-grouped ( $\alpha_{95} < 10^\circ$ ) and generally parallel to time-averaged geomagnetic field directions. For other sites, moderate-coercivity magnetizations were less well-grouped ( $\alpha_{95} = 10-30^\circ$ ), apparently reflecting incomplete separation of TRM and IRM.

All 12 of the Type 3 sites showing CRM carried by SD magnetite were collected from biotite-rich regional ignimbrites, particularly the Kneeling Nun and Lemitar Tuffs. However, the directions of the CRMs are inconsistent from site to site, and most other sites from these units are free of CRM.

Petrographically, samples from these Type 3 sites are similar to some of the more highly oxidized Type 1 sites. Likewise, no systematic differences between Type 1 and 3 samples were revealed by rock-magnetic techniques, including thermomagnetic analyses (Fig. 5), IRM acquisition and

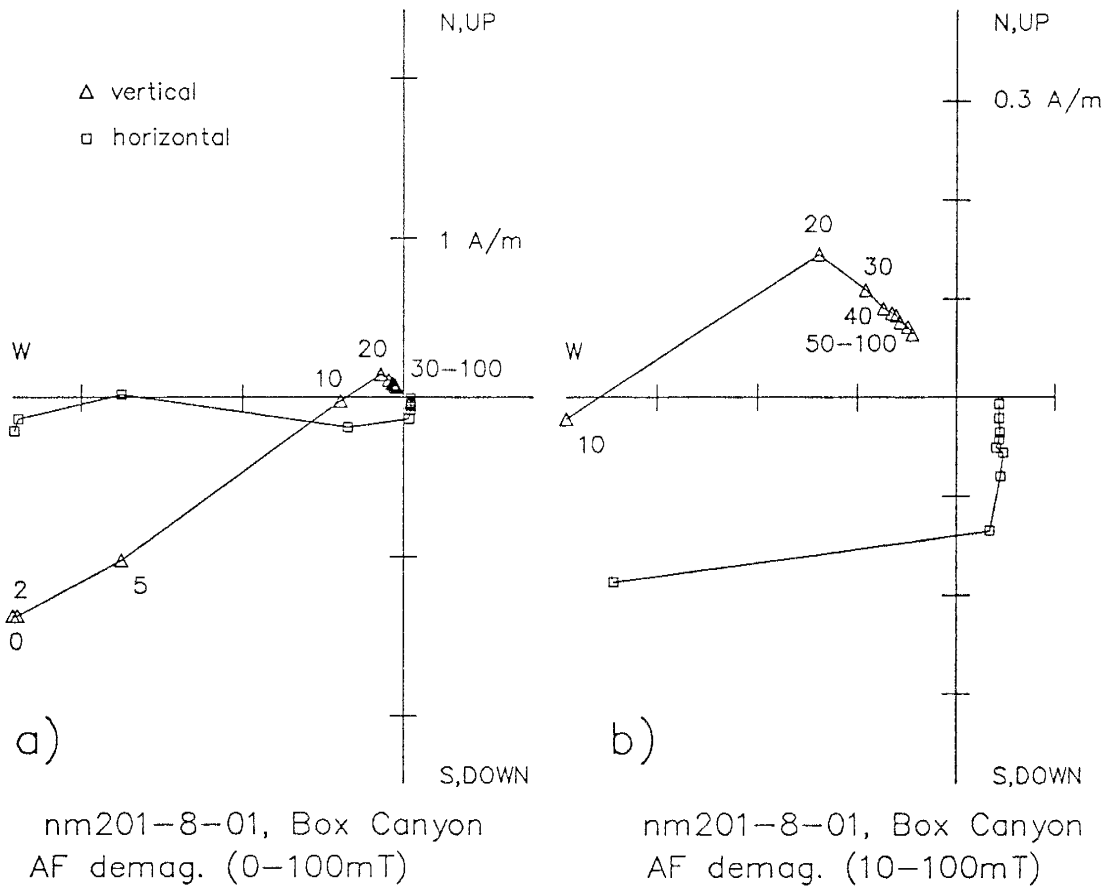


Figure 10. Orthogonal demagnetization diagrams of samples from site 201 reveal a combination of IRM and CRM components: a) AF demagnetization from NRM to 100 mT, b) a detailed view of 10 to 100 mT AF demagnetization behavior for the same specimen.

demagnetization experiments (Fig. 6e), and bulk susceptibility measurements (Fig. 2).

A second variety of Type 3 systematic multivectoral demagnetization behavior was exhibited by samples from 4 sites and indicates CRM carried by hematite. For each site, NRM directions were somewhat scattered ( $\alpha_{95}=26-31^\circ$ ), and both AF and thermal demagnetization revealed two RM components: a low-coercivity (MDI=10-40 mT), low-unblocking-temperature (<550°C) RM carried by titanomagnetite, and a high-coercivity (MDI>140 mT), high-unblocking-temperature (>590°C) hematite-carried RM. Resolution of these two magnetizations by PCA shows that the low-coercivity RMs are well grouped ( $\alpha_{95}=6-16^\circ$ ), and similar to expected time-averaged Oligocene geomagnetic field directions. At site 145 the high-coercivity hematite-carried RMs are also relatively well grouped, but show an Oligocene normal direction, opposite to the polarity of the low-coercivity RMs (Fig. 11). The high-coercivity hematite-carried RMs of the 3 sites, all located in strongly hydrothermally altered areas, are less well-grouped and show anomalous directions. The titanomagnetite-carried magnetizations of these 4 sites are apparently primary TRM and the hematite-carried magnetizations represent CRM acquired after initial post-emplacement cooling. This interpretation is supported by petrographic observations which show that some of these samples contain quenched, single-phase titanomagnetite

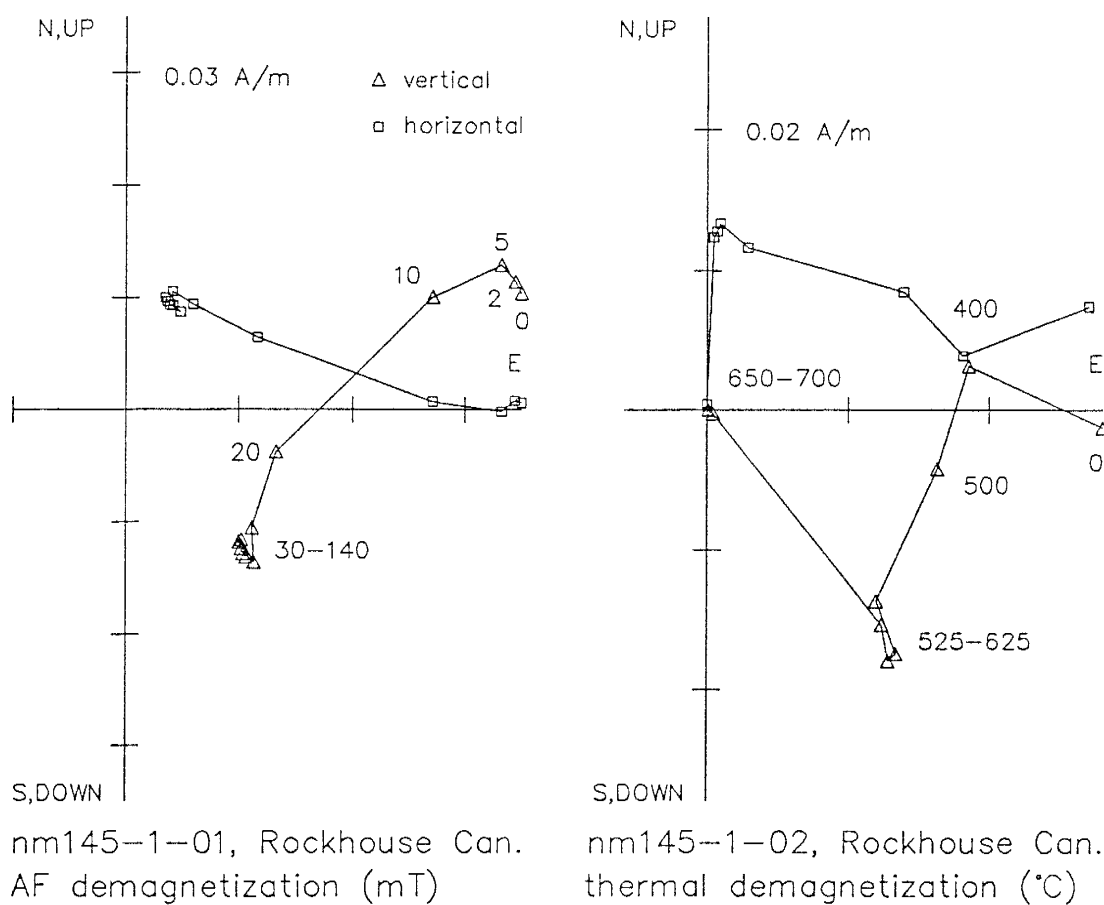


Figure 11. Orthogonal demagnetization diagram of samples from site 145 show a multicomponent magnetization which includes CRM carried by hematite and TRM carried by magnetite. Magnetizations of this nature are rare in the ignimbrites examined in this study and apparently reflect low-temperature oxidation of single-phase titanomagnetite quenched in unwelded distal ignimbrite facies.



partially altered to hematite or titanohematite, presumably at low (sub-deuteric) temperatures.

#### **TRM plus random lithic-hosted magnetizations (Type 4)**

Samples from 5% of the ignimbrite sites exhibited scattered RM components which could not be removed by AF or thermal demagnetization procedures. All 23 Type 4 sites were collected in poorly welded, lithic-rich, ignimbrites, most of which are zeolitized. Some of these ignimbrites are local, dome-related units; others represent the basal portions of larger regional units.

The dispersion of NRM vectors of samples from Type 4 sites was large ( $\alpha_{95}=20$  to  $180^\circ$ ) and demagnetization behavior varied widely among individual samples of each site, ranging from complex multivectoral behavior to nearly univectoral single-component decay (Fig. 12). Anomalous directions, strongly divergent from expected time-averaged Oligocene field directions, were exhibited by many of the samples, even by those showing univectoral demagnetization behavior (Fig. 12a). AF and thermal demagnetization reduced within-site dispersion in some sites ( $\alpha_{95}=14-76^\circ$ ), but increased dispersion in others ( $\alpha_{95}=23-180^\circ$ ). At the demagnetization level which minimized scatter, about half of the sites (11 out of 23) showed site-mean directions within  $40^\circ$  of time-averaged Oligocene field directions, and the remaining sites showed anomalous mean directions.

The Type 4 behavior of these poorly welded ignimbrites appears to reflect randomly directed magnetizations carried

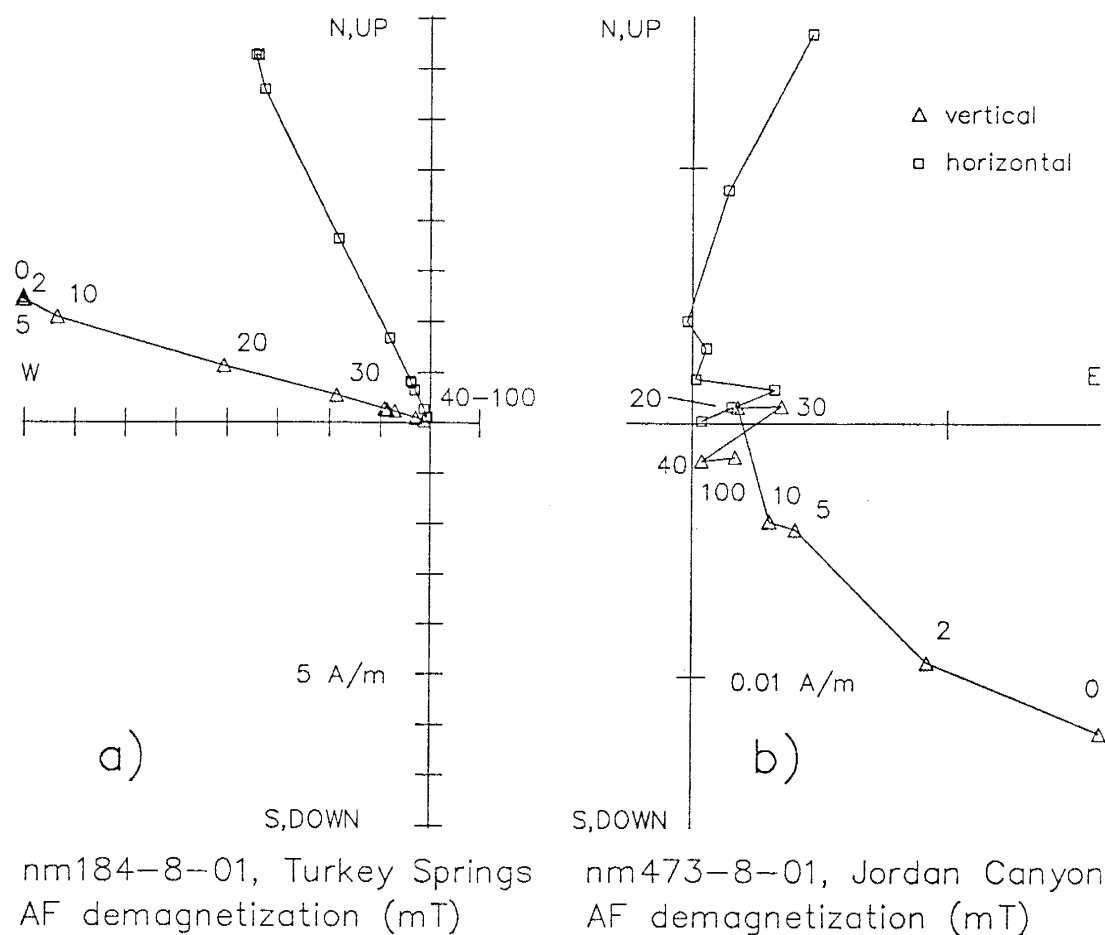


Figure 12. Orthogonal demagnetization of samples from sites 184 and 483 show randomly directed magnetizations carried by lithic fragments. Apparently these poorly welded distal ignimbrites were insufficiently hot to reset the pre-existing magnetizations of the lithic fragments. Magnetizations of this nature are relatively common in some poorly welded, lithic-rich units.

by lithic fragments. Apparently these ignimbrites were not hot enough to reset the RM of included lithics. In addition to these random lithic-hosted magnetizations, the tuffaceous matrix of some Type 4 samples appears to carry significant TRM, as shown by the similarity of their site-mean directions with time-averaged Oligocene field directions. The relative contributions of TRM and lithic-hosted magnetizations vary among the Type 4 sites and among different samples in each site. The univectoral demagnetization behavior shown by some Type 4 samples may indicate RM dominated either by TRM or by magnetizations of a single lithic fragment. Multivectoral behavior may represent demagnetization of multiple lithic fragments with a range of coercivity or unblocking-temperature spectra.

#### **Acceptance/Rejection criteria**

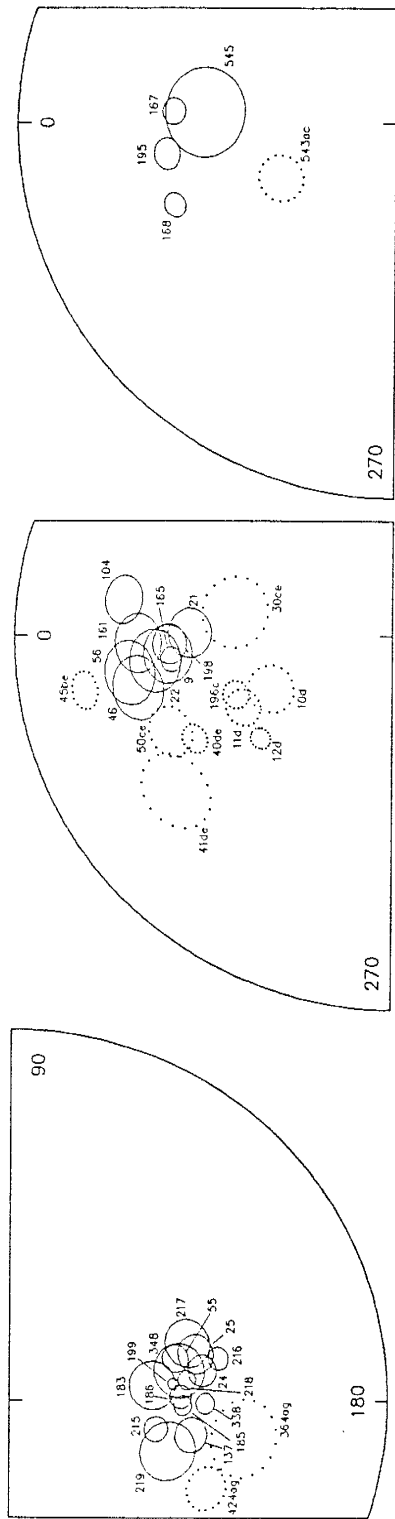
Site-mean RM directions,  $k$ , and  $\alpha_{95}$  values were calculated for each site (Table 3) using procedures described above. An arbitrary value of  $\alpha_{95} < 10^\circ$  was selected a cutoff value for data suitable for detailed stratigraphic correlation. Of the total 404 sites studied, 345 sites met this criterion; data from the remaining 59 sites have been excluded from the following figures and from calculations of unit-mean directions. Excluded sites include 13% of Type 2 sites, 73% of type 3 sites, and all Type 4 sites. Despite their rejection for lack of precision, data from most of these excluded sites yield unambiguous determinations of magnetic polarity.

## REMANENCE DIRECTIONS

Well-studied units ( $n \geq 4$ )

From 4 to 43 acceptable ( $\alpha_{95} < 10^\circ$ ) site-mean directions have been determined from each of 22 ignimbrites (Figs. 13, 14, Table 3, Appendix 1). Twenty-one of these units (Table 1) are regional (extent=40-225 km), single-cooling-unit, rhyolitic ignimbrites. Sites are distributed over much of the areal extent of each unit, and together represent a wide range of ignimbrite facies, including intracaldera facies, densely welded proximal outflow facies, and unwelded distal fringes as thin as 1.5 m. The 22nd unit is the tuff of Garcia Camp, a multi-cooling unit pyroclastic apron associated with the Indian Peak dome complex (Duffield et al., 1987).

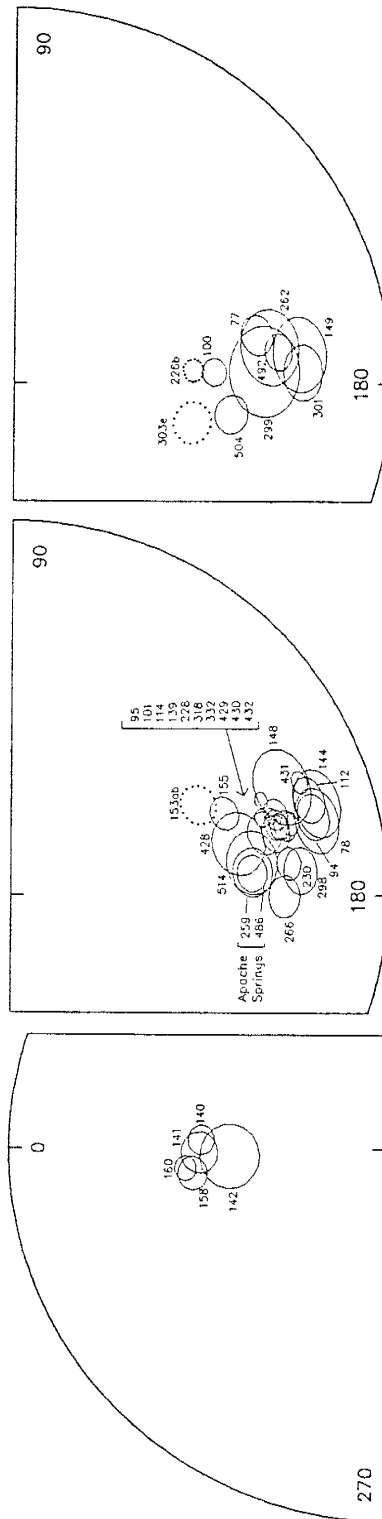
Polarities of magnetizations inferred to be TRM were found to be entirely consistent within each of these 22 ignimbrites. Sixteen of the units show reversed polarity and 6 are normal (Table 1, Fig. 15). With some exceptions, site-mean TRM directions were found to be spatially uniform within individual units. The majority of site-mean directions for each unit are tightly grouped ( $k=38-457$ ) and show considerable overlap among the site  $\alpha_{95}$  confidence cones (Figs. 13, 14). For 15 of the 22 ignimbrites, the well-grouped sites are accompanied by one or more "anomalous" sites, arbitrarily defined as sites with mean directions which diverge more than  $15^\circ$  from the unit-mean direction (anomalous sites are dotted in Figures 13 and 14).



a) tuff of Turkey Springs 24.3 Ma

b) Lemitar Tuff 28.0 Ma

c) tuff of Caronita Canyon 28.0 Ma

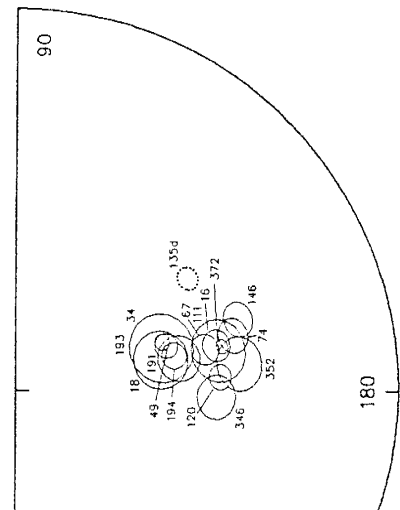


d) tuff of Triangle C Ranch 28.1 Ma

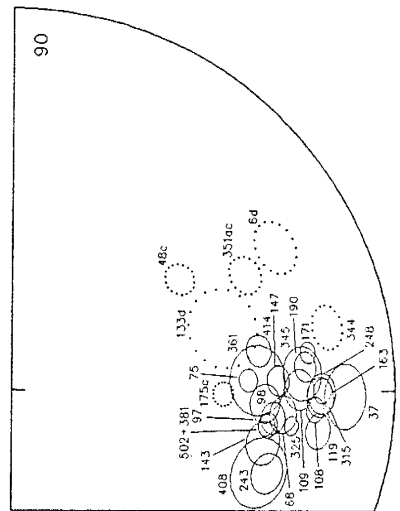
e) Bloodgood Canyon Tuff 28.1 Ma

f) Shelley Peak Tuff 28.1 Ma

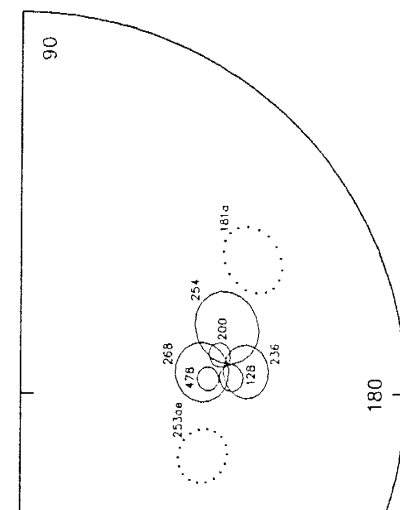
Figure 13 (a-f). Caption on following page.



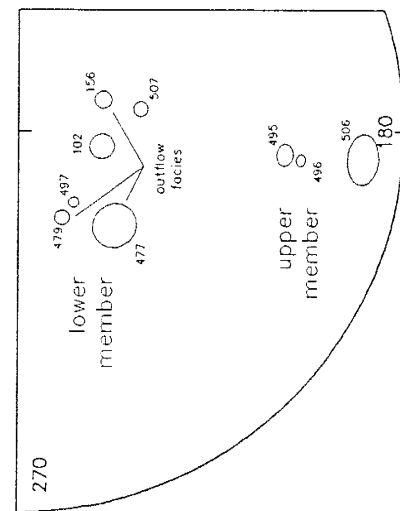
g) tuff of Garcia Camp 28.1 Ma



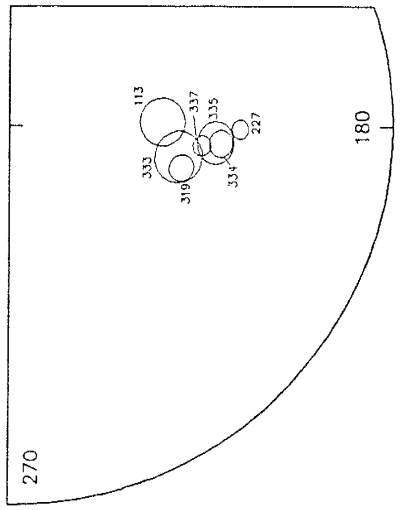
h) Vicks Peak Tuff 28.6 Ma



i) Caballo Blanco Tuff 31.7 Ma



k) Tadpole Ridge Tuff 31.4 Ma



j) Davis Canyon Tuff 29.0 Ma

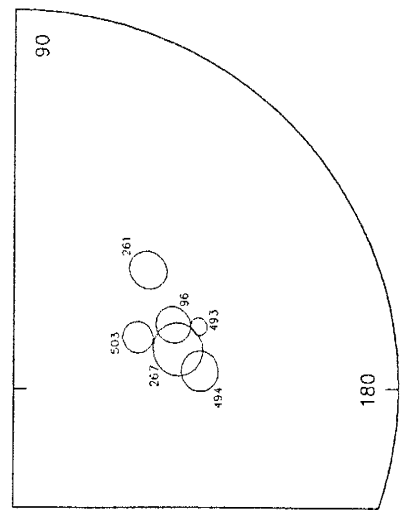
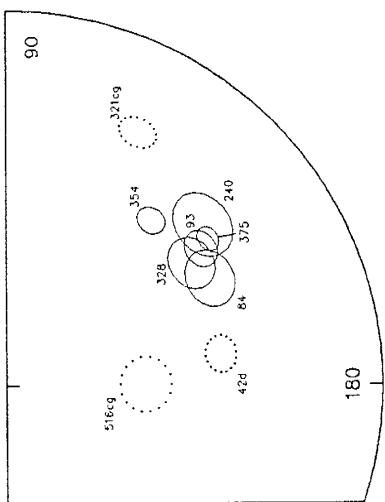
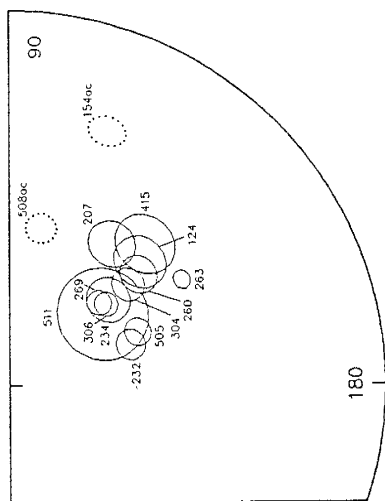


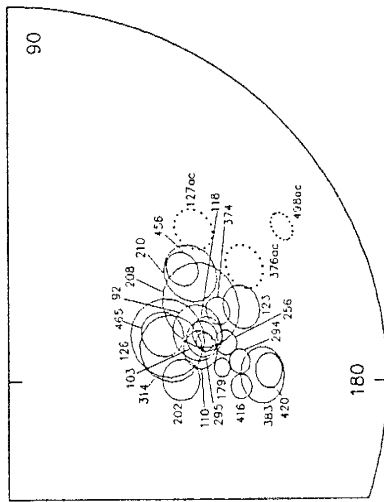
Figure 13 (g-l). Caption on following page.



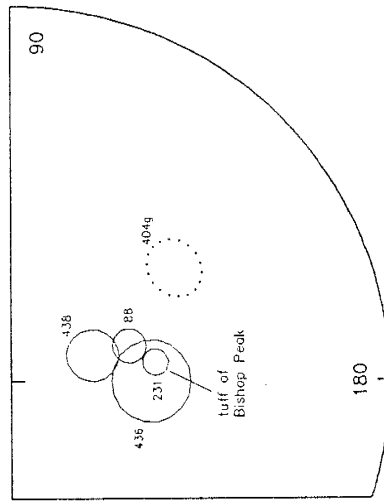
m) Hells Mesa Tuff 32.1 Ma



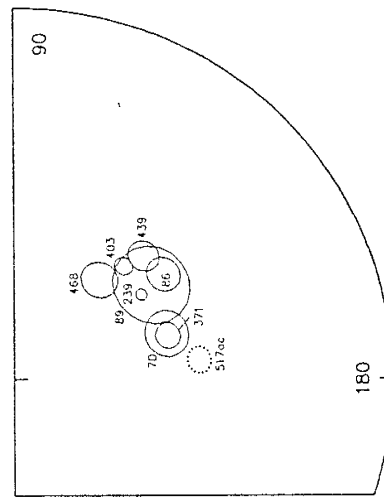
n) Box Canyon Tuff 33.5 Ma



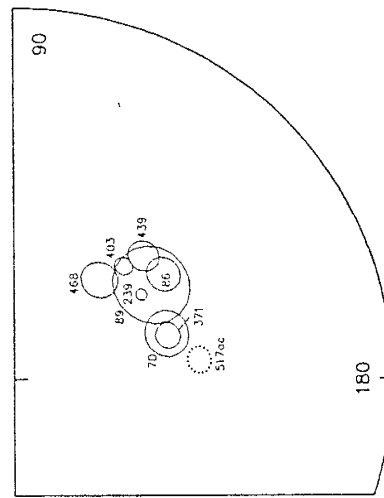
o) Blue Canyon Tuff 33.7 Ma



p) Rockhouse Canyon Tuff 34.4 Ma

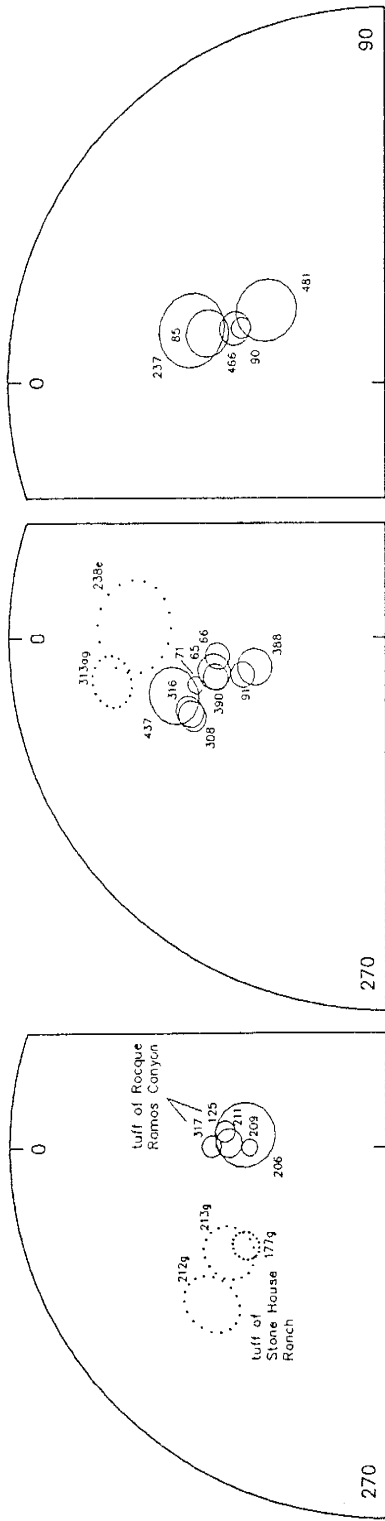


q) tuff of Lebya Well 34.7 Ma



r) Kneeling Nun Tuff 34.9 Ma

Figure 13 (m-r). Caption on following page.



s) Bell Top 4 Tuff 35.0 Ma      t) tuff of Farr Ranch 35.6 Ma      u) Datil Well Tuff 35.5 Ma

Figure 13. Stereographic projections of site-mean remanence data for 22 relatively well-constrained ignimbrites ( $\geq 4$  sites per unit). Ellipses show cone of 95% confidence ( $\alpha_{95}$ ) for each site mean direction. All sites in the northern hemisphere (normal polarity) show positive inclinations (lower hemisphere), and the opposite is true for reversed polarity sites in the southern hemisphere. Anomalous sites ( $>15^\circ$  from the unit-mean direction) are dotted, with the reason denoted by the letter following the site number, keyed as in Table 3.



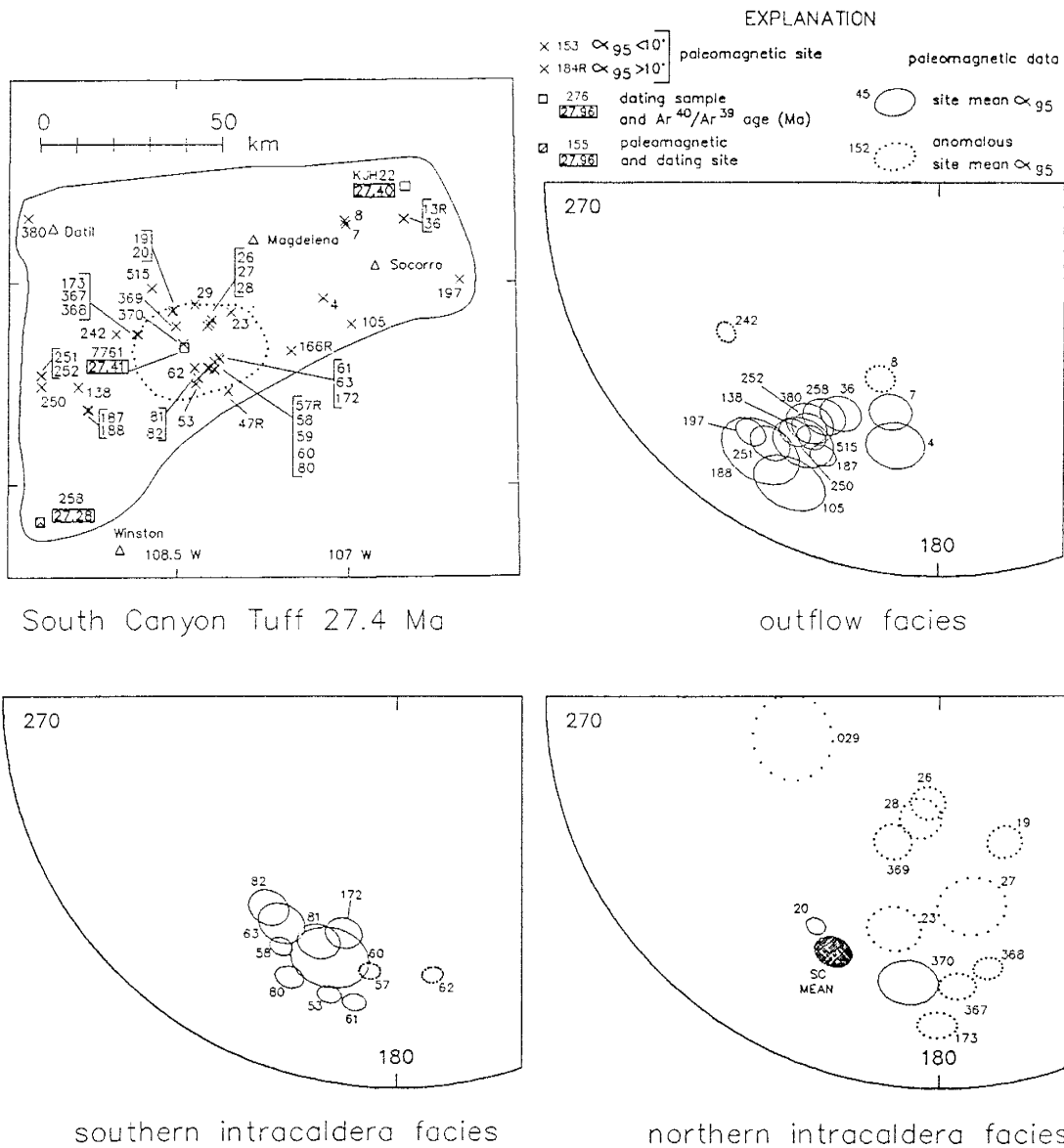


Figure 14. Stereographic projections of site-mean remanence data and detailed site locations from three facies of the South Canyon Tuff. The large dispersion of sites from the thick (>500 m) northern intracaldera facies are discussed in the text. Symbols are the same as in Figure 13.

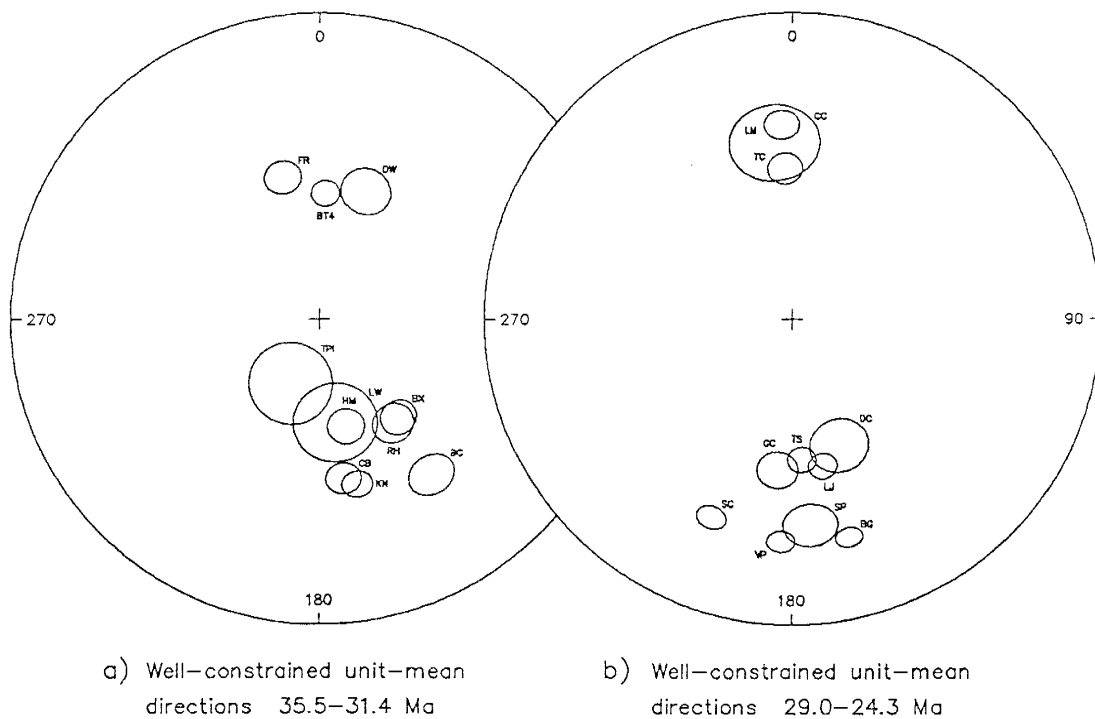


Figure 15. Stereographic projections of unit-mean ignimbrite remanence directions for well-constrained ignimbrites ( $n \geq 4$ ) a) 35.5-31.4 Ma, b) 29-24.3 Ma. Symbols are the same as in Figure 3.

These anomalous sites probably do not represent accurate records of ancient geomagnetic fields. As discussed below, several sources of error apparently contribute to the anomalous site-mean directions, including: tectonic rotations and structural attitude errors, unremoved CRM or IRM components, and effects of protracted cooling of thick intracaldera facies (Figs. 13,14). After excluding the anomalous sites, unit-mean directions and cones of confidence were calculated for each of the 22 relatively well-studied ignimbrites. The  $\alpha_{95}$  values for 19 of the ignimbrites range from 3.1 to 7.5° (Table 1, Fig. 15). The remaining 3 units show lower precisions ( $\alpha_{95}=10-11^\circ$ ), largely reflecting small numbers of sites per unit (n=4 to 6; Table 1, Figs. 13 c,k,q).

Vertical, as well as lateral, uniformity of ignimbrite magnetization directions is demonstrated by data from four sites collected as stratigraphic sequences of samples from two units (Fig. 7). Samples from these four sites, all unaltered and exhibiting Type 1 demagnetization behavior, show within-site dispersion in NRM directions ranging from  $\alpha_{95}=3^\circ$  to 7°, similar to dispersion in Type 1 sites with samples from a common stratigraphic level. NRM intensities show stratigraphic variations which are proportional to variations in bulk susceptibility, i.e. lower in oxidized flow tops and higher in vitrophyres and densely welded basal portions of units (Fig. 7). Both properties are thought to

primarily reflect variations in magnetite concentration (Schlinger et al., 1988; Dankers, 1978).

Significant vertical variation in NRM directions was previously reported from a stratigraphic sequence of samples from the Lemitar Tuff at its type section in the Lemitar Mountains (Fig. 4 in McIntosh, 1983). This variation was originally interpreted as a possible record of secular variation during cooling, but subsequent work suggests that it instead reflects variable contributions of CRM components.

#### Poorly studied units (n=1-3)

Figures 14l, 14t, 16 and Table 3 present site-mean data from 9 ignimbrites for which only 2 or 3 site-mean directions have been determined. Six of the units (Figs. 14l, 14t, 16a,b,d,e) show reasonably good agreement among site-mean directions (unit-mean  $\alpha_{95}=5.2-14.2^\circ$ ; Table 3). The remaining 3 units show less well grouped site-mean directions ( $\alpha_{95}=16.3-28.0^\circ$ ), which may in some cases reflect incorrect correlation of these poorly studied units.

Figure 17 and Table 3 summarize data for units from which only single sites have been analyzed. Altogether, the 55 acceptable ( $\alpha_{95}<10^\circ$ ) sites represent 23 regional ignimbrites and 20 local, dome-related units. Of these 43 total units, 29 show reversed polarity and 14 show normal polarity.

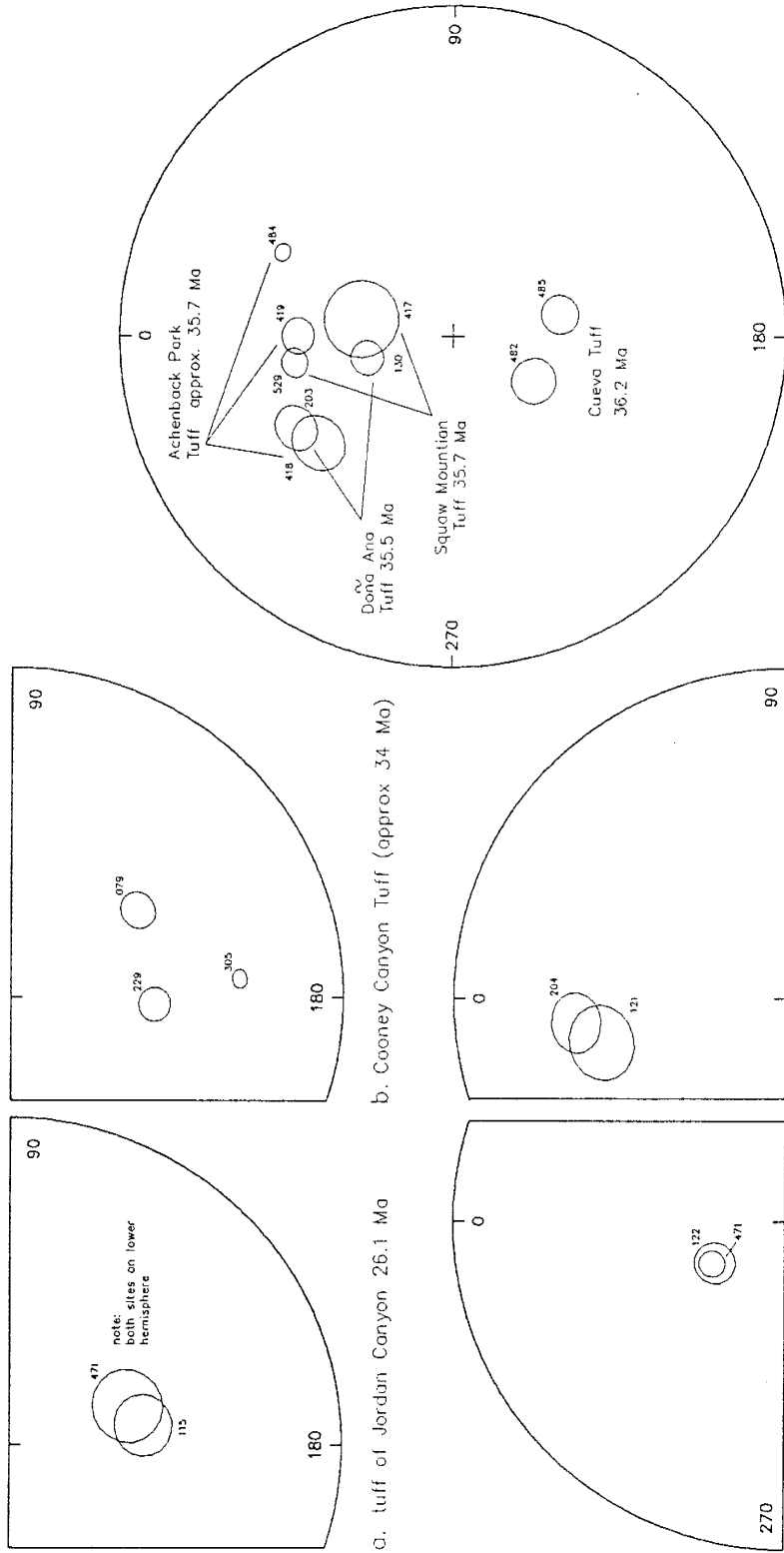
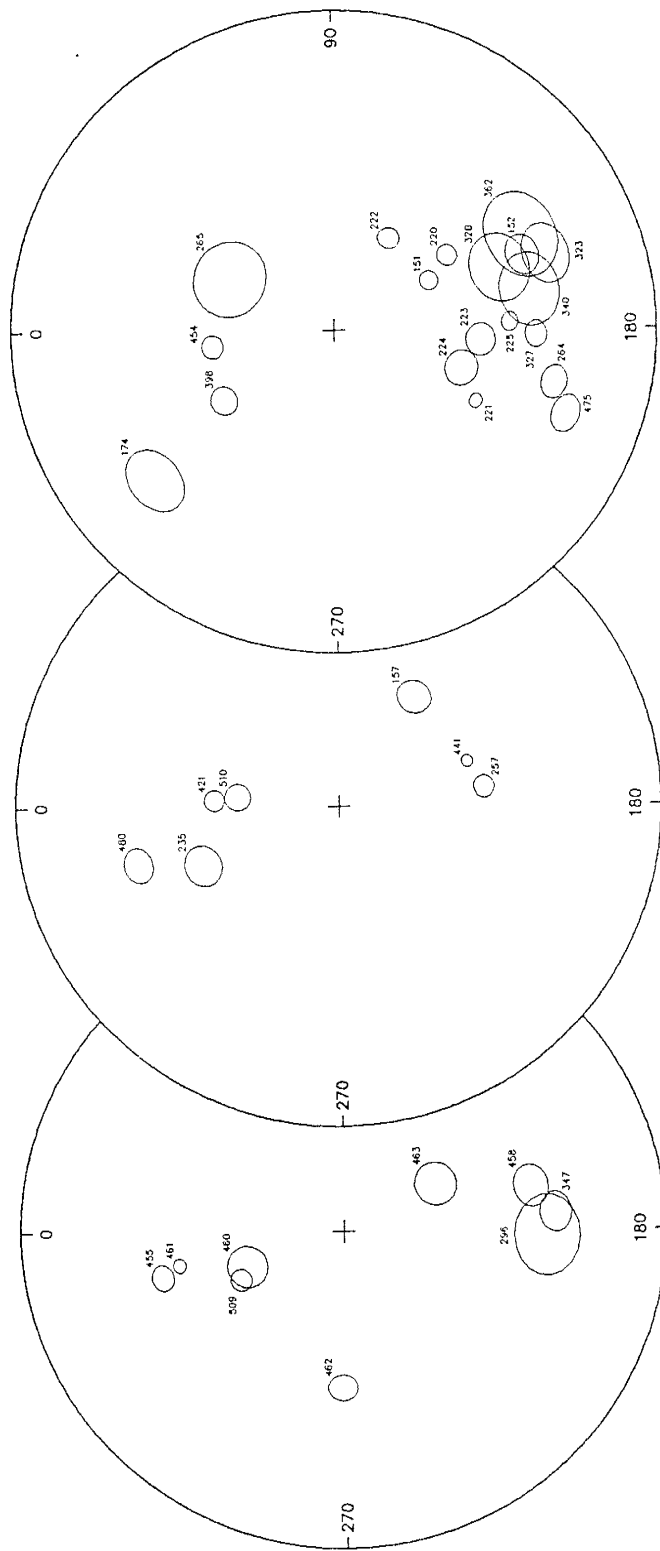


Figure 16. Stereographic projections of site-mean data for ignimbrites with 2 to 3 sites per unit. Symbols are the same as in Figure 13, except that sites from the tuff Slash Ranch show anomalous southerly directions with positive inclinations.



a) Single-site ignimbrites 36-32 Ma b) Single-ignimbrites 29-26 Ma c) Dome-related ignimbrites 35.5-24 Ma

Figure 17. Stereographic projections of site-mean data for ignimbrites for which only one site has been analyzed: a, b) regional and sub-regional ignimbrites (5-125 km extent), separated into 2 age groups, c) local, dome-related units (generally <5 km extent).

## DISCUSSION

## Evaluation of remanence quality

AF demagnetization behavior appears to be the most appropriate criteria by which to judge which ignimbrites sites carry remanence suitable for paleomagnetic correlation. About 90% of sampled ignimbrite sites carry moderate to high intensity ( $10^3$  to 1 A/m), well-defined TRM. About half of these sites show well-grouped NRM vectors and Type 1 univectoral AF and thermal demagnetization behavior. The other half of the TRM-bearing sites show Type 2 demagnetization behavior, indicating lightning-induced IRMs. These IRMs are in almost all cases readily removable by AF demagnetization in peak inductions of 10-100 mT, leaving well-grouped vectors which decay univectorally toward the origin in response to further AF and thermal demagnetization. All Type 1 sites and nearly all Type 2 sites yield precise site-mean remanence directions with  $\alpha_{95}=2-10^\circ$ .

The characteristic magnetization vectors of Type 1 and Type 2 samples are composed of variable proportions of one to three parallel components. These components include: 1) low-unblocking-temperature ( $<580^\circ\text{C}$ ), moderate-coercivity (MDI=10-50 mT) RM carried by SD and PSD magnetite, 2) high-unblocking-temperature ( $580-720^\circ\text{C}$ ), high-coercivity (MDI>140 mT) RM carried by hematite, and 3) RM, apparently carried by maghemite, showing the unusual combination of high

unblocking temperature (580-650°C) and low to moderate coercivity (MDI=10-50 mT).

The remanence in most samples is dominantly carried by titanium-poor SD and PSD magnetite. This remanence is interpreted as a TRM acquired during rapid post-emplacement cooling. Magnetite of this nature is common in ignimbrites elsewhere (Reynolds, 1977; Geissman et al., 1983; Rosenbaum, 1986), and some evidence suggests that it forms, at least in part, during post-emplacement welding (Schlinger et al., 1988).

Hematite carries a small but significant fraction of remanence in most samples, but dominates the remanence in oxidized tops of outflow sheets and in some areas of hydrothermal oxidation. Hematite is present in greater concentrations than magnetite in most samples, in the form of dispersed microcrystalline hematite, martite, and specular hematite in oxidized ilmenite and biotite. Although martite and microcrystalline hematite are known to form over a wide range of temperatures (Walker et al., 1981), an origin involving high-temperature deuteric oxidation is supported by their association with pseudobrookite and rutile (Haggerty, 1976).

In Type 1 and Type 2 samples, hematite- and magnetite-carried magnetizations are parallel, suggesting that both magnetizations were acquired nearly simultaneously during rapid post-emplacement deuteric oxidation and cooling. This remanence is here considered a TRM, although some of the



deuteric hematite may have actually formed below its Curie temperature, and would therefore carry, strictly speaking, a thermochemical remanent magnetization (Geissman and Van der Voo, 1980). Similar high-temperature deuteric hematite has been identified as a significant RM carrier in ignimbrites elsewhere (Geissman and Van der Voo, 1980; Weiss et al., 1989), although CRM-bearing authigenic hematite has also been reported from other ignimbrites (Reynolds, 1977; Hagstrum and Lipman, 1986).

One consequence of the presence of deuteric hematite in these ignimbrites is that the TRM directions were able to survive significant amounts of alteration. Samples from several of the Type 1 and 2 sites show effects of slight to advanced hydrothermal alteration, but still show TRMs that agree with unaltered portions of the correlative ignimbrite. Petrographic and paleomagnetic data indicate that, during alteration, magnetite was preferentially dissolved, effectively increasing the fraction of remanence carried by hematite. In cases where some magnetite remains, its RM is generally parallel to that of hematite. This indicates that no significant magnetizations are carried by authigenic hematite, because experimental evidence indicates that the RM of authigenic hematite should at least partially reflect the ambient field at the time of its formation (Heider and Dunlop, 1987; Johnson and Merrill, 1972). Even in cases of extreme alteration, where the NRM is carried entirely by

hematite, multiple non-parallel hematite-carried components were not resolved by AF or thermal demagnetization.

In addition to magnetite- and hematite-carried RMs, many Mogollon-Datil ignimbrite samples contain a third parallel RM apparently carried by maghemite. These high-unblocking-temperature, low-to-moderate coercivity RMs constitute a small fraction of the remanence in some samples, and dominate the remanence of few sites. Similar RM components have been reported from other ignimbrites (Rosenbaum, 1986; Weiss et al., 1989), but have not generally been ascribed to maghemite. Relative to magnetite, maghemite shows similar coercivity and theoretically higher Curie temperatures (Nagata, 1961). However, most natural maghemites invert to hematite at temperatures as low as 250°C, making the Curie temperature effectively unmeasurable (Nagata, 1961). Recent studies of synthetic maghemite, however, have shown that fine grain size (<1  $\mu\text{m}$ ) and/or acicular shape can raise the inversion temperature to 660°C or more, allowing measurement of true Curie temperatures of 645°C (Özdemir and Banerjee, 1984). SEM studies have shown that the abundant submicron oxide grains in most ignimbrites are elongate to acicular (Schlinger et al., 1988; Geissman et al., 1983). Oxidation of such grains could produce ultrafine, elongate maghemite grains with inversion temperatures higher than their 645°C Curie temperatures.

Titanohematite, rather than maghemite, has been suggested as the carrier of unusual high-unblocking-temperature, low-to-moderate coercivity RM components in other ignimbrites (Rosenbaum, 1986; Weiss et al., 1989). Synthetic mineral data, however, suggest that the addition of titanium to hematite lowers the Curie temperature much more effectively than it reduces coercivity, and thus could not account for the unusual magnetizations (Nagata and Akimoto, 1956). Furthermore, thermomagnetic analyses of samples in which these unusual magnetizations comprise a large portion of the NRM generally show irreversibly decreased magnetizations after heating in air to 580°C or more (Fig. 5d,e). Titanohematite should be stable under these experimental conditions (Stacy and Banerjee, 1974).

The timing of formation and RM acquisition of fine-grained maghemite is uncertain. Maghemite is generally observed to form at temperatures of 100-250°C (Özdemir and Dunlop, 1985), and carries scattered CRM components in some ignimbrites (Reynolds, 1977). RMs carried by maghemite in Mogollon-Datil ignimbrites, however, are generally well-grouped and parallel to magnetite-carried TRM. This suggests that the maghemite formed and acquired its remanence during rapid post-emplacement cooling. Alternatively it may have formed during subsequent low-temperature oxidation and "inherited" the TRM directions of parent magnetite grains. Under experimental conditions, the RM of maghemite formed by low-temperature oxidation of SD

acicular magnetite is parallel to the RM of the parent grains rather than to the applied field (Johnson and Merrill, 1974; Özdemir and Dunlop, 1985; Heider and Dunlop, 1987). Regardless of oxidation temperature, then, the direction of the maghemite-carried RMs should represent a faithful record of the geomagnetic field shortly after emplacement of the ignimbrite.

Some sites in Mogollon-Datil ignimbrites carry more complex magnetizations. TRMs in samples from about 4% of the studied sites are masked by CRMs which limit the utility of the data for stratigraphic correlation. Some sites in biotite-rich units show anomalously directed CRM components, which show low unblocking temperatures ( $<580^{\circ}$ ), but distinctly higher coercivity spectra than the TRM resolved by PCA. These CRM components are apparently carried by authigenic SD and PSD magnetite, perhaps formed during hydrothermal alteration. Other biotite-rich sites may contain similar but undetected CRM components. A relatively high degree of scatter is shown by the mean directions of Type 1 and Type 2 sites from most of the biotite-rich ignimbrites, including the Lemitar, Kneeling Nun, Hells Mesa, Shelley Peak, and Tadpole Ridge Tuffs (Fig. 13). These sites may possess small CRM components with coercivity and unblocking temperature spectra that completely overlap those of TRM components and are hence undetectable by AF and thermal demagnetization. Alternatively, the large dispersion of these units might reflect recording of secular

variation during initial cooling of these units. This explanation is considered unlikely because most of the sites are from thin (<50 m) outflow sheets which would have cooled and acquired remanence over a period of decades or less (Reihle, 1973). Furthermore, a record of syn-cooling secular variation should yield variations that are more consistent from site to site within individual units (e.g. Hagstrum and Gans, 1989).

Four other sites show CRMs carried by hematite. Samples from three of these sites show evidence of advanced hydrothermal alteration, and, in the fourth site, rapid quenching apparently preserved single phase titanomagnetite, which was then subject to low-temperature oxidation to titanohematite.

Finally, samples from about 6% of the sites, all in poorly welded, lithic-rich ignimbrite facies, contain significant randomly directed magnetizations carried by lithic clasts. Emplacement temperatures of these ignimbrites were apparently too low to fully reset the remanence of included lithic fragments, resulting in high within-site dispersion where the lithic-hosted components are large compared to the TRM of the ignimbrite matrix. In some cases the TRM of the permeable matrix may have been affected by zeolitization-related destruction of magnetite and/or hematite, allowing the remanence of less permeable lithic fragments to dominate the NRM. A microanalytical paleomagnetic study, similar to that of Geissman (1980),

would allow the RM of individual lithic fragments and lithic-free matrix to be determined separately, thereby testing the above hypothesis and possibly extracting accurate TRM directions from these sites. It is noteworthy that several other sites from unwelded, lithic-rich portions of ignimbrites showed well-grouped Type 1 or Type 2 behavior. Apparently the temperatures attained by included lithic fragments are not always reflected in the general field appearance of an ignimbrite.

In summary, the remanence of 90% of the sampled sites in Mogollon-Datil ignimbrites consists of parallel components carried by magnetite, hematite, and maghemite. This magnetization can be measured to a precision of  $\alpha_{95}=2$  to  $10^\circ$  and is argued to represent an accurate record of the geomagnetic field during post-emplacement cooling. This remanence is dominantly a TRM, although the hematite and maghemite components may actually represent thermochemical remanent magnetizations. The remaining 10% of the sampled sites exhibit significant unremovable IRM, CRM, or lithic-hosted magnetizations and are unsuitable for use in detailed stratigraphic correlation.

#### **Attitude control and tectonic rotations**

In-situ paleomagnetic vectors of ignimbrites and other units have commonly been disturbed to some degree by a combination of tilting, fault-related movements, and larger scale tectonism. Application of paleomagnetism to ignimbrite correlation problems generally requires

structural corrections for which some uncertainty is unavoidable (MacDonald, 1980). Conversely, paleomagnetic data from independently correlated ignimbrites can be used to help constrain tectonic rotations (Hillhouse and Wells, 1987; Hagstrum and Gans, 1989).

Inaccuracy in structural attitude correction constitutes the greatest single source of uncertainty in this and other paleomagnetic studies of ignimbrites (e.g. Grommé et al., 1972; Geissman et al., 1982; Hagstrum and Gans, 1989). The local tectonic tilt correction process is based on three imperfect assumptions: 1) that the orientation of planar features can be precisely measured, 2) that these planar features represent the paleohorizontal at the time of emplacement and RM acquisition, and 3) that observed attitudes were produced by simple, one-stage tilting about a single horizontal axis (MacDonald, 1980).

The assumption of accurate measurement is generally least correct where map-scale features are not available and attitudes must be determined from local pumice foliations, welding breaks, and stratigraphic contacts. Variable and poorly defined pumice attitudes are probably responsible for some of the relatively large number of anomalous site-mean directions from pumice-poor, crystal-rich units such as the Caballo Blanco, Hells Mesa, and Kneeling Nun Tuffs (Fig. 13 l,n,r). Pumice foliation attitudes tend to be better defined in pumice-rich units, but, even in these cases, they commonly vary by a few to several degrees within individual

outcrops. Similarly, basal as well as upper contacts of units are in some cases quite irregular due to pre- or post-emplacment erosion.

The assumption that pumice foliations, contacts, and welding zonations were horizontal at the time of emplacement breaks down in areas where ignimbrites were emplaced in areas of significant topographic relief. Some of the anomalous site-mean directions in this study were collected near basal contacts of ignimbrites (e.g. site 29, Fig. 14d; site 45, Fig. 13b). Even well away from basal contacts, the use of pumice foliation attitudes to estimate structural attitude can generate errors in site-mean directions, particularly in areas of syn-welding flowage of ignimbrites (e.g. site 313, Fig. 13t).

All three assumptions can fail in areas of structural complexity. In general, site-mean data from sites in steeply dipping outcrops tend to deviate more from unit-mean directions than do data from more flat-lying outcrops (Fig. 18). Considering only data from outflow-facies sites in well-constrained units ( $\geq 5$  sites per unit), deviations average  $16^\circ$  in structurally complex areas (arbitrarily defined as areas locally showing maximum dips  $>25^\circ$ ), but average only  $7^\circ$  in areas of less structural complexity.

Most anomalous site-mean directions in this study are from sites from three highly extended tectonic domains (Terututu Butte, Lemitar Mountains, and Joyita Hills; Fig. 1), and from local structurally disturbed zones adjacent to



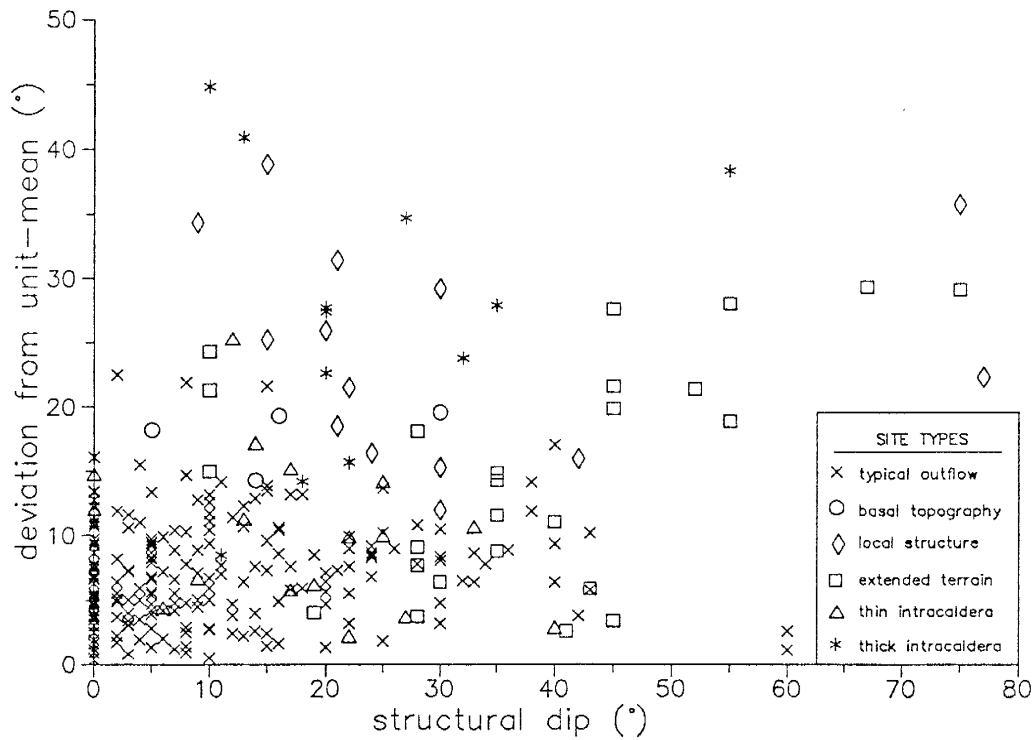
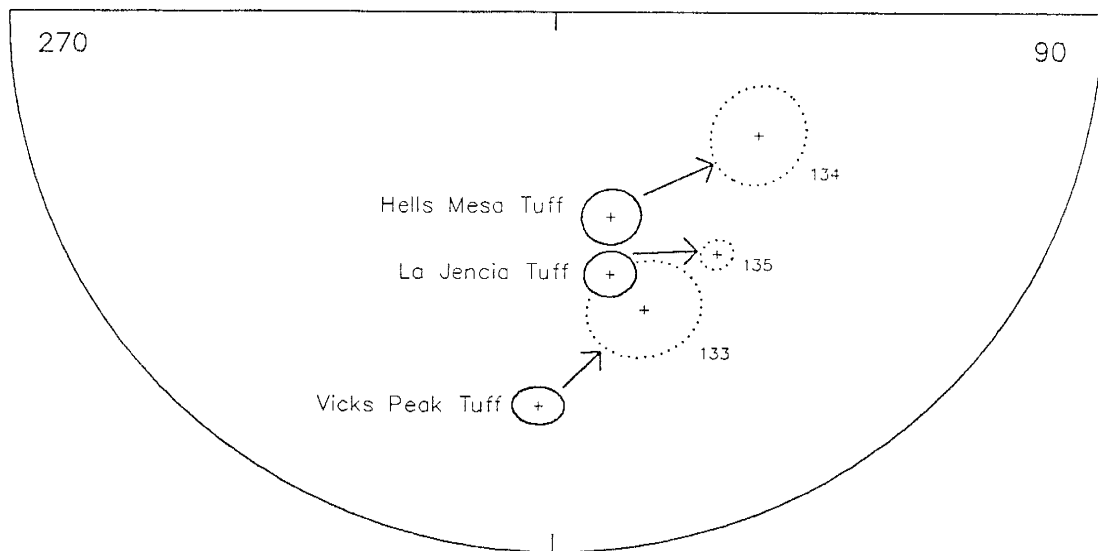


Figure 18. Relationship of structural dip versus deviation from unit-mean direction for sites in well-constrained ignimbrites (4 or more sites per unit). Explanation indicates probable reasons for anomalous directions of some sites, as discussed in text.

faults. In most cases, these anomalous site-mean directions show non-systematic errors in both inclination and declination (Figs. 13,14), and the errors probably reflect several factors, including: 1) measurement errors due to the lack of map-scale planar features in highly faulted areas, 2) local net rotations about non-horizontal axes, produced by listric faulting and multiple episodes of tilting, and 3) effects of pre-eruptive topography in areas where extension was synvolcanic, as in the Lemitar Mountains (Fig. 1), an area of extreme domino-style extension (Chamberlin, 1983)

Some tectonically extended areas also show evidence for systematic tectonic rotations about vertical axes. This effect is most pronounced at two localities. Figure 19 presents data from a sequence of 3 regional ignimbrites exposed at Terututu Butte, an isolated fault block protruding through basin-fill sediments in the Rio Grande rift at the northeastern corner of the volcanic field (Fig. 1). After correction for tilt, all three site-mean directions deviate systematically from the regional mean directions of each unit, implying net counterclockwise rotation of the fault block of about  $25^\circ$ . An alternative interpretation, considered unlikely, is that the deviations reflect a  $20^\circ$  error in attitude determination, perhaps due to emplacement of all three units along the wall of a paleovalley. Similar anomalous mean directions, also consistent with counter-clockwise rotations, are shown by



### Tectonic rotation of Turututu sites

Figure 19. Paleomagnetic evidence for 25° net counter-clockwise rotation of Turututu Butte. The mean directions of individual sites (dotted outlines) in three regional ignimbrites are systematically offset from the respective unit-mean directions (solid outlines).

some sites from the Lemitar Mountains (e.g. sites 40 and 41, Fig. 13b, site 6, Fig. 13h).

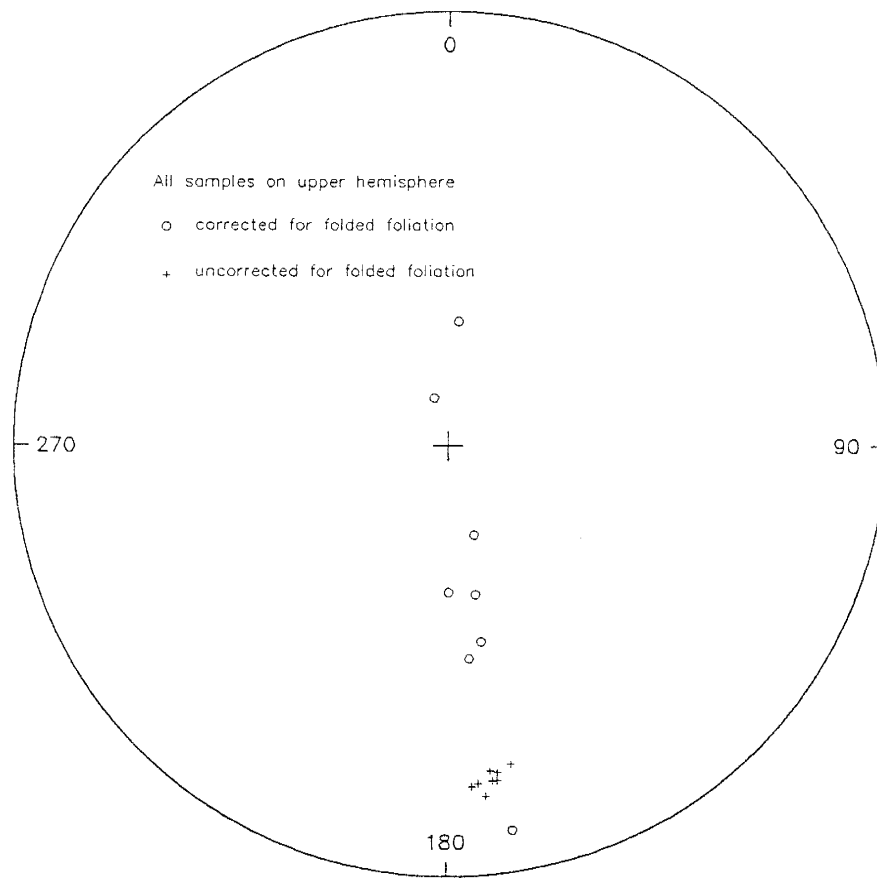
Paleomagnetic correlation of ignimbrites is clearly problematic in areas of high structural complexity. Such areas should be avoided if possible if the goal is to determine the unit-mean direction of an ignimbrite. Paleomagnetic identification of ignimbrites within disturbed areas may require the collection of several sites, in order to recognize structural errors at different scales. In some cases, particularly where only limited outcrops are available within small isolated fault slivers, measurement errors and tectonic rotations may result in structural errors so large that only paleomagnetic polarity can be used for correlation.

Although structural rotations complicate the process of paleomagnetic correlation, paleomagnetic data can be used to constrain tectonic rotations in structurally disturbed portions of independently correlated regional ignimbrites. Paleomagnetic data from widespread, petrologically distinctive ignimbrites in the Basin and Range province have been successfully used to identify tectonic rotations of 20-35° (Wells and Hillhouse, 1989; Hagstrum and Gans, 1989). If a stratigraphic sequence of regional ignimbrites is present, as at Terututu Butte (Fig. 19), then tectonic rotations can be documented with increased confidence. Regional ignimbrites are far better suited for paleomagnetically constraining local tectonic rotations than

sediments or local volcanic units, in which the effects of secular variation and tectonic rotations may not be separable (e.g. Golembek and Brown, 1988; Hudson and Geissman, 1988).

#### **Paleomagnetic effects of flowage in outflow sheets**

Several workers (Rosenbaum, 1986; Ellwood, 1982; Geissman, 1980; Hagstrum and Gans, 1989) have presented evidence that sub-Curie-temperature flowage may locally alter TRM directions of ignimbrites. Opportunities to investigate this effect in some Mogollon-Datil ignimbrites are provided by uncommon but well-developed examples of primary or secondary (Chapin and Lowell, 1979) folding of pumice foliations. Three sites were collected from severely folded outcrops, and several others were collected from moderately folded or lineated areas. At each site, the application of a uniform structural correction to individual sample data yielded within-site groupings as tight as most unfolded sites (Fig. 20). Scatter was increased if individual samples were corrected for within-site differences in foliation attitudes (Fig. 20). These failed fold tests indicate that magnetization occurred after folding was complete, implying that plastic deformation of these units took place at temperatures higher their maximum unblocking temperatures (580-700°C). These data furthermore indicate that the TRM directions of these ignimbrites are not significantly effected by flowage-related magnetic anisotropy.



site 171, rheomorphic Vicks Peak Tuff

Figure 20. Paleomagnetic fold test indicates that flowage folding of foliation in site 171 the Vicks Peak Tuff was complete prior to magnetization. TRM vectors are tightly grouped if a uniform structural correction is applied, but become scattered around the fold axes if sample data are corrected for local bedding contortions.

**Outflow vs. intracaldera facies**

Limited data from 4 Mogollon-Datil cauldron sequences suggest that thinner intracaldera-facies ignimbrites are paleomagnetically similar to their correlative outflow sheets, but that thicker intracaldera facies show more scattered site-mean directions.

This relationship is best established for the South Canyon Tuff, erupted at 27.4 Ma from the Mt. Withington cauldron, a "trapdoor" cauldron hinged along its southern edge (Fig. 14; Ferguson, 1986). TRM directions of 12 sites from the thinner (<500m), southern portion of the intracaldera ignimbrite are well grouped, and their cone of 95% confidence overlaps with that of 14 sites in the outflow sheet (Fig. 14, Table 3). Furthermore, one 210 m stratigraphic sequence of samples from the thinner intracaldera facies shows no significant stratigraphic variation in inclination or declination (Fig. 7c).

In contrast to thinner intracaldera facies, thick (>500 m) sections of South Canyon Tuff from the northern portion of the Mt. Withington cauldron show variable site-mean TRM directions. Individual samples from these sites show simple Type 1 and 2 magnetizations and their TRM directions are generally tightly grouped within individual sites (Fig. 14c, Table 3). However, between-site scatter is large ( $\alpha_{95}=12.7^\circ$ ), and the mean direction (D=187, I=-46) is significantly offset toward the expected mean axial dipole direction (D=170.5, I=-50), compared with the mean direction

of the outflow facies (Fig. 14b;  $D=204$ ,  $I=-30$ ,  $\alpha_{95}=3.6^\circ$ ; Table 3).

Less numerous data from three other cauldron sequences generally support the relationships shown by the South Canyon Tuff data. Sites from three units in the 9000 m thick Organ cauldron sequence (Seager and McCurry, 1988) show generally high within-unit dispersion (Fig. 16e). Furthermore, site-mean directions from two sites in the Squaw Mountain Tuff differ from those of Bell Top tuff member 3, a possibly correlative outflow sheet (McIntosh, dissertation, Chapter C). Conversely, the mean directions two sites from relatively thin portions of the intracaldera Apache Springs Tuff, collected near the margin of the Bursum cauldron, agree closely with data from its correlative outflow facies, the Bloodgood Canyon Tuff (Fig. 13e).

Paleomagnetic data from the Tadpole Ridge Tuff also show reasonably good agreement between the outflow facies and one of the two intracaldera-facies cooling units (Fig. 13k). The two intracaldera cooling units (upper and lower members of Finnell, 1976), are present within the caldera and yield distinctive TRM directions approximately  $50^\circ$  apart (Fig. 13k). Given modern mid-latitude secular variation rates (e.g.  $4.5^\circ/\text{century}$  in Hawaii; Holcomb et al., 1985), these TRM directions suggest that the two members were erupted at least several centuries apart. Alternatively, these two members may have been erupted in more rapid succession during a magnetic field excursion or polarity



transition. In either case, the distinctly steep TRM directions of three outflow-facies sites are strong evidence that the outflow sheet and the lower intracaldera member were emplaced simultaneously (Fig. 13k).

Dispersed site-mean TRM directions within thick intracaldera-facies ignimbrites most probably are a record of paleosecular variation which occurred during protracted cooling. Sufficiently slow cooling would delay RM acquisition in portions of the intracaldera facies, producing dispersed site-mean directions and a facies-mean direction offset towards the mean axial dipole direction. A protracted cooling history of this nature has been proposed to explain varied TRM directions in the thick (1350-1650 m) intracaldera facies of the Sunshine Peak Tuff, Colorado (Reynolds et al., 1986).

Alternatively, the scattered site-mean directions in the thick intracaldera-facies units might reflect non-horizontality of pumice foliations during initial cooling. Pumice foliations were the only available indicator of attitude for these sites, and the structurally corrected intracaldera paleomagnetic data are based on the assumption that these foliations were originally horizontal. Pumice-foliation orientations vary considerably within the Mt. Withington cauldron, but it is uncertain to what degree this variation reflects synvolcanic deformation and how much is due postvolcanic tectonism which produced multiple generations of normal faulting (Ferguson, 1986). In any

case, random attitude errors would not be expected to produce the observed systematic distribution of intracaldera-facies TRM directions around the time-averaged axial dipole field direction.

Remagnetization caused by younger intrusive rocks is a third process that may have affected the RM of intracaldera units. Reheating by adjacent plutons has been proposed to explain why corrections for pumice foliations cause increased between-site dispersion in the Amalia Tuff within the Questa cauldron (Hagstrum et. al., 1982; Hagstrum and Lipman 1986). Intrusive reheating by the underlying Organ Mountain batholith (Seager and McCurry, 1988) may also have locally remagnetized Organ cauldron units (Fig, 161). However, intrusive reheating is considered unlikely in the intracaldera-facies South Canyon Tuff, because neither plutonic rocks nor their contact metamorphic aureoles are exposed in the Mt. Withington cauldron.

A final possible explanation for the anomalous data from thick intracaldera-facies ignimbrites might be sub-blocking-temperature welding, flowage, or compaction. This process has evidently resulted in systematic variations in magnetization directions in the >300 m thick Topopah Springs Member ignimbrite, Nevada (Rosenbaum, 1986) and in the Fish Canyon Tuff, Colorado (Ellwood, 1982). In most cases, however, individual sites from these units show multivectoral demagnetization behavior and/or poor within-site grouping, in strong contrast to the well-grouped

within-site data from the intracaldera South Canyon Tuff. In addition, sub-blocking-temperature compaction generally results in flattened RM inclinations (Rosenbaum, 1986), and would not explain the steepened inclinations in the thick intracaldera facies of the South Canyon Tuff.

Although more work on intracaldera facies is needed, the available data suggest that detailed paleomagnetic correlations between outflow and intracaldera-facies ignimbrites may be applicable only to thinner (<500 m) intracaldera facies, and that results from thicker intracaldera facies should be applied with caution.

#### **Utility of paleomagnetism as a correlation criterion**

Successful paleomagnetic correlation of ignimbrites requires, above all else, that the units in question carry precisely measurable TRM components, acquired during rapid post-emplacement cooling. As discussed in previous sections, this requirement is well satisfied by 90% of the studied sites in Mogollon-Datil ignimbrites.

Because geomagnetic field directions vary non-uniquely through time, paleomagnetism constitutes a negative correlation criterion, i.e. disagreement of TRM directions is negative evidence for correlation, yet agreement is only permissive evidence. Paleomagnetic correlation for any set of units is favored by large angular differences among their mean TRM directions. Between-unit angular differences must exceed uncertainties introduced by measurement and structural correction errors.

Unit-mean TRM for the 22 relatively well-studied Mogollon-Datil ignimbrites all fall within  $30^\circ$  of expected time-averaged field directions ( $D=350.5$  or  $-170.5$ ,  $I=50$  or  $-50$ ). All of these unit-mean directions are therefore within the expected range of typical secular variation (Irving and Pullaiah, 1976; McFadden and McElhinney, 1984; Holcomb et al., 1985). The angular dispersion of the unit-mean VGPs of these 22 ignimbrites ( $\sigma=14.7^\circ$ , with 95% confidence levels of  $17.3^\circ > \sigma > 11.8^\circ$ ; Cox, 1969) is similar to the  $14.5^\circ$  angular dispersion predicted by model C of Cox (1970) but are slightly smaller than the  $18.4^\circ$  angular dispersion predicted for  $34^\circ\text{N}$  latitude by model F of McFadden and McElhinny (1984). A VGP dispersion of  $18.3^\circ$  ( $n=65$ ,  $20.8 > \sigma > 11.8$ ) is shown by all the ignimbrites for which at least one acceptable ( $\alpha_{95} < 10^\circ$ ) site-mean direction has been determined. These data suggest that Oligocene secular variation was similar in magnitude to Quaternary secular variation (Holcomb, 1985).

None of the well-studied Mogollon-Datil ignimbrites have recorded excursions or polarity transition events. One less studied ignimbrite, the 26.1 Ma tuff of Slash Ranch does show an anomalous mean direction ( $\text{inc}=58$ ,  $\text{dec}=167$ ) which may have recorded an excursion, but this direction may reflect, at least in part, the small number of sites ( $n=2$ ) or the extreme zeolitization of the unit. The lack of recorded excursions or polarity transition events is unusual among paleomagnetic studies, many of which have reported one

to several units with distinctive mean TRM directions which differ by more than  $40^\circ$  from the expected time-averaged field direction (e.g. Grommé et al., 1972; Reynolds, 1977; Weiss et al., 1989).

Whether or not paleomagnetism can be used to distinguish between two units strongly depends on the actual difference in TRM direction between the units. In cases where the units in question differ in polarity, paleomagnetic correlation is unambiguous. Polarity is a simple binary variable which is insensitive to measurement and structural uncertainties, requiring only that the measured remanence is primarily a TRM. The application of polarity data to Mogollon-Datil correlation problems, however, is restricted by the small fraction (20%) and limited distribution of normally magnetized regional ignimbrites.

The majority of Mogollon-Datil correlation problems have required comparing TRM directions of units of the same polarity. In order to paleomagnetically distinguish between any two units, the angular difference between their unit-mean TRM directions must exceed the net uncertainty of the data set in question. The net uncertainty in a data set is the sum of measurement and structural uncertainties. As presented above, site-mean remanence directions in this study were measurable to precisions of  $\alpha_{95}=2-10^\circ$ , excluding about 10% of sites which show excessive CRM or lithic-hosted components. Site-mean structural uncertainties averaged

5-10° in most areas, reaching 15-25° in areas of synvolcanic extension and in ignimbrites emplaced over irregular topography. Unit-mean directions were measurable to a precision  $\alpha_{95}=3-8^\circ$ , provided that enough sites (typically  $n \geq 5$ ) were analyzed to average structural uncertainties. If, for example, data from a single distal site were compared to data from a well-studied unit, the net maximum uncertainty in the data would range from 12-26° in most areas, reaching 22-51° in tectonically disturbed areas. In order to be considered in disagreement, therefore, site-mean and unit-mean TRM directions would have to differ by 12-51°, depending on specific precision values and on the structural uncertainty of the particular site.

Whether the net uncertainties allow two units to be paleomagnetically distinguished depends critically on the angular difference between their mean TRM directions. As summarized in Table 4, the TRM directional differences among specific pairs of the relatively well-studied ignimbrites range from 2-49° (great circle). The success or failure of a specific paleomagnetic correlation depends on the particular units in question. In general, paleomagnetic unit identification is most successful for the 9 units with relatively distinctive TRM directions which diverge by more than 15° from the expected time-averaged Oligocene field direction (Table 4). Two examples will serve to illustrate this situation.

Table 4. Great circle differences in unit-mean directions for ignimbrites with 4 or more sites.

## a) Reversed polarity units.

Unit	inc	dec	axial		KN	LW	RH	BC	BX	HM	CB	TP	DC	LJ	VP	GC	SP	BG	SC
			$\alpha_{95}$	dipole															
Turkey Springs	-51.8	175.9	3.6	4	10	10	19	26	21	10	7	23	10	5	24	7	19	26	29
South Canyon	-30.7	202.1	3.5	30	30	37	47	48	49	38	28	40	38	32	17	22	23	32	
Bloodgood Canyon	-27.1	165.3	3.1	23	17	35	32	20	34	33	20	49	27	22	16	27	10		
Shelly Peak	-32.7	174.8	6.4	18	13	29	31	25	33	28	14	41	23	17	8	18			
Garcia Camp	-48.8	185.4	5.2	10	14	15	25	32	27	16	10	24	17	11	21				
Vicks Peak	-27.9	182.8	3.3	22	20	35	39	33	41	34	20	45	31	24					
La Jencia	-49.3	168.2	3.6	2	6	13	15	21	18	11	4	27	7						
Davis Canyon	-53.5	159.6	7.5	8	11	10	9	19	11	8	11	26							
Lower Tadpole R.	-71.1	203.8	11.0*	26	33	16	29	45	30	19	29								
Caballo Blanco	-46.0	171.4	4.4	4	4	16	19	22	21	15									
Hells Mesa	-60.2	166.0	4.8	11	17	3	12	27	14										
Box Canyon	-56.0	141.3	4.7	18	20	16	2	19											
Blue Canyon	-37.3	144.4	5.7	23	18	30	18												
Rockhouse Canyon	-55.6	144.8	5.4	16	19	15													
Lebya Well	-61.7	171.2	10.8*	12	18														
Kneeling Nun	-43.7	167.1	3.8	7															

## b) Normal polarity units.

Unit	inc	dec	axial		DW	FR	BT4TC	CC	
			$\alpha_{95}$	dipole					
Lemitar	36.6	356.9	4.3	14	23	16	20	13	5
Caronita Canyon	41.5	354.2	11.0*	9	21	11	16	8	
Triangle C Ranch	49.2	357.3	4.4	4	15	8	8		
Bell Top 4	56.1	2.7	3.6	10	10	12			
Farr Ranch	50.4	345.5	4.7	3	21				
Datil Well	53.3	19.9	6.4	18					

Explanation: Inc, dec, and  $\alpha_{95}$  are unit-mean inclination, declination, and cone of 95% confidence. Stars denote unit-mean directions not considered significant because of poor precision ( $\alpha_{95} > 10^\circ$ ). Abbreviations along top row correspond to unit names listed in first column. Axial dipole column shows difference between unit-mean direction and estimated mean axial dipole field ( $D=350.5$ ,  $I=50$ ).

Paleomagnetism has been successfully used to distinguish among 4 younger high-silica rhyolite ignimbrites in the north-central portion of the Mogollon-Datil volcanic field. These units are the Bloodgood Canyon Tuff (28.1 Ma) and tuff of Triangle C Ranch (28.1 Ma) from Mogollon area sources, and South Canyon Tuff (27.4 Ma) and tuff of Turkey Springs (24.3 Ma) from the cauldrons in the San Mateo Mountains. All four units are lithologically indistinguishable, particularly in their distal facies. Furthermore, the Bloodgood Canyon Tuff and tuff of Triangle C Ranch are too close in age to be resolved even by  $^{40}\text{Ar}/^{39}\text{Ar}$  analysis (McIntosh, dissertation, Chapter B). Paleomagnetic data, however, allow confident identification of each of the 4 units (Fig. 21). One unit, the tuff of Triangle C Ranch, shows normal polarity. The other three units show reversed polarity, but their unit-mean TRM directions are sufficiently distinct (26-33° apart; Table 4) to completely overcome uncertainties in measurement and structural attitude (Fig. 21).

Paleomagnetism has been less successful in distinguishing among 4 older lithologically similar low-silica rhyolite regional ignimbrites: the Kneeling Nun (34.9 Ma), Box Canyon (33.5 Ma), Hells Mesa (32.1 Ma), and Caballo Blanco (31.7 Ma) tuffs. All 4 units show reversed polarity, and their TRM directions differ by only 5-20° (Table 4). As a result, many of the site-mean directions from different units overlap (Fig. 22) making confident paleomagnetic



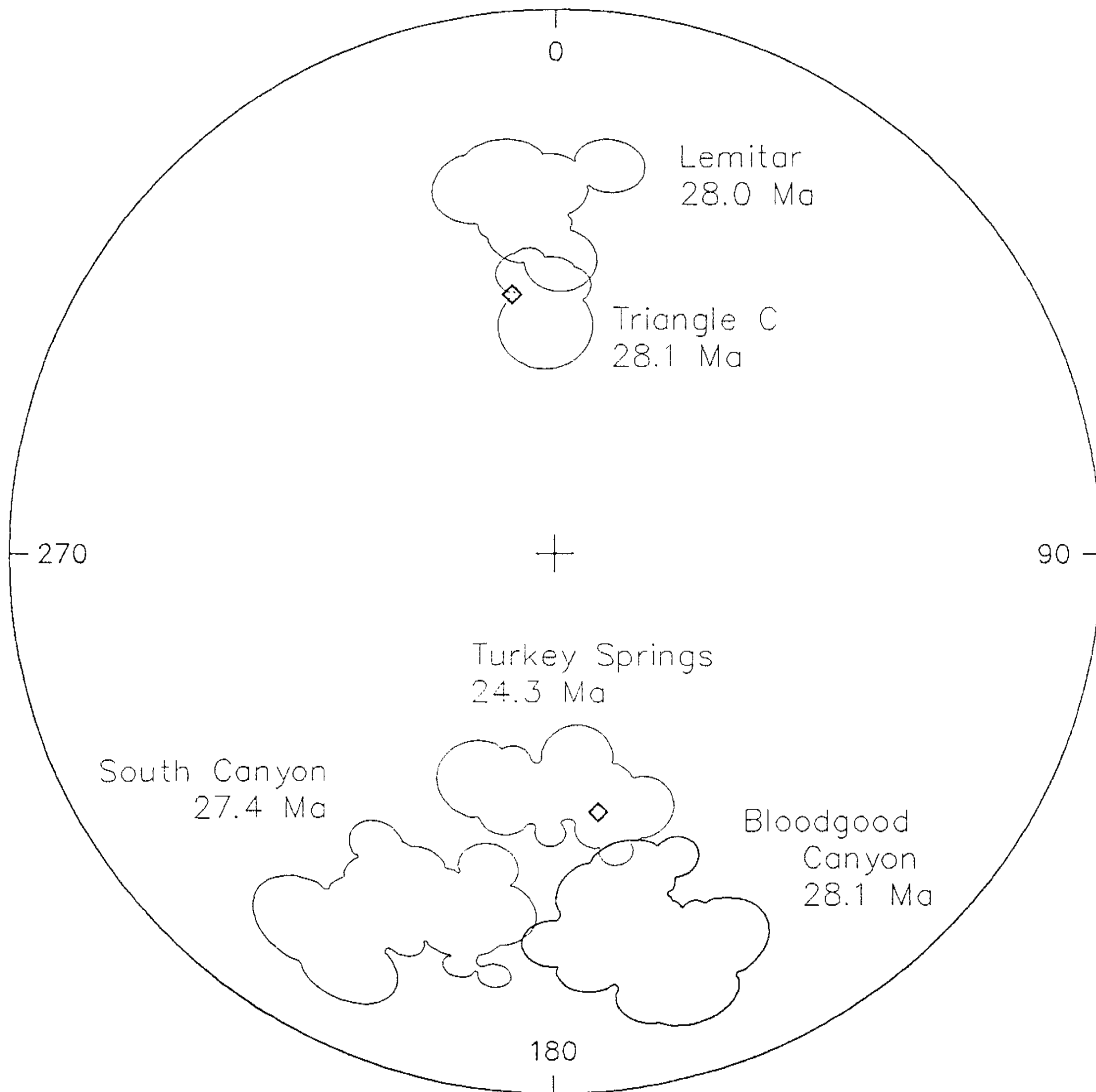


Figure 21. Little overlap is shown by site-mean data from 4 young (28.1-24.3 Ma), lithologically similar ignimbrites from the northern Mogollon-Datil volcanic field. Irregular outlines enclose site-mean ellipses for each unit and diamonds denote time-averaged Eocene-Oligocene normal and reversed field directions.

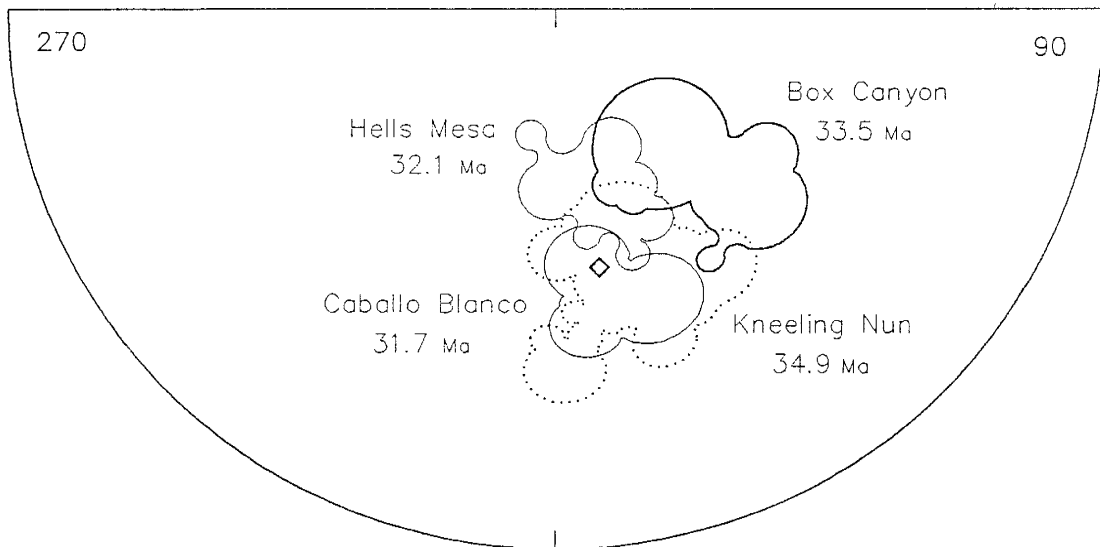


Figure 22. Considerable overlap is shown by site-mean data from 4 older (34.9-31.7 Ma), lithologically similar Mogollon-Datil ignimbrites. Irregular outlines enclose site-mean ellipses for each unit and diamonds denote time-averaged Eocene-Oligocene normal and reversed field directions.

identification of these 4 units impossible. Fortunately, all 4 units differ sufficiently in age to be readily resolved by  $^{40}\text{Ar}/^{39}\text{Ar}$  dating (McIntosh, dissertation, Chapter B).

In the final analysis, it appears that only about 40% of the studied Mogollon-Datil ignimbrites possess TRM directions that are sufficiently unique to allow confident identification by paleomagnetic data alone. For the remaining 60% of the ignimbrites, angular differences between TRM directions of different units (Table 4) are simply too small to be regularly resolved from measurement and structural uncertainties. This conclusion stands in contrast to studies in other volcanic fields which have yielded uniquely characteristic TRM directions for most or all individual ignimbrite units (Grommé et al., 1972; Reynolds, 1977; Weiss et al., 1987). The fact that not all Mogollon-Datil units are paleomagnetically resolvable reflects several factors, including the large number of ignimbrites analyzed, the high proportion that show reversed polarity, the paucity of recorded geomagnetic excursions, and the structural complexity of the volcanic field.

In spite of the non-unique nature of the TRM directions of many of the ignimbrites, paleomagnetic data have proven highly useful for resolving a large number of specific Mogollon-Datil correlations, particularly when used in concert with  $^{40}\text{Ar}/^{39}\text{Ar}$  data and other criteria such as lithology and stratigraphic position. These correlations

together have allow the development of an integrated, ignimbrite-based stratigraphic framework for the entire Mogollon-Datil volcanic field, as detailed in McIntosh et al. (1986) and McIntosh, dissertation, Chapter C.

#### **Paleomagnetic pole positions and assessment of non-dipole field behavior**

Diehl et al. (1988) used data from Mogollon-Datil ignimbrites and lavas to help refine the mid-Tertiary North American reference pole. Their study further suggested that the paleomagnetic poles of reversed and normal polarity units were not antipodal, and this was interpreted as reflecting persistent differences in zonal harmonics associated with the two geomagnetic polarity states (Diehl et al., 1988). Although the present contribution centers on stratigraphic correlation questions, the large quantity of data (103 independent records of the Eocene-Oligocene field) offers an excellent opportunity to re-examine differences between normal and reversed polarity states.

Mean RM directions and paleomagnetic poles of ignimbrites and lavas for this study, for Diehl et al. (1988), and for the combined data set are presented in Table 5 and Figure 23. For all three data sets, unit-mean directions and VGPs were first calculated from site data, then overall means were calculated by equally weighting each eruptive unit. In keeping with the procedure of Diehl et al. (1988), 2 ignimbrites and 3 lavas with VGPs diverging by more than 40° from the North American Oligocene reference

Table 5. Mean directions and paleomagnetic pole positions calculated from unit-mean ignimbrite and lava data.

data												plat	plong			
set	units	pol	n	inc	dec	k	a95	$\sigma$	$\delta$	(°N)	(°E)	k	a95	$\sigma$	$\delta$	
this study	ignimbrites (n≥4)	N	6	48.3	358.8	60.8	8.7	10.4	]5.6	83.9	150.9	59.5	8.8	10.5	]7.6	
		R	16	-48.4	170.3	21.5	8.1	17.5		76.7	167.4	26.2	7.3	15.8		
		N+R	22	-48.4	172.7	26.2	6.2	15.8		78.7	164.9	30.2	5.7	14.7		
	ignimbrites	N	23	52.4	350.5	28.9	5.7	15.1	]3.6	81.1	173.6	22.3	6.6	17.2	]2.4	
		R	42	-48.8	170.5	20.1	5.0	18.1		79.1	166.0	18.2	5.3	19.0		
		N+R	65	-50.1	170.5	22.6	3.8	17.0		79.8	168.4	19.6	4.1	18.3		
	lavas	N	13	63.1	354.1	16.2	10.6	20.1	]14.4	75.7	230.6	8.8	14.8	27.3	]16.3	
		R	25	-50.1	162.7	14.4	7.9	21.3		74.2	164.6	11.2	9.0	24.2		
	all units	N	36	56.1	351.1	21.9	5.1	17.3	]7.3	80.5	199.5	13.9	6.6	21.7	]7.2	
		R	67	-49.2	167.7	17.6	4.2	19.3		77.3	165.4	14.8	4.7	21.1		
		N+R	103	-51.7	168.8	18.5	3.3	18.8		78.8	175.0	14.3	3.8	21.4		
	Diehl et al., 1988	ignimbrites	N	7	54.0	353.8	19.1	11.7	18.5	]8.8	83.8	197.3	20.2	13.7	18.0	]9.1
R			21	-45.8	169.3	24.3	7.8	16.4	79.4		138.3	16.9	8.0	19.7		
lavas		N	16	55.7	353.1	11.6	7.7	23.8	]17.7	83.0	205.0	16.0	9.5	20.3	]15.0	
		R	17	-38.1	170.6	15.9	8.7	20.3		77.0	112.7	23.3	7.5	16.8		
all units		N	23	55.2	353.4	14.2	6.0	15.5	]13.0	83.1	201.3	18.0	7.3	18.9	]11.9	
		R	38	-42.4	169.9	19.3	5.7	19.2		78.5	125.4	19.5	5.4	18.2		
		N+R	61	-47.3	171.0	18.1	4.4	19.2		81.9	143.6	17.6	4.5	19.2		
combined data set		ignimbrites	N	24	52.0	350.3	28.8	5.6	15.1	]3.0	80.6	179.0	23.3	6.3	16.8	]4.4
			R	44	-49.1	169.1	19.4	5.0	18.4		77.7	161.4	18.3	5.2	18.9	
			N+R	68	-50.1	169.5	22.1	3.7	17.2		78.8	166.6	19.8	4.0	18.2	
		lavas	N	27	59.8	354.3	21.9	6.1	17.3	]15.2	77.4	230.5	14.2	7.7	21.5	]18.8
			R	40	-45.4	165.9	14.1	6.2	21.6		75.9	140.9	13.2	6.5	22.3	
	all units	N	51	56.1	352.2	23.7	4.2	16.6	]9.1	80.0	210.0	16.6	5.0	19.9	]11.5	
		R	84	-47.4	167.6	16.5	3.9	19.9		77.1	151.1	15.5	4.1	20.6		
		N+R	135	-50.7	169.1	17.8	3.0	19.2		79.5	169.2	14.9	3.3	21.0		

Explanation: symbols are as in Table 1, except that  $\sigma$  is circular standard deviation and  $\delta$  is angular deviation between directions or paleopoles of normal and reversed polarity data sets.

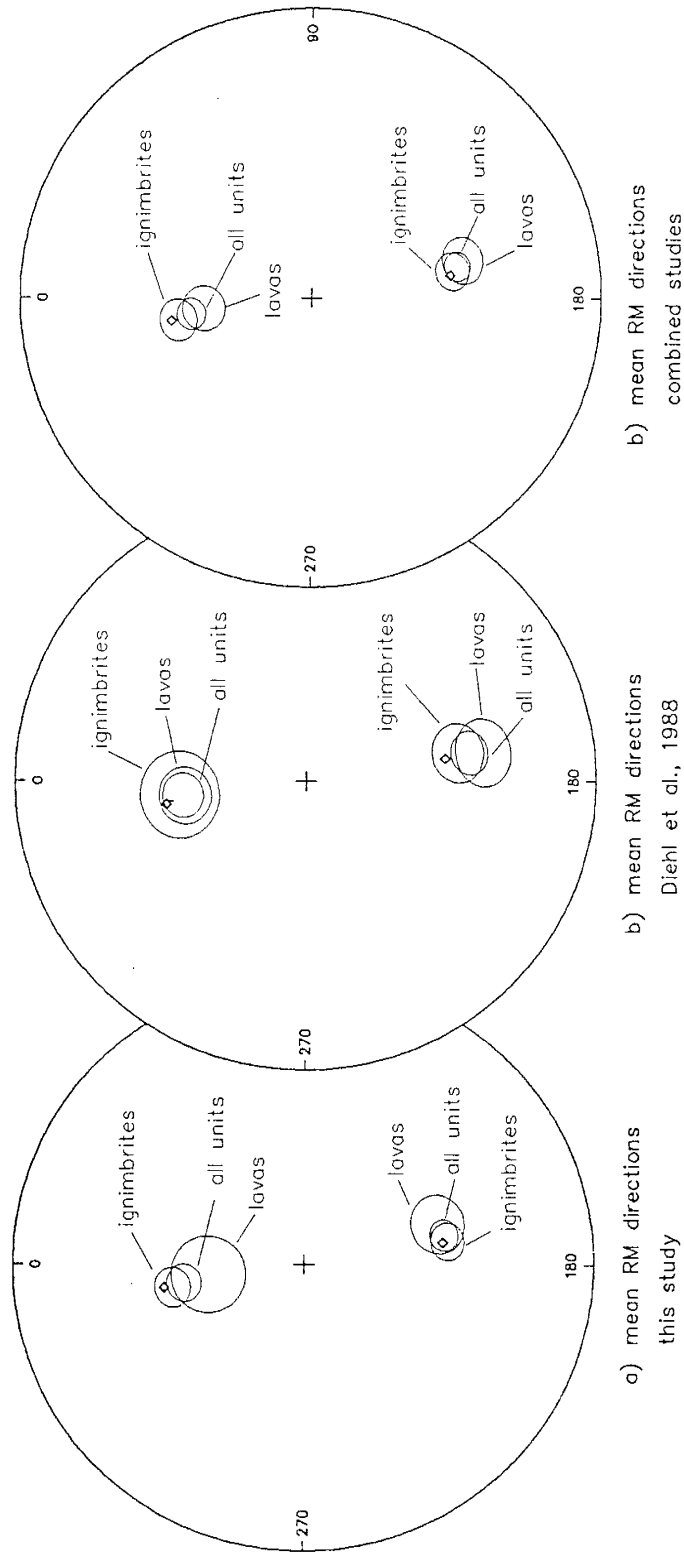


Figure 23. Mean paleomagnetic directions for Mogollon-Datil ignimbrites and lavas for a) this study, b) Diehl et al. (1988), and c) combined data set. Diamonds denote time-averaged Eocene-Oligocene normal and reversed field directions.

pole (81.5°N, 147.3°E; Diehl et al., 1988) were excluded from calculations of overall means.

The combined data set (68 ignimbrites, 67 lavas) was produced by merging this study (65 ignimbrites, 38 lavas) with Diehl et al. (1988) (28 ignimbrites, 33 lavas). A uniform arbitrary precision requirement of  $\alpha_{95} < 10^\circ$  was applied to all site-mean data, resulting in acceptance of 345 ignimbrite and 38 lava sites from this study (Tables 3 and 6) and 40 ignimbrite and 29 lava sites from Diehl et al. (1988). Six of the sites excluded from the combined data set (4 lava, 2 ignimbrite) were accepted by Diehl et al. (1988), who used a slightly less stringent minimum precision requirement  $\alpha_{95} < 15^\circ$ . Site-mean data from both studies were combined in calculations of unit-mean directions and VGPs for ignimbrites. In general, data from the two studies show excellent within-unit agreement (Table 1; Table 3; Diehl et al., 1988). Because most ignimbrites sampled by Diehl et al. (1988) were also analyzed in the present study, the total number of ignimbrites in the combined data set ( $n=68$ ) is only slightly larger than that of this study ( $n=65$ ).

In contrast to the conclusion of Diehl et al. (1988), this study and the combined data set show nearly antipodal mean RM directions and pole positions for normal and reversed ignimbrites. The angular differences ( $\delta$ ) in RM and mean VGP for ignimbrites of opposite polarity are respectively 3.6° and 2.4° for this study and 3.0° and 4.4° for the combined data set, compared to 8.8° and 9.1° angular

Table 6. Site-mean paleomagnetic data from Mogollon-Datil lavas.

site	lat (°N)	long (°W)	dip	str	dm	inc	dec	k	$\alpha_{95}$	n	type	site	lat (°N)	long (°W)	dip	str	dm	inc	dec	k	$\alpha_{95}$	n/t	type	
Rhyolitic Lavas																								
339	33.87	107.20	43	342	40	-42.6	178.5	839	3		4/4	2	373	33.80	108.12	0	0	30	-45.5	168.7	65	11	4/4	2
051	33.74	107.43	8	300	40	-29.6	181.0	513	4		4/4	2	377	33.91	108.26	0	0	40	-23.7	172.2	7	39	4/4	2 R
249	33.75	107.89	0	0	40	48.1	348.1	185	7		4/4	2	469	33.50	107.81	15	220	30	-24.1	221.3	6	40	4/4	2 R
189	33.69	107.76	4	180	30	52.3	342.3	240	6		4/4	1	470	33.49	107.83	10	210	30	-40.8	196.5	838	3	4/4	2
474	33.11	108.01	15	270	30	37.5	11.0	770	3		4/4	1	409	33.27	107.63	8	194	40	-53.7	179.6	38	15	4/4	2 R
442	33.33	107.76	10	180	40	42.9	250.2	611	5		3/4	2 E	446	33.91	106.97	8	0	40	-67.1	102.2	186	7	4/4	1
331	33.72	108.03	0	0	40	55.8	324.2	15	25		4/4	2 R	447	33.91	106.96	8	0	30	-73.8	126.9	62	12	4/4	1
489	33.27	108.41	0	0	50	63.8	289.0	121	8		4/4	2	449	33.92	106.96	0	0	40	-29.6	164.8	11	29	4/4	2 R
476	33.12	108.49	0	0	40	-46.7	171.6	697	3		4/4	2	450	33.93	106.96	8	0	30	-57.1	108.0	188	7	4/4	1
116	33.33	107.91	8	180	40	-57.6	151.0	175	7		4/4	1	072	33.70	107.28	15	300	20	-26.8	47.5	2	45	4/4	2 R
117	33.47	107.88	8	180	40	-43.9	159.2	2722	2		4/4	2	530	32.30	106.61	44	162	30	39.3	15.6	149	8	4/4	2
336	33.62	107.99	0	0	40	-25.4	173.5	13	28		4/4	2 R	357	33.51	107.43	26	315	40	-39.3	174.4	182	5	6/6	1
052	33.74	107.38	8	300	10	-27.6	173.7	472	4		4/4	2	452	32.92	107.65	17	10	30	71.4	357.6	275	6	4/4	1
350	33.55	107.50	20	132	30	-52.3	135.1	890	3		4/4	1	453	32.84	107.63	18	340	30	66.8	345.0	158	7	4/4	2
241	33.95	107.67	0	0	40	10.8	164.8	2	77		4/4	4 R	459	32.99	107.89	25	170	40	1.9	204.6	436	4	4/4	1 E
245	33.90	107.69	15	145	30	-72.1	130.4	404	5		4/4	2	464	32.72	107.58	12	135	30	-61.0	169.0	438	4	4/4	2
366	33.94	107.64	18	260	30	6.7	152.0	319	5		4/4	2 E	180	33.48	107.79	14	215	40	58.1	338.9	664	2	7/8	1
Mafic lavas																								
426	33.85	107.30	13	42	30	33.3	324.5	7	39		4/4	2 R	400	33.53	107.46	34	332	40	66.8	23.7	1019	3	4/4	1
363	33.87	107.69	6	145	40	59.0	328.1	9	32		4/4	2 R	406	33.43	107.82	13	160	30	69.2	322.5	331	5	4/4	2
035	34.16	106.83	67	180	40	65.7	324.3	48	10		6/8	2	356	33.53	107.46	34	332	40	-66.1	173.3	165	7	4/4	2
244	33.88	107.68	15	145	40	57.1	72.9	588	5		3/4	1	043	34.16	106.81	52	207	10	-20.7	185.0	83	10	4/4	2
326	33.88	108.26	0	0	40	-31.1	185.5	150	8		4/4	1	355	33.53	107.46	28	317	40	-55.6	157.4	146	8	4/4	2
379	34.16	107.94	0	0	40	-34.2	173.8	41	15		4/4	2 R	322	33.53	107.42	24	295	40	-30.4	102.5	9	27	5/5	2 R
099	33.74	108.70	20	212	10	-55.9	151.2	276	7		3/4	1	044	34.16	106.81	52	207	30	-31.4	207.7	18	16	6/4	2 R
393	33.54	107.43	15	0	40	-58.5	206.7	6	25		8/8	2 R	310	33.52	107.46	25	267	40	-33.7	124.0	50	13	4/4	2 R
136	34.41	106.68	10	212	40	53.5	333.2	120	11		3/4	2 R	358	33.51	107.43	26	315	40	-33.5	170.6	234	8	3/4	2
353	33.54	107.46	36	325	30	43.8	354.1	47	14		4/4	1 R	395	33.51	107.44	41	310	30	-0.8	148.3	2	87	4/8	2 R
440	33.46	107.85	10	180	40	74.2	339.7	1856	2		4/4	1	359	33.50	107.43	15	25	40	59.5	293.4	26	25	3/4	3 R
402	33.53	107.45	34	332	40	-45.8	171.6	194	7		4/4	2	397	33.51	107.44	41	310	40	29.5	333.4	38	20	3/4	2 R
410	33.27	107.63	8	194	30	-58.7	207.2	49	13		4/4	2 R	391	33.50	107.42	16	0	30	74.1	184.1	1	180	4/4	3 R
401	33.53	107.46	34	332	30	-71.9	156.9	116	9		4/4	2	392	33.50	107.42	15	0	40	74.2	307.3	5	45	4/4	3 R
407	33.43	107.83	13	160	40	-22.7	132.3	318	7		3/4	2	087	34.15	107.85	7	152	40	70.9	312.8	4	50	4/4	2 R
444	33.90	106.97	8	0	30	-38.0	145.8	587	4		4/4	2	399	33.49	107.45	34	332	30	42.3	19.6	13	26	4/4	2 R

Explanation: Site mean paleomagnetic data at AF demagnetization level (dm); inc and dec are site-mean inclination and declination; k is Fishers (1953) precision parameter; n/t is number of samples used in mean/total; type denotes demagnetization behavior: 1=TRM, 2=TRM+IRM, 3=TRM+CRM; R=rejected because  $\alpha_{95} < 10^\circ$ ; E=excluded from pole mean because of anomalous VGP.



differences in the ignimbrite data of Diehl et al. (1988). Using the conditional test of McFadden and Lowes (1981), the 4.4° difference in mean VGP of normal and reversed ignimbrites in the combined data set cannot be considered statistically different beyond a confidence level of 60%. Furthermore, the cones of 95% confidence for normal and reversed ignimbrites from all three data sets include the expected time-averaged Oligocene field direction (Fig. 23).

Unlike the ignimbrites, mean RM directions of normal and reversed lavas are significantly non-antipodal ( $\delta=14.4^\circ$ ,  $17.7^\circ$ , and  $15.2^\circ$  respectively for the present, Diehl et al. (1988), and combined data sets). These angular differences and the corresponding differences in mean VGP are all significant at the 99% confidence level (McFadden and Lowes, 1981). Furthermore, these lava data are sufficiently non-antipodal that poles determined from combined lava and ignimbrite data diverge by  $11.5^\circ$  (Table 5), an angular difference that is also significant at the 99% confidence level (McFadden and Lowes, 1981).

However, although both this study and Diehl et al. (1988) show non-antipodal lava data, the two data sets show generally poor agreement. In the present study, normal polarity lavas show steeper inclinations than normal polarity ignimbrites, whereas reversed polarity lavas and ignimbrites agree (Fig. 23a). Diehl et al. (1988) reported, conversely, that normal lavas agree closely with the normal

ignimbrites, but reversed lavas show shallower inclinations (Fig. 23b).

It is unlikely that the difference between the antipodal ignimbrite data and non-antipodal lava data reflects actual behavior of the mid-Tertiary geomagnetic field. Ignimbrites and lavas were sampled in the same geographic area and were erupted during the same period of time (36-24 Ma). The ignimbrite data almost certainly represent a more accurate record of ancient fields than do the lava data. The mean RM directions of ignimbrites show significantly better between-study agreement than the lavas. Although the total number of ignimbrite and lava units are similar, the ignimbrites are represented by more sites per unit, averaging 5.7 sites/ignimbrite versus 1 site/lava. Lavas also show generally higher within-site dispersion than ignimbrites (Table 6; Diehl et al. 1988), and, in this study, lavas are represented by fewer samples per site ( $n=4-6$ ; Table 6) than ignimbrites. Furthermore, compared to ignimbrite unit-mean data, the mean directions and VGPs of lavas show higher circular standard deviations ( $\sigma=17-24^\circ$  for lava VGPs and  $\sigma=14-20^\circ$  for ignimbrite VGPs; Table 5).

There are several possible explanations for the non-antipodal RM directions of normal and reversed polarity lavas. First, secular variation may be incompletely averaged in the data set. The actual number of independent records of the Eocene-Oligocene field may be considerably less than the number of units sampled, if sequences of flows

were erupted rapidly relative to secular variation (e.g. Doell and Cox, 1967; Geissman et al., 1989). Second, the structural corrections for lavas may include relatively large errors, due in part to lack of eutaxitic foliation in lavas. Third, the RM directions of lavas may include unremoved, unrecognized CRM or viscous RM components. Although none of these explanations would necessarily be expected to systematically bias the data, they could introduce random errors resulting in non-antipodal data sets. Errors of this nature might help explain the between-study differences in lava data described above.

If lavas are excluded from the data set, then paleomagnetic data from the Mogollon-Datil volcanic field do not support the presence of long-term differences in the harmonics of the normal and reversed polarity states (Merrill et al., 1979). This interpretation does not necessarily invalidate the conclusions Diehl et al. (1988), which were based on published data from several other mid-Tertiary volcanic fields as well as on their Mogollon-Datil data set. Perhaps, however, the hypothesis of non-antipodal mid-Tertiary geomagnetic field behavior should be re-examined using only high-precision paleomagnetic data, i.e. data from units represented by several different individual sites.

The mean paleomagnetic pole calculated for ignimbrites from the combined data set of this study and Diehl et al. (1988) is located at  $78.8^{\circ}\text{N}$ ,  $166.6^{\circ}\text{E}$  ( $n=68$  unit-mean VGPs,

$K=19.8$ ,  $A_{95}=4.0^\circ$ ). This pole position differs by  $4.9^\circ$  from the Mogollon-Datil pole ( $81.9^\circ\text{N}$ ,  $143.6^\circ\text{E}$ ) of Diehl et al. (1988), and differs by  $4.2^\circ$  from their North American 20-40 Ma reference pole ( $81.5^\circ\text{N}$ ,  $147^\circ\text{E}$ ). All three poles are statistically indistinguishable at the 95% confidence interval (McFadden and Lowes, 1981).

### CONCLUSIONS

1. Well-grouped TRM directions ( $\alpha_{95} < 10^\circ$ ) were resolved for 90% of the 404 studied sites in regional and local ignimbrites of the Mogollon-Datil volcanic field. These TRM components are carried by high-temperature deuteric oxidation assemblages of magnetite, hematite, and probable cation-deficient magnetite. TRM components in about 10% of the studied sites are obscured by alteration-related CRM components or lithic-hosted components carried by lithic fragments in some lithic-rich, poorly welded ignimbrite facies.
2. The largest source of uncertainty in individual site-mean directions is uncertainty in structural attitude. This uncertainty is typically less than  $10^\circ$  but reaches  $15\text{-}25^\circ$  in zones of extreme tectonic extension and areas where ignimbrites were emplaced over irregular topography. Systematic declination errors at some localities indicate net tectonic rotation of fault blocks about vertical axes.

3. Excluding sites with large structural attitude errors, site-mean TRM directions are laterally and vertically consistent within individual ignimbrite outflow sheets, including both densely welded proximal and poorly welded distal facies. None of the sites in outflow sheets show evidence of significant syn-cooling secular variation or sub-blocking temperature flowage. Given a sufficient number of sites (typically  $n \geq 5$ ) unit-mean TRM directions of regional outflow sheets can be determined to a precision of  $\alpha_{95} = 2$  to  $8^\circ$ . The TRM directions within thick ( $>500$  m) intracaldera facies are considerably less consistent, probably reflecting either geomagnetic secular variation during slow post-emplacement cooling or pumice foliations that were not horizontal during cooling.

4. The TRM directions of 22 ignimbrite outflow units have been relatively well-constrained ( $n \geq 4$ ). Of these, 16 show reversed polarity and 6 are normal. The 22 unit-mean directions deviate from the expected time-averaged Eocene-Oligocene field directions by angles ranging  $2^\circ$  to  $30^\circ$ . This angular deviation exceeds  $15^\circ$  for 9 of the ignimbrites, yielding relatively distinctive directions which are particularly effective correlation criteria. The range of angular deviations of the 22 well-constrained unit-mean directions and the circular standard deviation of their VGPs ( $14.7^\circ$ ) is typical of expected mid-Tertiary secular

variation. None of the units were erupted during geomagnetic excursions.

5. Paleomagnetism has helped resolve many long standing ignimbrite correlation problems in the Mogollon-Datil volcanic field and has been instrumental in the development of an ignimbrite-based time-stratigraphic framework. It has proven most effective when combined with  $^{40}\text{Ar}/^{39}\text{Ar}$  dating and lithologic, geochemical, and stratigraphic data (McIntosh et al., 1986; McIntosh, dissertation, Chapter C).

6. In contrast to the conclusion of Diehl et al. (1988), the mean directions of normal and reversed polarity Mogollon-Datil ignimbrites are nearly antipodal ( $176.4^\circ$  apart). A combined data set from this study and Diehl et al. (1988) yields mean VGPs for normal and reversed polarity ignimbrite subsets that are only  $4.4^\circ$  apart; this difference is statistically insignificant even at the 63% level. The mean directions of normal and reversed lavas for this study are indeed significantly non-antipodal ( $165.6^\circ$  apart), but do not agree closely with the results of Diehl et al. (1988), reflecting at least in part additional complications in the lava data set. The ignimbrite data set is believed to represent a superior record of the Eocene-Oligocene field and does not support long term differences in the zonal harmonics of the normal and reversed polarity states.

## REFERENCES

- Best, M.G., Shuey, R.T., Caskey, C.R., and S.K. Grant, Stratigraphic relations of members of the Needles Range Formation at type localities in southwestern Utah, *Geol. Soc. Am. Bull.*, 84, 3269-3278, 1973.
- Bogue, S.W., and R.S. Coe, Paleomagnetic correlation of Columbia River basalt flows using secular variation, *J. Geophys. Res.*, 86, 11883-11897, 1981.
- Bornhorst, T.J., Major- and trace-element geochemistry and mineralogy of Upper Eocene to Quaternary volcanic rocks of the Mogollon-Datil volcanic field, southwestern New Mexico, Unpublished Ph.D. dissertation, Albuquerque, Univ. New Mexico, 1104 p, 1980.
- Chamberlin, R.M., Cenozoic domino-style crustal extension in the Lemitar Mountains, New Mexico: A summary, *New Mexico Geol. Soc. Guidebook 34*, p. 111-118, 1983.
- Chapin, C.E., and G.R. Lowell, Primary and secondary flow structures in ash-flow tuffs in the Gribbles Run Paleovalley, Central Colorado, *Spec. Pap. Geol. Soc. Am.* 180, 137-154, 1979.
- Chapin, C.E., Chamberlin, R.M., Osburn, G.R., White, D.W., and A.R. Sanford, Exploration framework of the Socorro geothermal area, New Mexico. in Chapin, C.E., and Elston, W.E., eds., *Field guide to selected cauldrons and mining districts of the Datil-Mogollon volcanic field, New Mexico*, *New Mexico Geol. Soc. Special Pub.* 7, 114-129, 1978.
- Chapin, C.E., and W.R. Seager, Evolution of the Rio Grande rift in the Socorro and Las Cruces areas, *New Mexico Geol. Soc. Guidebook*, 26, 297-322, 1975.
- Cox, A., Confidence limits for the precision parameter  $k$ , *Geophys. J. R. Astron. Soc.*, 18, 545-549, 1969.
- Cox, A., Latitude dependence of the angular dispersion of the geomagnetic field, *Geophys. J. R. Astron. Soc.*, 20, 253-269, 1970.
- Dalrymple, B., Cox, A., and R.R. Doell, Potassium-argon age and paleomagnetism of the Bishop Tuff, California, *Geol. Soc. Am. Bull.*, 76, 665-674, 1965.
- Dankers, P.H.M., Magnetic properties of dispersed natural iron oxides of known grain size, unpublished Ph.D. dissertation, Univ. Utrecht, Netherlands, 143 p, 1978.

- Diehl, J.F., McClannahan, K.M., and T.J. Bornhorst, Paleomagnetic results from the Mogollon-Datil volcanic field, southwestern New Mexico, and a refined mid-Tertiary reference pole for North America, *J. Geophys. Res.*, 93, 4869-4879, 1988.
- Diehl, J.F., McClannahan, K.M., Bornhorst, T.J., and S.D. Sheriff, Paleomagnetic results from early Oligocene rocks of the Mogollon-Datil volcanic field, southwestern New Mexico, *EOS Trans. AGU*, 63, 913, 1982.
- Deino, A.L., and M.G. Best, Use of high-precision single-crystal  $^{40}\text{Ar}/^{39}\text{Ar}$  Ages and TRM data in correlation of an ash-flow deposit in the Great Basin, *Geol. Soc. of Amer. Abstr. with Progs.*, 20, A397, 1988.
- Doell, R.R., and A. Cox, An analysis of paleomagnetic data, in Collinson, D.W., Creer, K.M., and Runcorn, S.K., (eds.), *Methods in Paleomagnetism*, Elsevier, New York, 340-346, 1967.
- Duffield, W.A., Richter, D.H., and S.S. Priest, Preliminary geologic map of the Taylor Creek Rhyolite, Catron and Sierra Counties, New Mexico, *U.S. Geol. Surv. Open File Rep. 87-515*, 1:50,000, 1987.
- Ellwood, B.B., Estimates of flow direction of calc-alkaline welded tuffs and paleomagnetic data reliability from anisotropy of magnetic susceptibility measurements: central San Juan Mountains, southwest Colorado, *Earth Planet. Sci. Lett.*, 59, 303-314, 1982.
- Elston, W.E., Mid-Tertiary ash flow tuff cauldrons, southwestern New Mexico, *J. Geophys. Res.*, 89, 8733-8750, 1984.
- Ferguson, C.A., Geology of the east-central San Mateo Mountains, Socorro County, New Mexico, New Mexico Bureau Mines Open File Rep. 252, 135p, 1986.
- Finnell, T.L., Geologic map of the Twin Sisters quadrangle, Grant County, New Mexico, *U.S. Geol. Surv. Misc. Field Studies Map MF-779*, 1976.
- Fisher, R.A., Dispersion on a sphere, *Proc. R. Soc. London, Ser. A*, 217, 295-305, 1953.
- Geissman, J.W., Paleomagnetism of ash-flow tuffs: microanalytical recognition of TRM components, *J. Geophys. Res.*, 85, 1487-1499, 1980.
- Geissman, J.W., and R. Van der Voo, Thermochemical remanent magnetization in Jurassic silicic volcanics from



- Nevada, U.S.A., *Earth Planet. Sci. Lett.*, 48, 385-396, 1980.
- Geissman, J.W., Van der Voo, R., and K.L. Howard, A paleomagnetic study of the structural deformation in the Yerington district, Nevada, I. Tertiary units and their tectonism, *Am. J. Sci.*, 282, 1042-1079, 1982.
- Geissman, J.W., Newberry, N.G., and D.R. Peacor, Discrete single-domain and pseudo-single domain titanomagnetite particles in silicic glass and ash-flow tuff, *Can. J. Earth Sci.*, 20, 334-338, 1983.
- Geissman, J.W., Harlan, S.S., Brown, L., Turrin, B., and L.D. McFadden, Bruhnes chron geomagnetic excursion recorded during the late Pleistocene, Albuquerque Volcanoes, New Mexico, U.S.A., *in* F.J. Lowes, ed., *Geomagnetism and Paleomagnetism*, 123-136, 1989.
- Geissman, J.W., and S.S. Harlan, in preparation. Paleomagnetic evidence for tectonic rotations in the Hoover Dam area, Nevada, in review, 1989.
- Golembek, M.P., and L.L. Brown, Clockwise rotation of the Mojave Desert, *Geology*, 16, 126-130, 1988.
- Gose, W.A., Paleomagnetic studies of Miocene ignimbrites from Nevada, *Geophys. J. R. Astron. Soc.*, 20, 241-252, 1970.
- Grommé, C.S., McKee, E.H., and M.C. Blake, Paleomagnetic correlations and potassium-argon dating of middle Tertiary ash-flow sheets in eastern Great Basin, Nevada and Utah, *Geol. Soc. Am. Bull.*, 83, 1619-1638, 1972.
- Haggerty, S.E., Oxidation of opaque minerals in basalts, in *Oxide Minerals, Mineralogical Society of America Short Course Notes*, v. 3, p. H1-H100, 1976.
- Hagstrum, J.T., and P.B. Gans, Paleomagnetism of the Oligocene Kalamazoo Tuff: Implications for Middle Tertiary extension in east central Nevada, *J. Geophys. Res.*, 94, 1827-1842, 1989.
- Hagstrum, J.T., Lipman, P.W., and D.P. Elston, Paleomagnetic evidence bearing on the structural development of the Latir volcanic field near Questa, New Mexico, *J. Geophys. Res.*, 87, 7833-7842, 1982.
- Hagstrum, J.T., and P.W. Lipman, Paleomagnetism of the structurally deformed Latir volcanic field, northern New Mexico: Relations to formation of the Questa Caldera and development of the Rio Grande rift, *J. Geophys. Res.*, 91, 7383-7402, 1986.

- Heider, F., and D.J. Dunlop, Two types of chemical remanent magnetization during the oxidation of magnetite, *Phys. Earth Planet. Inter.*, 46, 24-45, 1987.
- Hildreth, W. and G. Mahood, Correlation of ash-flow tuffs, *Geol. Soc. Am. Bull.*, 96, 968-974, 1985.
- Hillhouse, J.W., and R.E. Wells, Assessment of rotations in the eastern Mojave Desert, California and Arizona, from paleomagnetism of the Peach Springs Tuff, *EOS Trans. AGU*, 67, 922, 1986.
- Hoblitt, R.P., Reynolds, R.R., and E.E. Larson, Suitability of non-welded pyroclastic-flow deposits for studies of magnetic secular variation. A test based on deposits emplaced on Mount St. Helens, Washington, in 1980, *Geology*, 13, 242-245, 1985.
- Holcomb, R., Champion, D., and M. McWilliams, Dating recent Hawaiian lava flows using paleomagnetic secular variation, *Geol. Soc. Am. Bull.*, 97, 829-839, 1986.
- Hudson, M.R., and J.W. Geissman, Paleomagnetic and structural evidence for middle Tertiary counter-clockwise block rotation in the Dixie Valley region, west-central Nevada, *Geology*, 15, 638-642, 1987.
- Irving, E., and G. Pullaiah, Review of the geomagnetic field, magnetostratigraphy, and relative magnitude of paleosecular variation in the Phanerozoic, *Earth Sci. Rev.*, 12, 35-64, 1976.
- Johnson, H.P., and R.T. Merrill, Magnetic and mineralogical changes associated with low temperature oxidation of magnetite, *J. Geophys. Res.*, 77, 334-341, 1972.
- Johnson, H.P., and R.T. Merrill, Low temperature oxidation of single-domain magnetite, *J. Geophys. Res.*, 79, 5533-5534, 1974.
- Kirschvink, J.L., The least-squares line and plane and the analysis of paleomagnetic data, *Geophys. J. R. Astron. Soc.*, 62, 699-718, 1980.
- MacDonald, W.D., Net tectonic rotation, apparent tectonic rotation, and the structural tilt correction in paleomagnetic studies, *J. Geophys. Res.*, 85, 3659-3669, 1980.
- Marvin, R.F., Naeser, C.W., Bikerman, M., Mehnert, H.H., and J.C. Ratté, Isotopic ages post-Paleocene igneous rocks within and bordering the Clifton 1° x 2° quadrangle,

- Arizona-New Mexico, New Mexico Bureau Mines Bull., 118, 63 p, 1987.
- McClannahan, K.M., Diehl, J.F., and T.J. Bornhorst, Further paleomagnetic results from early Oligocene volcanic rocks from the Mogollon-Datil volcanic field, southwestern New Mexico, EOS Trans. AGU, 64, 687, 1983.
- McClannahan, K.M., Paleomagnetic investigation of mid-Tertiary volcanic rocks of the Mogollon-Datil volcanic field, southwestern New Mexico, unpublished M.S. thesis, Michigan Tech University, Houghten, Michigan, 65 p., 1984.
- McFadden, P.L., and F.J. Lowes, The discrimination of mean directions drawn from Fisher distributions, Geophys. J. R. Astron. Soc., 76, 19-33, 1981.
- McFadden, P.L., and M.W. McElhinney, A physical model for paleosecular variation, Geophys. J. R. Astron. Soc, 78, 809-830, 1984.
- McIntosh, W.C., Preliminary results from a paleo- and rock-magnetic study of Oligocene ash-flow tuffs in Socorro County, New Mexico, New Mexico Geol. Soc. Guidebook 34, 205-210 , 1983.
- McIntosh, W.C., Progress toward calibration of the Mid-Tertiary geomagnetic polarity time scale using high-precision  $^{40}\text{Ar}/^{39}\text{Ar}$  dated ignimbrites in southwestern New Mexico, Geol. Soc. Am. Abstr. with Progs., 20, A65-66, 1988.
- McIntosh, W.C., Timing and distribution of ignimbrite volcanism in the Eocene-Oligocene Mogollon-Datil volcanic field of southwestern New Mexico, IAVCEI Field Excursion Guide, New Mexico Bureau Mines Memoir 46, p.58-59.
- McIntosh, W.C., Sutter, J.F., Chapin, C.E., Osburn, G.R., and J.C. Ratté, A stratigraphic framework for the Mogollon-Datil volcanic field based on paleomagnetism and high-precision  $^{40}\text{Ar}/^{39}\text{Ar}$  dating of ignimbrites - a progress report, New Mexico Geol. Soc. Guidebook 37, 183-195, 1986.
- Merrill, R.T., McElhinney, M.W., and D.J. Stevenson, Evidence for long-term asymmetries in the Earth's magnetic field and possible implications for dynamo theories, Phys. Earth Planet. Inter., 20, 75-82, 1979.
- Nagata, T., Rock Magnetism, 2nd Ed., Maruzan, Tokyo, 350p., 1961.

- Nagata, T., and Akimoto, S., Magnetic properties of ferromagnetic ilmenites, *Geofis. Pura. Appl.*, 34, 36, 1956.
- Osburn, G.R., and C.E. Chapin, Nomenclature for Cenozoic rocks of the northeast Mogollon-Datil volcanic field, New Mexico, New Mexico Bureau of Mines Stratigraphic Chart 1, 1983a.
- Osburn, G.R., and C.E. Chapin, Ash-flow tuffs and cauldrons in the northeast Mogollon-Datil volcanic field, a summary, *New Mexico Geol. Soc. Guidebook* 34, 197-204, 1983b.
- Özdemir, Ö., and S.K. Banerjee, High-temperature stability of maghemite, *Geophys. Res. Lett.*, 11, 161-164, 1984.
- Özdemir, Ö., and D.J. Dunlop, An experimental study of chemical remanent magnetizations of synthetic monodomain titanomaghemites with initial thermoremanent magnetizations, *J. Geophys. Res.*, 90, 11513-11523, 1985.
- Ratté, J.C., Marvin, R.F., and C.W. Naeser, Calderas and ash-flow tuffs of the Mogollon Mountains, *J. Geophys. Res.*, 89, 8713-8732, 1984.
- Ratté, J.C., and W.C. McIntosh, Geologic map of the Horse Mountain West Quadrangle, U.S. Geol. Surv. Open File Rep. 89-210, scale 1:24,000, 1989.
- Reihle, J.R., Calculated compaction profiles of rhyolitic ash-flow tuffs, *Geol. Soc. Am. Bull.*, 82, 2193-2216, 1973.
- Reynolds, R.L., Paleomagnetism of welded tuffs of the Yellowstone Group, *J. Geophys. Res.*, 82, 3677-3693, 1977.
- Reynolds, R.R., Hudson, M.R., and K. Hon, Paleomagnetic evidence for the timing of collapse and resurgence of the Lake City Caldera, San Juan Mountains, Colorado, *J. Geophys. Res.*, 91, 9599-9613, 1986.
- Rosenbaum, J.G., Paleomagnetic directional dispersion produced by plastic deformation in a thick Miocene welded tuff, southern Nevada: Implications for welding temperatures, *J. Geophys. Res.*, 91, 12817-12834, 1986.
- Roy, J.L., and J.K. Park, The magnetization process of certain red beds: Vector analysis of chemical and thermal results, *Can. J. Earth Sci.*, 11, 437-471, 1974.

- Schlinger, C.M., Rosenbaum, J.G., and D.R. Veblen, Fe-oxide microcrystals in welded tuff from southern Nevada: Origin of remanence carriers by precipitation in volcanic glass, *Geology*, 16, 556-559, 1988.
- Seager, W.R., Clemons, R.E., Hawley, J.W., and R.E. Kelley, Geology of the northwest part of Las Cruces 1° x 2° sheet, New Mexico, New Mexico Bureau of Mines Geological Map 53, scale 1:125,000, 1982.
- Seager, W.R., and M. McCurry, The cogenetic Organ cauldron and batholith, south central New Mexico: Evolution of a large-volume ash flow cauldron and its source magma chamber, *J. Geophys. Res.*, 93, 4421-4433, 1988.
- Stacey, F.D., and S.K. Banerjee, *The Physical Principles of Rock Magnetism*, Elsevier, Amsterdam, 195 p, 1974.
- Strangway, D.E., Simpson, J., and D. York, Paleomagnetic studies of volcanic rocks from the Mogollon Plateau area of Arizona and New Mexico, *in* *Cenozoic Volcanism*, New Mexico Geol. Soc. Special Pub. 5, 119-124, 1976.
- Walker, T.R., Larson, E.E., and R.P. Hoblitt, The nature and origin of hematite in the Moenkopi Formation (Triassic), Colorado Plateau: A contribution to the origin of magnetism in red beds, *J. Geophys. Res.*, 86, 317-333, 1981.
- Weiss, S.J., Noble, D.C., and E.H. McKee, Paleomagnetic and cooling constraints on the duration of the Pahute Mesa-Trail Ridge eruptive event and associated magmatic evolution, Black Mountain volcanic center, southwestern Nevada, *J. Geophys. Res.*, 94, 6075-6084, 1989.
- Zijderveld, J.D.A., A.C. demagnetization of rocks: analysis of results, *in*: Collinson, D.W., Creer, D.W., and Runcorn, S.K. (eds.), *Methods in Paleomagnetism*. Elsevier, Amsterdam, 254-286, 1967.

High-Precision  $^{40}\text{Ar}/^{39}\text{Ar}$  sanidine geochronology of  
ignimbrites in the Mogollon-Datil volcanic field,  
southwestern New Mexico

William C. McIntosh<sup>1</sup>, John F. Sutter<sup>2</sup>,  
Charles E. Chapin<sup>1</sup> and Laura L. Kedzie<sup>1</sup>

<sup>1</sup>N.M. Bureau of Mines and Mineral Resources, N.M. Institute  
of Mining and Technology, Socorro, New Mexico, 87801

<sup>2</sup>U.S. Geological Survey, Reston, Va., 20292

ABSTRACT

$^{40}\text{Ar}/^{39}\text{Ar}$  age spectra have been obtained from 85  
sanidine separates from 36 ignimbrites and one rhyolitic  
lava in the latest Eocene-Oligocene Mogollon-Datil volcanic  
field of southwestern New Mexico. Of the 97 measured age  
spectra, 94 yield weighted-mean plateau ages each giving  
single-spectrum precision ( $1\sigma$ ) of  $\pm 0.25$ - $0.4\%$  ( $\pm 0.07$ - $0.14$   
Ma). Replicate plateau age determinations for 8 different  
samples show within-sample precisions averaging  $\pm 0.25\%$ .

Plateau ages from multiple ( $n=3$  to  $8$ ) samples of  
individual ignimbrites show within-unit precision ( $1\sigma$ ) of  
 $\pm 0.1$ - $0.4\%$  ( $\pm 0.04$ - $0.13$  Ma). This within-unit precision  
represents a several-fold improvement over published K-Ar  
data for the same ignimbrites, and is similar to the range  
of precisions reported from single-crystal laser fusion  
studies. A further indication of the high precision of  
unit-mean  $^{40}\text{Ar}/^{39}\text{Ar}$  ages is their close agreement with  
independently established stratigraphic order.

Two samples failed to meet plateau criteria, apparently  
due to geologic contamination by older feldspars. Effects

of minor contamination are shown by 6 other samples which yield slightly anomalous plateau ages.

$^{40}\text{Ar}/^{39}\text{Ar}$  plateau ages permit resolution of units differing in age by 0.5% (0.15 m.y.) or less. This high resolution, combined with paleomagnetic studies, has helped to correlate ignimbrites among isolated ranges and has allowed development of an integrated time-stratigraphic framework for the volcanic field.

Mogollon-Datil ignimbrites range in age from 36.2 to 24.3 Ma. Ignimbrite activity was strongly episodic, being confined to 4 brief (<2.6 m.y.) eruptive episodes separated by 1-3 m.y. gaps. Ignimbrite activity generally tended to migrate from the southeast towards the north and west.

#### INTRODUCTION

The need for high-resolution  $^{40}\text{Ar}/^{39}\text{Ar}$  geochronology is acute in mid-Tertiary silicic volcanic fields, where major ignimbrites (ash-flow tuffs) have in some cases been erupted at intervals of 0.2 m.y. or less, and differences in eruption ages are unresolvable by conventional K-Ar geochronology. Under the best circumstances, conventional K-Ar dating yields within-sample precisions near  $\pm 1.0\%$  (Lanphere, 1988); in practice, however, within-unit standard deviations of reported K-Ar ages from individual ignimbrites may exceed  $\pm 5\%$  (e.g. Marvin et al, 1987).

$^{40}\text{Ar}/^{39}\text{Ar}$  dating techniques can yield ages which are several times more precise than the best conventional K-Ar ages. This high precision chiefly results from the ability

to simultaneously measure radiogenic  $^{40}\text{Ar}$  and  $^{40}\text{K}$  (as reactor-produced  $^{39}\text{Ar}$ ) on a single aliquot of sample (Turner, 1968; Roddick, 1983). Furthermore, the  $^{40}\text{Ar}/^{39}\text{Ar}$  method can provide accurate ages without extracting all Ar from a sample, thereby overcoming the chronic problem of incomplete  $^{40}\text{Ar}$  extraction in K-Ar dating of sanidine and anorthoclase (McDowell, 1983).

Currently, the two variations of the  $^{40}\text{Ar}/^{39}\text{Ar}$  method used for high-precision age determinations are age spectra (e.g. Lanphere, 1988) and laser-heating total fusions (e.g. Dalrymple and Duffield, 1988). Age spectra offer two advantages. First, the shape of the age spectrum allows identification of samples which have been affected by Ar loss or excess Ar. Second, precision can be increased by statistically treating incremental heating step data using plateau or isotope correlation methods. On the other hand, the laser-heating total fusion method offers advantages of small blank, single grain sample size, rapid analysis, and easy identification of contamination. Within-sample and within-unit precisions of about  $\pm 0.5\%$  have reported for biotite and bulk-sample plateau ages (e.g. Lanphere, 1988), and laser-heating  $^{40}\text{Ar}/^{39}\text{Ar}$  total-fusion dating of small samples or single crystals of sanidine may offer even higher precision (Dalrymple and Duffield, 1988; Deino and Best, 1988; Deino, 1989).

This paper reports the results of a  $^{40}\text{Ar}/^{39}\text{Ar}$  sanidine age spectra study of regional ignimbrites in the Mogollon-



Datil volcanic field of southwestern New Mexico. The application of this data to Mogollon-Datil volcanic stratigraphy and to calibration of the mid-Tertiary magnetic polarity time scale is discussed in other papers (McIntosh et al, 1986; McIntosh, dissertation, Chapters C and D).

#### MOGOLLON-DATIL VOLCANIC FIELD

The Mogollon-Datil volcanic field is the northern tip of a once contiguous Late Eocene-Oligocene volcanic field that extended from southwestern New Mexico into Chihuahua, Mexico (Fig. 1). This relatively accessible volcanic field has been the focus of numerous mapping, stratigraphic, geochemical, petrologic, and isotopic studies (e.g. see references in Ratté et al., 1984; Osburn and Chapin; 1983a). The general history of Mogollon-Datil activity resembles that of the San Juan volcanic field of Colorado (Lipman et al., 1978). Activity began with andesitic volcanism from about 40 to 36 Ma, which was followed by episodic bimodal silicic and basaltic andesite activity from 36 to 24 Ma (Cather et al., 1987; Elston, 1984). The silicic sequence includes about 25 widespread ( $>1000 \text{ km}^2$ ), voluminous ( $100\text{-}1300 \text{ km}^3$ ), high- and low-silica rhyolitic ignimbrites. Source cauldrons have been identified for many of these ignimbrites (Osburn and Chapin, 1983b; Elston, 1984), but regional correlations of outflow sheets have been problematic. Although local stratigraphic sequences have been established by detailed mapping (e.g. Ratté et al., 1984; Seager et al., 1982), longer range correlations have

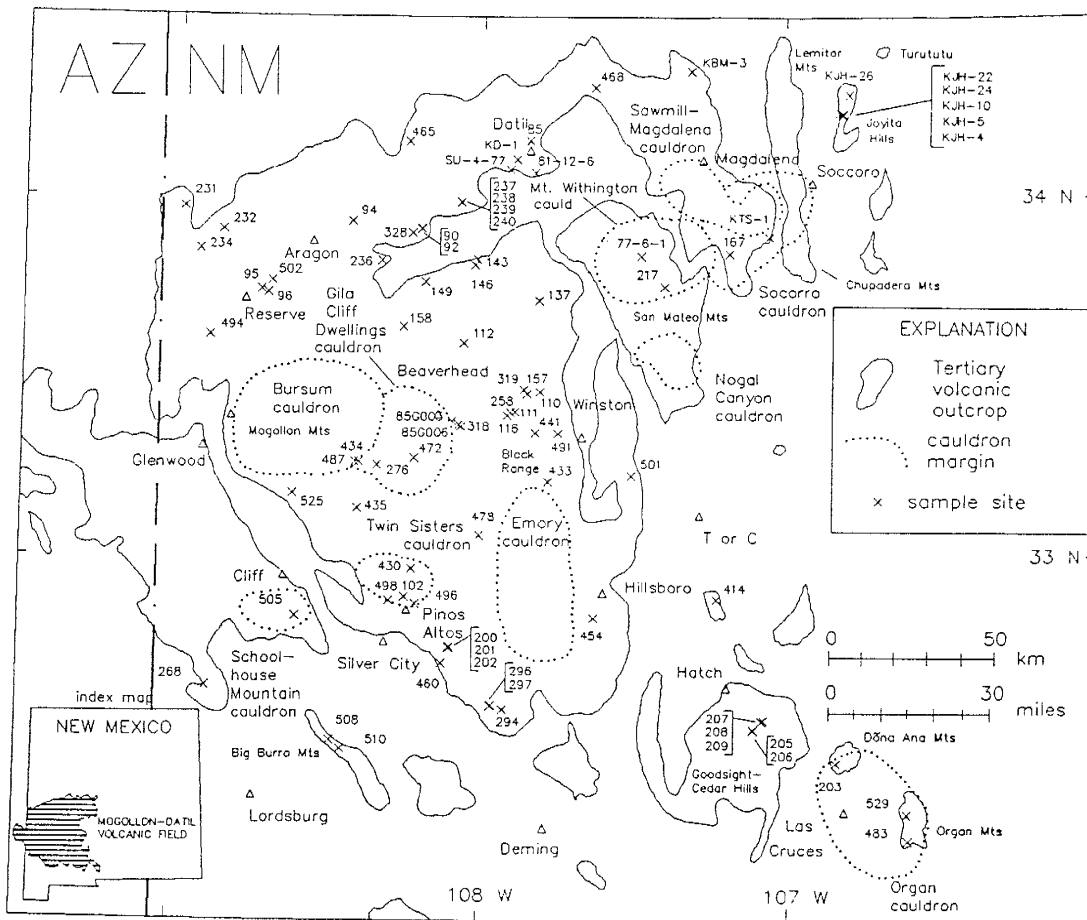


Fig. 1. Map of  $^{40}\text{Ar}/^{39}\text{Ar}$  dating samples from the Mogollon-Datil volcanic field. Numbered crosses show sample locations (precise positions in Appendix 3).

been hampered by extensional faulting and tectonism, and by lithologic similarities among units (McIntosh et al., 1986; Hildreth and Mahood, 1985).

Conventional K-Ar and fission-track data have proven too imprecise to allow reliable correlation of many Mogollon-Datil regional ignimbrites. For most units, only a small number of K-Ar dates are available, and these data in many cases disagree with independently established stratigraphic relationships (e.g. Clemens, 1976). In cases where several K-Ar or fission-track dates have been determined for individual units, within-unit standard deviations generally exceed  $\pm 5\%$ , or about  $\pm 1.4$  Ma (e.g. Marvin et al, 1987). For many of the units, sanidine K-Ar dates are significantly younger than biotite K-Ar ages, apparently reflecting incomplete extraction of Ar from sanidine (McDowell, 1983).

$^{40}\text{Ar}/^{39}\text{Ar}$  age spectra from Mogollon-Datil ignimbrites yield plateau ages far more precise than published K-Ar data.  $^{40}\text{Ar}/^{39}\text{Ar}$  dating and paleomagnetic studies have helped to reliably correlate ignimbrites among isolated ranges, thereby solving some of the volcanic field's long standing stratigraphic problems. These data, in combination with existing mapping and stratigraphic data, have aided the development of a Mogollon-Datil regional time-stratigraphic framework (McIntosh et al., 1986; McIntosh, dissertation, Chapter C).

Mogollon-Datil ignimbrites are well-suited for  $^{40}\text{Ar}/^{39}\text{Ar}$  analysis. Most of the units contain abundant sanidine, a K-rich, anhydrous mineral that is highly retentive of argon (Zeitler, 1987). Furthermore, stratigraphic relationships established by detailed mapping (e.g. Ratté et al, 1984) and paleomagnetic correlations (McIntosh et al., 1986) provide opportunities to stratigraphically test the precision of  $^{40}\text{Ar}/^{39}\text{Ar}$  results.

#### METHODS

A total of 83 samples were collected from 36 ignimbrites and one rhyolite lava (Fig. 1). Outcrops showing evidence of weathering, hydrothermal alteration, or K-metasomatism were avoided. Sanidine separates (>99% purity; 20-200 $\mu$  grain size) were prepared using heavy liquid and magnetic techniques, ultrasonic probe, and abrasion mill (Goldich and Fischer, 1986). In addition to the above samples, two sanidine separates from the Bloodgood Canyon Tuff (85006) and the Taylor Creek Rhyolite (85G003) were obtained from B. Dalrymple to facilitate inter-laboratory calibration with the U.S. Geological Survey continuous laser  $^{40}\text{Ar}/^{39}\text{Ar}$  facilities at Menlo Park (Dalrymple and Duffield, 1988).

Sample purity and sanidine mineralogy was assessed by optical microscope, x-ray diffraction, and electron microprobe. In the electron microprobe study, 5 to 8 grains from each of 57 samples were analyzed with an electron beam widened to 20 $\mu$  to minimize volatilization of Na. Narrower

1-2  $\mu$  beams were also used to assess zonation and exsolution.

Seven separate packages of samples were each irradiated for 20 hours in the constant-flux portion of the Central Thimble facility of the U.S. Geological Survey TRIGA reactor using the procedures of Dalrymple et al. (1981). Each irradiation package contained 10-40 tin or aluminum capsules, each containing 50-200 mg of sanidine. Neutron fluxes within packages were monitored both vertically and radially using MMhb1 (520.4 Ma, Sampson and Alexander, 1987) and FCT-3 (Fish Canyon Tuff sanidine, 27.83 Ma, recalculated from Kunk et al., 1985, using the above age for MMhb1). The geometry of samples and monitors was carefully controlled ( $\pm 0.5$  mm), because uncertainty in neutron flux ( $J$ ) is one of the chief factors which limits the precision of the  $^{40}\text{Ar}/^{39}\text{Ar}$  method. Monitors in the earlier irradiations revealed a 0.5-1.0% radial flux gradient across the width of the packages; in the final two irradiations this gradient was reduced by rotating the package about its vertical axis at a rate of about 1 rph.

Age spectra were measured at the U.S. Geological Survey  $^{40}\text{Ar}/^{39}\text{Ar}$  dating facility at Reston, Va. Samples were heated in induction or low-blank resistance furnaces for 15-30 minute intervals in 3-9 incremental temperature steps. The number of heating steps were kept low in order to maximize the size of gas fractions, thereby minimizing uncertainties in measurement of  $^{36}\text{Ar}$ . Temperatures were controlled to

$\pm 10^\circ\text{C}$  in the resistance furnace and  $\pm 50^\circ\text{C}$  in the induction furnace. For all but three samples, gas fractions were analyzed using the faraday cup on a VG-Micromass 1200B spectrometer, which has a detection limit of about  $1.5 \times 10^{-16}$  moles for  $^{36}\text{Ar}$ ,  $^{37}\text{Ar}$ ,  $^{38}\text{Ar}$ , and  $^{39}\text{Ar}$  and about  $1.5 \times 10^{-15}$  moles for  $^{40}\text{Ar}$ . Precision of argon isotopic measurements for a single analysis was about  $\pm 3.0 \times 10^{-16}$  moles for isotope concentrations less than  $3.0 \times 10^{-13}$  moles, and a maximum of  $\pm 0.1\%$  of the signal for larger concentrations. Three small samples (40-60 mg) were analyzed with the electron multiplier, which provided a detection limit about 25 times lower than the faraday cup. The extraction system blank at furnace temperatures of  $1450^\circ$  was typically about  $3-15 \times 10^{-14}$  moles  $^{40}\text{Ar}$  for the resistance furnace, and about  $2-5 \times 10^{-13}$  moles  $^{40}\text{Ar}$  for the induction furnace.

Plateau gas fractions were selected from age spectra using the criteria of Fleck et al. (1977), whereby plateaus consist of two or more contiguous incremental heating steps, yielding more than 50% of the  $^{39}\text{Ar}$ , which differ in age by less than critical value (Dalrymple and Lanphere, 1969). In addition, initial or final steps which were small ( $<5\%$  total  $^{39}\text{Ar}$ ) or showed large errors ( $>1\%$ ) were excluded from plateaus. Mean plateau ages were calculated by weighting the age of each plateau gas fraction according to the inverse of its analytical variance. Uncertainty of each plateau age was calculated by quadratically combining the standard deviation of plateau gas fractions ages with the

measured uncertainty in irradiation parameter J (about  $\pm 0.25\%$ ) and uncertainties in isotopes produced by interfering reactions during irradiation (Dalrymple et al., 1981).

#### SANIDINE MINERALOGY

Electron microprobe analyses of 57 Mogollon-Datil K-feldspar samples show that all are Na-rich sanidines, ranging in composition from  $Or_{66}Ab_{33}$  to  $Or_{33}Ab_{59}$  (Fig. 2, Table 1). Ca contents are low, ranging from  $An_{0.4}$  to  $An_{4.3}$  and averaging  $An_{1.5}$ . No evidence of zonation or exsolution was shown by microprobe traverses of individual grains, and between-grain variations within individual samples were small ( $1\sigma$  typically  $< \pm 2\%$ ).

In thin section, virtually all of the sanidines appear clear and unaltered, although a some show minor iron-staining along fractures. A few samples from intra-caldera facies have minor clay alteration along cleavages, but these impurities were almost entirely removed during the mineral separation process. No exsolution of feldspar phases was observed on the microscopic scale, although many of the sanidines appear chatoyant in hand specimen.

X-ray diffraction patterns show that most of the sanidine samples have undergone significant cryptoperthitic exsolution to K-rich and Na-rich phases. All of the samples show characteristic high-sanidine x-ray peaks (Fig. 3). The d-spacings of the 201, 204, and 060 peaks indicate a high degree of Al/Si disorder, with calculated "T1" values

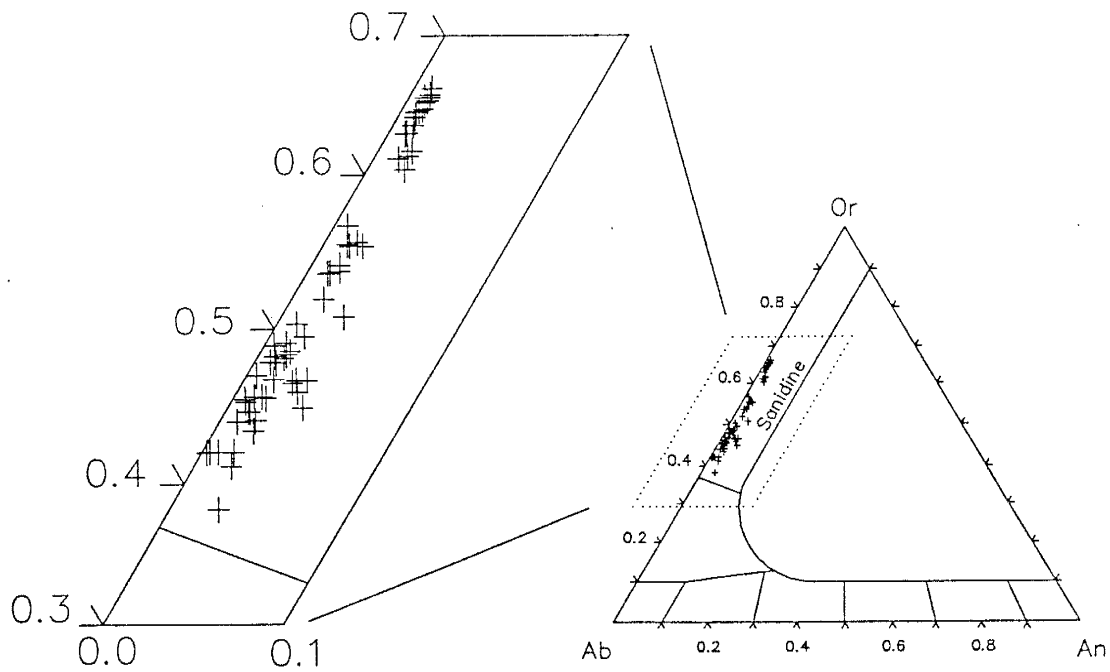


Fig. 2. Sanidine compositions determined by electron microprobe. A portion of the sanidine field is enlarged at the left. Each cross represents averaged data from 5-8 analyzed grains.



Table 1. Weighted-mean plateau ages and mineralogical data for Mogollon-Datil sanidines.

unit	sample	sanidine mineralogy						total gas		plateau		$\sigma$		$\sigma_X$	
		K/Ca	Or	Ab	An	Ex	Ir	age (Ma)	% <sup>39</sup> Ar	n	age(Ma)	Ma	%	Ma	%
Turkey Springs	unit mean	33.2								2	24.33 ±0.03	(±0.12%)			
	137	33.8	56	43	2		56	24.3	100.0	5	24.35 ±0.09	(±0.37%)			
	217	32.6	54	44	2	E	56	24.3	100.0	5	24.31 ±0.09	(±0.37%)			
Jordan Canyon	472	40.0	49	51	1	U	56	26.6	69.4	2	26.10 ±0.12	(±0.46%)			
South Canyon	unit mean	29.8								3	27.36 ±0.07	(±0.26%)	±0.04	(±0.15%)	
	KJH-22	31.6					22	27.6	74.0	3	27.40 ±0.07	(±0.26%)			
	77-6-1	19.0	44	54	2		32	27.4	88.7	4	27.41 ±0.07	(±0.26%)			
	258	38.7	56	43	1	E	54	27.4	65.7	2	27.28 ±0.08	(±0.29%)			
Walking X Creek	510	31.4					56	27.8	100.0	5	27.58 ±0.10	(±0.36%)			
Lemitar	unit mean	27.7								2	28.00 ±0.08	(±0.29%)			
	KTS-1	24.5					20	28.0	56.5	4	27.94 ±0.10	(±0.36%)			
	KJH-24	30.8					22	28.1	68.3	5	28.05 ±0.07	(±0.25%)			
Caronita Canyon	167	24.3				E	32	27.9	67.9	5	27.96 ±0.07	(±0.25%)			
Triangle C	158:mean	46.2	61	38	1					2	28.05 ±0.14	(±0.50%)			
	158	46.2					32	28.0	70.5	5	27.95 ±0.08	(±0.29%)			
	158	46.2					32	28.1	80.2	4	28.15 ±0.07	(±0.25%)			
Apache Springs	487	30.4	50	48	1		54	27.9	90.7	3	27.98 ±0.09	(±0.32%)			
Bloodgood Canyon	unit mean	40.4								8	28.05 ±0.04	(±0.14%)	±0.01	(±0.05%)	
	94	43.8	48	51	1	E	56	28.1	100.0	5	28.11 ±0.10	(±0.36%)			
	95	40.9	48	51	1		56	28.2	97.7	4	28.06 ±0.10	(±0.36%)			
	112	36.0	48	50	2		56	29.3	100.0	5	28.04 ±0.10	(±0.36%)			
	276	48.8	44	55	1	E	54	28.1	84.4	4	27.99 ±0.12	(±0.43%)			
	318	40.8	49	50	1	E	54	28.0	67.4	2	28.05 ±0.07	(±0.25%)			
	430	41.4				E	54	28.0	71.4	2	28.06 ±0.08	(±0.29%)			
	434: mean	49.2	45	54	1	E	20			2	28.09 ±0.05	(±0.18%)			
	434	49.4					54	28.1	90.6	3	28.05 ±0.09	(±0.32%)			
	434	48.9					56	28.2	98.8	5	28.12 ±0.10	(±0.36%)			
	85G006	22.4	43	55	2		54	28.1	63.9	2	28.03 ±0.08	(±0.29%)			
Diablo Range	435	34.0	48	51	1	E	54	28.1	90.6	3	28.05 ±0.08	(±0.29%)			
Shelley Peak	149:mean	25.7	56	42	2	E	20			2	28.59 ±0.11	(±0.37%)			
	149	25.7					32	28.5	60.2	3	28.67 ±0.08	(±0.28%)			contaminated? (1.9% too old)
	149	25.6					32	28.5	100.0	3	28.52 ±0.09	(±0.32%)			
Garcia Camp	319	25.4	52	46	2	E	54	28.1	92.1	3	28.10 ±0.09	(±0.32%)			
Taylor Creek	unit mean	26.1								2	28.10 ±0.18	(±0.66%)			
	116	29.1	45	53	2		42	28.2	84.7	4	28.23 ±0.10	(±0.35%)			
	85G003	23.1	48	50	2		54	28.0	91.7	3	27.97 ±0.10	(±0.36%)			
Vicks Peak	unit mean	56.5								3	28.56 ±0.06	(±0.19%)	±0.03	(±0.11%)	
	KJH-10	43.2					22	28.6	73.4	3	28.51 ±0.08	(±0.28%)			
	143	46.1	42	57	1		32	28.6	63.1	4	28.62 ±0.08	(±0.28%)			
	414	80.3	42	58	0	E	54	29.0	60.8	2	28.56 ±0.08	(±0.28%)			
	502	52.8	41	57	2		56	30.4	80.7	3	30.69 ±0.11	(±0.36%)			contaminated? (7.5% too old)
Lookout Mountain	unit mean	34.4								2	28.69 ±0.03	(±0.10%)			
	433	32.2	45	53	1	E	54	28.7	97.8	3	28.67 ±0.12	(±0.42%)			
	441	36.6	45	54	1	E	54	28.8	91.6	3	28.72 ±0.11	(±0.38%)			

Table 1 (continued). Weighted-mean plateau ages and mineralogical data for Mogollon-Datil sanidines.

unit	sample	sanidine mineralogy					ir	total gas		plateau age(Ma)	$\sigma$		$\sigma_X$	
		K/Ca	Or	Ab	An	Ex		age (Ma)	% <sup>39</sup> Ar n		Ma	%	Ma	%
La Jencia	unit mean	25.2							4	28.85 ±0.04	(±0.14%)	±0.02 (±0.08%)		
	KJH-4	28.8					20	28.9	71.0	5	28.83 ±0.08	(±0.28%)		
	KJH-5	27.8					20	28.8	59.8	4	28.81 ±0.09	(±0.31%)		
	146:mean	24.2	44	54	1	E			2	28.90 ±0.11	(±0.39%)			
	146	24.2					32	29.1	82.3	5	28.98 ±0.08	(±0.28%)		
	146	24.2					32	28.9	100.0	3	28.82 ±0.08	(±0.28%)		
	111	22.2	45	53	2		42	28.8	74.9	4	28.86 ±0.09	(±0.31%)		
Mud Hole	157	25.7	50	48	2	E	54	29.1	65.4	2	29.09 ±0.11	(±0.38%)		
Davis Canyon	unit mean	36.7								2	29.01 ±0.11	(±0.38%)		
	96	30.1	47	52	2		32	29.1	100.0	3	29.09 ±0.08	(±0.28%)		
	494	43.3					56	28.8	59.8	2	28.93 ±0.10	(±0.35%)		
Little Mineral Creek	491	19.5	56	42	2		56	29.0	100.0	5	29.01 ±0.10	(±0.35%)		
Tadpole Ridge	496	10.0					56	31.4	94.8	5	31.39 ±0.11	(±0.35%)		
Caballo Blanco	unit mean	62.8								5	31.65 ±0.06	(±0.17%)	±0.03 (±0.09%)	
	200	61.9	64	35	1	E	42	31.7	95.3	5	31.66 ±0.11	(±0.35%)		
	236	62.4				E	56	31.7	100.0	5	31.64 ±0.11	(±0.35%)		
	268	63.4	63	36	1	E	54	31.7	92.7	3	31.71 ±0.12	(±0.38%)		
	478	59.4	66	34	1		54	31.6	88.2	3	31.56 ±0.12	(±0.38%)		
	525	66.9					56	31.7	100.0	5	31.67 ±0.11	(±0.35%)		
Hells Mesa	unit mean	56.7								4	32.06 ±0.10	(±0.30%)	±0.06 (±0.17%)	
	KJH26:mean	65.2	64	35	1	E				6	32.06 ±0.10	(±0.31%)	±0.05 (±0.15%)	
	KJH-26	62.5					20	32.2	100.0	8	32.25 ±0.08	(±0.25%)		
	KJH-26	88.6					22	32.1	87.6	5	32.10 ±0.11	(±0.35%)		
	KJH-26	55.4					54	32.0	92.1	3	31.99 ±0.11	(±0.34%)		
	KJH-26	61.0					56	32.0	73.8	3	31.99 ±0.11	(±0.34%)		
	KJH-26	61.3					56	32.0	72.8	3	32.03 ±0.11	(±0.35%)		
	KJH-26	62.6					56	32.0	100.0	5	32.01 ±0.11	(±0.34%)		
	KD-1	62.1					20	32.2	54.2	2	32.11 ±0.10	(±0.31%)		
	KBM-3	45.7					22	32.3	77.8	3	32.15 ±0.11	(±0.34%)		
	SU-4-77	53.8					16	31.9	93.5	5	31.93 ±0.09	(±0.28%)		
Box Canyon	unit mean	48.6								7	33.51 ±0.13	(±0.40%)	±0.05 (±0.15%)	
	201	52.7	64	35	1	E	42	33.5	76.4	4	33.52 ±0.12	(±0.36%)		
	207	49.4	66	33	1	E	54	33.6	87.1	3	33.57 ±0.09	(±0.27%)		
	232	53.7	65	34	1		54	33.4	78.6	3	33.29 ±0.14	(±0.42%)		
	234	54.9	65	33	1	U	54	34.6	64.0	2	33.62 ±0.10	(±0.30%)		
	297	52.8	65	34	1	E	54	33.4	81.5	2	33.36 ±0.10	(±0.30%)		
	505	22.6					56	33.7	90.8	3	33.65 ±0.12	(±0.36%)		
	508	54.2					56	33.5	65.1	2	33.55 ±0.12	(±0.36%)		
Blue Canyon	unit mean	29.5								2	33.66 ±0.03	(±0.09%)		
	240	29.3				U	42	33.7	79.8	4	33.64 ±0.11	(±0.33%)		
	328	29.7	62	36	2	U	56	33.7	100.0	7	33.68 ±0.12	(±0.36%)		
	81-12-6:mean	27.6	62	36	2					2	33.98 ±0.03	(±0.08%)		
	81-12-6	27.6					32	34.0	84.2	6	34.00 ±0.09	(±0.27%)	contaminated? (1.0% too old)	
	81-12-6	27.6					32	34.0	78.0	3	33.96 ±0.08	(±0.24%)		
Rockhouse Canyon	468	30.7	54	45	1	E	56	34.4	93.8	3	34.42 ±0.12	(±0.35%)		
	239	32.9	61	37	2		42	34.9	80.3	4	34.88 ±0.11	(±0.32%)	contaminated? (1.3% too old)	
Table Mountain	296	32.6	61	37	1	E	56	34.0	70.7	3	33.96 ±0.12	(±0.35%)		
Mimbres Tuff	454	25.9	42	56	2		56	34.5	100.0	5	34.57 ±0.12	(±0.35%)		
Bishop Peak	231	10.9	45	51	4	U	54	34.8	64.0	2	34.70 ±0.10	(±0.29%)		

Table 1 (continued). Weighted-mean plateau ages and mineralogical data for Mogollon-Datil sanidines.

unit	sample	sanidine mineralogy					Ir	total gas		plateau age (Ma)	$\sigma$		$\sigma X$	
		K/Ca	Or	Ab	An	Ex		age (Ma)	% <sup>39</sup> Ar		n	Ma	%	Ma
Kneeling Nun	unit mean	61.2								4	34.89 ±0.05	(±0.15%)	±0.03 (±0.08%)	
	92	63.0				E	56	35.0	73.0	3	34.90 ±0.12	(±0.34%)		
	202	49.9	64	35	1	E	56	34.9	100.0	5	34.89 ±0.12	(±0.34%)		
	208	62.0	63	36	1		54	34.9	86.8	3	34.83 ±0.15	(±0.43%)		
	294	62.4	61	37	1	E	56	34.9	100.0	5	34.96 ±0.12	(±0.34%)		
	498	61.9					56	35.0	100.0	5	35.17 ±0.12	(±0.34%)	contam? (0.9-1.4% too old)	
	110	60.7	66	33	1	E	32	35.3	67.1	4	35.35 ±0.12	(±0.34%)		
	465	68.4				E	56	45.8			no plateau		contaminated	
Bell Top #4	unit mean	11.4								3	34.86 ±0.04	(±0.11%)	±0.02 (±0.07%)	
	206	10.9	38	59	3	E	54	35.1	82.7	3	35.01 ±0.13	(±0.37%)		
	209	11.1					56	34.9	100.0	5	34.94 ±0.12	(±0.34%)		
	501	12.2					56	35.1	63.8	2	34.93 ±0.12	(±0.34%)		
Sugarlump #2	460	23.7	48	50	2		56	35.2	58.9	2	35.17 ±0.12	(±0.34%)		
Farr Ranch	238	12.8	51	46	4	U	42	35.6	89.3	5	35.57 ±0.13	(±0.37%)		
Datil Well	unit mean	12.3								2	35.48 ±0.07	(±0.20%)		
	85:mean	12.4	47	50	4					2	35.53 ±0.03	(±0.08%)		
	85	12.4					32	35.6	81.5	4	35.55 ±0.10	(±0.28%)		
	85	12.4					32	35.6	91.4	4	35.51 ±0.10	(±0.28%)		
	237	14.1	47	50	3		42	35.4	92.7	4	35.43 ±0.13	(±0.37%)		
	90	10.4	46	51	3		32	36.4			no plateau		contaminated	
Dona Ana	203	62.8					56	35.5	100.0	5	35.49 ±0.11	(±0.31%)		
Bell Top #3	205:mean	72.7	47	53	1					2	35.69 ±0.02	(±0.06%)		
	205	71.3					42	35.7	83.0	4	35.71 ±0.12	(±0.34%)		
	205	73.2					54	35.7	88.1	3	35.68 ±0.14	(±0.39%)		
Squaw Mountain	529	18.7					56	36.0	72.3	3	35.75 ±0.12	(±0.34%)		
Lower Cueva	483	1	60.9				56	36.2	94.9	4	36.20 ±0.13	(±0.36%)		
	482	1	02.6	42	58	0	56	35.6			no plateau		altered	

Explanation: K/Ca is molar ratio determined from <sup>37</sup>Ar/<sup>39</sup>Ar measurements; Or, Ab, and An are percent orthoclase, albite, and anorthite end members in sanidine analyzed by microprobe (average of 5-8 analyzed crystals); Ex is degree of exsolution shown by x-ray diffraction: E=cryptoperthitic exsolution, U=unexsolved; Ir is irradiation package number; %<sup>39</sup>Ar is % of total <sup>39</sup>Ar in age plateau; n is the number of heating steps in age plateau or samples used for mean age;  $\sigma$  is single-spectrum, within sample, or within-unit 1 sigma error;  $\sigma X$  is within-unit standard deviation of the mean; final column also identifies samples apparently contaminated by older feldspar and indicates their deviation from the unit-mean age.

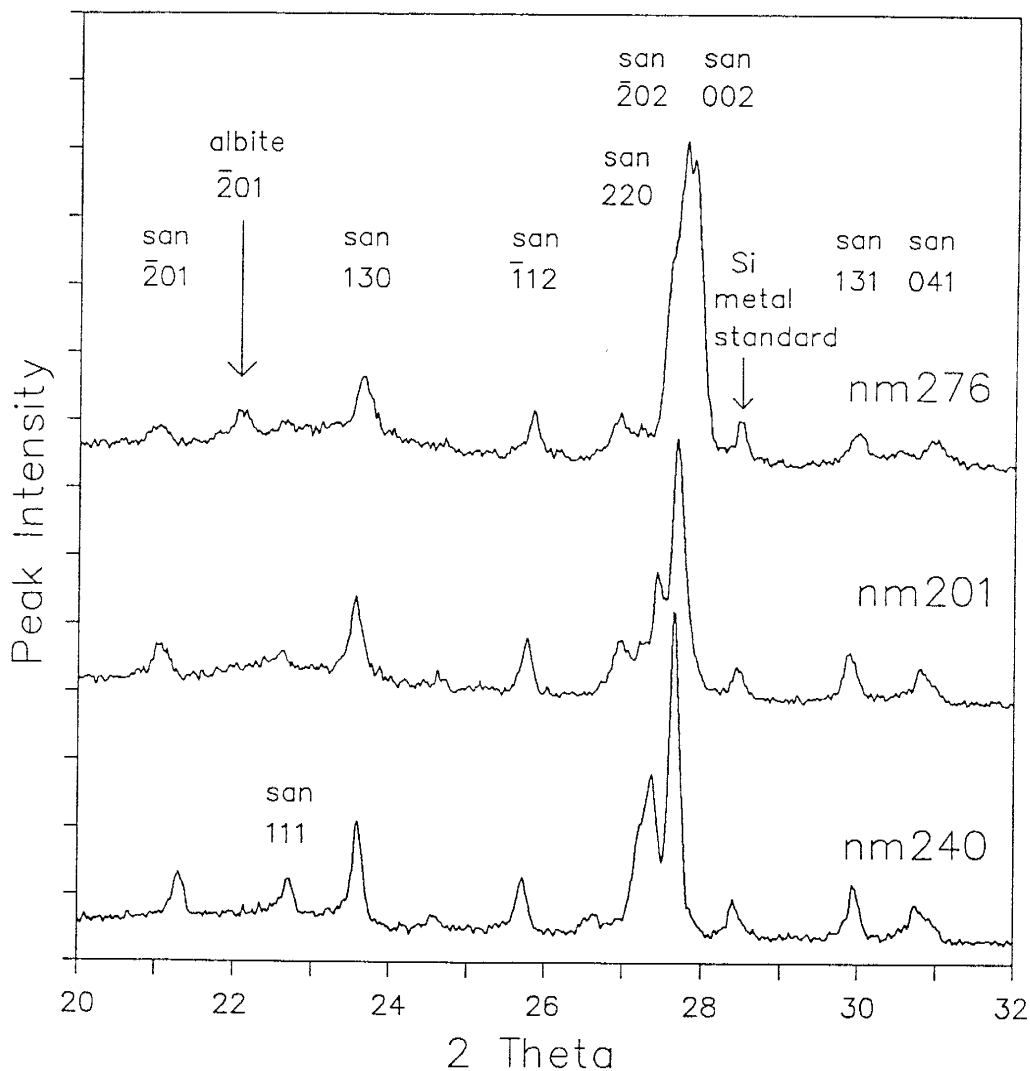


Fig. 3. X-ray diffraction spectra showing evidence of exsolution of K-rich and Na-rich phases within sanidines. The upper two spectra show subdued sanidine peaks (especially 111) and weak to distinct albite peaks characteristic of about 85% of the analyzed sanidines. The lower spectrum, indicating homogeneous sanidine, is characteristic of 15% of the samples. Si metal was used to provide a standard reference peak.

ranging from .285 to .301 ( a  $T_1=.275$  represents total disorder, whereas larger values represent increasing order; Kroll and Ribbe, 1987). However, in 85% of the 37 analyzed samples (Table 1), some of the sanidine peaks are subdued (e.g. 111 peak, Fig. 3) and accompanied by weak to distinct albite peaks (e.g. 201 peak, Fig. 3). Most of these exsolved sanidines also show high strain indices, calculated from the position of 201, 204, and 060 peaks (Fig. 4; Kroll and Ribbe, 1987). No correlation was found between the degree of exsolution and the coefficient of Al/Si disorder. Similar submicroscopic exsolution of sanidines is common in ignimbrites elsewhere, and apparently occurs during post emplacement deuteric cooling (Snow and Yund, 1985). As will be shown below, there is no evidence that this exsolution allowed any argon leakage from these samples.

#### AGE SPECTRA RESULTS

Individual incremental heating step gas fractions of Mogollon-Datil sanidines typically contained from  $10^{-13}$  to  $10^{-11}$  moles of  $^{39}\text{Ar}$  (Table 2). With the exception of small initial and final heating step gas fractions, radiogenic yields were generally high, typically 90-97% for induction-heated samples and 95-99.9% for resistance-heated samples (Table 2, Appendix 3).

Of the 97 measured age spectra, 94 satisfy the plateau criteria described above. Representative plateau spectra are presented in Figure 5 and Table 2 (see Appendix 3 for complete data set). The majority of these plateaus are flat

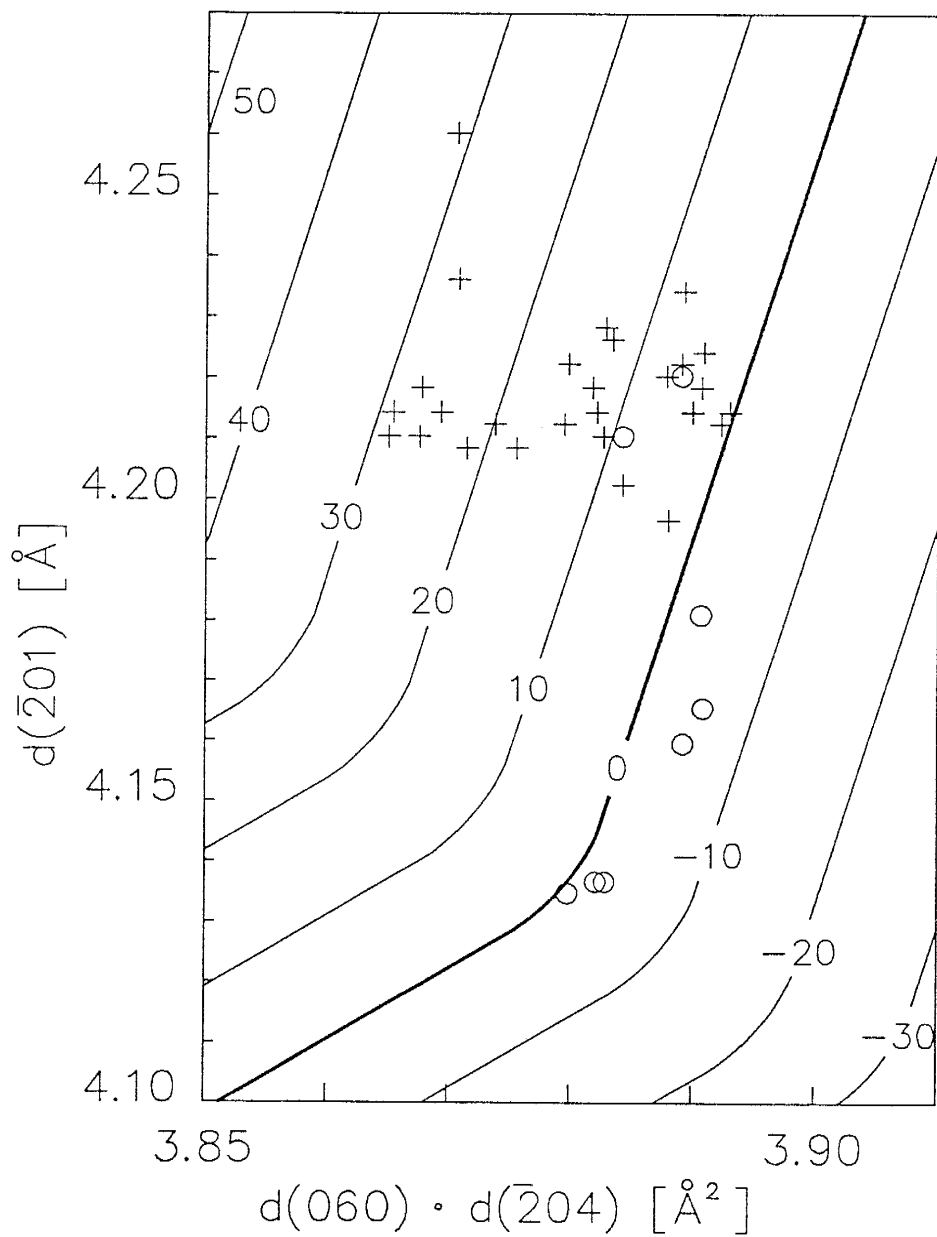


Fig. 4. Contour diagram showing relationship of strain index and d-spacing of 201, 204, and 060 x-ray diffraction peaks. Circles and crosses respectively represent unmixed and mixed sanidines from Mogollon-Datil ignimbrites. Strain index and contours are after Kroll and Ribbe, 1987.



Table 2 (continued).  $^{40}\text{Ar}/^{39}\text{Ar}$  analytical data from selected samples, also shown graphically in Figure 5.

temp(°C)	$^{40}\text{Ar}/^{39}\text{Ar}$	$^{37}\text{Ar}/^{39}\text{Ar}$	$^{36}\text{Ar}/^{39}\text{Ar}$	% $^{39}\text{Ar}$	%rad	$^{39}\text{Ar}$ (moles)	K/Ca	age(Ma)	$\pm 1\sigma$
nm465	Kneeling Nun, sanidine		J= 0.005021		RD-56	weight=	0.1988	disc=296.5	
850	3.927	9.790E-03	4.354E-04	3.1	96.7	6.822E-13	53.1	34.11 ± 0.74	
1160	4.426	8.033E-03	7.687E-05	27.2	99.5	6.010E-12	64.7	39.45 ± 0.12	
1240	4.892	7.499E-03	8.280E-05	33.3	99.5	7.373E-12	69.3	43.56 ± 0.20	
1550	5.980	7.239E-03	9.871E-05	33.9	99.5	7.505E-12	71.8	53.11 ± 0.17	
1550	6.699	7.578E-03	2.947E-05	2.5	99.9	5.599E-13	68.6	59.63 ± 1.44	
	total gas						68.4	45.81	
	no plateau								
nm110	Kneeling Nun, sanidine		J= 0.004595		RD32	weight=	0.1137	disc=296.5	
650	8.066	9.238E-03	1.231E-02	4.0	54.8	1.94E-14	56.3	36.29 ± 0.10	
950	5.124	8.870E-03	2.780E-03	8.6	83.9	4.21E-14	58.6	35.27 ± 0.09	
1050	4.885	8.549E-03	1.991E-03	8.1	87.8	3.96E-14	60.8	35.22 ± 0.09	
1125	4.655	8.544E-03	1.231E-03	12.3	92.1	6.02E-14	60.9	35.18 ± 0.09	
1200	4.679	8.578E-03	1.267E-03	16.3	91.9	7.99E-14	60.6	35.29 ± 0.09	
1275	4.628	8.515E-03	1.021E-03	14.1	93.4	6.89E-14	61.1	35.46 ± 0.09	
1400	4.591	8.483E-03	9.387E-04	18.2	93.8	8.92E-14	61.3	35.36 ± 0.09	
1550	4.727	8.411E-03	1.426E-03	18.5	91.0	9.05E-14	61.8	35.30 ± 0.09	
	total gas						60.7	35.34	
	plateau	1200- 1550		67.1				35.35 ± 0.12	
nm502	Vicks Peak, sanidine		J= 0.005030		RD-56	weight=	0.1982	disc=296.5	
850	4.397	1.125E-02	4.014E-03	5.5	73.0	1.036E-12	46.2	28.89 ± 0.57	
1075	3.480	8.976E-03	8.789E-04	13.8	92.5	2.577E-12	57.9	28.99 ± 0.37	
1200	3.539	9.379E-03	4.300E-04	24.7	96.4	4.609E-12	55.4	30.68 ± 0.14	
1350	3.522	1.046E-02	3.776E-04	51.4	96.8	9.610E-12	49.7	30.69 ± 0.09	
1550	3.615	1.074E-02	5.258E-04	4.5	95.7	8.472E-13	48.4	31.12 ± 0.90	
	total gas						52.8	30.37	
	plateau	1200- 1550		80.7				30.69 ± 0.11	
nm482	Cueva, sanidine		J= 0.005017		RD-56	weight=	0.1985	disc=296.5	
850	4.178	4.180E-03	5.429E-04	7.9	96.2	1.397E-12	124.4	36.01 ± 0.24	
1125	4.113	4.767E-03	3.455E-04	23.8	97.5	4.177E-12	109.1	35.94 ± 0.14	
1235	4.057	5.762E-03	5.099E-04	42.8	96.3	7.517E-12	90.3	35.01 ± 0.10	
1375	4.197	4.714E-03	5.127E-04	23.6	96.4	4.143E-12	110.3	36.24 ± 0.15	
1550	4.371	4.634E-03	1.686E-03	1.9	88.6	3.425E-13	112.2	34.68 ± 1.83	
	total gas						102.6	35.60	
	no plateau								

Explanation: Each data set is preceded by sample number, unit name, irradiation parameter (J), irradiation batch number, sample weight, and measured discrimination of atmospheric argon. Columns in data sets give temperature of incremental heating steps, ratios of Ar isotopes ( $^{40}\text{Ar}$ =initial and radiogenic,  $^{39}\text{Ar}$ =potassium-derived,  $^{37}\text{Ar}$ =Calcium derived,  $^{36}\text{Ar}$ =initial), % of total  $^{39}\text{Ar}$  in heating step, radiogenic yield of  $^{40}\text{Ar}$ , moles of potassium derived  $^{39}\text{Ar}$ , K/Ca ratio calculated from  $^{37}\text{Ar}/^{39}\text{Ar}$  ratio, age, and  $1\sigma$  error. Lines following each data step show total gas K/Ca and age, and plateau temperature range,  $^{39}\text{Ar}$  percent, age, and error (method of Fleck et al., 1981).



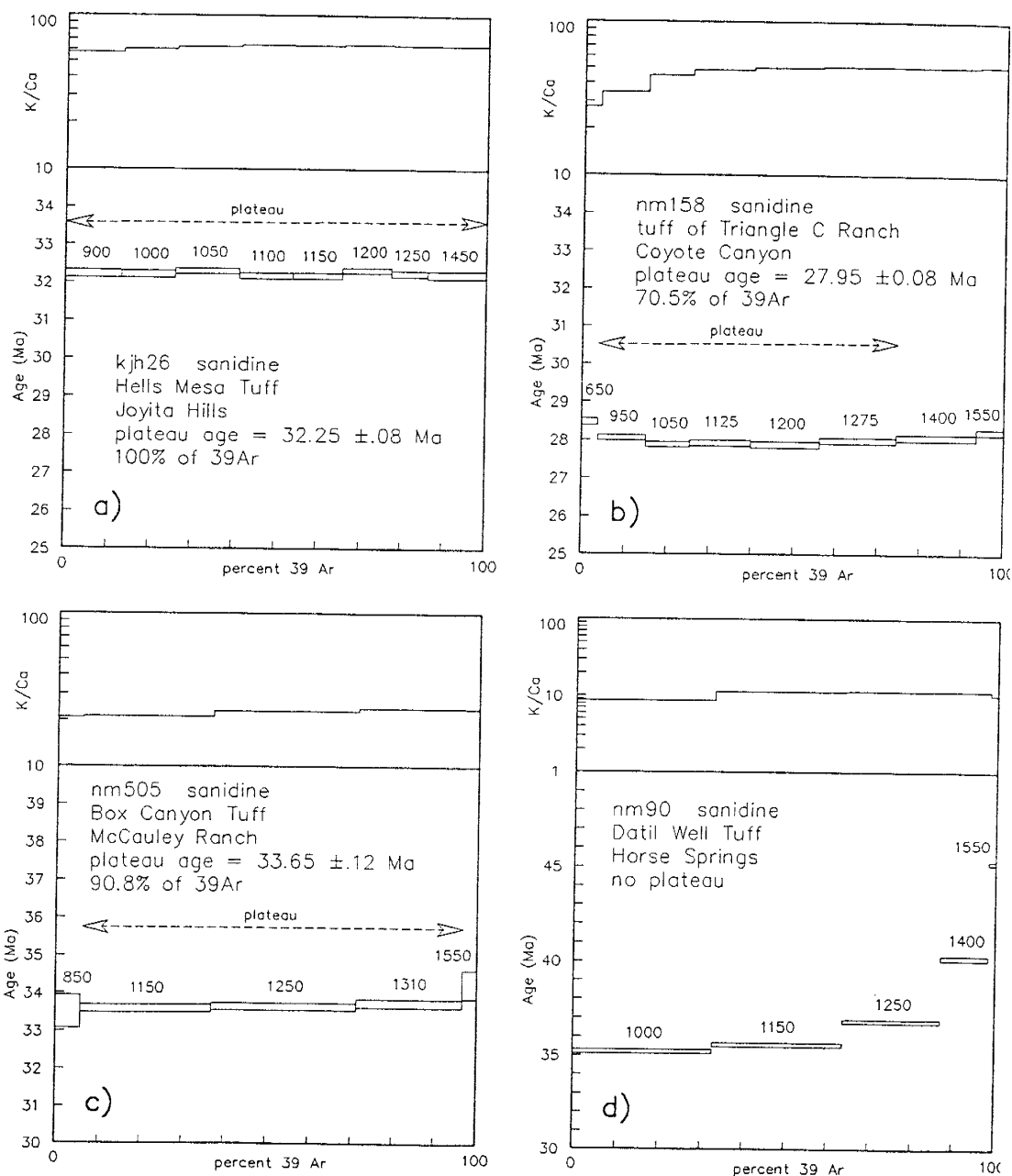


Fig. 5. Representative age spectra from Mogollon-Datil sanidines: a) concordant plateau age spectrum and flat K/Ca spectrum typical of 80% of analyzed sanidines, b) concordant plateau age spectrum accompanied by a somewhat discordant K/Ca spectrum, c) age spectrum that climbs in age slightly with increasing temperature, d) strongly climbing age spectrum (continued on following page).

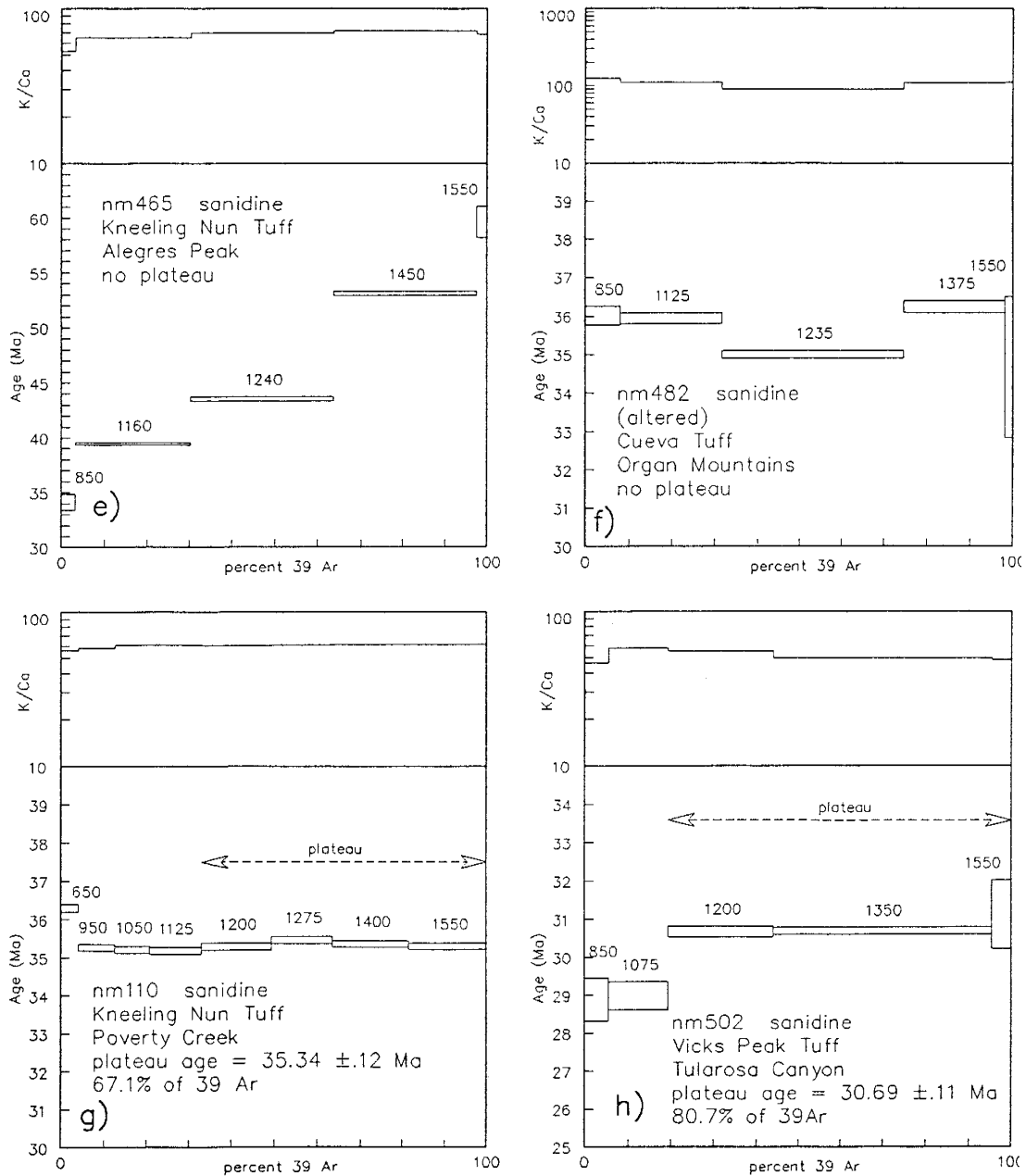


Fig. 5 (continued). Representative age spectra from Mogollon-Datil sanidines: e) strongly climbing age spectra; both d and e indicate contamination by older K-feldspar, f) irregular discordant age spectrum of an altered sanidine, g) concordant plateau age spectrum of an apparently contaminated sample, h) somewhat discordant age spectrum, still meeting plateau criteria, of an apparently contaminated sample.

(Fig. 5a, 5b), although age spectra that climb gently with increasing temperature are not uncommon (Fig 5c). Plateaus generally contain from 75 to 100% of the total released  $^{39}\text{Ar}$ , and discordant gas fractions are typically limited to initial or final heating increments showing high variance and low radiogenic yields (Table 2).

Individual weighted-mean plateau ages show precisions ( $1\sigma$ ) of  $\pm 0.25$  to  $\pm 0.45\%$  ( $\pm 0.07$  to  $\pm 0.14$  Ma) and generally agree within  $1\sigma$  of total-gas ages (Tables 1 and 2). The largest sources of error in individual (single-spectrum) plateau ages are the uncertainty in measurement of  $^{36}\text{Ar}$  and the  $\pm 0.25\%$  uncertainty in  $J$ . Uncertainty in reactor produced  $^{40}\text{Ar}$  also contributed slightly ( $<0.1\%$ ) to single-spectrum uncertainties. Calcium derived Ar isotopes were not a significant source of error in this study, because of the generally low Ca content of the sanidines.

Two of the 3 spectra which failed to meet plateau criteria show severe increases in age with temperature, climbing from about 35 Ma at 850-1000°C to 45-60 Ma at 1650°C (sample 90 and 465, Fig. 5d, 5e, and Table 2). These two climbing spectra apparently reflect the presence of older xenocrystic or lithic K-feldspar, as will be discussed below. The third spectrum which failed to meet plateau criteria (sample 482, Fig. 5f, Table 2) is somewhat U-shaped. The total gas age (35.6 Ma) is about 2% less than the 36.20 Ma plateau age of another sample from the same unit (sample 483, Table 1). As will be discussed below,

this discordant spectrum may be related to sanidine alteration or to reheating by an adjacent pluton.

Excellent reproducibility among different irradiation packages is indicated by data sample KJH-26, which was analyzed in 4 of the 7 irradiations. The 6 plateau ages from this sample range from 31.93 to 32.25 Ma, averaging 32.06 Ma with a  $1\sigma$  uncertainty of  $\pm 0.3\%$  or  $\pm 0.10$  Ma (Table 2). Pairs of replicate plateau ages were also determined from 7 other samples (Table 1). Mean deviations for these age pairs range from 0.06 to 0.50%, averaging  $\pm 0.25\%$ , and indicate similar reproducibility within packages (average deviation =  $\pm 0.3\%$ ) and between packages (average deviation =  $\pm 0.2\%$ ) (Table 1).

The best indication of overall precision of  $^{40}\text{Ar}/^{39}\text{Ar}$  plateau ages for an individual ignimbrite is the small standard deviations in age obtained by averaging analyses of several different samples of one unit. These within-unit uncertainties range from  $\pm 0.1$  to  $\pm 0.4\%$  ( $\pm 0.04$ - $0.13$  Ma) for the 9 units for which 3 or more plateau ages have been determined (Table 1). The most comprehensively dated unit is the extensive ( $20,000 \text{ km}^2$ ) Bloodgood Canyon Tuff, for which eight widely separated samples yielded plateau ages ranging from 27.99 to 28.11 Ma, and averaging 28.06 Ma  $\pm 0.04$  Ma ( $1\sigma$ ) (Fig. 6, Table 1).

Six plateau age determinations (indicated in Table 1) are anomalously old with respect to either other plateau ages from the same units or to established stratigraphic

fission track zircon:  $28.2 \pm 2.1$  Ma

fission track sphene:  $28.1 \pm 2.2$  Ma

K-Ar sanidine:  $26.9 \pm 1.3$  Ma

K-Ar biotite:  $28.8 \pm 1.4$  Ma

$^{40}\text{Ar}/^{39}\text{Ar}$  sanidine:  $28.05 \pm 0.04$  Ma

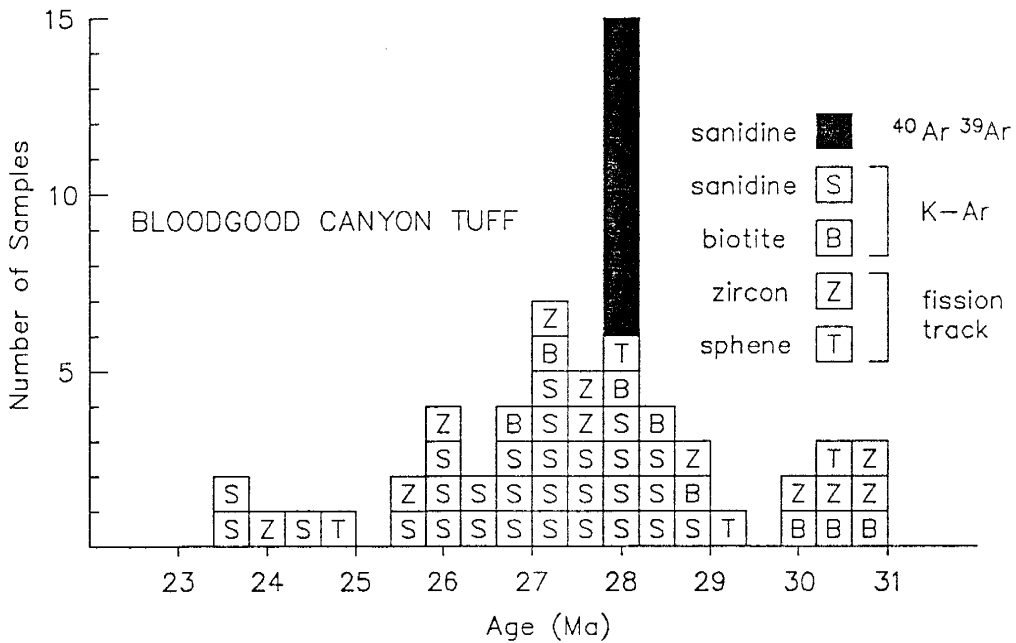


Fig. 6. A comparison of 8  $^{40}\text{Ar}/^{39}\text{Ar}$  sanidine plateau ages with published conventional K-Ar and fission-track ages from the Bloodgood Canyon Tuff (Marvin et al, 1987). Each box denotes a single age determination. The large standard deviation of the published data in part reflects its acquisition from several different laboratories.

relationships. As will be discussed later, these anomalous ages apparently reflect contamination by older K-feldspar. Three of the anomalous samples were collected from units containing less than 1% phenocrystic sanidine, and therefore highly susceptible to contamination by lithic or xenocrystic K-feldspar.

K/Ca molar ratios in sanidines were determined for each heating step during  $^{40}\text{Ar}/^{39}\text{Ar}$  dating. Mean K/Ca ratios range from 10 to 161 and generally agree closely with those determined from microprobe analyses (Table 2). K/Ca spectra range from almost flat (Fig. 5a, 5c) to somewhat discordant (Fig. 5b), but their shapes do not show any simple relation to the shape of the  $^{40}\text{Ar}/^{39}\text{Ar}$  spectra.

## DISCUSSION

### Precision and resolution

The relative merits of plateau ages vs. isotope correlation methods in analyses of  $^{40}\text{Ar}/^{39}\text{Ar}$  incremental heating data have been discussed in detail by others (e.g. Roddick et al., 1980; Dalrymple and Lanphere, 1988; Lanphere, 1988). Plateau age analysis has been employed in this study, because the uniformly high radiogenic yields (90-99.9%) of individual gas fractions result in excessive errors in slope and intercept for isotope correlation methods.

The precision of  $^{40}\text{Ar}/^{39}\text{Ar}$  plateau ages of Mogollon-Datil ignimbrites can be quantified on three levels: single-

spectrum (analytical plus irradiation uncertainties), within-sample (standard deviation of replicate plateau ages), and within-unit (standard deviation of multiple samples of the same unit). Within-sample and within-unit mean ages are inherently more precise than single-spectrum ages, because of averaging of analytical and irradiation uncertainties, particularly where samples were irradiated in several different packages. Of these, within-unit precision is most important to geological interpretations, because it ultimately controls resolution of the  $^{40}\text{Ar}/^{39}\text{Ar}$  dating method.

In this study, the average within-unit precision is  $\pm 0.2\%$  for the 8 ignimbrites from which 3 or more samples have been dated (Tables 1 and 3). The highest within-unit precisions are shown by the Kneeling Nun Tuff ( $\pm 0.06\%$ ,  $n=4$ ), Bloodgood Canyon Tuff ( $\pm 0.11\%$ ,  $n=8$ ), and tuff #4 of the Bell Top Formation ( $\pm 0.11\%$ ,  $n=3$ ). Box Canyon Tuff shows the lowest within unit precision ( $\pm 0.41\%$ ,  $n=7$ ; Table 3). Data from apparently contaminated samples, discussed above, were excluded from within-unit precision calculations for two units (Kneeling Nun and Vicks Peak Tuffs, Table 1).

The within-unit precision of the  $^{40}\text{Ar}/^{39}\text{Ar}$  plateau ages is several times better than that of published K-Ar and fission track ages for the same units. This comparison is best seen for the Bloodgood Canyon Tuff, the most-dated unit in this study, and also the object of considerable K-Ar and fission track dating. Within-unit  $1\sigma$  precision of  $^{40}\text{Ar}/^{39}\text{Ar}$

Table 3. Comparison of precision of this and other  $^{40}\text{Ar}/^{39}\text{Ar}$  studies of mid-Tertiary ignimbrites.

method	mineral	unit	age(Ma)	n	$\sigma$		$\sigma X$		ref
					Ma	%	Ma	%	
plateau	sanidine	South Canyon	27.36	3	$\pm 0.07$	$\pm 0.26$	$\pm 0.04$	$\pm 0.15$	1
plateau	sanidine	Bloodgood Canyon	28.06	8	$\pm 0.04$	$\pm 0.14$	$\pm 0.01$	$\pm 0.05$	1
plateau	sanidine	Vicks Peak	28.56	3	$\pm 0.06$	$\pm 0.19$	$\pm 0.03$	$\pm 0.11$	1
plateau	sanidine	Caballo Blanco	31.65	5	$\pm 0.06$	$\pm 0.17$	$\pm 0.03$	$\pm 0.09$	1
plateau	sanidine	Hells Mesa	32.06	5	$\pm 0.10$	$\pm 0.30$	$\pm 0.06$	$\pm 0.17$	1
plateau	sanidine	Box Canyon	33.51	7	$\pm 0.13$	$\pm 0.40$	$\pm 0.05$	$\pm 0.15$	1
plateau	sanidine	Kneeling Nun	34.89	4	$\pm 0.05$	$\pm 0.15$	$\pm 0.03$	$\pm 0.08$	1
plateau	sanidine	Bell Top #4	34.96	3	$\pm 0.04$	$\pm 0.11$	$\pm 0.02$	$\pm 0.07$	1
K-Ar	sanidine	Bloodgood	26.9	28	$\pm 1.3$	$\pm 4.8$	$\pm 0.2$	$\pm 0.9$	2
K-Ar	biotite	Bloodgood	28.8	8	$\pm 1.4$	$\pm 4.9$	$\pm 0.5$	$\pm 1.7$	2
K-Ar	sphene	Bloodgood	28.1	4	$\pm 2.2$	$\pm 7.8$	$\pm 1.1$	$\pm 3.9$	2
K-Ar	zircon	Bloodgood	28.2	10	$\pm 2.1$	$\pm 7.4$	$\pm 0.7$	$\pm 2.4$	2
plateau	biotite	Rat Creek	26.47	2**	$\pm 0.08$	$\pm 0.32$	$\pm 0.06$	$\pm 0.22$	3
plateau	biotite	Showshoe Mtn.	26.78	2**	$\pm 0.10$	$\pm 0.38$	$\pm 0.07$	$\pm 0.27$	3
laser	sanidine	Taylor Cr. Lava	28.21	7	$\pm 0.04$	$\pm 0.13$	$\pm 0.01$	$\pm 0.05$	4
laser	sanidine	Bloodgood Canyon	28.19	2**	$\pm 0.01$	$\pm 0.05$	$\pm 0.01$	$\pm 0.04$	4
laser	sanidine	Pahranagat Lakes	22.65	5	$\pm 0.02$	$\pm 0.08$	$\pm 0.01$	$\pm 0.04$	5
laser	sanidine	Nine Hill	25.11	5	$\pm 0.02$	$\pm 0.07$	$\pm 0.01$	$\pm 0.03$	6
laser	sanidine	New Pass	25.07	3	$\pm 0.04$	$\pm 0.15$	$\pm 0.02$	$\pm 0.09$	6

Explanation: n=number of samples/unit, \*\* = n too few for meaningful  $\sigma$ , references:  
 1) this study, 2) data compiled in Marvin et al. (1987), 3) Lanphere (1988),  
 4) Dalrymple and Duffield (1988), 5) Deino and Best (1988), 6) Deino (1989).



plateau ages from the Bloodgood Canyon Tuff of  $\pm 0.11\%$  ( $28.05 \pm 0.04$  Ma) compares to  $\pm 5\%$  for K-Ar sanidine and biotite data, and  $\pm 7-8\%$  for fission track zircon and sphene data (Table 3; Fig. 6). The precision of published K-Ar ages improves somewhat if data from different laboratories are considered separately (e.g. mean Bloodgood Canyon K-Ar sanidine ages from the U.S. Geological Survey laboratory in Denver give a precision of  $\pm 4\%$  ( $27.2 \pm 1.1$  Ma), but the precision of  $^{40}\text{Ar}/^{39}\text{Ar}$  plateau ages is still much higher. Also significant is the younger mean age of K-Ar sanidine data ( $26.9 \pm 1.3$  Ma;  $n=28$ ), compared to the mean of  $^{40}\text{Ar}/^{39}\text{Ar}$  plateau ages. This discrepancy almost certainly reflects incomplete extraction of  $^{40}\text{Ar}$  in the K-Ar dating process (McDowell, 1983).

The precision of  $^{40}\text{Ar}/^{39}\text{Ar}$  plateau ages in this study compares favorably to that of other  $^{40}\text{Ar}/^{39}\text{Ar}$  plateau and laser-fusion age studies of mid-Tertiary ignimbrites (Table 3). Plateau ages of biotite and sanidine from the San Juan volcanic field yielded single-spectrum and within-sample precisions ( $1\sigma$ ) of about  $\pm 0.5\%$  (Table 3; Lanphere, 1988). Within-unit precision for pairs of samples from two units is about  $\pm 0.3-0.4\%$ . Generally higher within-sample and within-unit precisions have been reported from laser fusion studies of Great Basin ignimbrites (Deino and Best, 1988; Deino, 1989) and two Mogollon-Datil units (Dalrymple and Duffield, 1988). The within-unit precisions of these studies range from  $\pm 0.05$  to  $\pm 0.15$  (Table 3),

similar to the best within-unit precisions determined in this study.

Increased resolution is the chief goal of the high-precision  $^{40}\text{Ar}/^{39}\text{Ar}$  dating studies of mid-Tertiary ignimbrites, but resolution is more difficult to quantify than precision. Most  $^{40}\text{Ar}/^{39}\text{Ar}$  dating studies (e.g. Deino, 1989; Dalrymple and Duffield, 1988) cite the standard error of the mean ( $\sigma_X = \sigma/n^{1/2}$ ) as a measure of resolution. Because  $\sigma_X$  varies inversely as  $n^{1/2}$ , it can therefore be improved by increasing the number of dated samples.

In this study,  $\sigma_X$  ranges from  $\pm 0.05\%$  ( $n=8$ , Bloodgood Canyon Tuff) to  $\pm 0.17\%$  ( $n=4$ , Hells Mesa Tuff), excluding units with  $n < 3$  (Table 1). Other  $^{40}\text{Ar}/^{39}\text{Ar}$  studies of mid-Tertiary ignimbrites (Table 3) have determined  $\sigma_X$  of about  $\pm 0.3\%$  for plateau ages (Lanphere, 1988) and  $\sigma_X$  of  $\pm 0.03\%$  to  $\pm 0.09\%$  for laser-fusion ages (Dalrymple and Duffield, 1988; Deino and Best, 1988; Deino, 1989).

But how does  $\sigma_X$  translate to actual resolution of ignimbrite correlation problems? Stratigraphic sequences offer the most rigorous tests of this question. In some cases, actual resolution is less than that suggested by  $\sigma_X$ . For example, laser fusion data from a sequence of two Great Basin ignimbrites (Table 3; Deino, 1989) yield an age for the overlying unit that is 0.15% older than the underlying unit, although the sum of the  $\sigma_X$  values for the two units is only 0.12%. In this study, the mean ages of better studied units ( $n \geq 3$ ) all agree with independently established

stratigraphic order, although the most closely erupted pair of well-constrained units (Kneeling Nun and Bell Top #4 Tuffs, Table 3) differ in mean age by 0.09 Ma. Good agreement with stratigraphic order is also shown by more poorly constrained units in this study. The best examples are data from a sequence of 9 ignimbrites erupted over a 1.6 m.y. period from calderas near the northern and western margins of the volcanic field (Fig. 7). The stratigraphic order of these units has been unequivocally demonstrated by detailed mapping (Osburn and Chapin, 1983a; Ratté et al, 1984), augmented by paleomagnetic correlations (McIntosh et al, 1986a; McIntosh, dissertation, Chapter A). Except for one apparently contaminated sample, all of the mean  $^{40}\text{Ar}/^{39}\text{Ar}$  plateau ages agree with established stratigraphic relationships within the limits of single-spectrum ( $n=1$ ) or within-unit ( $n\geq 2$ )  $1\sigma$  uncertainty. Data from this study suggest that resolution can be conservatively estimated at about  $3 \times \sigma_X$  ( $\pm 0.1-0.5\%$ ) for better-studied units ( $n\geq 3$ ) and about  $\pm 0.5\%$  for more poorly studied units.

Besides their generally lower resolution, poorly studied units are more susceptible to errors introduced by contamination or alteration. This risk is reduced for samples collected within a well-established stratigraphic context.

#### Accuracy

At the present time, the precision of the  $^{40}\text{Ar}/^{39}\text{Ar}$  dating method is much higher than its accuracy. Monitors of

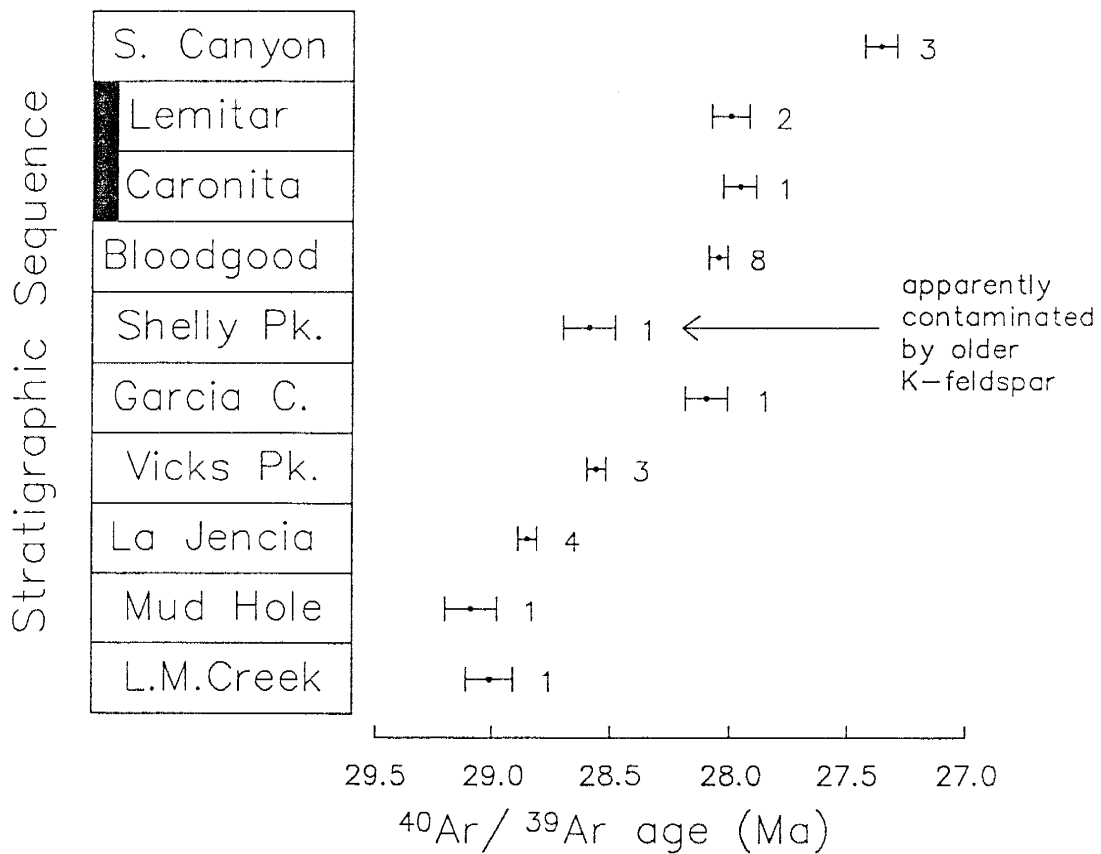


Fig. 7. The order of  $^{40}\text{Ar}/^{39}\text{Ar}$  ages from this 29.0 to 27.4 Ma sequence of 9 ignimbrites agrees closely with independently determined stratigraphic order (column), except for the apparently contaminated sample of Shelly Peak Tuff.

predetermined age are required to precisely measure neutron fluxes, hence all  $^{40}\text{Ar}/^{39}\text{Ar}$  ages are determined relative to standards dated by the K-Ar method. The uncertainty in K-Ar ages of  $^{40}\text{Ar}/^{39}\text{Ar}$  dating standards (about 0.5-1.0%; Samson and Alexander, 1987) therefore limits the ultimate accuracy of  $^{40}\text{Ar}/^{39}\text{Ar}$  ages. Furthermore, inter-laboratory errors are introduced by presently limited application of inter-laboratory standards.

An example of this problem is provided by data from the Bloodgood Canyon Tuff and Taylor Creek Rhyolite. The mean ages (respectively  $28.06 \pm 0.04$  Ma and  $28.10 \pm 0.18$  Ma; Table 3) determined for these units using monitor FCT-3 are both about 0.5% younger than the mean ages determined by Dalrymple and Duffield (1988) using monitor SB-3 (Table 3). Dalrymple (personal communication, 1989) has subsequently remeasured the same samples and recalibrated monitor ages, which yielded mean ages for the Bloodgood Canyon and Taylor Creek Rhyolite, respectively of  $27.94 \pm 0.06$  Ma and  $27.90 \pm 0.03$  Ma, about 0.4% younger than this study's mean ages.

Interlaboratory differences of this nature are commonly larger than analytical uncertainty and primarily reflect calibration problems among various monitors. This problem could be greatly reduced by more widespread acceptance of mid-Tertiary sanidine standards such as Fish Canyon Tuff (Kunk et al., 1985).

### Cryptoperthitic exsolution

Cryptoperthitic exsolution is common in Mogollon-Datil ignimbrite sanidines. Some 85% of the samples are exsolved to some degree, as shown by x-ray diffraction data and macroscopic chatoyancy. Most of the less common unexsolved sanidines are from vitrophyres or poorly welded distal ignimbrite facies.

Cryptoperthitic exsolution does not appear to degrade the precision of  $^{40}\text{Ar}/^{39}\text{Ar}$  plateau ages. The age spectra of exsolved and unexsolved sanidines show no systematic differences in shape, precision, or weighted mean plateau ages. None of the exsolved sanidines yield age spectra indicative of argon loss (Turner, 1968), and the average single-spectrum precision for exsolved sanidines ( $\pm 0.32\%$ ) is almost identical to that of unexsolved sanidines ( $\pm 0.35\%$ ). Likewise, the weighted mean plateau ages of exsolved and unexsolved sanidines from the same unit (Box Canyon, Table 1) are indistinguishable.

Apparently, the boundaries between lamellae do not allow significantly increased diffusion of  $^{40}\text{Ar}$ . The high Ar retentivity of these exsolved sanidines stands in contrast the less retentive nature typical of exsolved orthoclase and microcline (e.g. Foland, 1974; Zeitler, 1987). The high strain indices indicated by XRD measured lattice spacings (Fig. 4), suggests that much of the inter-lamellae strain may be in the form of deformation rather than dislocations.

### Alteration

The effects of sanidine alteration on  $^{40}\text{Ar}/^{39}\text{Ar}$  age spectra was not systematically addressed in this study. Partial to complete alteration of sanidine to sericite or clays is common in intra-caldera facies of Mogollon-Datil ignimbrites, and is also observed in hydrothermally altered outflow facies. In addition, pervasive potassium metasomatism has altered ignimbrites in a 1400 km<sup>2</sup> area in the northern part of the field (Chapin and Lindley, 1986), but sanidines are generally unaffected. In a few areas of extreme metasomatism, Na-rich sanidines have been partially replaced by K-rich adularia (Lindley, 1985).

Altered sanidines were generally avoided in this study, although four slight to moderately altered samples from the Organ Cauldron area were analyzed (203, 529, 483, and 482 in Table 1). Three of these samples yielded concordant plateaus, although individual gas fractions showed generally high variance and low radiogenic yields. The fourth sample (482, Table 1, Fig. 5f) gave a discordant age spectrum which failed to meet plateau criteria and furthermore showed a total gas age about 2% younger than sample 483 from the same unit. The high K/Ca ratios of samples 482 and 483 may have been elevated by K-metasomatism. Furthermore, the Organ Cauldron intra-calderas facies ignimbrites have been intruded by co-magmatic granitic plutons (Seager and McCurry, 1988), which may have produced heating or hydrothermal alteration in the ignimbrites.

### Contamination

As presented above, 8 of the 85 samples dated in this study show evidence of geological contamination by older feldspars. Contamination by foreign feldspars is not surprising in ignimbrites, which commonly contain abundant lithic and xenocrystic material derived from both vent walls and pre-eruptive ground surfaces (Hildreth and Mahood, 1986).

The two samples showing strongly discordant spectra (90 and 465 in Table 2 and Fig. 5a) apparently contain older non-volcanic microcline which was not entirely removed during mineral separation. Both samples were collected from thin (<10 m), non-welded, distal ignimbrite facies which were observed in thin section to contain cross-twinned, non-volcanic microcline, amounting to about 5% of total K-feldspar. A local source for the contaminant microcline is suggested by the fact that nearby samples of the same ignimbrites (85 and 92 in Table 2) contain no observable microcline and show flat age spectra. The microcline in samples 90 and 465 was apparently incompletely reset isotopically by heating in the ignimbrite, probably reflecting short residence time in the flowing ash-flow and rapid post-emplacement cooling of the thin distal ignimbrite. Under burial conditions microcline shows closure temperatures as low as 150°C (Harrison and Bé, 1983).



Less severe contamination appears to be manifested as relatively flat age spectra which yield anomalously old plateau ages. Sample 502, from the sanidine-poor (<0.5%) Vicks Peak Tuff, shows an age spectrum which is somewhat discordant but still meets plateau criteria (Fig. 5g). The lower temperature end of this spectrum agrees with the mean Vicks Peak age, but the higher temperature plateau gas fractions are 7.5% older.

The remaining 5 samples giving anomalously old plateau ages all show flat to gently climbing age spectra which are well within plateau criteria (Fleck et al., 1977). No microcline was observed in any of these samples. Three samples from relatively well dated units (81-12-6, 498, 110) give plateau ages that are 0.9 to 1.4% ( $2-3\sigma$ ) older than their respective unit mean ages (Table 2). The plateau age of a fourth sample (239, from the Rockhouse Canyon Tuff) is 1.3% older than the only other correlative sample (468, Table 2). A fifth sample (149, the only dated sample of Shelly Peak Tuff) gives a reproducible plateau age of 28.59 Ma (Table 2), that is 1.9% older than well-dated 28.1 Ma underlying units (Fig. 7).

The relatively flat spectra of the 5 samples showing slightly anomalous ages may reflect contamination by sanidine from slightly older ignimbrites, which would show an argon release spectrum similar to the phenocrystic sanidine. Alternatively, the anomalous ages might reflect

contamination by non-volcanic K-feldspar which has been almost completely reset by reheating.

Two factors that seem to increase probability of contamination by older K-feldspar are low sanidine content and proximity to contemporaneous Precambrian highlands. Three of the 9 apparently contaminated samples (149, 502, 239) represent extremely sanidine-poor (<0.5%) units. In addition, 4 of the samples (239, 81-12-6, 465, 90) are located immediately north of the Morenci uplift, a mid-Tertiary uplift of Precambrian rock that is no longer exposed but is indicated by sedimentologic data (Cather and Johnson, 1984).

The above data, together with other studies (e.g. Bogaard et al., 1987; Lippolt et al., 1986), clearly demonstrate that only in some cases can feldspar contamination be detected from the shape of sanidine age spectra. More reliable means of identifying contamination include analyzing multiple samples from each unit and studying suites of samples for which a stratigraphic order has been independently determined. Although not utilized in this study, a third powerful approach to the contamination problem is continuous laser  $^{40}\text{Ar}/^{39}\text{Ar}$  analysis of single feldspar grains (Lo Bello et al., 1987).

#### History of Mogollon-Datil ignimbrite activity

The plateau ages determined from Mogollon-Datil ignimbrites range from 36.2 to 24.3 Ma and indicate that ignimbrite activity was strongly episodic. Activity was

confined to 4 brief (<2.6 m.y.) eruptive episodes separated by 1-3 m.y. gaps during which no caldera-forming eruptions occurred (Fig. 8). Throughout the 11.8 m.y. interval of ignimbrite activity, caldera location generally tended to migrate from the southeast towards the north and west. Mogollon-Datil ignimbrite episodes 1,3, and 4 closely parallel the timing of ignimbrite activity in the San Juan volcanic field of Colorado (McIntosh, dissertation, Chapter C), indicating regional tectonic control of caldera-forming rhyolitic eruptions.

The generalized history of the 4 Mogollon-Datil ignimbrite eruptive episodes are summarized below. Details of ignimbrite timing, distribution, and stratigraphy are presented in McIntosh, dissertation, Chapter C.

Episode 1 (36.2-33.5 Ma): Rhyolitic ignimbrite activity, dominantly low-silica, commenced at the southeast edge of the field with eruption of the Organ Mountains caldera and associated outflow sheets at 36.2 and 35.7 Ma, closely followed by eruption of the nearby Doña Ana caldera at 35.5 Ma. Two thin 35.6-35.5 Ma outflow sheets are also present in the northeastern portion of the field (Fig. 2), but their source is unknown. Major caldera-forming activity shifted 100 km northwest of the Organ Mountains with eruption of the Kneeling Nun Tuff (>900 km<sup>3</sup>) at 34.9 Ma. Several less voluminous ignimbrite eruptions followed in the interval from 34.9 to 33.5 Ma. Sources for most of these units were near the eastern edge of the field, although Box

# MOGOLLON-DATIL POLARITY RECORD

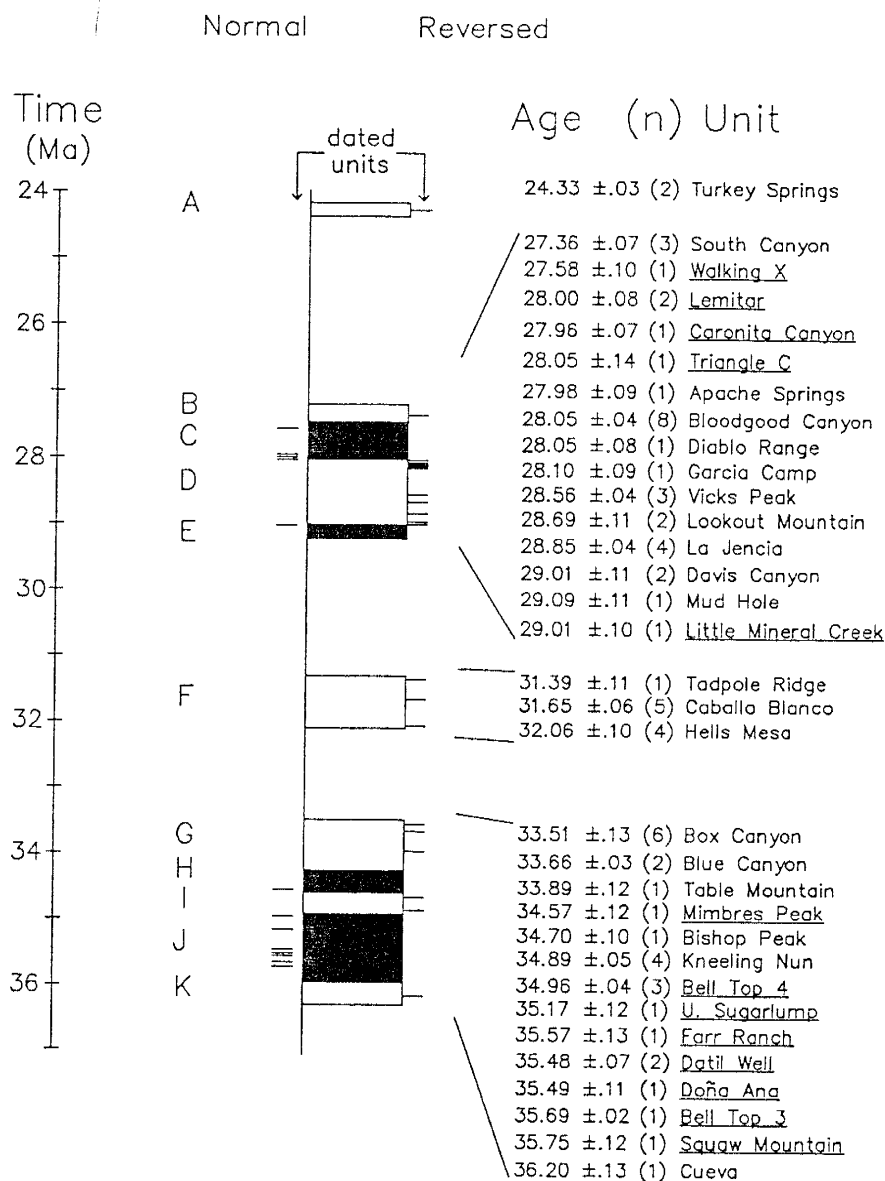


Fig. 8. Composite stratigraphic section and magnetic polarity record of well-dated Mogollon-Datil ignimbrites, showing episodic nature of volcanism. Polarity intervals are lettered (black=normal, white=reversed), and adjacent horizontal lines depict dated ignimbrites. Right column shows mean  $^{40}\text{Ar}/^{39}\text{Ar}$  plateau ages, unit names, polarity (normal units underlined), and number of age determinations (in parentheses). The majority of the stratigraphic relationships can be unequivocally demonstrated, independently of age data, using field relations and paleomagnetic correlation.

Canyon Tuff (33.5 Ma; Fig. 2) was almost certainly erupted from a caldera south of the Mogollon-Datil volcanic field.

Episode 2 (32.1-31.4 Ma): After a 1.4 m.y. hiatus, low-silica rhyolitic ignimbrite activity shifted north and west, producing the Hells Mesa (32.1 Ma, 1200 km<sup>3</sup>), Caballo Blanco (31.7 Ma, a.k.a. Fall Canyon), and Tadpole Ridge (31.4 Ma) Tuffs.

Episode 3 (29.0-27.4 Ma): Following a 2.4 m.y. hiatus, the "ignimbrite flare-up" occurred, producing within a span of 1.6 m.y. more than 12 regional units, primarily high-silica rhyolites, totalling >6000 km<sup>3</sup>. Well-dated units within this interval include Davis Canyon (29.0 Ma), La Jencia (28.9 Ma), Vicks Peak (28.6 Ma), Bloodgood Canyon (28.1 Ma), Lemitar (28.0), and South Canyon (27.4 Ma) Tuffs. Calderas for these units were located near the western and northern margins of the volcanic field. At least one caldera to the south of the Mogollon-Datil field was also active during this interval, as evidenced by a 27.6 Ma distal-facies outflow sheet in the Big Burro Mountains (Fig. 2).

Episode 4 (24.3 Ma): After a 2.9 m.y. hiatus, Mogollon-Datil ignimbrite activity ended with the eruption of the high-silica rhyolite tuff of Turkey Springs at 24.3 Ma, from a caldera near the northern edge of the field.

As detailed elsewhere (McIntosh, dissertation, Chapter D) and summarized in Figure 8, paleomagnetic data and <sup>40</sup>Ar/<sup>39</sup>Ar plateau ages precisely constrain 7 geomagnetic

polarity reversals which occurred during Mogollon-Datil activity. This polarity record can be confidently correlated with the polarity record of well-dated San Juan units, and furthermore has potential to aid in radiometric calibration of the worldwide Magnetic Polarity Time Scale determined from marine magnetic anomalies.

#### CONCLUSIONS

1)  $^{40}\text{Ar}/^{39}\text{Ar}$  age spectra from 85 sanidine separates yield weighted average plateau ages with single-spectrum precision ( $1\sigma$ ) of  $\pm 0.3\text{-}0.4\%$  ( $\pm 0.07\text{-}0.14$  Ma) and within-unit  $1\sigma$  precision of  $\pm 0.1\text{-}0.4\%$  ( $\pm 0.04\text{-}0.13$  Ma). Depending on the number of dated samples per unit,  $^{40}\text{Ar}/^{39}\text{Ar}$  plateau ages presently allow resolution of units differing in age by less than 0.5% (0.12-0.15 m.y.), and offer potential resolution of less than 0.2% (0.03-0.04 m.y.).

2)  $^{40}\text{Ar}/^{39}\text{Ar}$  age spectra from 8 sanidine separates show elevated apparent ages which apparently reflect contamination by older xenocrystic of lithic K-feldspar. Two of these spectra show ages which increase with extraction temperature, but 6 meet the plateau criteria of Fleck et al. (1977).

3) The within-unit precision of Mogollon-Datil sanidine  $^{40}\text{Ar}/^{39}\text{Ar}$  plateau ages far exceeds that of published K-Ar and fission-track data, and shows good agreement with independently established stratigraphic order. Furthermore, plateau ages from some of the better studied units show within-unit precisions which are similar to those reported

from laser-fusion  $^{40}\text{Ar}/^{39}\text{Ar}$  dating studies. These plateau ages have helped resolve many of the long standing ignimbrite correlation problems in the Mogollon-Datil volcanic field. The combination of  $^{40}\text{Ar}/^{39}\text{Ar}$  plateau ages, paleomagnetic studies, and existing stratigraphic data has allowed the development of a comprehensive, ignimbrite-based, time stratigraphic framework for the Mogollon-Datil volcanic field.

4)  $^{40}\text{Ar}/^{39}\text{Ar}$  plateau data indicate that Mogollon-Datil ignimbrite activity ranged from 36.2 to 24.3 Ma and was strongly episodic, being confined to 4 brief (<2.6 m.y.) eruptive episodes separated by 1-3 m.y. gaps during which no caldera-forming eruptions occurred.

## REFERENCES

- Berggren WA, Kent DV, Flynn JJ (1985) Jurassic to Paleogene: Part 2, Paleogene geochronology and chronostratigraphy. In: NJ Snelling (ed), The Chronology of the Geological Record. Geol Soc London Mem 10:141-195
- Bogaard PVD, Hall CM, Schmincke H, York D (1987)  $^{40}\text{Ar}/^{39}\text{Ar}$  Laser dating of single grains: Ages of Quaternary tephra from the East Eifel volcanic field, FRG. Geophys Res Lett 14:1211-1214
- Cather SM, McIntosh WC, Chapin CE (1987) Stratigraphy, age, and rates of deposition of the Datil Group (Upper Eocene-Lower Oligocene), west-central New Mexico. New Mexico Geology 9:50-54
- Cather SM, Johnson BD (1984) Eocene tectonics and depositional setting of west-central New Mexico and eastern Arizona. New Mexico Bureau of Mines and Mineral Resources, Circular 192, 33 p
- Chapin CE, Lindley JI (1986) Potassium metasomatism of igneous and sedimentary rocks in detachment terranes and other sedimentary basins: Economic implications. Arizona Geol Soc Digest 16:118-126
- Clemons RE (1976) Sierra del las Uvas ash-flow field, south central New Mexico. In: Tectonics and mineral resources of southwestern North America. New Mexico Geological Society, Guidebook 34:111-118
- Dalrymple GB, Lanphere MA (1969) Potassium-argon dating. Principles, techniques and applications to geochronology. WH Freeman, San Francisco, pp 258
- Dalrymple GB, Alexander EC Jr, Lanphere MA, and others (1981) Irradiation of samples for  $^{40}\text{Ar}/^{39}\text{Ar}$  dating using the Geological Survey TRIGA reactor. U S Geol Surv Prof Paper 1176, pp 55
- Dalrymple GB, Lanphere MA (1988) Correlation diagrams in  $^{40}\text{Ar}/^{39}\text{Ar}$  dating: Is there a correct choice?. Geophys Res Lett 15:589-591
- Dalrymple GB, Duffield WA (1988) High-Precision  $^{40}\text{Ar}/^{39}\text{Ar}$  dating of Oligocene rhyolites from the Mogollon-Datil volcanic field using a continuous laser system. Geophys Res Lett 15:463-466
- Deino AL, Best MG (1988) Use of high-precision single-crystal  $^{40}\text{Ar}/^{39}\text{Ar}$  ages and TRM data in correlation of an ash-flow deposit in the Great Basin. Geol Soc Am Abstr with Progs 20:397



- Deino AL (1989) Single-crystal  $^{40}\text{Ar}/^{39}\text{Ar}$  dating as an aid in correlation of ash flows: examples from the Chimney Spring/New Pass Tuffs and the Nine Hill/Bates Mountain Tuffs of California and Nevada. Continental Magmatism Abstracts, New Mexico Bureau of Mines and Mineral Resources Bull 131, p 70
- Elston WE (1984) Mid-Tertiary ash flow tuff cauldrons, southwestern New Mexico. J Geophys Res 89:8733-8750
- Fleck RJ, Sutter JF, Elliot DH (1977) Interpretation of discordant  $^{40}\text{Ar}/^{39}\text{Ar}$  age-spectra of Mesozoic tholeiites from Antarctica. Geochim Cosmochim Acta 41:15-32
- Foland KA (1974)  $^{40}\text{Ar}$  diffusion in homogeneous orthoclase and an interpretation of Ar diffusion in K-feldspars. Geochim Cosmochim Acta 38:151-166
- Goldich SS, Fischer LB (1986) Air-abrasion experiments in U-Pb dating of zircon. Isotope Geoscience 58:195-215
- Harrison TM, McDougall I (1982) The thermal significance of potassium feldspar K-Ar ages inferred from  $^{40}\text{Ar}/^{39}\text{Ar}$  spectrum results. Geochim Cosmochim Acta 46:1811-1820
- Harrison TM, Bé K (1983)  $^{40}\text{Ar}/^{39}\text{Ar}$  age spectrum analysis of detrital microclines from the southern San Joaquin Basin, California: an approach to determining the thermal evolution of sedimentary basins. Earth Planet Sci Lett 64:244-256
- Hildreth W, Mahood G (1985) Correlation of ash-flow tuffs. Geol Soc Am Bull 96:968-974
- Hildreth W, Mahood G (1986) Ring fracture eruption of the Bishop Tuff. Geol Soc Am Bull 97:396-403
- Kedzie LL (1984) High-precision  $^{40}\text{Ar}/^{39}\text{Ar}$  dating of major ash-flow tuff sheets, Socorro, New Mexico (MS thesis). Socorro, New Mexico Inst of Mining and Technology, pp 197
- Kedzie LL, Sutter JF, Chapin CE (1985) High-precision  $^{40}\text{Ar}/^{39}\text{Ar}$  ages of widespread Oligocene ash-flow tuff sheets near Socorro, New Mexico. EOS Trans AGU 17:625
- Kroll H, Ribbe PH (1987) Determining (Al, Si) distribution and strain in alkali feldspars using lattice parameters and diffraction-peak positions: A review. Am Mineral 72:491-506

- Kunk MJ, Sutter JF, Naeser CW (1985) High-precision  $^{40}\text{Ar}/^{39}\text{Ar}$  ages of sanidine, biotite, hornblende, and plagioclase from the Fish Canyon Tuff, San Juan volcanic field, south-central Colorado. EOS Trans AGU 17:636
- Lanphere MA (1988) High-resolution  $^{40}\text{Ar}/^{39}\text{Ar}$  geochronology of Oligocene volcanic rocks, San Juan Mountains, Colorado. Geochim Cosmochim Acta 52:1425-1434
- Lindley JI (1985) Potassium metasomatism of Cenozoic volcanic rocks near Socorro, New Mexico. PhD Thesis, Univ North Carolina, Chapel Hill, pp 563
- Lipman PW (1987) Oligocene central San Juan caldera cluster, Colorado. Geol Soc Am Abstr with Progs 19:315
- Lipman PW, Doe BR, Hedge CE, Steven TA (1978) Petrologic evolution of the San Juan volcanic field, southwestern Colorado: Pb and Sr isotopic evidence. Geol Soc Am Bull 89:59-82
- Lippolt HJ, Fuhrmann U, Hradetzky H (1986)  $^{40}\text{Ar}/^{39}\text{Ar}$  age determinations on sanidines of the Eifel volcanic field (Federal Republic of Germany): constraints on age and duration of a middle Pleistocene cold period. Chemical Geology 59:187-204
- Lo Bello PH, Féraud G, Hall CM, York D, Lavina P, Bernat M (1987)  $^{40}\text{Ar}/^{39}\text{Ar}$  step-heating and laser fusion dating of a Quaternary pumice from Neschers, Massif Central, France: The defeat of xenocrystic contamination. Chemical Geology 66:61-71
- Marvin RF, Naeser CW, Bikerman M, Mehnert HH, Ratté JC (1987) Isotopic ages post-Paleocene igneous rocks within and bordering the Clifton 1° x 2° quadrangle, Arizona-New Mexico. New Mexico Bureau Mines and Mineral Resources Bull 118, 63 p
- McDowell FW (1983) K-Ar dating: incomplete extraction of radiogenic argon from alkali feldspar. Isotope Geoscience 1:119-126
- McIntosh WC, Sutter JF, Chapin CE, Osburn GR, Ratté JC (1986) A stratigraphic framework for the Mogollon-Datil volcanic field based on paleomagnetism and high-precision  $^{40}\text{Ar}/^{39}\text{Ar}$  dating of ignimbrites - a progress report. New Mexico Geol Soc Guidebook 37:183-195
- Osburn GR, Chapin CE (1983a), Nomenclature for Cenozoic rocks of the northeast Mogollon-Datil volcanic field, New Mexico. New Mexico Bureau of Mines and Mineral Resources Stratigraphic Chart 1

- Osburn GR, Chapin CE (1983b) Ash-flow tuffs and cauldrons in the northeast Mogollon-Datil volcanic field: a summary. New Mexico Geol Soc Guidebook 34:197-204
- Ratté JC, Marvin RF, Naeser CW (1984) Calderas and ash-flow tuffs of the Mogollon Mountains. J Geophys Res 89:8713-8732
- Roddick JC (1983) High precision intercalibration of  $^{40}\text{Ar}/^{39}\text{Ar}$  standards. Geochim Cosmochim Acta 47:887-898
- Roddick JC, Cliff RA, Rex DC (1980) The evolution of excess argon in Alpine biotites -  $^{40}\text{Ar}/^{39}\text{Ar}$  analysis. Earth Planet Sci Lett 48:185-208
- Samson SD, Alexander CE (1987) Calibration of the interlaboratory  $^{40}\text{Ar}/^{39}\text{Ar}$  dating standard, MMhb-1. Isotope Geoscience 66:27-34
- Seager WR, Clemons RE, Hawley JW, Kelley RE (1982) Geology of the northwest part of Las Cruces  $1^\circ \times 2^\circ$  sheet, New Mexico. New Mexico Bureau of Mines and Mineral Resources, Geological Map 53, scale 1:125,000
- Seager WR, McCurry M (1988) The cogenetic Organ cauldron and batholith, south central New Mexico: Evolution of a large-volume ash flow cauldron and its source magma chamber. J Geophys Res 93:4421-4433
- Snow E, Yund RA (1985) Thermal history of a Bishop Tuff section as determined from the width of cryptoperthite lamellae. Geology 13:50-53
- Turner G (1968) The distribution of potassium and argon in chondrites. In: Origin and Distribution of the Elements, LH Ahrens (ed), Pergamon, London, p 387-398
- Zeitler PK (1987) Argon diffusion in partially outgassed alkali feldspars: Insights from  $^{40}\text{Ar}/^{39}\text{Ar}$  analysis. Chemical Geology 65:167-181

Ages and distribution of ignimbrites in the Mogollon-Datil volcanic field, southwest New Mexico: a stratigraphic framework using  $^{40}\text{Ar}/^{39}\text{Ar}$  dating and paleomagnetism

William C. McIntosh<sup>1</sup>, Charles E. Chapin<sup>1</sup>,  
Jim Ratté<sup>2</sup>, and John F. Sutter<sup>3</sup>

<sup>1</sup>New Mexico Bureau of Mines and Mineral Resources,  
Socorro, NM 87801

<sup>2</sup>U.S. Geological Survey, Federal Center, Denver, CO 80225

<sup>3</sup>U.S. Geological Survey, 981 National Center, Reston, VA  
20222

ABSTRACT

The combination of high-precision  $^{40}\text{Ar}/^{39}\text{Ar}$  sanidine plateau ages and paleomagnetic data provides reliable long-distance correlation criteria for 25 discontinuously exposed regional ignimbrites in the 40,000 km<sup>2</sup>, Eocene-Oligocene Mogollon-Datil volcanic field of southwestern New Mexico.

$^{40}\text{Ar}/^{39}\text{Ar}$  age spectra from sanidine separates (97 spectra, 85 samples, 36 units) are characteristically flat and, with few exceptions, yield plateau ages showing within-sample and within-unit precisions less than  $\pm 0.5\%$ . Precise relative  $^{40}\text{Ar}/^{39}\text{Ar}$  ages, which agree closely with independently established stratigraphic order, have been determined for 7 ignimbrites (3 to 8 samples per unit) and preliminary ages have been determined for another 26 units (1 to 2 samples per unit).

Regional and local ignimbrite outflow sheets show stable paleomagnetic remanence directions which are uniform over most of their extents, including facies ranging from thick, densely welded proximal ignimbrites to unwelded

distal fringes as thin as 1.5 m. The largest sources of dispersion in the paleomagnetic data set (404 sites in 25 regional and 54 local ignimbrites) are uncertainties in determinations of the paleohorizontal, and local, fault-related tectonic rotations, particularly in strongly extended areas.

$^{40}\text{Ar}/^{39}\text{Ar}$  and paleomagnetic correlation criteria are complementary:  $^{40}\text{Ar}/^{39}\text{Ar}$  data serve to resolve age differences between paleomagnetically similar units, and paleomagnetism helps distinguish between units that are altered, lack sanidine, or are too close in age to be resolved even by the  $^{40}\text{Ar}/^{39}\text{Ar}$  method.

Used in concert with lithologic and stratigraphic position data,  $^{40}\text{Ar}/^{39}\text{Ar}$  ages and paleomagnetic directions allow accurate long-range ignimbrite correlations which provide reliable ties between previously established subregional stratigraphic sequences. Regional stratigraphic markers now shown to be more extensive than previously believed include Kneeling Nun Tuff (34.9 Ma), Box Canyon Tuff (33.5 Ma), Caballo Blanco Tuff (31.7 Ma), Vicks Peak Tuff (28.6 Ma), and Bloodgood Canyon Tuff (28.1 Ma).

A precise, comprehensive, ignimbrite-based, time-stratigraphic framework has been developed for the Mogollon-Datil volcanic field. This framework provides significant age constraints for sequences of lavas and sedimentary rocks for which precise ages cannot be measured. Within the context of this stratigraphic framework, Mogollon-Datil

igneous units provide an inherently discontinuous but precise record of Late Eocene-Oligocene geomagnetic polarity. This polarity record is useful for correlations within and between volcanic fields, and has potential to help calibrate the Magnetic Polarity Time Scale.

Mogollon-Datil ignimbrite activity ranged from 36.2 to 24.3 Ma and was highly episodic, being confined to 4 brief (<2.6 m.y.) eruptive intervals separated by 1.5 to 3 m.y. long hiatuses. Cauldron-forming activity originated in the 36.1-35.4 Organ/Doña cauldron area and subsequently migrated north and west. Rhyolitic activity was most intense between 29 and 27.4 Ma; this interval is characterized by alternating ignimbrite eruptions from the Mogollon and Socorro cauldron complexes, punctuated by 2 brief intervals (29.0-28.7 Ma and 28.1 Ma) of extensive rhyolitic dome and flow eruptions in the central Black Range area between the two complexes.

#### INTRODUCTION

Our understanding of the stratigraphy and eruptive history of the Mogollon-Datil volcanic field has been substantially advanced during the last five years by the application of  $^{40}\text{Ar}/^{39}\text{Ar}$  and paleomagnetic techniques. Since the late 1950s this 40,000 km<sup>2</sup> late Eocene-Oligocene volcanic field (Figs. 1,2) has been the focus of numerous mapping, stratigraphic, geochemical, petrologic, and isotopic studies, primarily by workers from New Mexico Universities, New Mexico Bureau of Mines and Mineral

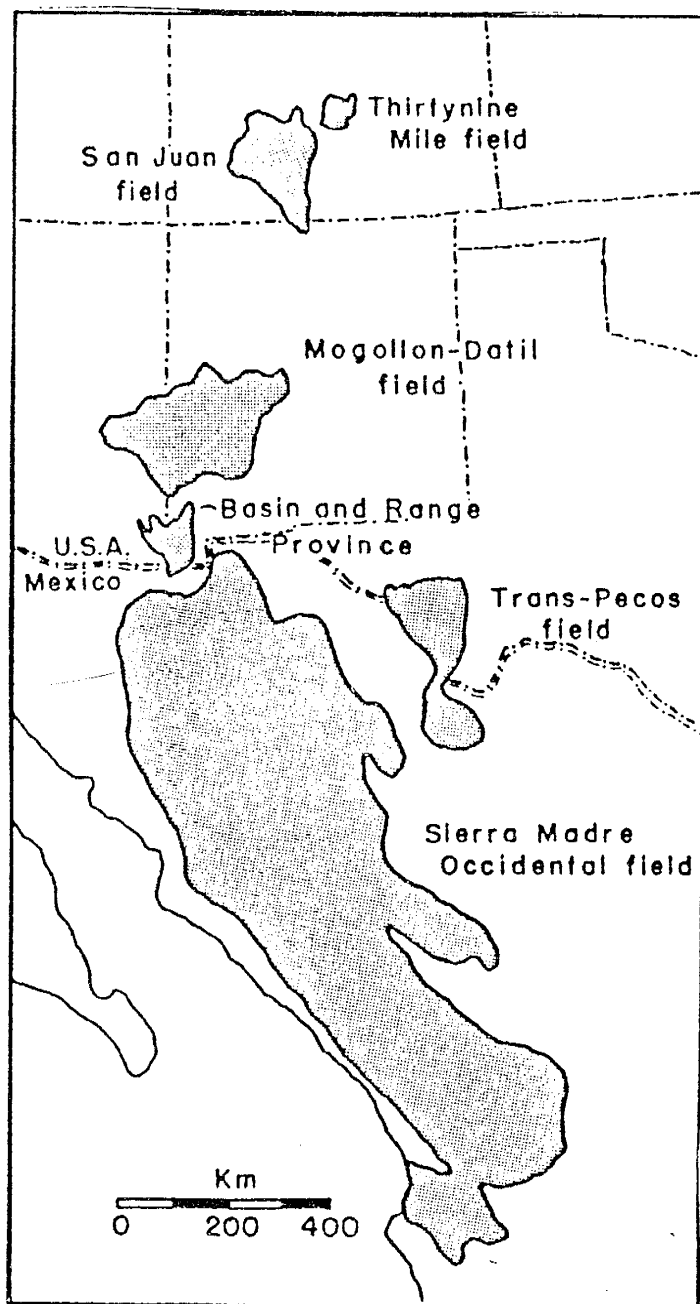


Fig. 1. Generalized map showing present day extent of mid-Tertiary silicic volcanic fields of southwestern North America.

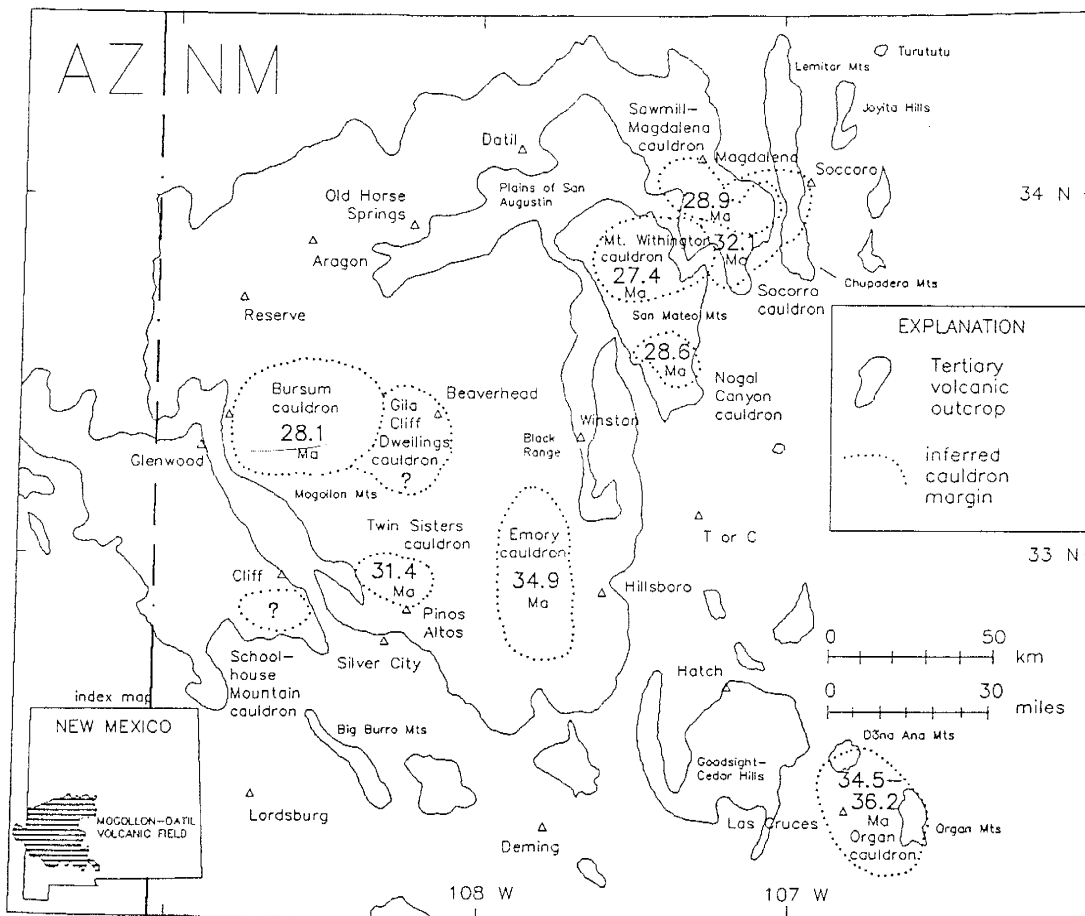


Fig. 2. Map of the Mogollon-Datil volcanic field showing inferred cauldrons, their ages, and generalized outcrop distribution of Late Eocene-Oligocene volcanic rocks.



Resources, and the U.S. Geological Survey. Detailed geologic mapping has been successfully used to unravel the stratigraphy in subregions of the field (e.g. Ratté et al., 1984; Osburn and Chapin; 1983a; Seager et al., 1982) and K-Ar studies have constrained ages of many units to within a few million years (Elston et al., 1973; Osburn and Chapin, 1983a; Marvin et al., 1987). However, synthesis of subregional stratigraphic data into an integrated, field-wide stratigraphic framework has been frustrated by the inability to correlate ignimbrites (ash-flow tuffs) over long distances.

The 25 regional ignimbrites in the Mogollon-Datil sequence constitute potentially ideal time-stratigraphic marker horizons. However, although these ignimbrites have been instrumental in deciphering subregional stratigraphic sequences, regional correlations have proven difficult. Correlations based solely on mapping are hampered by discontinuous outcrop patterns produced by basin-and-range extension. Lithology, although useful as a first-order criterion, has proven unreliable for long-distance correlations. Many stratigraphically distinct units are lithologically similar, and individual units show lateral, vertical, and sectoral variations in mineralogy, chemistry, welding texture, and in phenocryst concentration and size, analogous to variations shown by ignimbrites elsewhere (Hildreth and Mahood, 1985). Attempts to geochemically fingerprint ignimbrites have been largely unsuccessful

(Bornhorst, 1980), and conventional K-Ar dating techniques lack the resolution required by most of the correlation problems (e.g. Marvin et al., 1987).

This paper describes how the combination of paleomagnetic analysis and high-precision  $^{40}\text{Ar}/^{39}\text{Ar}$  dating has led to the resolution of many long-standing Mogollon-Datil ignimbrite correlation problems and has allowed the development of an integrated stratigraphic framework for the field. This report concentrates on the stratigraphy and eruptive history of the ignimbrites; no lithologic or geochemical data are reported. Furthermore, no attempt has been made to address the history of voluminous mafic to intermediate lavas that are associated with the ignimbrites, because individual lavas show limited lateral extent and generally lack mineral phases suitable for high-precision  $^{40}\text{Ar}/^{39}\text{Ar}$  dating.

#### GEOLOGIC SETTING AND PREVIOUSLY ESTABLISHED STRATIGRAPHY

The late Eocene-Oligocene Mogollon-Datil volcanic field of southwestern New Mexico is part of a discontinuous belt of Mid-Tertiary silicic volcanic fields (Fig. 1) that extends from the San Juan Mountains in Colorado southward into central Mexico. The boundaries of the Mogollon-Datil field are not formally defined, particularly along its southern edge, where it merges gradually with a zone of basin-and-range terrain which separates it from formerly contiguous volcanic terrain in Chihuahua, Mexico. For the purposes of this report, the Mogollon-Datil field is

considered to extend as far south as Las Cruces and Lordsburg, N.M., and excludes the complex volcanic sequence of Hidalgo County, N.M. (Elston, 1984).

Activity of mid-Tertiary volcanic fields of southwestern north America was generally initiated by eruptions of intermediate-composition andesite and basaltic andesite. Cauldron-forming rhyodacite to rhyolite eruptions typically joined more mafic activity after several million years (Lipman et al., 1972, 1978). Most proposed models explain this mid-Tertiary pulse of volcanism as a consequence of a transient episode of low-angle subduction of the Farallon Plate (e.g. Lipman et al., 1972, Cross and Pilger, 1982). Alternative models interpret magmatism as a result of uplifted isotherms following post-Laramide crustal thinning (Mutschler et al., 1987). In the Mogollon-Datil field, initial andesitic volcanism was active from about 40 to 36 Ma, and was followed by episodic bimodal basaltic andesite and silicic activity from 36 to 24 Ma (Cather et al., 1987; Elston, 1984; McIntosh, dissertation, Chapter B).

The Mogollon-Datil silicic sequence includes domes, flows, intrusives, and numerous ignimbrites. Individual ignimbrites range widely in form, volume, and distribution, from enormous ( $>1250 \text{ km}^3$ ), cauldron-derived, densely welded outflow sheets to tiny ( $<0.1 \text{ km}^2$ ), unwelded pyroclastic aprons surrounding domes. Because of incomplete exposures, estimates of original volume and area for these ignimbrite necessarily involve many assumptions. An arbitrary, but

less subjective way to quantify the size of these units is lateral extent (Table 1). The Mogollon-Datil silicic sequence includes 25 regional ignimbrites of >40 km known extent and numerous smaller subregional to local units (54 sampled in this study). Twelve of the regional ignimbrites are major units with approximate volumes of 200-1250 km<sup>3</sup> (Table 1).

From mid-Oligocene to the present time, the Mogollon-Datil volcanic field has experienced inhomogeneously distributed extensional tectonism (Chapin and Seager, 1975). As a result, originally contiguous ignimbrite sheets are now discontinuously exposed in fault-block mountain ranges separated by infilled basins. Structural complexity varies widely from range to range, in extreme cases showing low-angle faulting and steep (45-90°) dips indicative of extension in excess of 100% (Chamberlin, 1983).

Subregional stratigraphic sequences of ignimbrites established prior to this study are summarized in Figure 3. Detailed mapping was the primary method used to establish these sequences; individual ignimbrites were identified mainly by their lithology and stratigraphic position relative to other units. Published K-Ar dates from these subregional sequences generally range from 36 to 24 Ma, but multiple dates from individual units typically vary by ±10% or more (Fig. 3; Elston et al., 1973; Chapin et al., 1975; Marvin et al., 1987). Furthermore, K-Ar dates in many cases

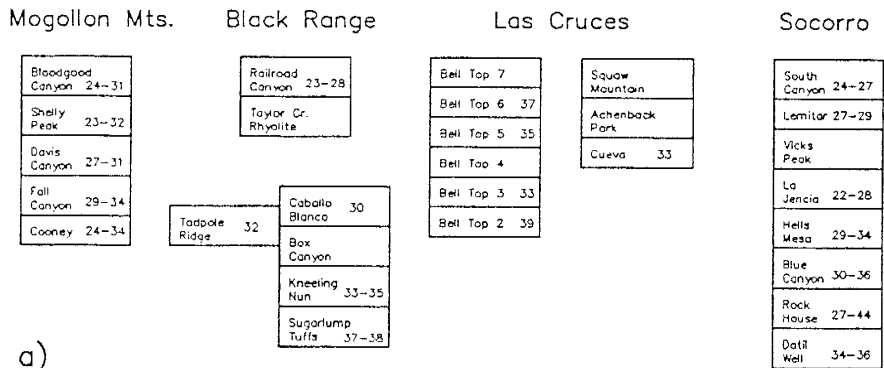
Table 1. Summary of  $^{40}\text{Ar}/^{39}\text{Ar}$ , paleomagnetic, and stratigraphic data for Mogollon-Datil ignimbrites.

Stratigraphic Unit	ref	extent (km)	volume ( $\text{km}^3$ )	$^{40}\text{Ar}/^{39}\text{Ar}$ n	Ma	$\sigma(\text{Ma})$	plateau age	pol	n/nt	inc	dec	$\alpha_{95}$	Caldera or source	Correlative Units (ref)	Published Miscorrelations (ref)
<b>EPISODE 4</b>															
*Turkey Springs	8	62		2	24.33	$\pm 0.03$		R	15/19	-51.8	175.9	3.6			South Can (6), Railroad Can (13)
<b>EPISODE 3</b>															
*Slash Ranch	24	22		1	26.10	$\pm 0.12$		N	2/3	57.6	166.9	13.0		Jordan Canyon (4)	
South Canyon	18	135	700	3	27.36	$\pm 0.07$		R	22/43	-30.7	202.1	3.5	Mt. Withington		Lemitar (6)
*Walking X Ranch	15			1	27.58	$\pm 0.10$		N	1/1	64.0	5.7				
Lemitar	18	78	450	2	28.00	$\pm 0.08$		N	10/21	36.6	356.9	4.3	Baldy?		
Caronita Canyon	18	40	50	1	27.96	$\pm 0.07$		N	4/5	41.5	354.2	11.0	Baldy?		Hells Mesa (1)
*Triangle C Ranch	19	58		1	28.05	$\pm 0.14$		N	5/6	49.2	357.3	4.4	Bursum?		
Apache Springs	20	35	1200	1	27.98	$\pm 0.09$		R	2/2	-35.8	166.1	30.6	Bursum		
Bloodgood Canyon	20	155	1000	8	28.05	$\pm 0.04$		R	22/23	-27.1	165.3	3.1	Bursum		Railroad Can (23)
Diablo Range	21	10		1	28.05	$\pm 0.08$		R	1/1	-24.8	200.3		dome		
Shelly Peak	20	96	100-200	1	(28.1)			R	8/10	-32.7	174.8	6.4	Gila Cliff D.?		Apache Springs (23)
Garcia Camp	7	25		1	28.10	$\pm 0.09$		R	7/7	-48.8	185.4	5.2	dome		
Vicks Peak	18	200	1050	3	28.56	$\pm 0.04$		R	24/31	-27.9	182.8	3.3	Nogal Can.	Tularosa Can (23), Wahoo Can (13)	
*Lookout Mtn.	28			2	28.69	$\pm 0.03$		R	1/1	-55.4	160.8		dome	Diamond Creek (28)	
La Jencia	18	158	1250	4	28.85	$\pm 0.04$		R	15/24	-49.3	168.2	3.6	Sawmill/Magdalena	Wahoo Can (13)	
Davis Canyon	20	125	200-400	2	29.01	$\pm 0.11$		R	6/7	-53.5	159.6	7.5	Gila Cliff D.?		
*Mud Hole	14			1	29.09	$\pm 0.11$		R	1/1	-55.9	124.5		dome?		
*Stiver Canyon	28			(29)				R	1/1	-52.7	172.6		dome?		
*Little Min. Cr.	28			1	29.01	$\pm 0.10$		N	1/1	58.0	3.1		dome		
*Monument Canyon	17	25		(29)				N	1/1	35.2	344.0				
*Pueblo Creek 4	12			(29)				N	1/1	51.8	336.9				
<b>EPISODE 2</b>															
u. Taopole Ridge	9	28		1	31.39	$\pm 0.11$		R	3/3	-23.3	185.2	16.3	Twin Sisters		
L. Taopole Ridge	9	45		(31.4)				R	6/6	-71.1	203.8	11.0	Twin Sisters		Terry Canyon (17), Tvt (10)
Caballo Blanco	27	143		5	31.65	$\pm 0.06$		R	6/8	-46.0	171.4	4.4	Emory?		Fall Canyon (18)
Hells Mesa	18	152	1200	4	32.06	$\pm 0.10$		R	10/18	-60.2	166.0	4.8	Socorro		

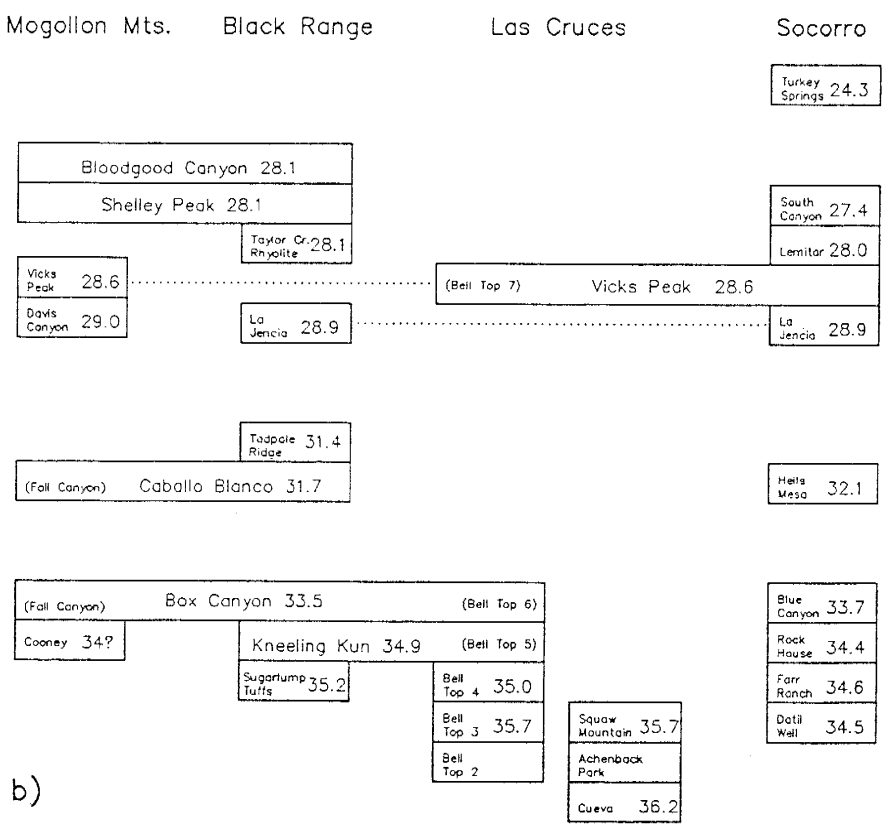
Table 1 (continued). Summary of  $^{40}\text{Ar}/^{39}\text{Ar}$ , paleomagnetic, and stratigraphic data for Mogollon-Datil ignimbrites.

Stratigraphic Unit	extent (km)	volume (km <sup>3</sup> )	$^{40}\text{Ar}/^{39}\text{Ar}$ n	Ma	$\sigma$ (Ma)	age	pol	n/nt	direction inc dec	$\alpha_{95}$	Caldera	Correlative Units (ref)	Published Miscorrelations (ref)
EPIISODE 1													
Box Canyon	3	225	7	33.51	$\pm 0.13$		R	12/17	-56.0	141.3	4.7		
Blue Canyon	18	135	2	33.66	$\pm 0.03$		R	6/9	-37.3	144.4	5.7	[ Bell Top 6 (2), Fall Can (20) Cherokee Canyon (11)	SugarLump (3)
*Table Mountain	3	70?	1	33.89	$\pm 0.12$		R	1/1	-36.9	181.5			SugarLump (3)
Cooney	20	142	1	34.42	$\pm 0.12$		R	3/3	-46.7	168.7	28.0		
Rockhouse Can.	18	142	1	34.57	$\pm 0.12$		N	1/1	58.7	353	5.4	dome	
Mimbres Peak	5	72	1	34.70	$\pm 0.10$		R	4/4	-61.7	171.2	10.8		
*Lebya Well	22	213	4	34.89	$\pm 0.05$		R	21/28	-43.7	167.1	3.8	Emory	Bishop Peak (12) Bell Top 5 (2)
*Kneeling Nun	5	213	4	34.89	$\pm 0.05$		R	21/28	-43.7	167.1	3.8		SugarLump (3)
*Stone House Ran.	14	112	3	34.96	$\pm 0.04$		N	3/3	43.5	323.9	18.3		
Bell Top 4	2	50?	1	35.17	$\pm 0.12$		N	5/5	56.1	2.7	3.6		
upper SugarLump	27	42?	1	35.48	$\pm 0.07$		N	2/2	62.3	337.7	8.1		
Lower SugarLump	27	42?	1	35.57	$\pm 0.13$		N	2/2	44.0	347.3	12.1		
basal SugarLump	27	42?	1	35.57	$\pm 0.13$		N	1/1	49.2	271.1			
*Farr Ranch	22	143	1	35.57	$\pm 0.13$		N	9/13	50.4	345.5	4.7		
Datil Well	28	140	2	35.48	$\pm 0.07$		N	5/5	53.3	19.9	6.4		
Bell Top 3	2	41	2	35.69	$\pm 0.02$		N	2/2	69.9	329.9	1.6		
Bell Top 2	2	15	2	35.69	$\pm 0.02$		N	2/2	39.7	350.0	17.3		
Doña Ana	26	8	1	35.49	$\pm 0.11$		N	2/2	54.4	155.3	48.5	Doña Ana (intracaldera)	
Squaw Mountain	25	11	1	35.75	$\pm 0.12$		N	2/2	58.8	178.0	44.5	Organ (intracaldera)	
Achenback Park	25	13	1	35.75	$\pm 0.12$		N	3/3	50.0	177.0	35.6	Organ (intracaldera)	
*U. Steeple Rock	16	16	1	36			N	1/1	50.8	26.7			
*L. Steeple Rock	16	16	1	36			N	1/1	-60.8	158.7			
u. Rubio Peak	27	13	1	36.20	$\pm 0.13$		R	1/1	-63.8	152.6			
l. Rubio Peak	27	13	1	36.20	$\pm 0.13$		R	1/1	-40.1	166.5			
Cueva	25	13	1	36.20	$\pm 0.13$		R	2/3	-53.4	220.3	67.8	Organ (intracaldera)	

Explanation: \* denotes informal unit name; regional ignimbrites are underlined; ages in parentheses are based on stratigraphic constraints; extent is maximum exposed width (extents based on uncertain correlations are queried); volume estimates are after McIntosh et al., 1986; n is number of plateau ages used in mean;  $\sigma$  is standard deviation of multiple ages or analytical error of single ages; pol is magnetic polarity; n/nt is number of sites used in unit-mean/total sites; inc, dec, and  $\alpha_{95}$  are unit-mean inclination, declination, and cone of 95% confidence ( $\alpha_{95}$  omitted for units with results from less than three sites); known source areas are shown in caldera column, dome denotes small volume units derived from rhyolitic domes. References: 1) Bowring, 1980; 2) Clemens, 1976; 3) Elston, 1973; 4) Elston et al., 1975; 5) Elston et al., 1975; 6) Donze, 1980; 7) Duffield et al., 1987; 8) Ferguson, 1986; 9) Finnell, 1976; 10) Finnell, 1982; 11) Finnell, 1988; 12) Finnell, 1988; 13) I. Finnell, 1988, pers. com.; 14) R. Harrison, 1988, pers. com.; 15) Hedlund, 1978; 16) D. Hedlund, unpublished map; 17) Krier, 1980; 18) Osburn and Chapin, 1983a; 19) J. Ratté, 1988, pers. com.; 20) Ratté et al., 1984; 21) Ratté and Gaskill, 1975; 22) Ratté and McIntosh, 1989; 23) Rhodes and Smith, 1976; 24) Richter, 1978; 25) Seager and McCurry, 1988; 26) Seager et al., 1976; 27) Seager et al., 1982; 28) Woodard, 1982.



a)



b)

Fig. 3. Evolution of understanding of the stratigraphy of the largest regional ignimbrites in the Mogollon-Datil volcanic field. a) Subregional stratigraphic sequences determined prior to this study. Numbers show range of published K/Ar data (Ma) rounded to the nearest million years. Sources: Ratté et al., 1984; Marvin et al., 1987; Gleason, 1976; Seager and McCurry, 1988; Elston, 1984; Johnson and Chapin, 1983a. b) Revised generalized stratigraphic sequences for the same areas, showing  $^{40}\text{Ar}/^{39}\text{Ar}$  ages, and correlations aided by  $^{40}\text{Ar}/^{39}\text{Ar}$  and paleomagnetic data.

disagree with established stratigraphic order (e.g. Bell Top sequence, Fig. 3, Clemons, 1976).

Mapping, lithology, and K-Ar data have not proven to be adequate criteria for correlation of ignimbrites between established subregional sequences. Once outside of familiar stratigraphic context, specific ignimbrites become more difficult to identify, particularly at their thin, unwelded distal fringes, where they can be easily confused with local dome-derived units. Two good examples of the difficulties of long-distance correlation, both detailed in Marvin et al. (1987), are the long standing Bloodgood Canyon/Railroad Canyon question and the difficulty of distinguishing look-alike ignimbrites in the area where units from Mogollon, Black Range, and Socorro centers overlap.

In addition to the problems of correlating ignimbrite outflow sheets is the question of determining their source cauldrons. Source cauldrons have been reliably identified for only seven of the major Mogollon-Datil regional ignimbrites (Table 1; Fig. 2; Osburn and Chapin, 1983b; Elston, 1984). Three additional cauldrons have been identified by mapping, but these have not been reliably matched with outflow sheets (Organ/Doña Ana cauldron, Seager and McCurry, 1988; Gila Cliff Dwellings cauldron, Ratté et al., 1984; Schoolhouse Mountain cauldron, Wahl, 1980).

#### METHODS: $^{40}\text{Ar}/^{39}\text{Ar}$ DATING AND PALEOMAGNETISM

Mogollon-Datil ignimbrites are well-suited to paleomagnetic and  $^{40}\text{Ar}/^{39}\text{Ar}$  analysis. Rhyolitic ignimbrites



from many areas have been shown to be high-quality recorders of ancient geomagnetic fields (e.g. Grommé et al., 1972, Reynolds, 1977, Geissman et al., 1983). High-relief and the arid New Mexico climate provide well-exposed, unweathered outcrops in which alteration is generally minimal, although K-metasomatism or hydrothermal alteration have affected some areas (Chapin and Lindley, 1986). Most of the units contain abundant sanidine, a K-rich, anhydrous mineral that is highly retentive of argon and ideal for  $^{40}\text{Ar}/^{39}\text{Ar}$  age spectrum studies (Zeitler, 1987). Finally, and perhaps most importantly, existing detailed mapping and stratigraphy offer a framework in which these techniques can be applied and also provide opportunities to test the precision of both methods.

The details of  $^{40}\text{Ar}/^{39}\text{Ar}$  and paleomagnetic procedures and results from this study are covered in two other papers (McIntosh, dissertation, Chapters A and B). The conclusions of these papers are summarized in the following paragraphs, which also discuss some general aspects of these two powerful techniques. During the course of this study, both techniques were first applied to established subregional stratigraphic sequences. Once the ages and paleomagnetic directions of established units were determined, longer range correlations were addressed.

Paleomagnetic analysis is a well-established, inexpensive method for correlation of ignimbrites. Many ignimbrites, both welded and non-welded, possess uniform

thermoremanent magnetization (TRM) directions representing an accurate record of the geomagnetic field direction during rapid post-emplacement cooling (Dalrymple et al., 1965; Grommé et al. 1972; Best et al., 1973; Reynolds, 1977; Hoblitt et al., 1985; Hildreth and Mahood, 1985; Weiss et al., 1989). Because of reversals and secular variation of the geomagnetic field, paleomagnetic analysis can potentially distinguish between volcanic units differing in age by as little as centuries (Grommé et al., 1972; Bogue and Coe, 1981; Holcomb et al., 1985). Paleomagnetic analysis offers the further potential of constraining tectonic rotations (Hagstrum and Gans, 1989; Wells and Hillhouse, 1989; Geissman and Harlan, in prep) and of placing precisely dated units within the established magnetic polarity time scale (McIntosh, dissertation, Chapter D).

For the paleomagnetic portion of this study, a total of 3055 oriented samples were collected from 404 sites in 25 regional and 54 local ignimbrites. With a few exceptions, sites were field drilled and oriented by suncompass. Much care was taken in assessment of structural attitude at each site, because attitude is commonly the largest uncertainty in paleomagnetic studies of ignimbrites (Grommé et al., 1972, Geissman et al., 1982; Hagstrum and Gans, 1989). The remanent magnetizations (RMs) of standard-sized specimens were measured using spinner and cryogenic magnetometers, utilizing both alternating field and thermal demagnetization

procedures. A variety of techniques were also used to assess magnetic mineralogy, including reflected light microscopy, thermomagnetic analyses, and isothermal remanent magnetization (IRM) acquisition and demagnetization experiments.

Paleo- and rock-magnetic data show that Mogollon-Datil ignimbrites generally carry uniform, well-defined RMs that provide reliable correlation criteria. About 90% of the sites exhibit well-grouped ( $\alpha_{95} < 10^\circ$ ) RMs carried by finely dispersed, high-temperature-oxidation assemblages of magnetite, hematite, and maghemite. These RMs, interpreted as thermoremanent magnetization (TRM), are readily separated from abundant lightning-induced isothermal components. For the remaining 10% of sites, primarily in altered or poorly-welded, lithic-rich tuff, the original TRMs are obscured by chemical remanence or randomly directed, lithic-hosted RMs.

Within individual ignimbrite outflow sheets, TRM directions are generally laterally and vertically consistent, in both densely welded proximal and poorly welded distal facies. Discordancies in individual site-mean directions primarily reflect uncertainties in structural corrections, particularly in areas of locally strong tectonic extension. The magnetizations of these outflow sheets show no evidence of syncooling secular variation or sub-blocking-temperature flowage (unlike Rosenbaum, 1986). Unit-mean TRM directions of all 22 well-constrained (4 to 22 sites per unit) ignimbrite outflow sheets (Fig. 4) lie

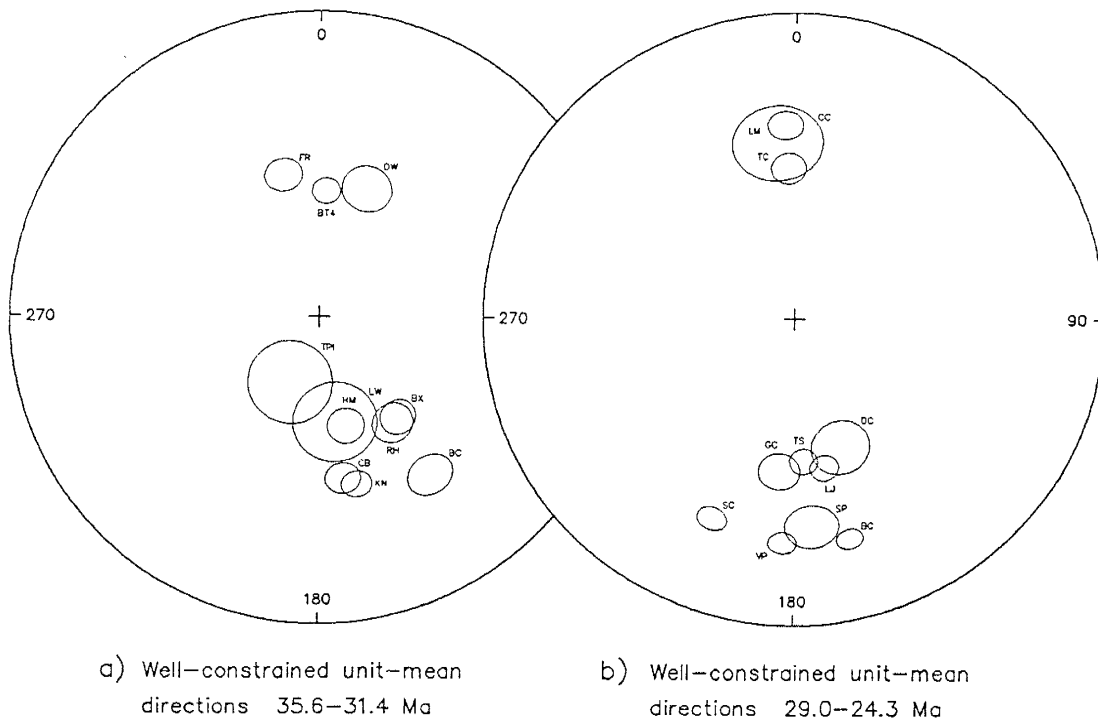


Fig. 4. Unit-mean paleomagnetic directions for 22 better-studied (4 or more sites per unit) Mogollon-Datil ignimbrites: a) Episode 1 and 2 units, b) Episode 3 and 4 units. Ovals show cones of 95% confidence, and abbreviations are explained in Figure 5. Unit mean data is also given in Table 1.

within  $30^\circ$  of the time-averaged late Eocene-Oligocene field ( $D=170.5$ ,  $I=50$ ; Diehl et al., 1988). Distinctive to unique unit-mean TRM directions, differing  $15-30^\circ$  from the time-averaged field, provide strong correlation criteria for 9 of these units. Compared to outflow sheet data, the site-mean TRMs of thick ( $>500$  m) intracauldron facies ignimbrites are poorly grouped, apparently reflecting either secular variation during protracted cooling or large discrepancies between eutaxitic foliations and the syncooling paleohorizontal.

$^{40}\text{Ar}/^{39}\text{Ar}$  dating techniques can yield ages which are several times more precise than the best conventional K-Ar or fission-track data. This high precision chiefly results from the ability to simultaneously measure radiogenic  $^{40}\text{Ar}$  and  $^{40}\text{K}$  (as reactor-produced  $^{39}\text{Ar}$ ) on a single aliquot of sample (Turner, 1968; Roddick, 1983). Furthermore, the  $^{40}\text{Ar}/^{39}\text{Ar}$  method can provide accurate ages without extracting all Ar from a sample, thereby overcoming the chronic problem of incomplete  $^{40}\text{Ar}$  extraction in K-Ar dating of sanidine and anorthoclase (McDowell, 1983).

The  $^{40}\text{Ar}/^{39}\text{Ar}$  method also allows the use of incremental heating to generate age spectra for individual samples. The shape of age spectra help identify effects of  $^{40}\text{Ar}$  loss, excess  $^{40}\text{Ar}$ , or contamination by older material. Furthermore, precision can be increased by statistically treating incremental step-heating data using plateau or isotope correlation methods.

A total of 85 samples from 36 ignimbrites were collected for  $^{40}\text{Ar}/^{39}\text{Ar}$  dating. Weathered or altered outcrops were avoided and, in all but a few cases, the same outcrops sampled for dating were also sampled for paleomagnetic analysis. Ultrapure sanidine separates were prepared and irradiated, along with flux monitors of known age (FCT-3, 27.83 Ma, Kunk et al., 1985; Mmhb1, 520.4 Ma, Sampson and Alexander, 1983), in the constant-flux portion of the central thimble of the U.S. Geological Survey TRIGA reactor (Dalrymple et al., 1981). Age spectra were measured at the U.S. Geological Survey  $^{40}\text{Ar}/^{39}\text{Ar}$  dating facility at Reston, Va.

A total of 97  $^{40}\text{Ar}/^{39}\text{Ar}$  age spectra were measured, 94 of which met the plateau age criteria of Fleck et al. (1981), and plateau ages were calculated by weighting gas fractions according to the inverse of their variance. Replicate plateau age determinations ( $n=2$  to 6) for 8 different samples show within-sample precisions averaging  $\pm 0.25\%$ . Plateau ages from multiple ( $n=3$  to 8) samples of individual ignimbrites show within-unit precision ( $1\sigma$ ) of  $\pm 0.1$ - $0.4\%$  ( $\pm 0.04$ - $0.13$  Ma). In sharp contrast, conventional K-Ar and fission-track ages on the same units generally show relative errors ( $1\sigma$ ) in excess of  $\pm 5\%$  ( $\pm 1.3$ - $2.2$  Ma) (Marvin et al., 1987; Ratté et al., 1984). A further indication of the high precision of these  $^{40}\text{Ar}/^{39}\text{Ar}$  age determinations is shown by their close agreement with established stratigraphic order, as discussed below.

$^{40}\text{Ar}/^{39}\text{Ar}$  and paleomagnetic data from Mogollon-Datil ignimbrites are compiled in Table 1. Excluded from this table are paleomagnetic data from 30 sparsely studied (1 site/unit), local, multi-cooling-unit ignimbrites related to rhyolite domes and flows (all data are presented in detail in McIntosh, dissertation, Chapter A and Appendices.)

#### HISTORY OF IGNIMBRITE ACTIVITY

$^{40}\text{Ar}/^{39}\text{Ar}$  plateau ages determined from Mogollon-Datil ignimbrites range from 36.2 to 24.3 Ma and indicate that ignimbrite activity was strongly episodic. Activity was confined to 4 brief (<2.6 Ma) eruptive episodes separated by 1-3 Ma gaps during which no cauldron-forming eruptions occurred (Fig. 5).

Geographic trends shown by cauldron activity are not simple. Cauldron activity was initiated at the southeastern edge of the field with 36.2-35.5 Ma eruptions of the Organ cauldron (Fig. 2). During the subsequent 8 m.y., the locus of cauldron activity in the southern part of the volcanic field migrated progressively 240 km northwestward, culminating in eruption of the Bursum cauldron at 28.1 Ma. At 32.1 Ma, or possibly earlier, cauldron activity also began in the northern part of the field. The 32.1 Ma Socorro cauldron is the oldest documented member of this northern cauldron sequence, although also present in the area are 35.6-33.7 Ma regional ignimbrites for which no source cauldrons have been recognized. The northern cauldron sequence shows a general east-to-west trend from

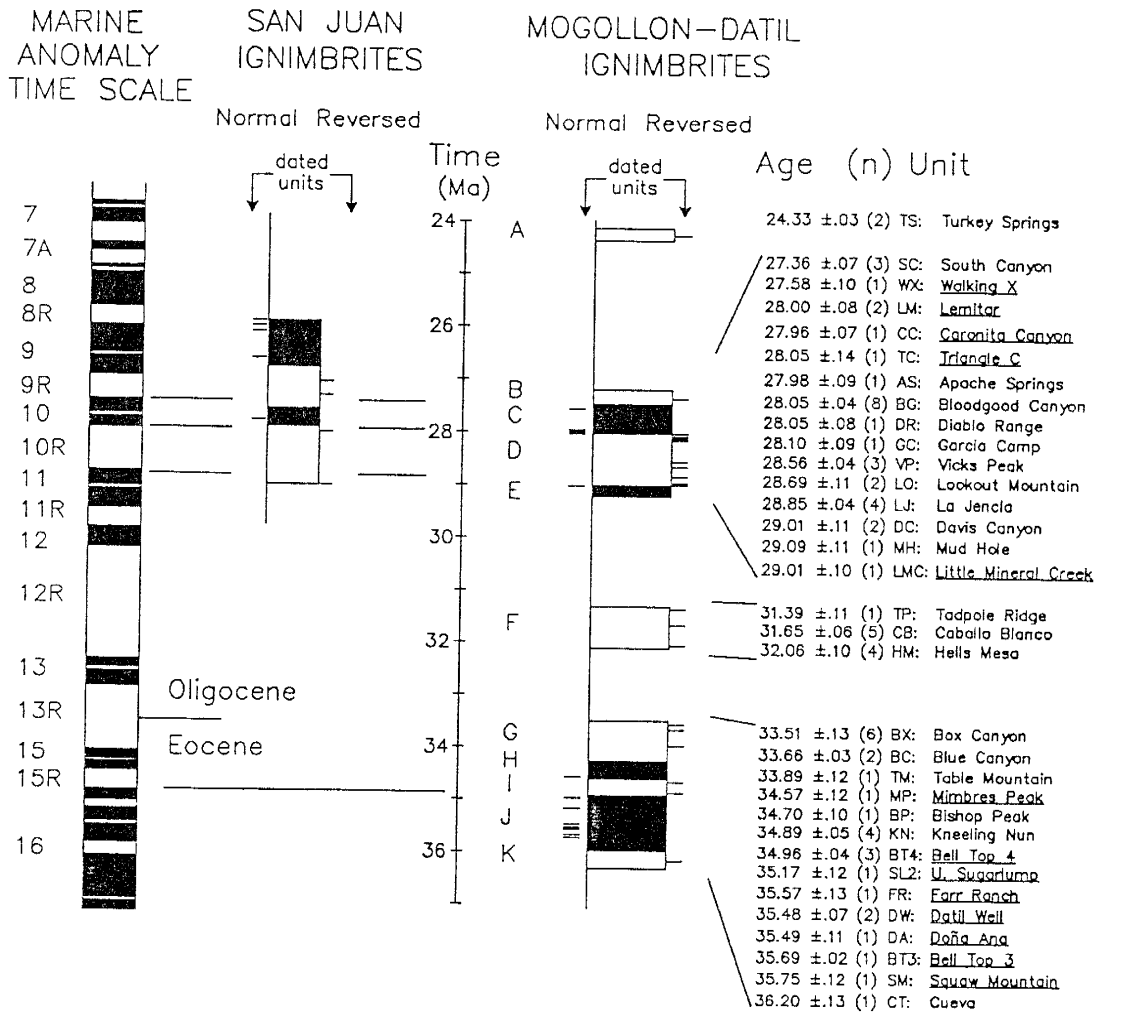


Fig. 5. A composite stratigraphic column for ignimbrites of the Mogollon-Datil volcanic field, summarizing  $^{40}\text{Ar}/^{39}\text{Ar}$  and magnetic polarity data, and demonstrating the highly episodic nature of ignimbrite volcanism. Black denotes normal paleomagnetic polarity and white denotes reversed. Right column gives mean  $^{40}\text{Ar}/^{39}\text{Ar}$  plateau ages, unit names and their abbreviations (used in Figs. 4 and 6), and the number of age determinations (in parentheses). Units are in stratigraphic order and normal units are underlined. Left column shows interpreted polarity record, with lettered polarity intervals. Horizontal lines adjacent to the polarity column each depict a dated ignimbrite. Errors represent the standard deviation of plateau ages for units with  $n > 2$ , and the analytical error for units with  $n \leq 2$ .

Also shown for comparison are the ignimbrite polarity record of the San Juan Volcanic field (after Lanphere, 1988; Diehl et al., 1974; Beck et al., 1977) and a proposed correlation with the marine magnetic anomaly time scale (McIntosh, dissertation, Chapter D).



32.1 to 24.3 Ma, but this trend is ill-defined, and only spans a distance of 70 km (Fig. 2).

The composite stratigraphic sequence of Mogollon-Datil ignimbrites (Fig. 5) provides a discontinuous but coherent record of Late Eocene-Oligocene polarity. This polarity record is valuable not only for Mogollon-Datil correlations, but has potential for correlations between volcanic fields and calibration of the worldwide Magnetic Polarity Time Scale (Fig. 3; McIntosh, dissertation, Chapter D).

Correlations based on  $^{40}\text{Ar}/^{39}\text{Ar}$  and paleomagnetism have allowed established subregional ignimbrite sequences to be assembled into a single, integrated time-stratigraphic framework for the entire Mogollon-Datil volcanic field (Fig. 6). This general framework is discussed after the following sections discuss the details of  $^{40}\text{Ar}/^{39}\text{Ar}$  and paleomagnetic correlations for ignimbrites in each of the 4 Mogollon-Datil eruptive intervals. Data are summarized on a unit-by-unit basis in Figures 7-34.

#### **Episode 1 (36.2 Ma-33.5)**

The 36.2 to 33.5 Ma interval of Mogollon-Datil ignimbrite volcanism is the longest, most complex, and least understood of the volcanic field's 4 eruptive episodes. Numerous ignimbrites, predominantly low-silica rhyolites, were erupted in this interval; data from 12 regional and 13 subregional to local units are listed in Table 1 and shown in Figures 6-16. Only one ignimbrite, the Kneeling Nun Tuff (Fig. 11, 34.9 Ma,  $>900 \text{ km}^3$ ), has been established as a

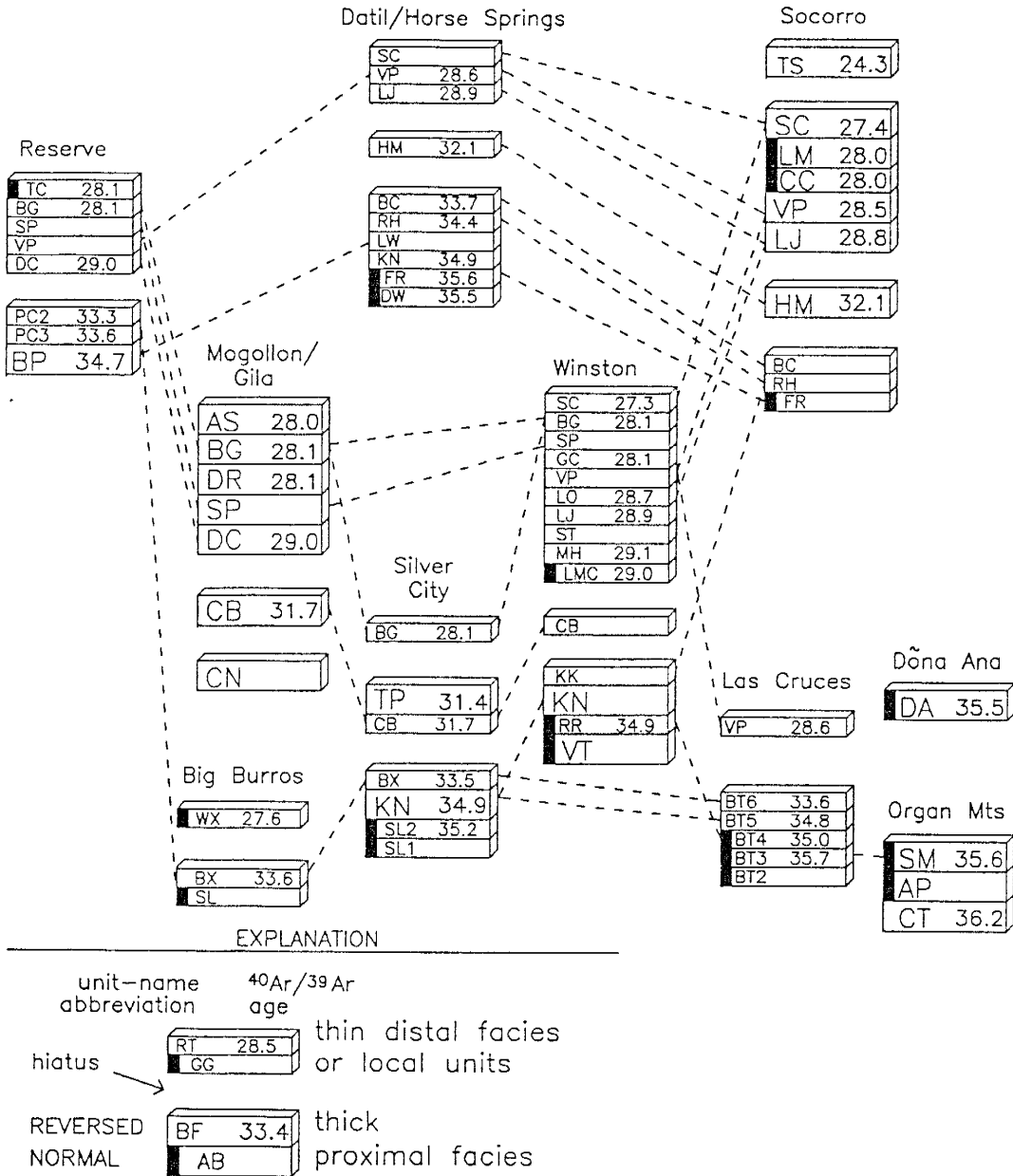


Fig. 6. Stratigraphic framework for Mogollon-Datil ignimbrites, showing generalized subregional stratigraphic columns in their approximate geographic positions. Each box depicts a locally named ignimbrite,  $^{40}\text{Ar}/^{39}\text{Ar}$  age, and paleomagnetic polarity (black bars = normal). Eruptive hiatuses are shown as gaps in columns and dashed lines are correlations based on  $^{40}\text{Ar}/^{39}\text{Ar}$  and paleomagnetic data.  $^{40}\text{Ar}/^{39}\text{Ar}$  ages refer to local data; some differ slightly from regional means (Figure 5, Table 1). Unit-name abbreviations are explained in Figure 5, plus: AP=Achenback Park, BT5 and BT6=Bell Top tuff members 5 and 6, CN=Cooney, KK=Koko Well, LW=Lebya Well, PC2 and PC3=Pueblo Creek 2 and 3, RR=Rocque Ramos, RH=Rockhouse Canyon, SL1 =lower Sugarlump, SP=Shelly Peak, ST=Stiver Canyon, VT=Victoria Tank.

large-volume unit. Several other units extend over large areas (1-10,000 km<sup>2</sup>) but are generally only 5 to 50 m thick. The unusually low aspect ratio (Walker et al., 1980) of these ignimbrites probably reflects some combination of subdued pre-eruptive topography and high energy or high mobility of the ash-flows.

In spite of the large number of Episode 4 ignimbrites, the Kneeling Nun Tuff is the only unit for which a source cauldron has been definitely identified (Emory cauldron, Elston et al., 1975). Cauldron features have also been documented in the Doña Ana and Organ Mountains (Seager and McCurry, 1988; Seager et al., 1976), but identification of correlative outflow sheets is still tentative, as discussed below. The paucity of source cauldrons for Episode 1 ignimbrites cauldrons is thought to primarily reflect concealment beneath extensional basins or overprinting by younger cauldrons. Alternatively, source cauldrons for these units may be very small features which have not yet been recognized in the course of geologic mapping.

Organ cauldron activity - 36.2 to 35.5 Ma: <sup>40</sup>Ar/<sup>39</sup>Ar data indicate that Mogollon-Datil ignimbrite activity initiated with 36.2 to 35.5 Ma cauldron-forming eruptions in the Organ and Doña Ana Mountains (Fig. 2). The presence of intracauldron-facies ignimbrites and cauldron structures in both areas have been documented by detailed mapping (Seager, 1981; Seager et al., 1976). The 9000-m-thick stratigraphic sequence within the Organ cauldron consists of three

distinct ignimbrites (Cueva, Achenback Park, and Squaw Mountain tuffs, in ascending order), and the entire sequence shows coherent normal geochemical zoning (Seager and McCurry, 1988). The Doña Ana intracauldron sequence includes a >800-m-thick multi-cooling-unit ignimbrite termed the Doña Ana Rhyolite Tuff (Seager et al., 1976). Based on published K-Ar data, the age of Organ and Doña Ana cauldron activity has been generally accepted to be about 33 Ma (Seager and McCurry, 1988).

$^{40}\text{Ar}/^{39}\text{Ar}$  plateau ages from single samples of the Cueva, Squaw Mountain, and Doña Ana tuffs are respectively 36.2, 35.8, and 35.5 Ma (Table 1), indicating that cauldron activity in this area is older than previously believed. The age difference between the Cueva and Squaw Mountain tuffs conforms with their stratigraphic order and the presence of a sedimentary interval above the Cueva Tuff (Seager and McCurry, 1988). The age difference between the Squaw Mountain and Doña Ana tuffs is not considered significant because only one sanidine sample has been dated per unit, and both showed slightly low radiogenic yields, apparently reflecting minor alteration along cleavages (McIntosh, dissertation, Chapter B).

Paleomagnetic data (Fig. 7) indicate reversed polarity for the Cueva Tuff and normal polarity for the Achenback, Squaw Mountain, and Doña Ana tuffs. Site-mean directions show considerable within-unit scatter (Fig. 7), but such scatter is typical for other thick (>500 m) intracauldron

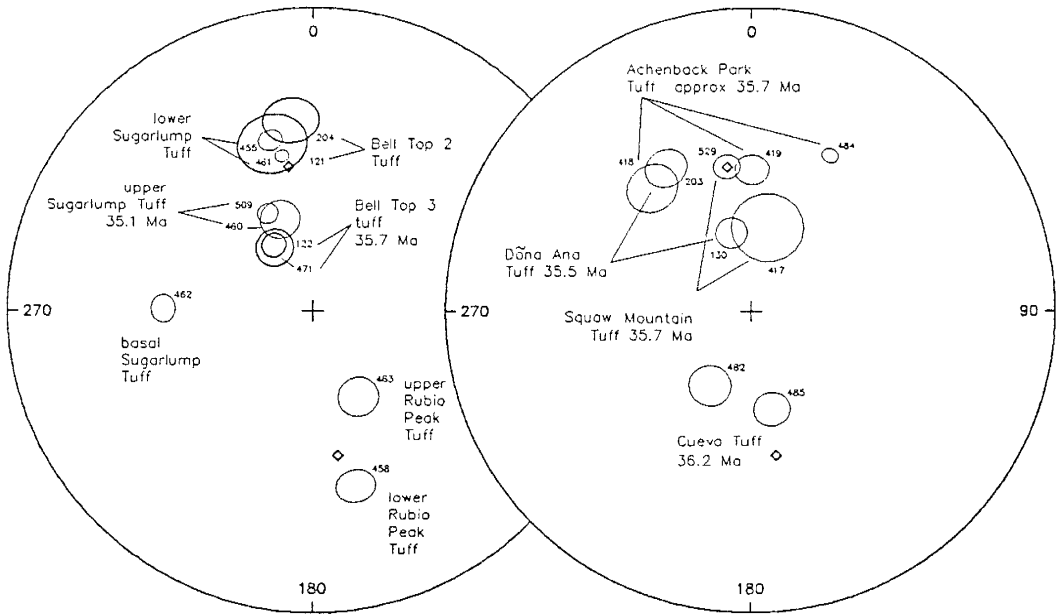
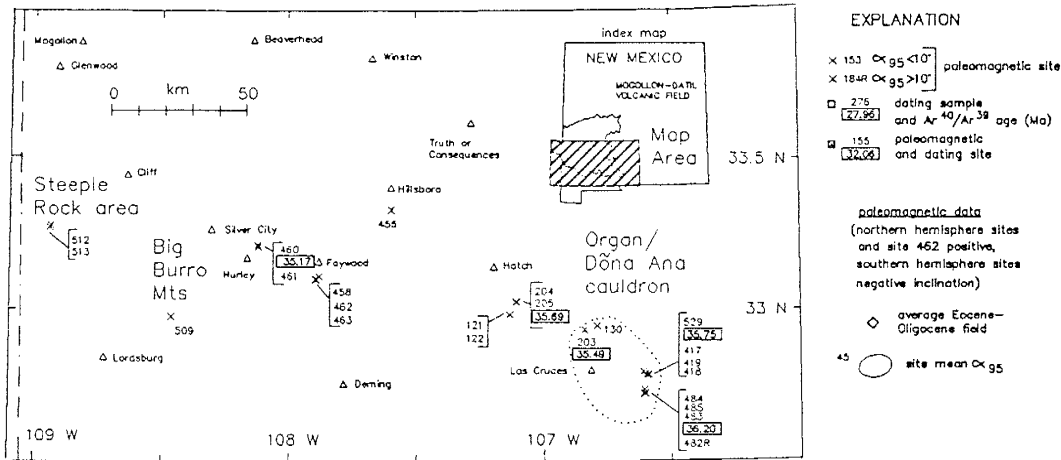


Fig. 7. Site location map,  $^{40}\text{Ar}/^{39}\text{Ar}$  plateau ages, and site-mean paleomagnetic data for 36.2–35.5 Ma Organ/Doña Ana intracauldron sequence and for 36–35 Ma outflow ignimbrites in the southern Mogollon-Datil volcanic field.

facies ignimbrites in the Mogollon-Datil volcanic field (McIntosh, dissertation, Chapter A) and elsewhere (e.g. Reynolds et al., 1987). Polarity/age data from these units agree well with the 35.6 to 35.0 Ma normal polarity interval shown by other Mogollon-Datil units, which is tentatively believed to correspond to normal polarity chron 16 of the marine magnetic anomaly time scale (Fig. 5; McIntosh, dissertation, Chapter D).

$^{40}\text{Ar}/^{39}\text{Ar}$  and paleomagnetic data indicate that the Organ and Doña Ana sequence are closely associated in time, and suggest that they are either portions of one (>35 km) large cauldron or parts of the same cauldron complex. Although the data are insufficient to definitely identify outflow facies for this cauldron/cauldron complex, tuffs 2 and 3 of the Bell Top Formation are attractive possibilities, as discussed in the following section.

Smaller volume ignimbrites - 35.7 to 35.0 Ma: The least understood stratigraphic interval within Episode 4 is the poorly exposed sequence of several small outflow-facies ignimbrites which predate the eruption of the 34.9 Ma Kneeling Nun Tuff. These units are generally thin (5-100 m), tend to be poorly welded, and are commonly intercalated with sedimentary sequences. The number of distinct ignimbrites in this interval is not accurately known, because of uncertainties in correlations.

In the southern part of the field (Fig. 7) the pre-Kneeling Nun interval is represented by tuffs 2,3, and 4 of

the Bell Top Formation (Clemons, 1976), by ignimbrite members of the Rubio Peak and Sugarlump Formations (Elston, 1957; Seager et al., 1982), and, probably, by the stratigraphically lowest ignimbrites in the Steeple Rock area. All these ignimbrites show normal polarity, except for the 2 locally exposed Rubio Peak tuffs and the lowest Steeple Rock unit (Table 1).  $^{40}\text{Ar}/^{39}\text{Ar}$  plateau ages from three of the normal polarity units range from 35.7 to 35.0 Ma (Table 1, Fig. 7).

The age and paleomagnetic polarity of these units indicate that they were erupted over the same time interval (chrons 16R and 16) as the Organ/Doña intracauldron sequence (Figs. 5,6; Table 1). Tuff 3 of the Bell Top Formation (Clemons, 1976) is the best candidate for a co-eruptive outflow sheet for the Achenback Park/Squaw Mountain sequence because of its similar age (35.7 Ma), normal magnetic polarity, and geographic proximity (Fig. 6). A second possibility is the underlying tuff 2 of the Bell Top Formation (Clemons, 1976), a locally exposed ignimbrite which also shows normal polarity, but has not yet been dated.

In addition to cauldron/outflow questions, there are also correlation problems among various outcrops of outflow sheets in the pre-Kneeling Nun interval. Two sites in the upper Sugarlump tuff (sites 460 and 509 in Fig. 7) yield steep site-mean directions that agree well with each other and with site-mean directions from Bell Top 3 tuff, but

$^{40}\text{Ar}/^{39}\text{Ar}$  ages from the two units differ by 0.4 Ma (Fig. 7). Likewise, the site-mean directions of two widely separated lower Sugarlump Tuff sites closely resemble RM direction from Bell Top 2 tuff (Fig. 7), but no  $^{40}\text{Ar}/^{39}\text{Ar}$  data are available.

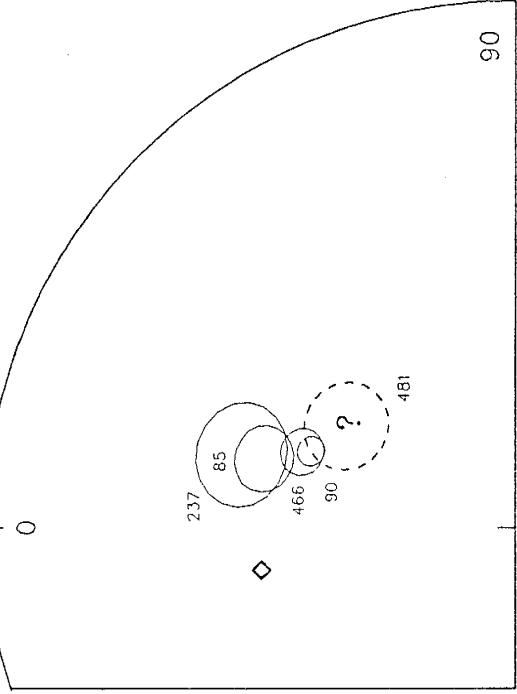
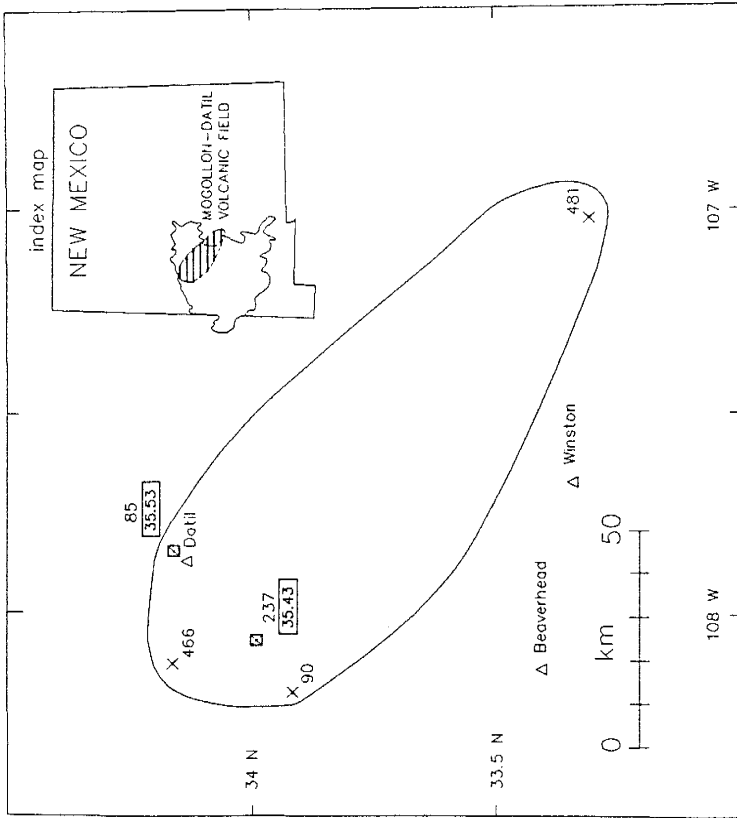
More confident correlations can be made for tuff 4 of the Bell Top Formation, the youngest pre-Kneeling Nun regional ignimbrite in the southern part of the field (Fig. 10; Clemons, 1976). The mapped extent of this unit is 68 km in the Goodsight-Cedar Hills area, and paleomagnetic and  $^{40}\text{Ar}/^{39}\text{Ar}$  data strongly support its correlation with a widespread pre-Kneeling Nun unit exposed in the Winston area (Fig. 6; tuff of Rocque Ramos Canyon of R. Harrison, pers. com., 1988) and the Salado Mountains (unnamed crystal tuff of Seager and Mayer, 1988). This correlation yields a total extent of at least 112 km for Bell Top 4 tuff (Table 1). The 35.0 Ma age and geographic proximity to the Emory cauldron suggest that Bell Top 4 tuff may be a precursor unit related to the 34.9 Ma Kneeling Nun Tuff. The 30 m thick tuff of Stone House Ranch (Fig. 10, Table 1), which is locally present between Bell Top 4 and Kneeling Nun in the Winston area, may be a similar precursor.

At least 2 regional pre-Kneeling Nun ignimbrites are also present in the northern part of the volcanic field. Datil Well Tuff (35.5 Ma), a well-exposed unit in the Datil area (Fig. 8), shows a distinctive northwesterly RM direction which supports correlation with a lithologically



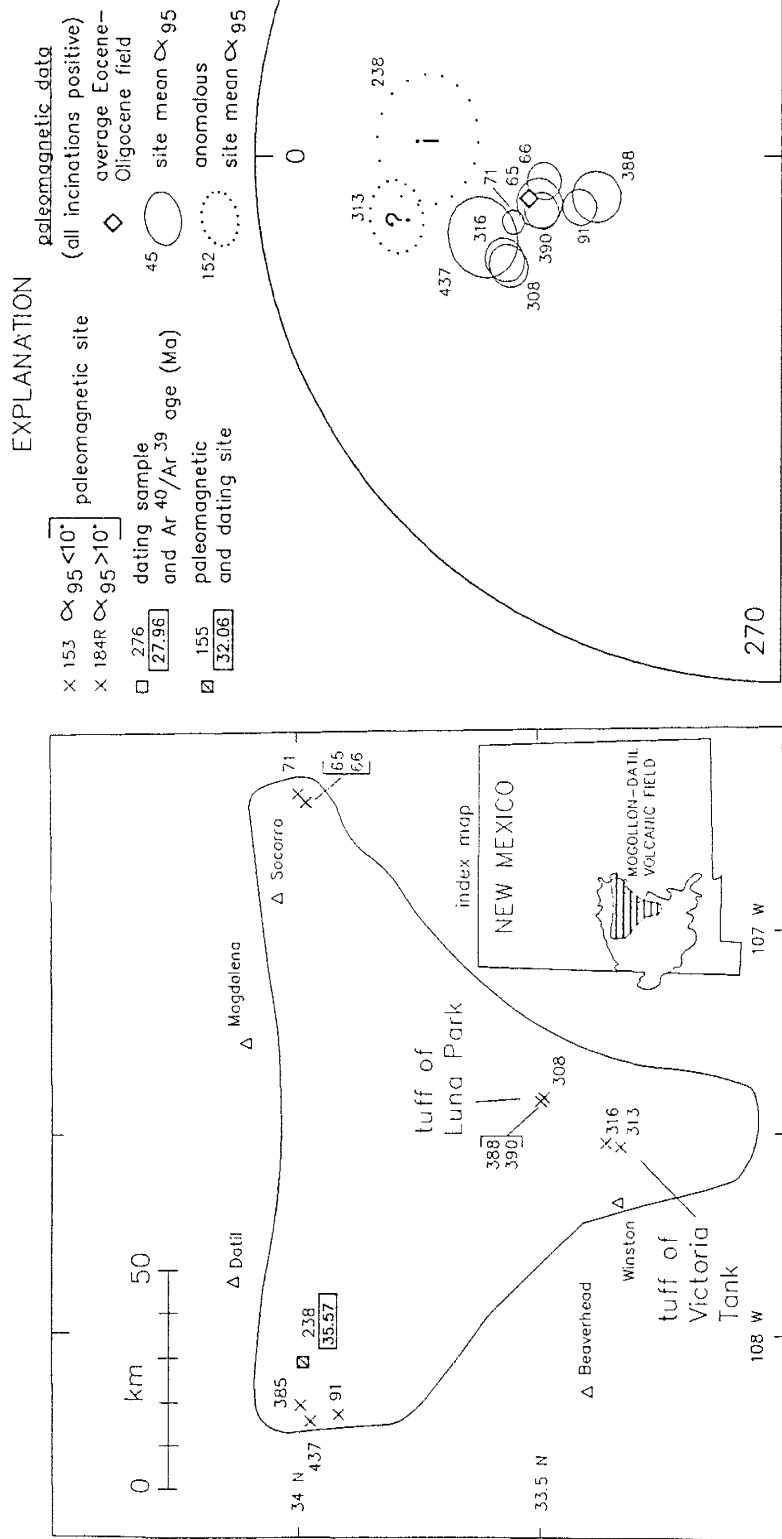
EXPLANATION

- X 153  $\times$  95 <10°
- X 184R  $\times$  95 >10°
- 276  $\square$  27.96
- 155  $\square$  32.06
- ◇ paleomagnetic site
- 45 site mean  $\times$  95
- 152 non-correlative unit?
- dating sample and Ar/<sup>40</sup>Ar/<sup>39</sup>Ar age (Ma)
- paleomagnetic and dating site
- paleomagnetic data (all inclinations positive)
- average Eocene-Oligocene field



Datil Well Tuff 35.5 Ma

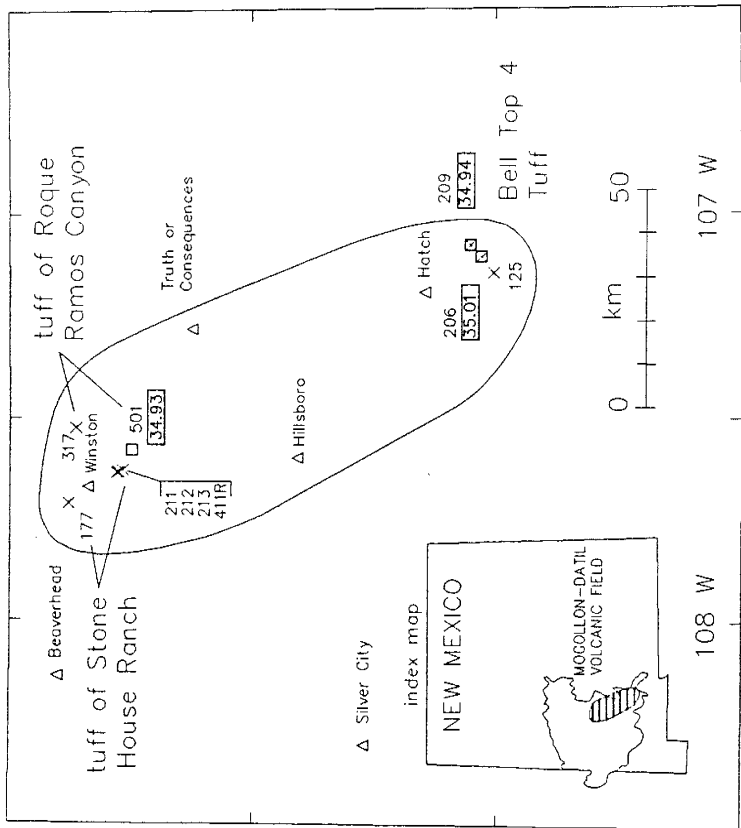
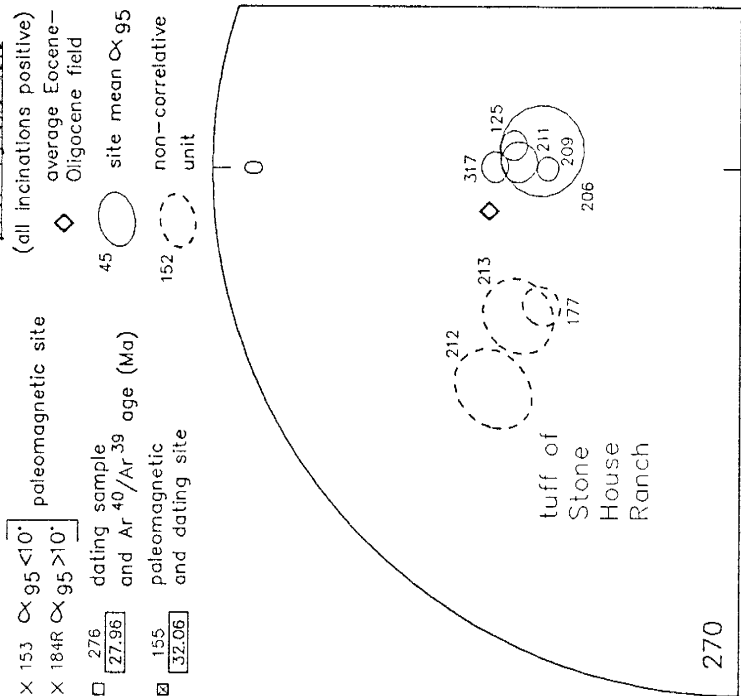
Fig. 8. Datil Well Tuff: site locations, extent, <sup>40</sup>Ar/<sup>39</sup>Ar plateau ages, and site-mean paleomagnetic data. Correlation between Datil Well Tuff and unit at site 481 is tentative.



tuff of Farr Ranch 35.6 Ma

Fig. 9. Tuff of Farr Ranch: site locations, extent, <sup>40</sup>Ar/<sup>39</sup>Ar plateau ages, and site-mean paleomagnetic data. Correlations with tuff of Luna Park and tuff of Victoria Tank are based mainly on paleomagnetic data and are considered tentative. In this and following figures, dotted ellipses indicate site-mean directions which differ by more than 15° from the unit-mean direction; possible reasons for these anomalous directions are suggested by letters within the ellipses: p=basal site in area of pre-eruptive topographic relief, f=local structural complexity, c=unremoved CRM, i=unremoved IRM, ?=possible incorrect unit identification. Capital letters indicate anomalous sites in highly extended areas: T=Turututu Butte, L=Lemitar Mountains, J=Joyita Hills, S=San Mateo Mountains.

EXPLANATION

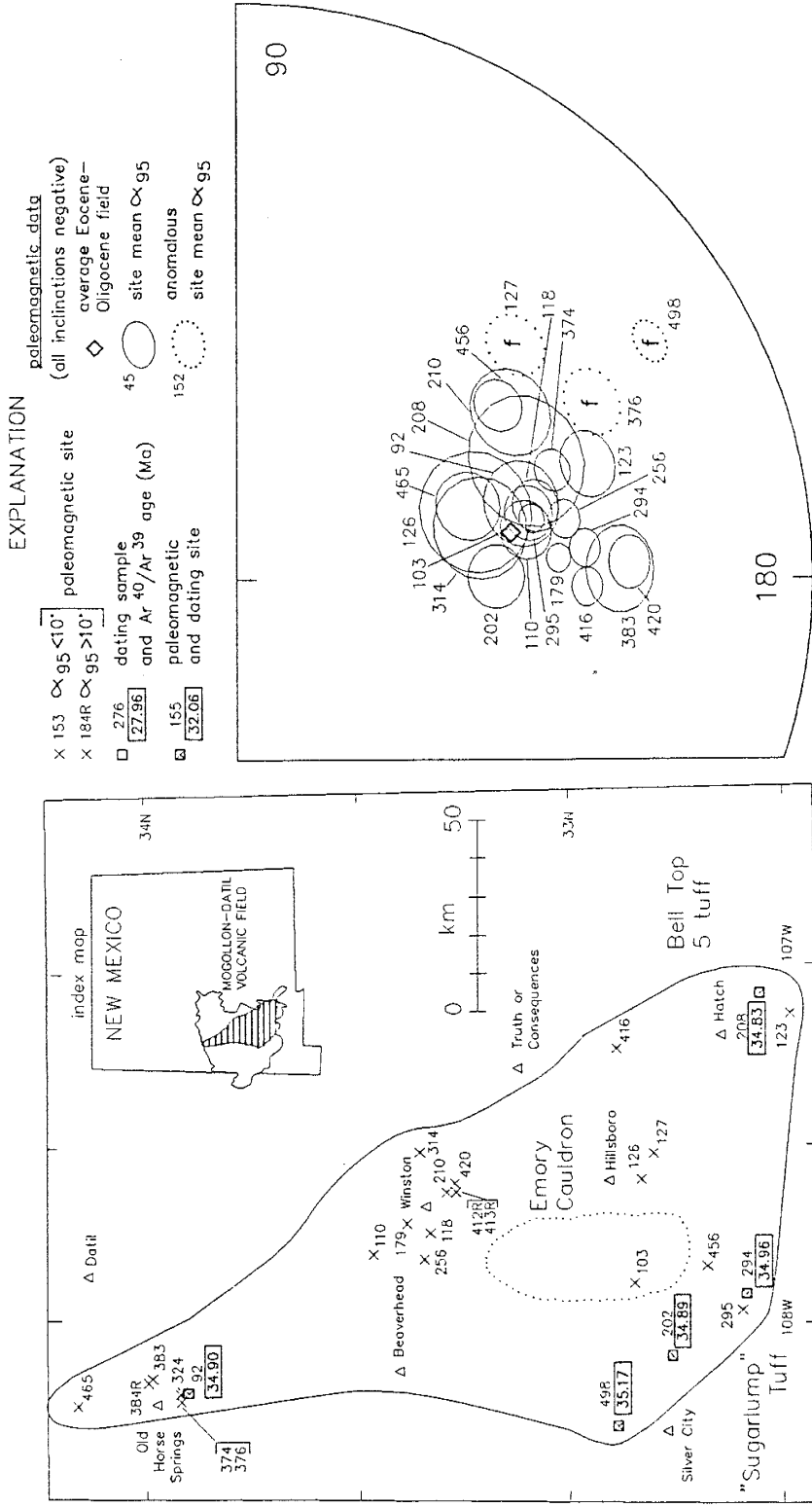


Bell Top 4 tuff

Fig. 10. Bell Top 4 Tuff: site locations, extent, <sup>40</sup>Ar/<sup>39</sup>Ar plateau ages, and site-mean paleomagnetic data. Correlation with tuff of Rocque Ramos Canyon is well-supported by distinctive site-mean paleomagnetic directions and <sup>40</sup>Ar/<sup>39</sup>Ar ages. Paleomagnetic data indicate that these two units do not correlate with the tuff of Stone House Ranch.

similar unit in an isolated outcrop 125 km to the southeast (site 481, Fig. 8). Paleomagnetic data also suggest a regional extent for the tuff of Farr Ranch (Fig. 9). This unit is lithologically identical to the locally underlying Datil Well Tuff and their  $^{40}\text{Ar}/^{39}\text{Ar}$  ages (respectively 35.6 and 35.5 Ma) are statistically indistinguishable. Site-mean RM directions, however, are quite different (Figs. 8,9) and indicate that some outcrops formerly mapped as Datil Well (Osburn and Chapin, 1983a) are actually Farr Ranch. Paleomagnetic data (Fig. 9) are furthermore consistent with correlation of Farr Ranch with tuff of Luna Park and Victoria Tank, two poorly known informal units exposed 40 to 100 km to the south (Hermann, 1988; Harrison, 1988, pers. com.). Source cauldrons are not known for Datil Well or Farr Ranch outflows sheets, but their distributions suggest vents somewhere in the northern part of the field.

Kneeling Nun Tuff - 34.9 Ma: The Kneeling Nun Tuff is the largest and best-studied unit in Episode 4. Its 34.9 Ma mean  $^{40}\text{Ar}/^{39}\text{Ar}$  age and reversed magnetic polarity suggest that was erupted shortly after the normal-to-reversed polarity transition between chrons 16 and 15R (Fig. 5).  $^{40}\text{Ar}/^{39}\text{Ar}$  and paleomagnetic data (Fig. 11) indicate that the outflow sheet extends well beyond its previously mapped extent (Elston et al., 1975). These data (Fig. 11) suggest that the Kneeling Nun outflow sheet correlates with Bell Top 5 tuff (Clemons, 1976), with part of the mapped Sugarlump Tuff near Faywood (Elston, 1957, Seager et al., 1982), and with a thin,



Kneeling Nun Tuff 34.9 Ma

Fig. 11. Kneeling Nun Tuff: site locations, extent,  $^{40}\text{Ar}/^{39}\text{Ar}$  plateau ages, and site-mean paleomagnetic data. These data indicate that the outflow sheet is more extensive than previously believed, and includes Bell Top tuff member 5 (Clemons, 1976). Letters classifying anomalous sites are explained in Figure 9.

unwelded unit overlying tuff of Farr Ranch in the Horse Springs area (Ratté and McIntosh, 1989). These correlations suggest that the volume of the Kneeling Nun Tuff may be considerably larger than the  $900 \text{ km}^3$  suggested by Elston et al. (1975).

The Kneeling Nun Tuff is the first of 4 large-volume, crystal-rich, low-silica rhyolites in the older portion of the Mogollon-Datil sequence. It is difficult or impossible to lithologically distinguish the Kneeling Nun Tuff (34.9 Ma) from Box Canyon Tuff (33.5 Ma), Hells Mesa Tuff (32.1 Ma), or Caballo Blanco Tuff (31.7 Ma). Furthermore, paleomagnetism is only marginally helpful for distinguishing among these 4 ignimbrites, because they all show unit-mean directions similar to the time-averaged Eocene-Oligocene field (Fig. 12). Fortunately, the age differences among these 4 units are all sufficiently large to be easily resolved by  $^{40}\text{Ar}/^{39}\text{Ar}$  dating (Table 1).

Smaller volume ignimbrites - 34.9 to 33.7 Ma: During the 1.3 m.y. interval following eruption of the Kneeling Nun Tuff, the southern portion of the Mogollon-Datil volcanic field was relatively quiescent. Mimbres Peak rhyolite domes and associated local ignimbrites were erupted in the southern Black Range, at least in part as moat-fill of the Emory cauldron (Elston et al., 1975). These units (Table 1) indicate a period of normal polarity near 34.6 Ma, interpreted as chron 15 (Fig. 5). The only other ignimbrite erupted in the southern part of the field during this

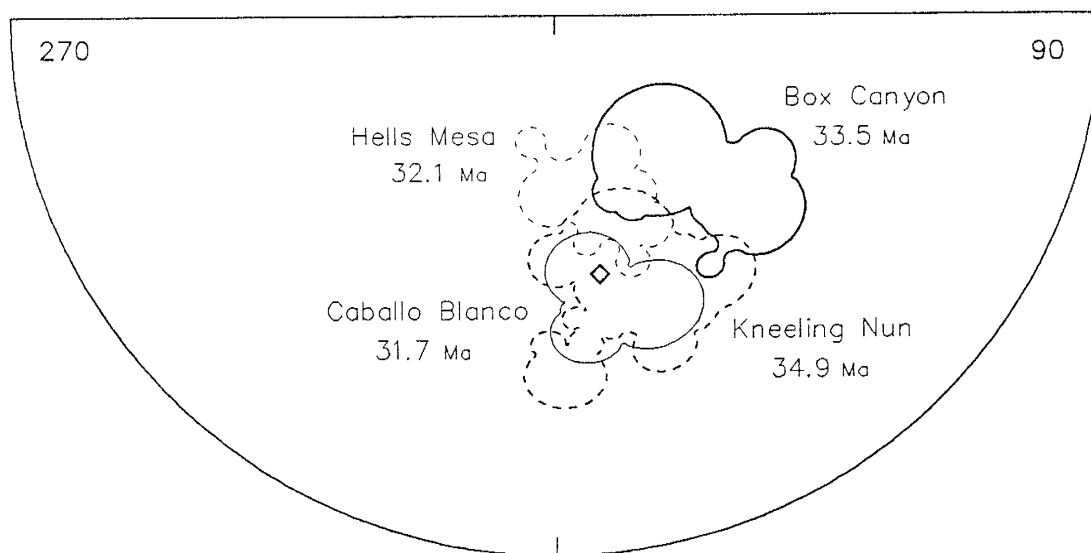


Figure 12. Considerable overlap is shown by site-mean data from 4 older (34.9-31.7 Ma), lithologically similar, crystal-rich, low-silica rhyolitic Mogollon-Datil ignimbrites. Irregular outlines enclose site-mean ellipses for each unit and diamonds denote time-averaged Eocene-Oligocene normal and reversed field directions.  $^{40}\text{Ar}/^{39}\text{Ar}$  data are more effective than paleomagnetism for distinguishing among these units.

quiescent period is a 34.0 Ma crystal-rich, low-silica unit locally exposed at Table Mountain, south of Faywood, N.M. (Table 1; herein termed tuff of Table Mountain, but mapped as a member of the Sugarlump Tuff by Elston, 1957, and Seager et al., 1982).

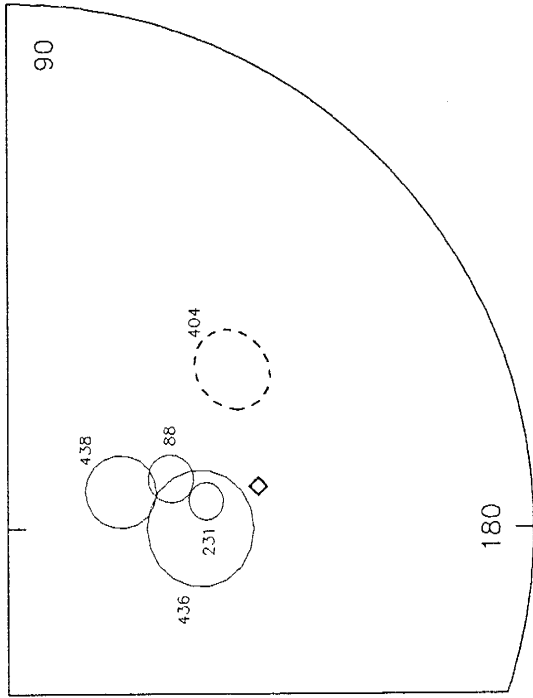
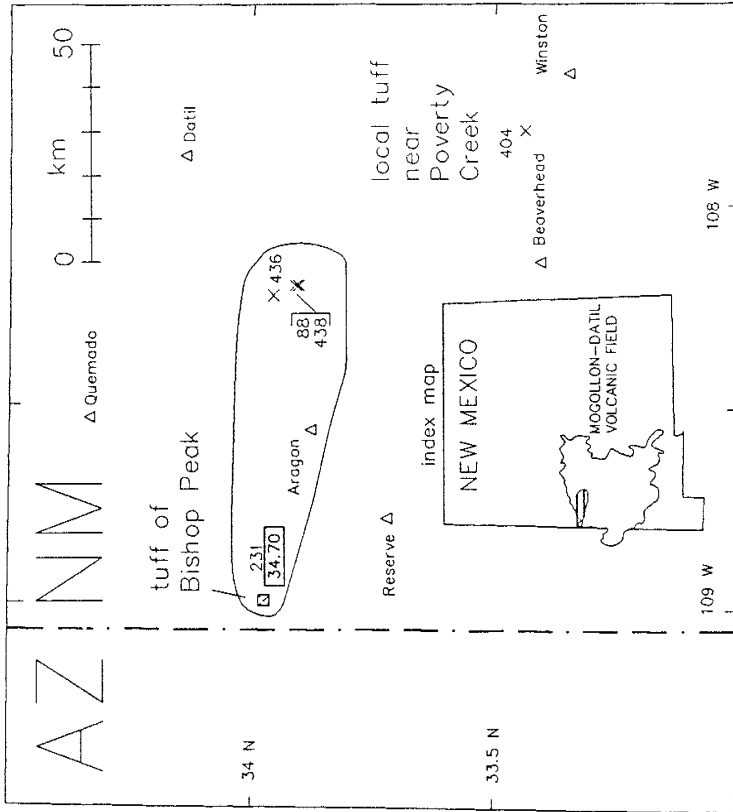
During this interval of quiescence in the southern part of the field, eruptions in the north produced three regional ignimbrites: tuff of Lebya Well (34.7 Ma), Rockhouse Canyon Tuff (34.4 Ma), and Blue Canyon Tuff (33.7 Ma). The tuff of Lebya Well (Fig. 13) was first recognized in the Horse Springs area by its stratigraphic position between 34.9 Ma Kneeling Nun and 34.4 Ma Rockhouse Canyon Tuff (Fig. 6). Although this unit has not been dated in the Horse Springs area, its stratigraphic position and distinctively steep RM direction suggests correlation with the 34.7 Ma Bishop Peak Tuff exposed 75 km to the west (Fig. 13). Paleomagnetic and  $^{40}\text{Ar}/^{39}\text{Ar}$  data generally confirm the mapped extents of the Rockhouse Canyon and Blue Canyon tuffs and also suggest correlations with isolated outcrops further south (Figs. 14, 16). Like Datil Well and Farr Ranch, source cauldrons are unknown for the Lebya Well, Rockhouse Canyon, and Blue Canyon outflow sheets, although their distributions indicate vents in the northern part of the field.

The Cooney Tuff, a complex unit embracing several thin ignimbrites separated by sedimentary sequences, may also have been erupted in the 34.9 to 33.7 Ma interval. Published K-Ar data from this unit, exposed near the western



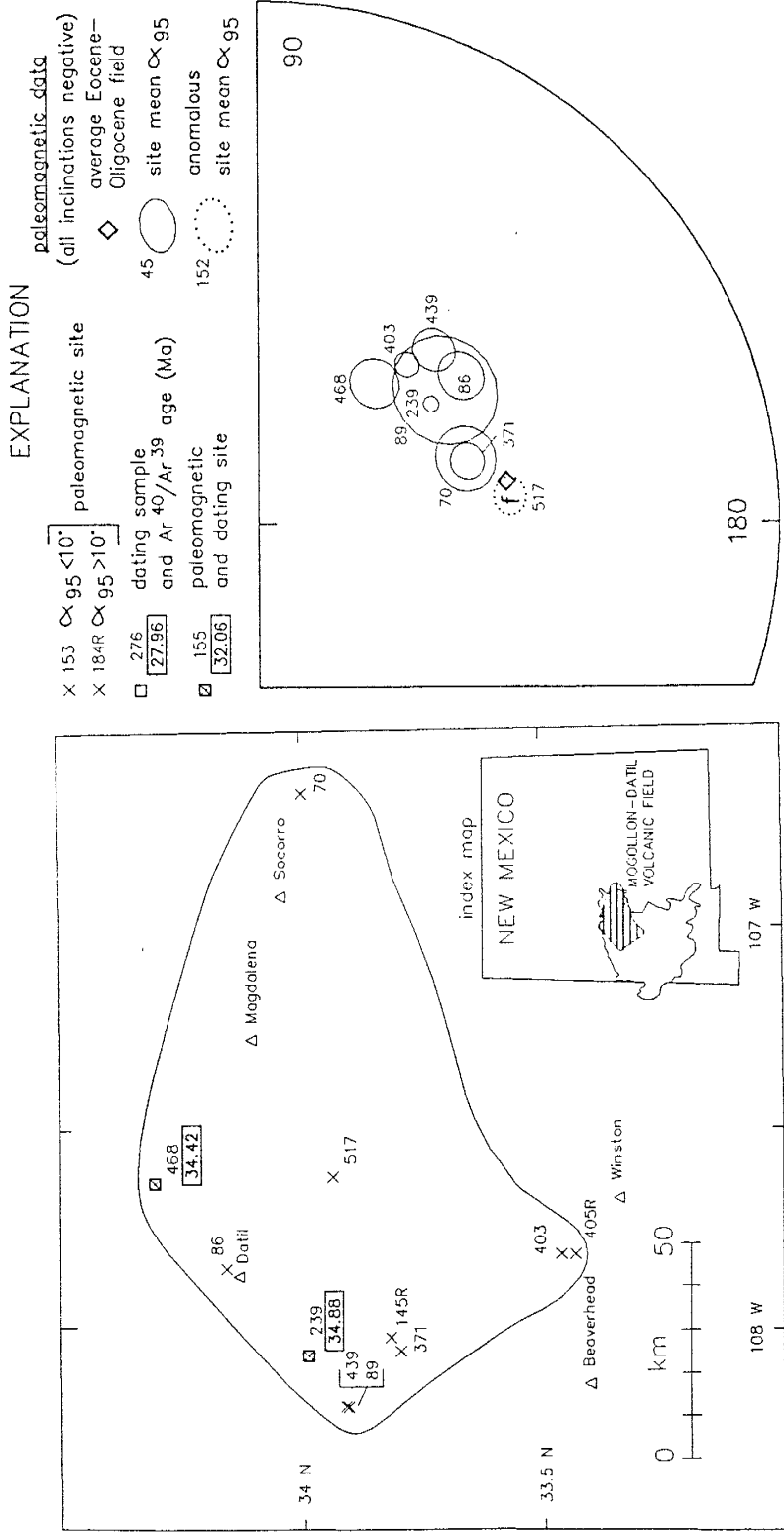
EXPLANATION

- X 153  $\alpha_{95} < 10^\circ$  paleomagnetic data (all inclinations negative)
- X 184R  $\alpha_{95} > 10^\circ$  average Eocene-Oligocene field
- 276 [27.96] dating sample and Ar<sup>40</sup>/Ar<sup>39</sup> age (Ma)
- ▣ 155 [32.06] paleomagnetic and dating site
- ◇ paleomagnetic site
- 45 site mean  $\alpha_{95}$
- 152 non-correlative unit



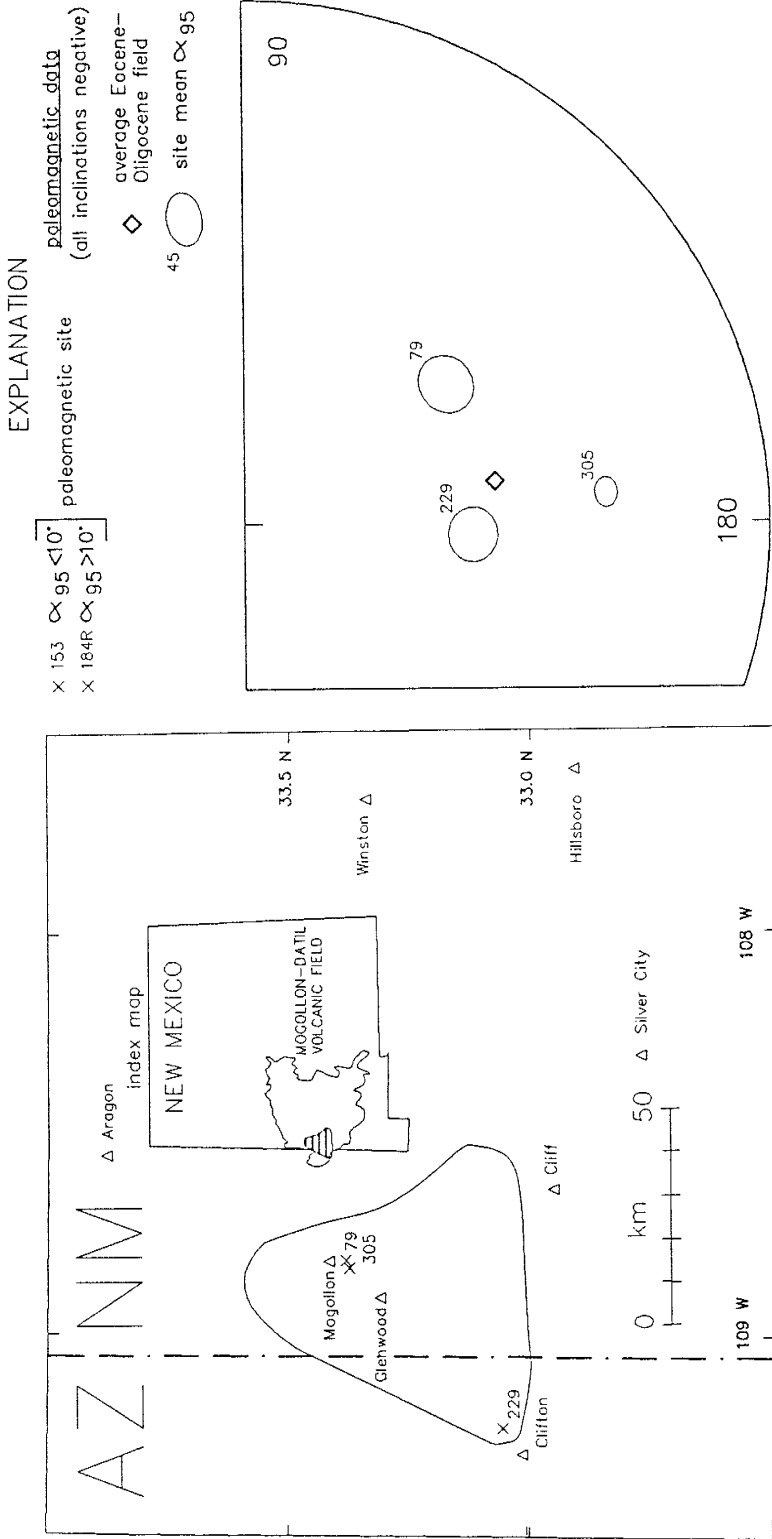
tuff of Lebya Well 34.7 Ma

Fig. 13. Tuff of Lebya Well: site locations, extent, <sup>40</sup>Ar/<sup>39</sup>Ar plateau ages, and site-mean paleomagnetic data. Steep site-mean RM direction support correlation with 34.70 Ma tuff of Bishop Peak, but oppose correlation with a Winston-area ignimbrite in the same stratigraphic position (site 404).



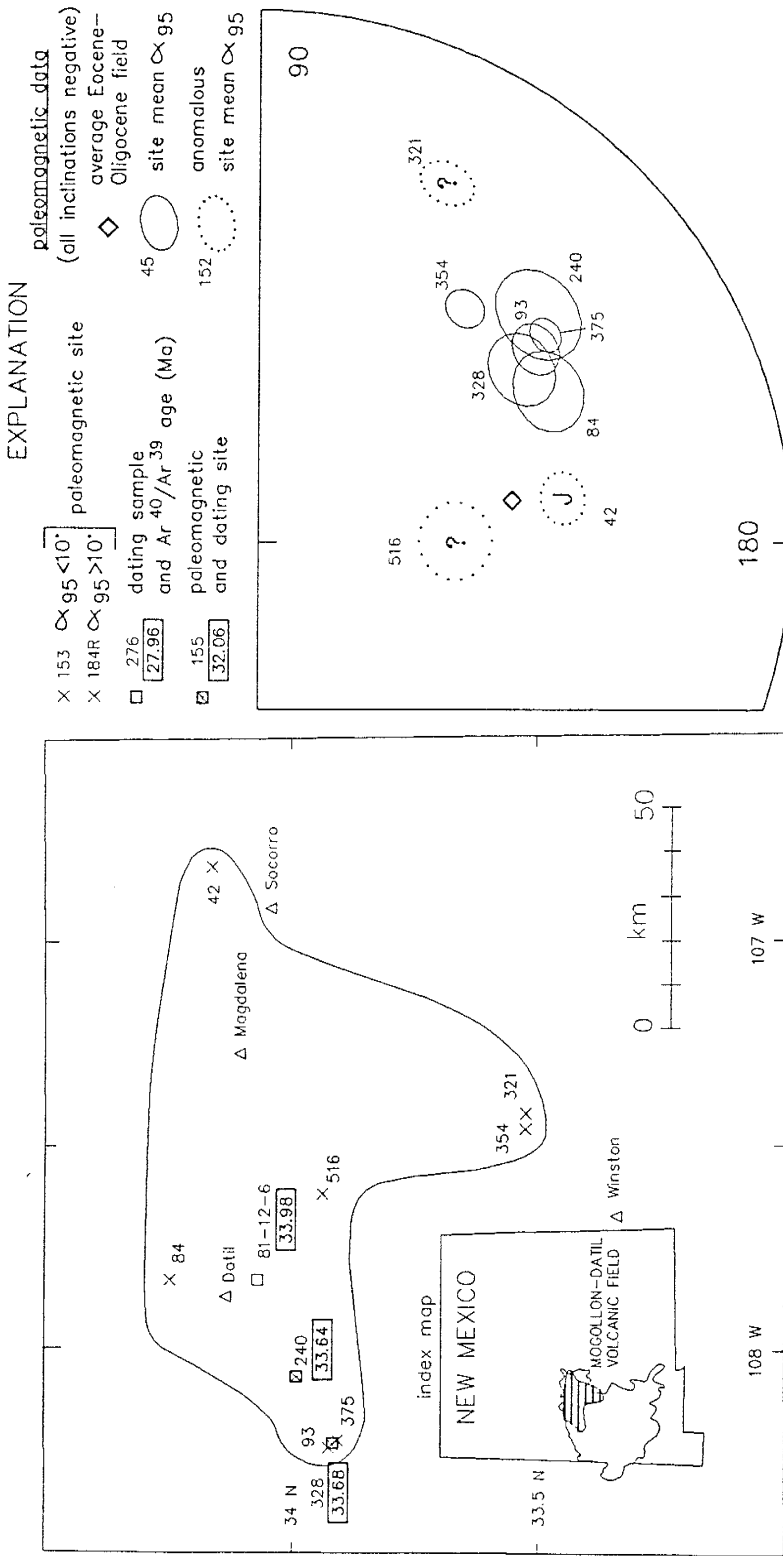
## Rockhouse Canyon Tuff 34.4 Ma

Fig. 14. Rockhouse Canyon Tuff: site locations, extent,  $^{40}\text{Ar}/^{39}\text{Ar}$  plateau ages, and site-mean paleomagnetic data. Letters classifying anomalous sites are explained in Figure 9.



Cooney Tuff (approx 34 Ma)

Fig. 15. Cooney Tuff: site locations and site-mean paleomagnetic data. Poorly grouped site-mean directions suggest that eruption of this multi-cooling-unit formation spanned a relatively long time period. No  $^{40}\text{Ar}/^{39}\text{Ar}$  ages have been obtained from the Cooney Tuff.

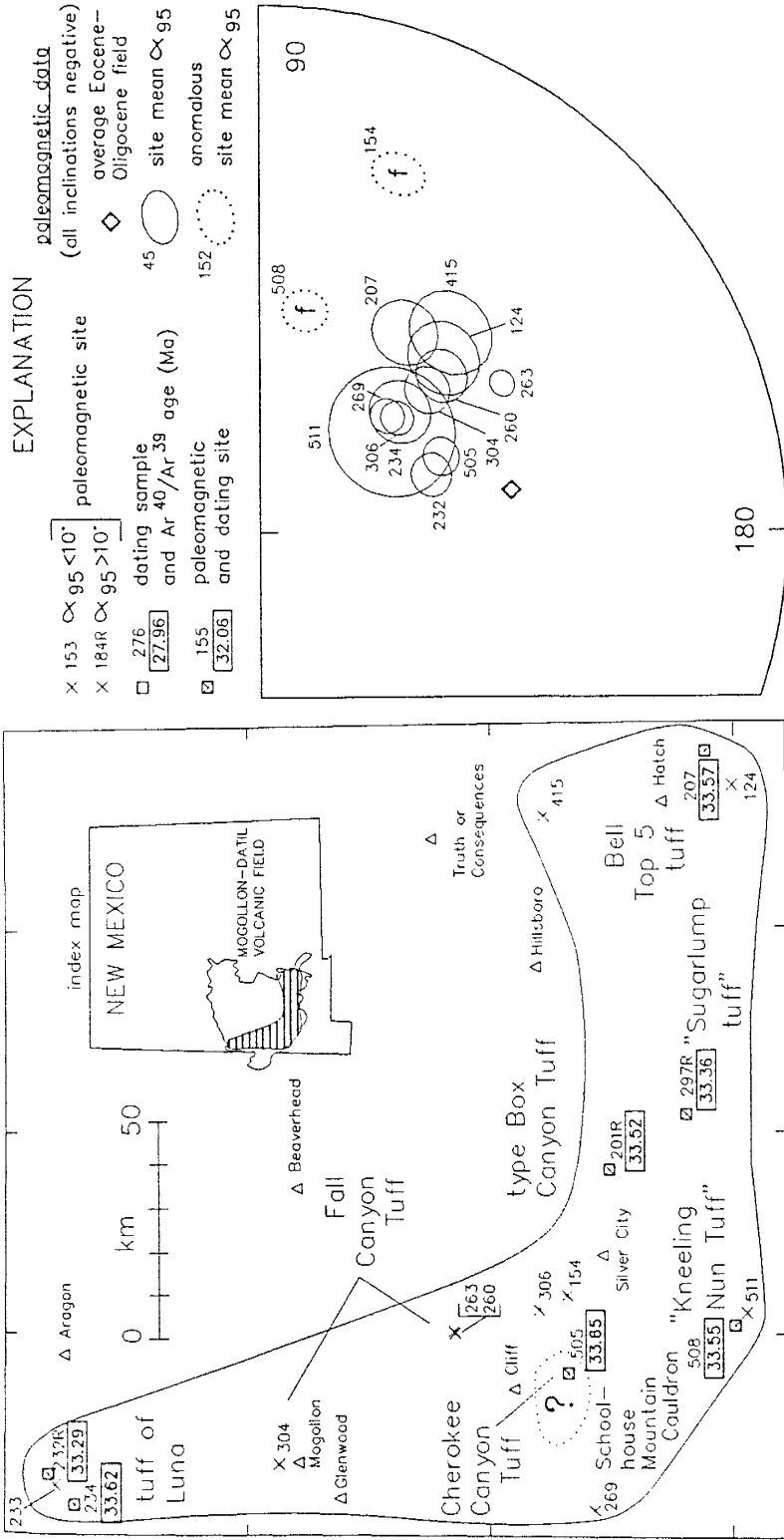


## Blue Canyon Tuff 33.7 Ma

Fig. 16. Blue Canyon Tuff: site locations, extent, <sup>40</sup>Ar/<sup>39</sup>Ar plateau ages, and site-mean paleomagnetic data. Letters classifying anomalous sites are explained in Figure 9.

edge of the field, suggest an age near 34 Ma, but samples bearing fresh sanidine suitable for  $^{40}\text{Ar}/^{39}\text{Ar}$  dating have not been found. Dispersed site-mean RM directions are shown by 3 sites in different members of the Cooney tuff and from a possibly correlative (Ratté et al., 1984) unit near Clifton, Az. (Fig. 15). These data suggest that eruption of the Cooney Tuff members may have spanned at least several centuries, and gives little hope for accurate long-range paleomagnetic correlation of this unit.

"Box Canyon" Tuff - 33.5 Ma: Box Canyon Tuff, the final ignimbrite erupted in Episode 1, has not been previously identified as a regional unit. This crystal-rich, low-silica unit was first recognized by Elston (1957) from its stratigraphic position between Kneeling Nun and Caballo Blanco tuffs.  $^{40}\text{Ar}/^{39}\text{Ar}$  plateau ages near 33.5 Ma, together with somewhat distinctively steep RM directions (Fig. 12), indicate that Box Canyon Tuff extends over much of the southern and western edges of the volcanic field (Fig. 17). Units now correlated with Box Canyon Tuff (Fig. 6) include Bell Top 6 tuff (Clemons, 1976), portions of mapped Sugarlump Tuff (Elston, 1957), mapped Kneeling Nun Tuff of Hedlund (1978), Cherokee Canyon Tuff (Finnell, 1988), portions of Fall Canyon Tuff (Ratté et al., 1984), and tuff of Luna (Finnell, 1988, pers. com.). No source has been determined for Box Canyon Tuff, although the vast extent suggests a large cauldron. One possibility is the poorly known Schoolhouse Mountain cauldron (Fig. 17), also



Box Canyon Tuff 33.5 Ma

Fig. 17. Box Canyon Tuff: site locations, extent,  $^{40}\text{Ar}/^{39}\text{Ar}$  plateau ages, and site-mean paleomagnetic data. These data indicate a much larger large regional extent for this unit than was previously known (e.g. Elston, 1957). Letters classifying anomalous sites are explained in Figure 9.

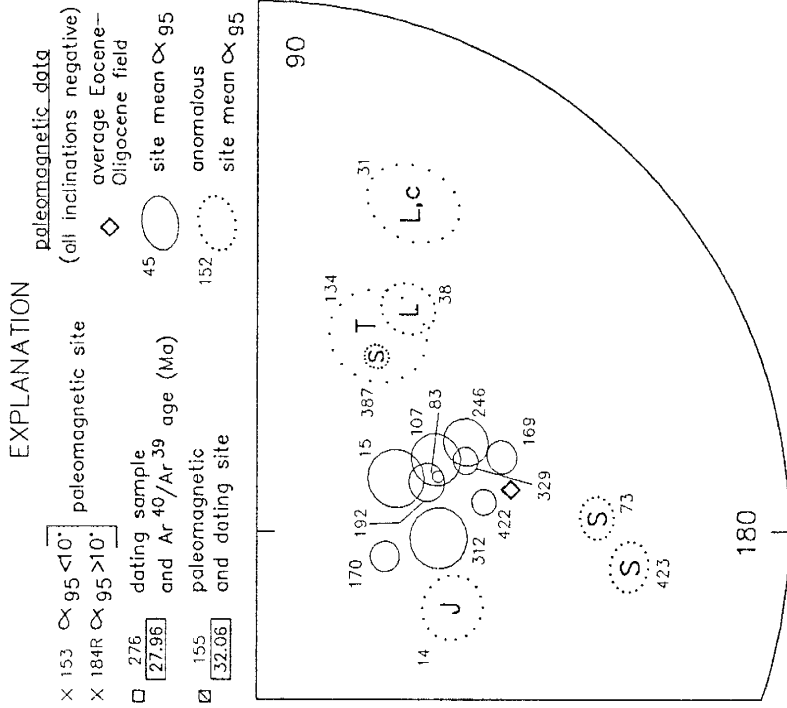
considered a possible source of the 31.7 Ma Caballo Blanco Tuff. Alternatively, Box Canyon Tuff may have been erupted from a cauldron south of the southern margin of the Mogollon-Datil volcanic field, as defined in this report.

#### **Episode 2 - 32.1 to 31.4 Ma**

The second brief but intense episode of Mogollon-Datil ignimbrite activity commenced at 32.1 Ma, 1.5 m.y. after the eruption of Box Canyon Tuff. Episode 2 spanned only 0.7 m.y. but produced 2 major regional units, Hells Mesa and Caballo Blanco tuffs, and a third thick but more localized unit, the Tadpole Ridge Tuff. All three of these units show reversed magnetic polarity; episode 2 apparently occurred within a single polarity interval, probably chron 12R (Fig. 5).

Hells Mesa Tuff - 32.1 Ma: The first Episode 2 ignimbrite, the 1250 km<sup>3</sup> Hells Mesa Tuff, erupted at 32.1 Ma from the Socorro cauldron (Fig. 18). The Hells Mesa Tuff is the oldest of five large-volume ignimbrites exposed in the Socorro area, and the extent of its cauldron and outflow sheet have been well established by a series of NMIMT thesis maps (referenced in Osburn and Chapin, 1983a). The outflow sheet shows a highly asymmetric distribution about the cauldron, extending almost 100 km to the west, but absent to the south and east. Four <sup>40</sup>Ar/<sup>39</sup>Ar ages from the northern part of the outflow sheet yield a mean of 32.06 ±.13 Ma.

Paleomagnetic data from the Hells Mesa Tuff generally support the mapped extent of the outflow sheet and



## Hells Mesa Tuff 32.1 Ma

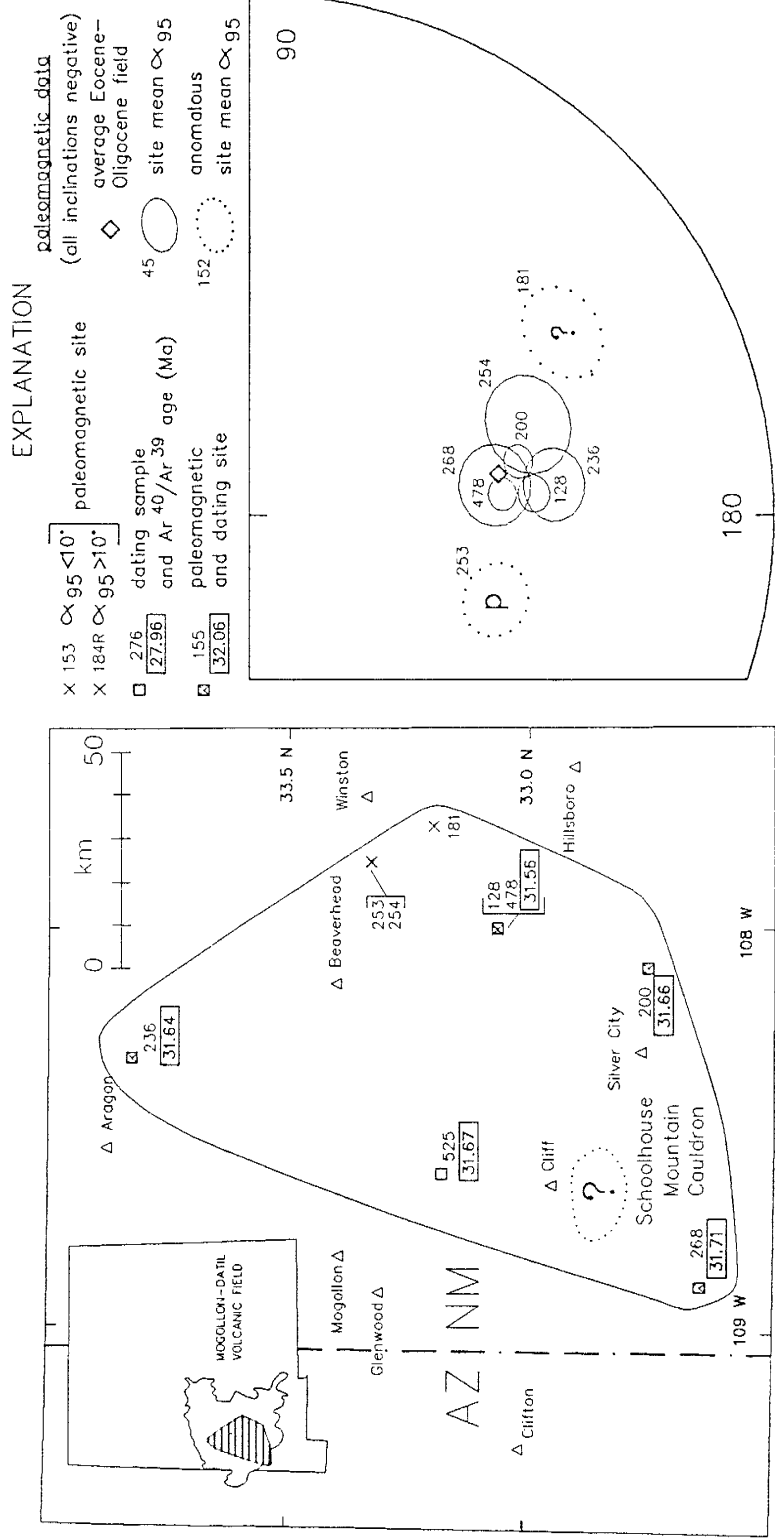
Fig. 18. Hells Mesa Tuff: site locations, extent, <sup>40</sup>Ar/<sup>39</sup>Ar plateau ages, and site-mean paleomagnetic data. The large fraction of anomalous sites reflects sampling in tectonically extended and faulted areas. Letters classifying anomalous sites are explained in Figure 9. The Socorro cauldron is well-established as the source of Hells Mesa Tuff (Osburn and Chapin, 1983a).



intracauldron facies. Mean directions from 10 of 17 sites are tightly clustered, but the remaining 7 sites are anomalous, plotting 15-42° from the unit mean (Fig. 18). Net rotations related to extreme tectonic extension in the Lemitar Mountains, Joyita Hills, and Turututu Butte are probably responsible for the anomalous declinations at sites 14, 134, 38, and 31, and the latter two sites also show alteration-related chemical remanent magnetizations (CRMs; McIntosh, dissertation, Chapter A). Site 423 and 73 are from a badly disrupted zone adjacent to a major fault, and non-paleohorizontal pumice foliations at the base of the Hells Mesa may explain the anomalous declination of site 387.

The unit-mean direction (D=166, I=-60) of the Hells Mesa Tuff is not a strong correlation criterion, because it is non-distinctive (only 11° from the time-averaged Eocene-Oligocene field direction) and similar to the lithologically indistinguishable Caballo Blanco, Box Canyon, and Kneeling Nun tuffs (Fig. 12). Tentatively though, paleomagnetic data from sites 312 and 329, together with stratigraphic sequence data, suggests that crystal-rich tuffs exposed in the southern San Mateo Mountains and the area north of Horse Springs represent distal Hells Mesa Tuff (Fig. 18).

Caballo Blanco Tuff - 31.7 Ma: The second Episode 2 ignimbrite, the Caballo Blanco Tuff, was erupted at 31.7 Ma and extends over some 10,000 km<sup>2</sup> of the southeastern Mogollon-Datil volcanic field. Although this unit was early



Caballo Blanco Tuff 31.7 MA

Fig. 19. Caballo Blanco Tuff: site locations, extent, <sup>40</sup>Ar/<sup>39</sup>Ar plateau ages, and site-mean paleomagnetic data. Letters classifying anomalous sites are explained in Figure 9.

recognized as a crystal-rich, low-silica ignimbrite overlying the Kneeling Nun in the southern Black Range (Elston, 1957; Elston et al., 1973), accurate assessment of its extent was prevented by inability to distinguish it from Kneeling Nun and Box Canyon tuffs.  $^{40}\text{Ar}/^{39}\text{Ar}$  data now allow reliable identification of the Caballo Blanco outflow sheet. Five dated samples, ranging from 31.56 to 31.71 Ma and averaging  $31.65 \pm 0.06$  Ma, suggest that the unit extends 70 km west and 100 km north of its mapped extent in the Black Range and Santa Rita areas (Fig. 19). The Caballo Blanco Tuff correlates with at least part of the mapped Fall Canyon Tuff of Ratté et al. (1984), including the type section (site 525 in Fig. 19). Although the unit-mean RM direction of Caballo Blanco Tuff is not particularly distinctive (Fig. 12), paleomagnetic data are consistent with a wide distribution for the unit. Site mean directions are tightly grouped except for 2 anomalous sites which reflect unremoved CRM or poor attitude control (respectively sites 253 and 181, Fig. 19).

Although no source cauldron has been established for this unit, three possibilities are under consideration. These are: the southern end of the Emory cauldron (as suggested in Abbitz, 1988), the Schoolhouse Mountain cauldron of Wahl (1981), and a now obliterated precursor to the Bursum cauldron (suggested by abundant large lithics at site 525).

Tadpole Ridge Tuff - 31.4 Ma: The third and last ignimbrite erupted during Episode 2 is the 31.4 Ma Tadpole Ridge Tuff, a thick, geographically restricted (40 km extent) unit exposed north of Pinos Altos, N.M. (Fig. 20). This mineralogically distinctive ignimbrite (low-silica rhyolite, 10-25% plagioclase and biotite phenocrysts) was mapped as a local unit by Finnell (1976), who recognized distinct upper and lower members. Our observations of abrupt thickness changes, coarse lithic breccias, and a high-angle basal unconformity suggest that much or all of the mapped Tadpole Ridge Tuff is lying within a small cauldron (herein termed the Twin Sisters cauldron) with an east-west margin located immediately north of Pinos Altos (Fig. 20). The northern margin of the proposed Twin Sisters cauldron (guessed at in Fig. 20) is buried by younger units.

Paleomagnetic data suggest a time break of at least centuries between eruption of the upper and lower members of the Tadpole Ridge Tuff, although neither paleosols nor significant sedimentary deposits are found along their mutual contact. The lower and upper intracauldron facies members respectively show unusually steep and unusually shallow unit-mean RM directions (Fig. 20). These directions are 49° apart, indicating that some 2000 yrs may have elapsed between eruption of the two units, given a typical average secular variation rate of 4.5° per century (Holcomb et al., 1985). Alternatively, these RM direction may have resulted from two closely spaced eruptions which occurred

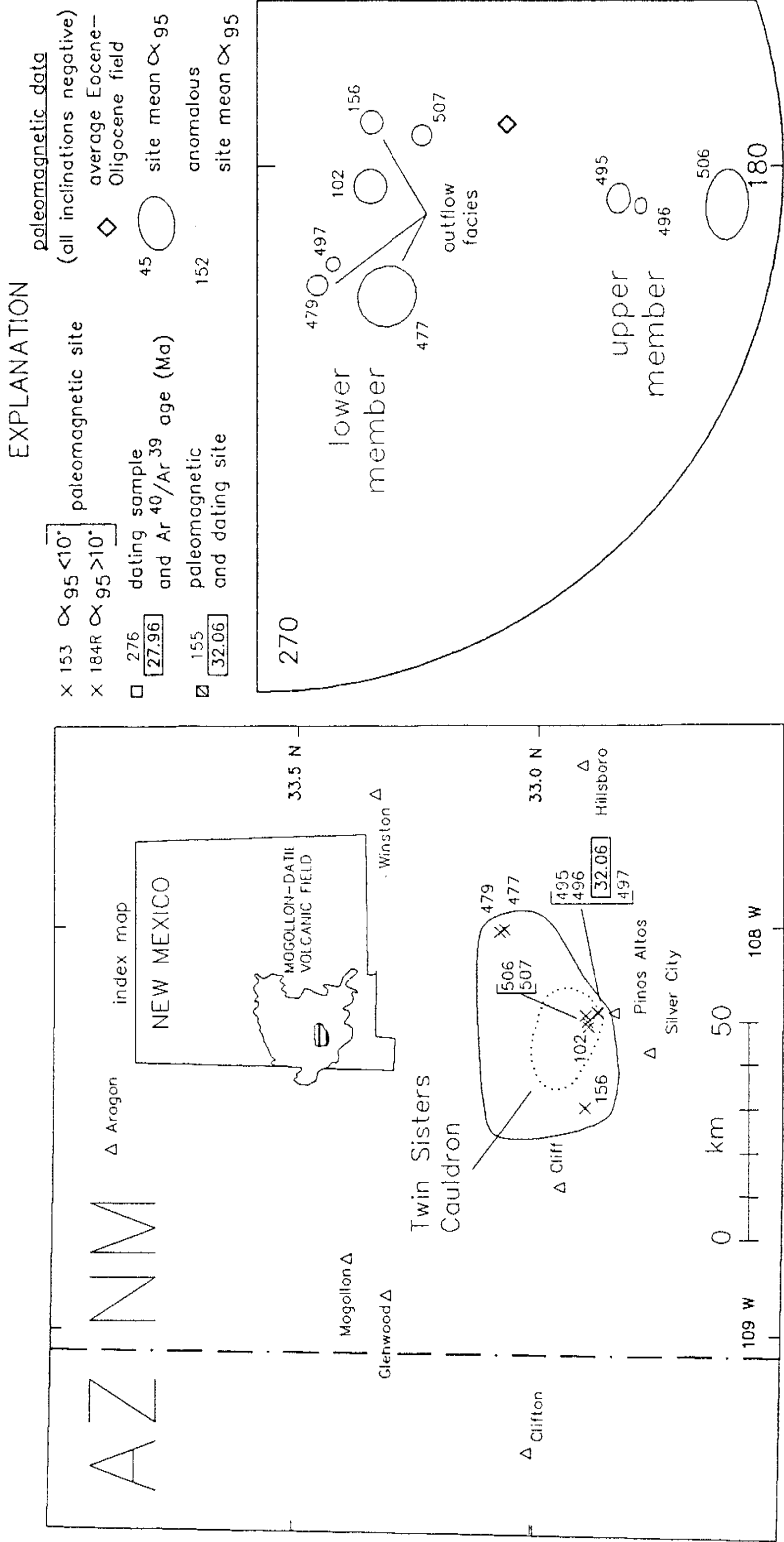


Fig. 20. Upper and lower members of Tadpole Ridge Tuff: site locations, extent, proposed source cauldron, <sup>40</sup>Ar/<sup>39</sup>Ar plateau ages, and site-mean paleomagnetic data. The wide difference between the RM directions of the 2 members indicates a time gap between their eruptions. Steep site-mean RM directions in the outflow facies support correlation with the lower intracauldron member.

during a rapidly changing field excursion or polarity transition event.

Paleomagnetic data have also helped to identify an outflow sheet associated with the lower member Tadpole Ridge Tuff. Two thin plagioclase-biotite tuffs, a member of Tvt of Finnell (1982) and tuff of Terry Canyon of Krier (1981), are respectively exposed 20 km west and 30 km northeast of the mapped extent of Tadpole Ridge Tuff. Correlation of these units with the lower member of the Tadpole Ridge Tuff is strongly supported by their distinctively steep site-mean directions (Fig. 20).

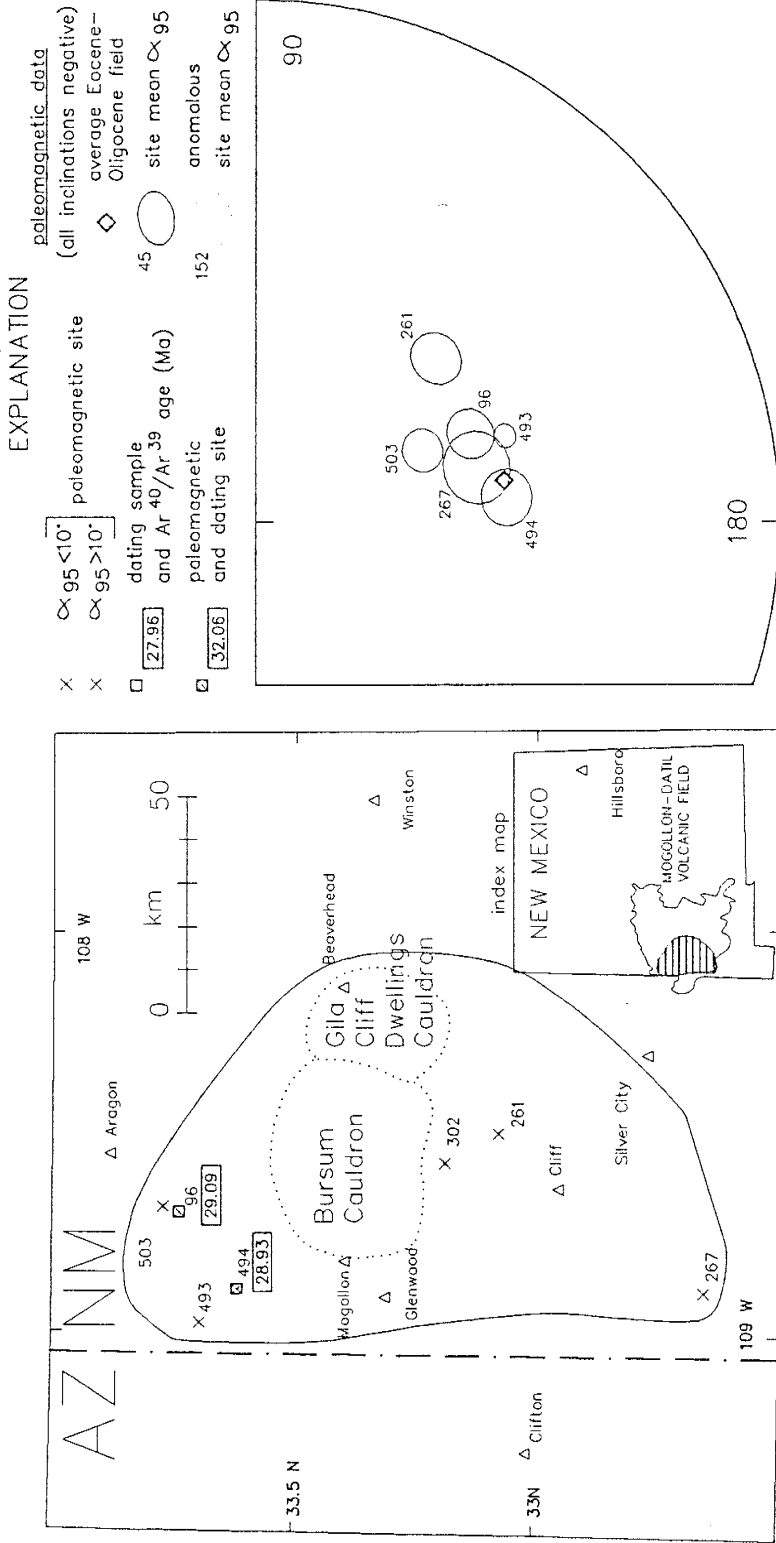
Due to low sanidine content (<0.5%), it has proven difficult to obtain an accurate  $^{40}\text{Ar}/^{39}\text{Ar}$  age for the Tadpole Ridge Tuff. An incorrect published age of 35.14 Ma (McIntosh et al., 1986) probably represents extreme xenocrystic contamination by sanidine from the Kneeling Nun Tuff, exposed in the nearby cauldron wall (site 498, Fig. 11) and locally observed to form abundant lithic fragments. The present 31.4 Ma age for the Tadpole Ridge tuff (upper member) should be considered tentative until more data are obtained. However, this age agrees well with K-Ar data (3 dates between 31.6 and 31.9 Ma) and is consistent with stratigraphic relationships of the outflow sheet, which is underlain by 31.7 Ma Caballo Blanco Tuff and overlain by 29.0 Ma Davis Canyon Tuff.

**Episode 3 - 29.0 to 27.4 Ma**

Following a 2.4 m.y. ignimbrite hiatus, the largest pulse of Mogollon-Datil ignimbrite activity began at 29.0 Ma. Within a span of 1.6 m.y., 9 major regional ignimbrites and at least 11 subregional to local units were erupted, totalling more than  $>6000 \text{ km}^3$  in volume (Table 1). The major units, primarily high-silica rhyolites, were erupted from two clusters of cauldrons, one located in the Mogollon Mountains near the western edge of the field and the second in the San Mateo and Magdalena mountains west of Socorro. The distribution and source cauldrons for Episode 3 ignimbrites are relatively well understood. Subregional stratigraphic sequences of major units around the two cauldron clusters were established by detailed mapping prior to this study (Ratté et al., 1984; Osburn and Chapin, 1983a).  $^{40}\text{Ar}/^{39}\text{Ar}$  and paleomagnetic data have helped to constrain eruptive timing of the Socorro and Mogollon centers, in part by identifying stratigraphic relationships of distal-facies ignimbrites in the overlap area between the two centers. These techniques have also helped to understand some of the more locally distributed units, of which one (tuff of Walking X Ranch, 27.6 Ma) may represent distal facies of a large ignimbrite erupted south of the Mogollon-Datil field.

**Davis Canyon Tuff - 29.0 Ma:**

The first major regional ignimbrite erupted in Episode 3 is the Davis Canyon Tuff (Fig. 21), which extends over a



## Davis Canyon Tuff 29.0 Ma

Fig. 21. Davis Canyon Tuff: site locations, extent, extent,  $^{40}\text{Ar}/^{39}\text{Ar}$  plateau ages, and site-mean paleomagnetic data. This unit may have been erupted from the Gila Cliff Dwellings cauldron (Ratté et al., 1984).



10,500 km<sup>2</sup> area of the southwestern Mogollon-Datil field. Two <sup>40</sup>Ar/<sup>39</sup>Ar plateau ages from the northern edge of this crystal-poor, high-silica rhyolitic outflow sheet yield a mean age of 29.0 Ma, and site-mean RM direction from 6 sites are well-grouped, supporting the distribution mapped by Ratté et al. (1984). The source cauldron for the Davis Canyon Tuff is not known, although its distribution is consistent with a source in either the Bursum or Gila Cliff Dwellings cauldron areas.

The unit-mean direction of the Davis Canyon Tuff, although near the expected time-averaged reversed field direction, is useful for distinguishing this unit from the lithologically similar Vicks Peak Tuff, which shows lower paleomagnetic inclination (Fig. 22). This distinction is particularly important in the overlap area of the two ignimbrites, where both were formerly mapped as tuff of Tularosa Canyon (Rhodes and Smith, 1976). The Davis Canyon Tuff represents the first of several reversed polarity units erupted between 29.0 and 28.0 Ma (Table 1), an interval tentatively correlated with chron 10R (Fig. 5; McIntosh, dissertation, Chapter D).

La Jencia Tuff - 28.9 Ma: The La Jencia Tuff is a well-mapped, crystal-poor, high-silica rhyolitic ignimbrite erupted from the Sawmill-Magdalena cauldron west of Socorro (Fig. 23; Osburn and Chapin, 1983a). Early <sup>40</sup>Ar/<sup>39</sup>Ar plateau ages of 28.9 Ma (Kedzie, 1984) were instrumental in recognizing the 3.2 m.y. eruptive hiatus between this unit

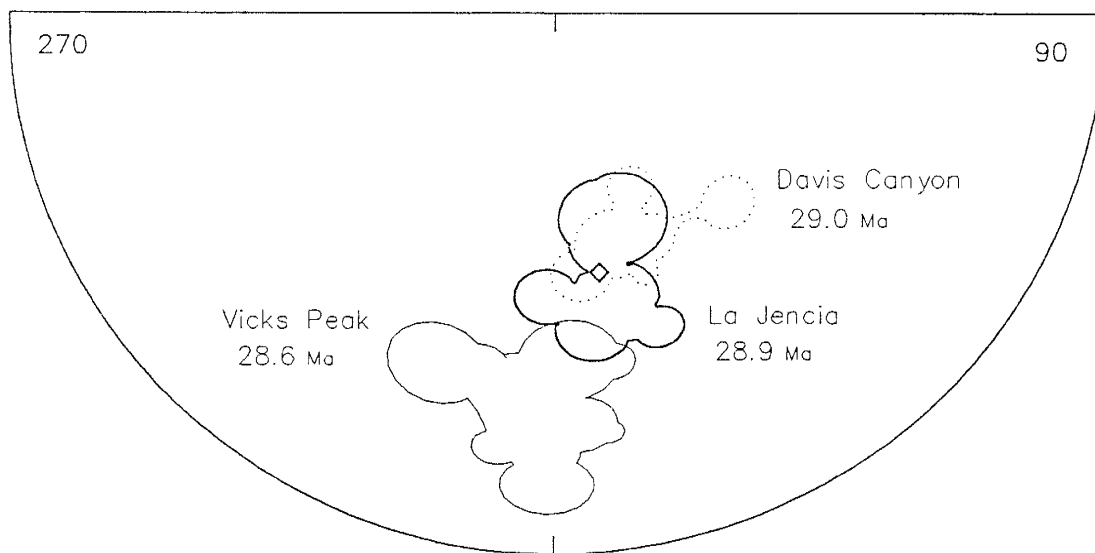
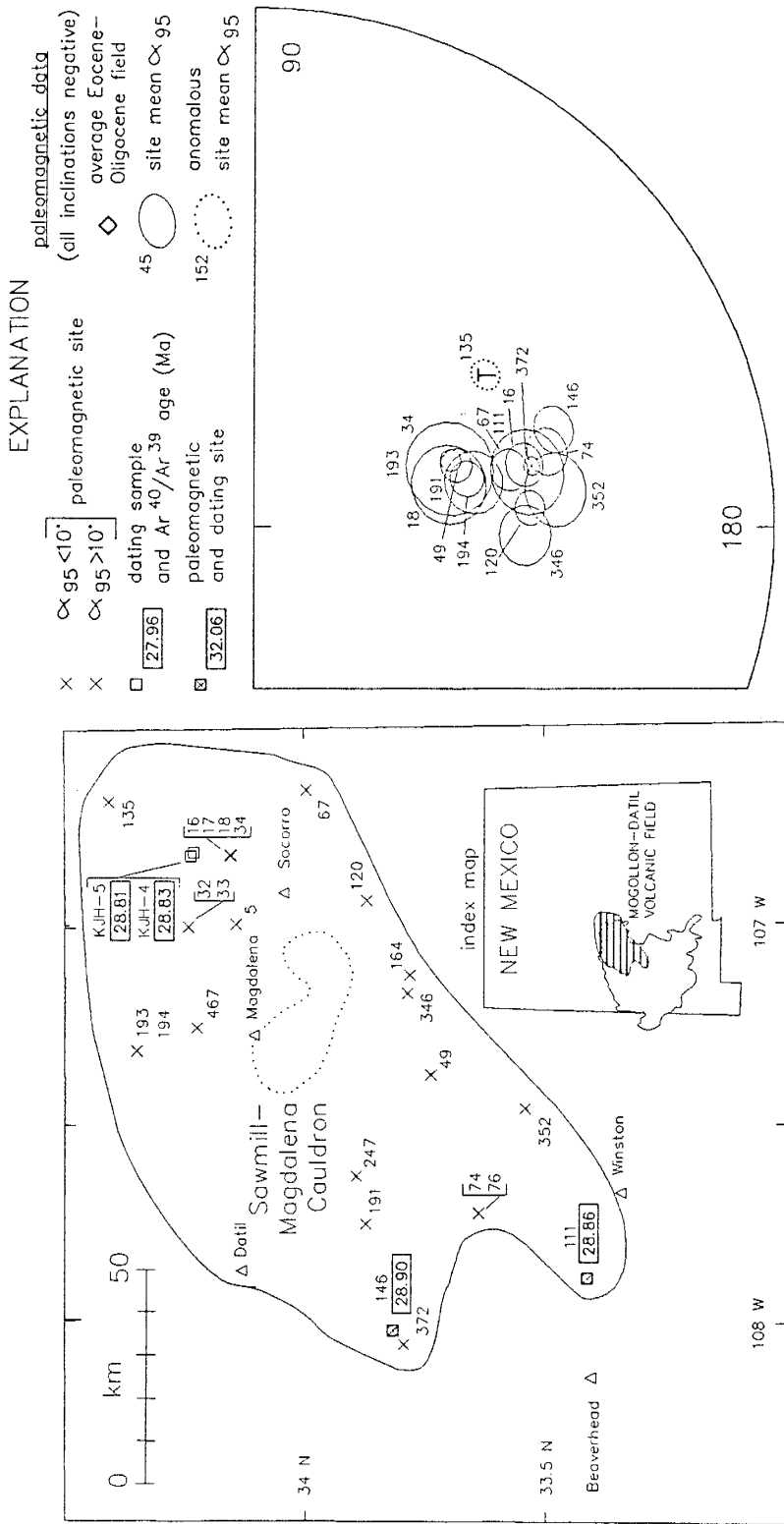


Fig. 22. Comparison of site-mean data from three 29.0-28.6 Ma crystal-poor, high-silica rhyolitic ignimbrites. Irregular outlines enclose site-mean ellipses for each unit and diamonds denote time-averaged Eocene-Oligocene normal and reversed field directions. The distinctively shallow direction of the Vicks Peak Tuff allows it to be distinguished from the Davis Canyon and La Jencia Tuffs, even in unwelded distal fringes.



## La Jencia Tuff 28.9 Ma

Fig. 23. La Jencia Tuff: site locations, extent, <sup>40</sup>Ar/<sup>39</sup>Ar plateau ages, and site-mean paleomagnetic data. Sawmill-Magdalena cauldron is the well-established source of this unit. Letters classifying anomalous sites are explained in Figure 9.

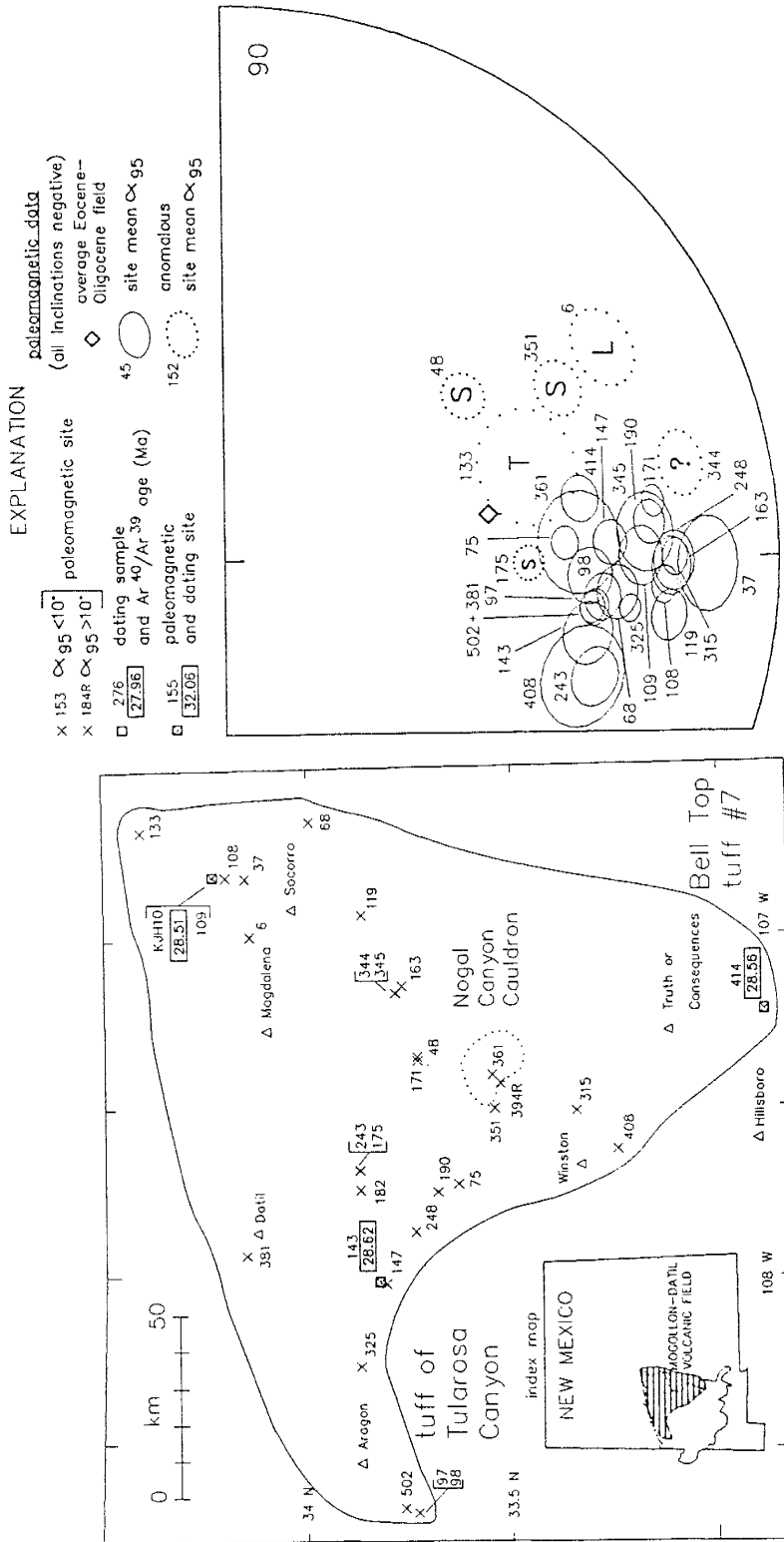
and the underlying 32.1 Ma Hells Mesa Tuff, whereas previous K-Ar data suggested a La Jencia age near 31 Ma (Chapin et al., 1975).

Paleomagnetic site-mean RM directions are well-grouped in the La Jencia Tuff, and, like the Davis Canyon Tuff, show a unit-mean direction similar to the expected time-averaged reversed polarity field. This RM direction provides a useful criteria for distinguishing between La Jencia and Vicks Peak tuffs (Fig. 22). Although the La Jencia and Davis Canyon Tuff are paleomagnetically indistinguishable, they have not been found to overlap.

Paleomagnetic and  $^{40}\text{Ar}/^{39}\text{Ar}$  data from the La Jencia Tuff support its previous mapped extent, but suggest that the unit extends even further to the southwest, as much as 80 km from its cauldron margin. Identified distal fringes of the La Jencia Tuff include outcrops along the south edge of the Plains of San Augustin (sites 146 and 372, Fig. 23) and in the central Black Range (site 111, Fig. 23).

Vicks Peak Tuff - 28.6 Ma: Vicks Peak Tuff, a crystal-poor high-silica rhyolitic ignimbrite erupted at 28.6 Ma from the Nogal Canyon cauldron in the southern San Mateo Mountains (Fig. 24), is the most widely distributed ignimbrite in the northern Mogollon-Datil volcanic field. Its 200 km exposed extent (Table 1) is exceeded only by Kneeling Nun and Box Canyon tuffs.

Site-mean RM directions for this unit are generally well grouped and show a distinctively shallow inclination



Vicks Peak Tuff - 28.6 Ma

Fig. 24. Vicks Peak Tuff: site locations, extent,  $^{40}\text{Ar}/^{39}\text{Ar}$  plateau ages, and site-mean paleomagnetic data. Vicks Peak Tuff is one of the most extensive ignimbrites in the field and includes Bell Top 7 tuff of Clemons (1976) and tuff of Tularosa Canyon of Rhodes and Smith (1976). Letters classifying anomalous sites are explained in Figure 9.

( $D=165^\circ$ ,  $I=-27^\circ$ ). A few sites show anomalous declinations, primarily due to fault-block rotations in highly extended areas (Fig. 24, McIntosh, dissertation, Chapter A). Three  $^{40}\text{Ar}/^{39}\text{Ar}$  age spectra yield a mean age of  $28.56 \pm .06$  Ma.

Paleomagnetic and  $^{40}\text{Ar}/^{39}\text{Ar}$  data indicate that tuff 7 of the Bell Top Formation (Clemons, 1976) and the upper part of the tuff of Tularosa Canyon (Rhodes and Smith, 1976) actually represent thin, unwelded distal facies of Vicks Peak Tuff (Fig. 24). This correlation provides a useful common stratigraphic tie among the ignimbrite sequences in the Socorro, Mogollon, and Las Cruces areas (Figs. 3,6).

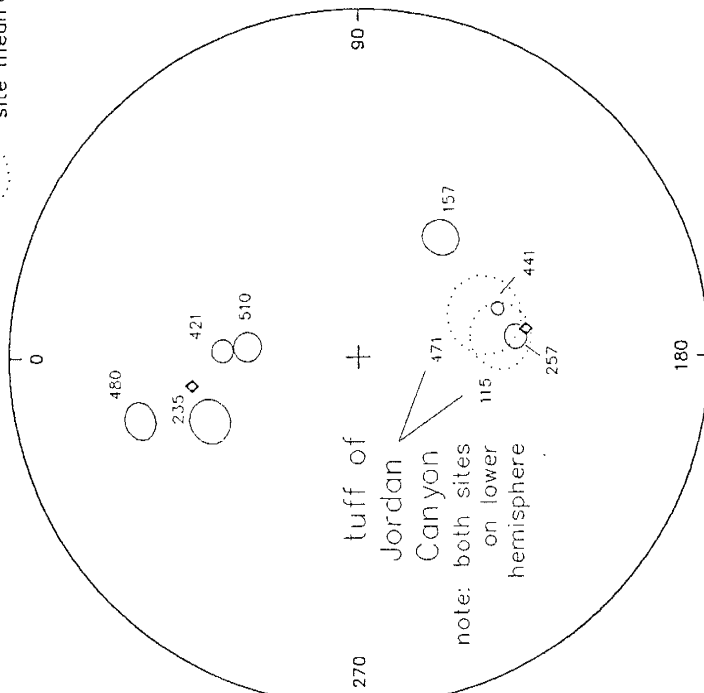
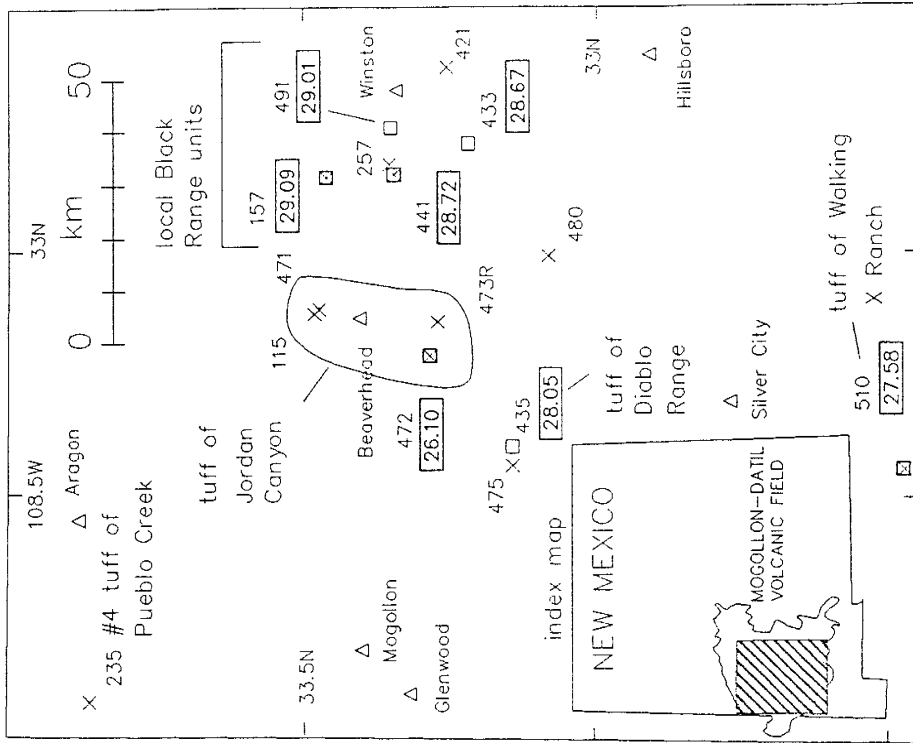
Smaller volume tuffs of the Black Range - 29.0 to 28.1 Ma:

Interlayered with regional ignimbrites in the central Black Range are several local small-volume ignimbrites apparently produced by persistent rhyolite dome/flow activity between 29.0 and 28.1 Ma (Table 1, Figs. 6, 25, 26). Most of these units are poorly to moderately welded and rich in rhyolite lava lithic fragments; many are directly overlain by rhyolitic lava with similar phenocryst assemblages (Woodard, 1982; Eggleston, 1982). Although of restricted extent, these units were investigated primarily because of their application to Magnetic Polarity Time Scale calibration (McIntosh, dissertation, Chapter D).

The eruption of these units apparently spanned a normal-to-reversed polarity reversal near 29.0 Ma (Figs. 5,6). The oldest units (tuffs of Monument Canyon and Little Mineral Creek (29.0 Ma)) show normal polarity and are

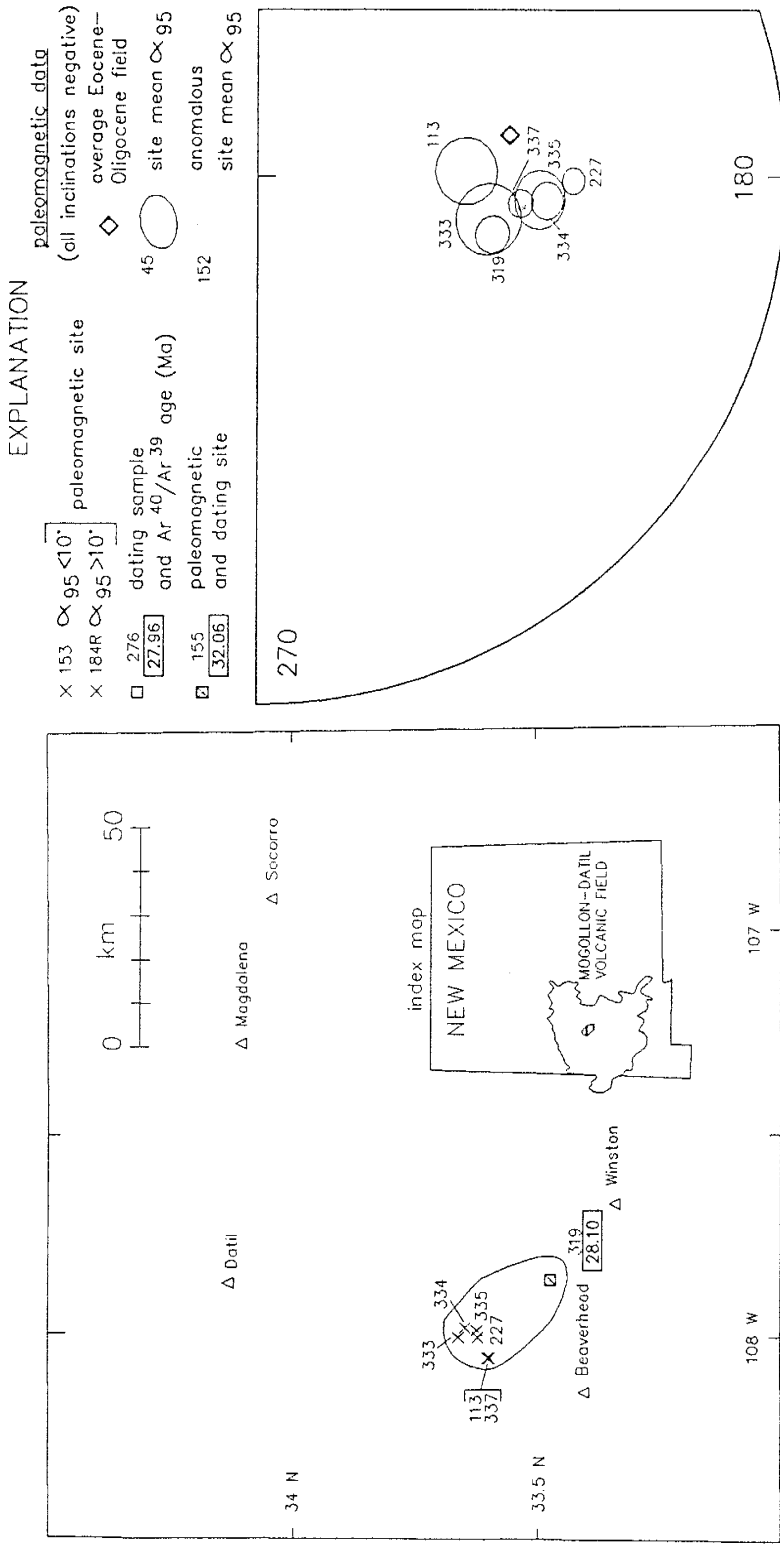
EXPLANATION

- X 153  $\propto$  95 <10°
  - X 184R  $\propto$  95 >10°
  - 276 [27.96]
  - 155 [27.96]
  - 276 [27.96] and Ar 40/Ar 39 age (Ma)
  - 155 [27.96] paleomagnetic and dating site
  - 45 site mean  $\propto$  95
  - 152 anomalous site mean  $\propto$  95
- paleomagnetic data inclinations:  
 northern hem = positive  
 southern hem = negative  
 (except Jordan Canyon)



Poorly studied Episode 3 smaller volume ignimbrites

Fig. 25. Site location map, <sup>40</sup>Ar/<sup>39</sup>Ar plateau ages, and site-mean paleomagnetic data for poorly studied Episode 3 ignimbrites.



tuff of Garcia Camp 28.1 Ma

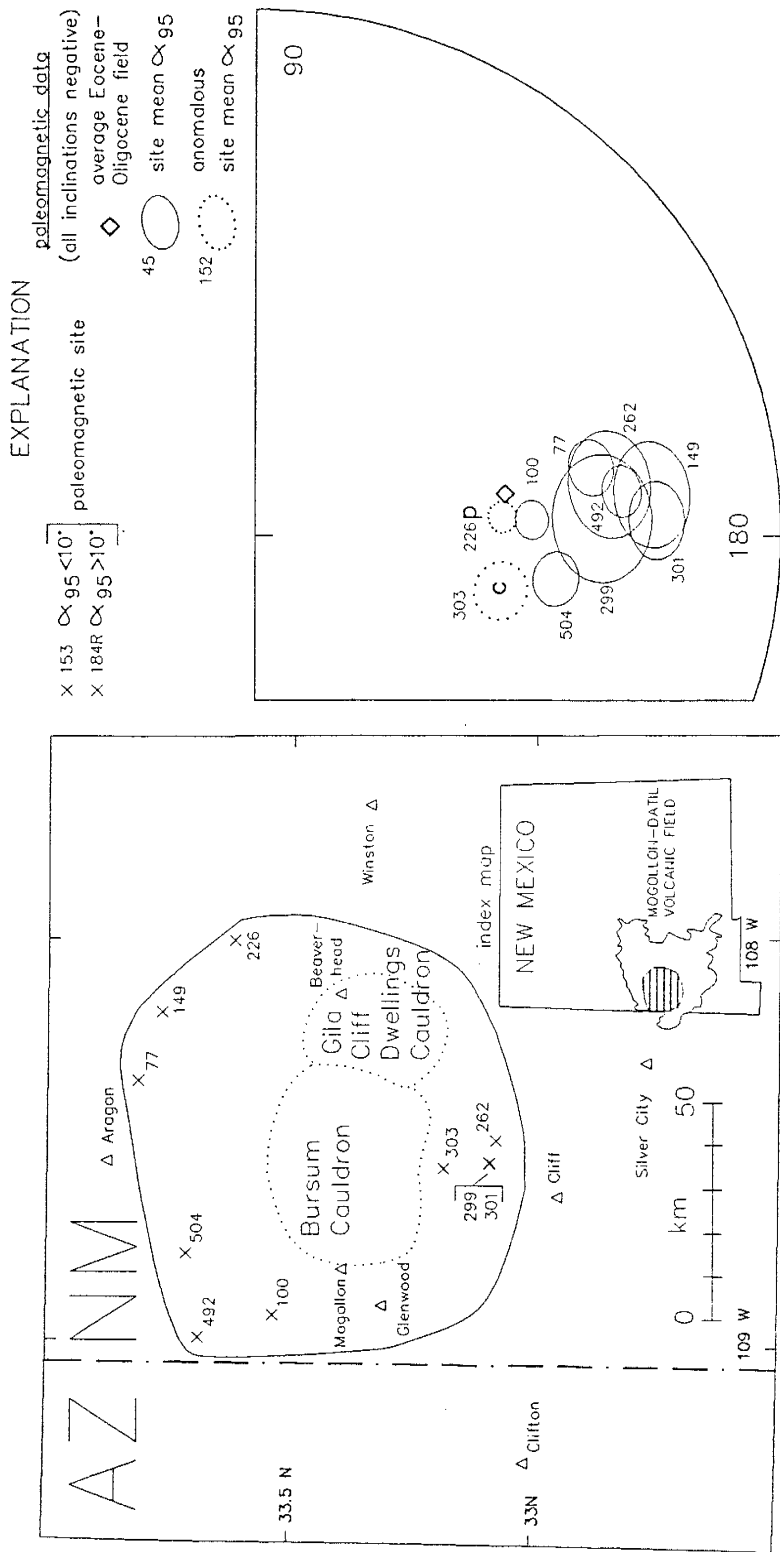
Fig. 26. Tuff of Garcia Camp: site locations, extent, <sup>40</sup>Ar/<sup>39</sup>Ar plateau ages, and site-mean paleomagnetic data. This multi-cooling-unit tuff is part of a pyroclastic apron surrounding Indian Peak rhyolitic domes (Duffield et al., 1988).



immediately overlain by a sequence of reversed polarity units (Stiver Canyon Tuff, tuff of Mud Hole (29.1 Ma), La Jencia Tuff (28.9 Ma regional unit discussed above), and tuff of Lookout Mountain (28.7 Ma, a.k.a. tuff of Diamond Creek, Woodard, 1982)). This polarity reversal, which shortly preceded eruption of Davis Canyon Tuff, is tentatively correlated with the reversal between chrons 11 and 10R (Fig. 5, McIntosh, dissertation, Chapter D).

A second pulse of Black Range dome eruptions, termed the Taylor Creek Rhyolites, occurred near 28.1 Ma (Duffield et al., 1987; Dalrymple and Duffield, 1988). These domes and associated ignimbrites all show reversed polarity (McIntosh, dissertation, Chapter A) and were apparently erupted near the end of Anomaly 10R (Fig. 5). One subregional dome-derived ignimbrite, the tuff of Garcia Camp, was studied in some detail (Fig. 26). Paleomagnetic site-mean directions from the tuff of Garcia Camp are tightly grouped (Fig. 26), indicating that this multi-cooling-unit ignimbrite was erupted over a brief interval of time. A single  $^{40}\text{Ar}/^{39}\text{Ar}$  plateau age of 28.10 Ma was determined, which compares to published mean  $^{40}\text{Ar}/^{39}\text{Ar}$  laser-fusion ages of  $28.21 \pm 0.04$  Ma for sanidines from tuff of Garcia Camp (Dalrymple and Duffield, 1988). The differences in ages is discussed in McIntosh, dissertation, Chapter B.

Shelly Peak Tuff - 28.1 Ma: Shelly Peak Tuff is a distinctive red-colored, plagioclase-biotite, low-silica rhyolitic ignimbrite erupted about 28.1 Ma from somewhere in



## Shelley Peak Tuff 28.1 Ma

Fig. 27. Shelly Peak Tuff: site locations, extent,  $^{40}\text{Ar}/^{39}\text{Ar}$  plateau ages, and site-mean paleomagnetic data. This unit may have been erupted from the Gila Cliff Dwellings cauldron (Ratté et al., 1984). Letters classifying anomalous sites are explained in Figure 9.

the Mogollon eruptive center. Paleomagnetic data from this widespread unit are moderately well-grouped in a shallow-inclination southerly direction (Fig. 27), although some of the sites show slightly anomalous directions and demagnetization behavior indicate of CRM components (Fig. 27; McIntosh, dissertation, Chapter A. These RM directions are sufficient to differentiate Shelly Peak Tuff from lithologically similar Tadpole Ridge Tuff (Fig. 20), but are not helpful in distinguishing between Shelly Peak Tuff and paleomagnetically similar Apache Springs Tuff (Fig. 28).

The age of the Shelly Peak Tuff is tightly bracketed at 28.1 Ma by the underlying tuff of Garcia Camp (28.1 Ma) and overlying Bloodgood Canyon Tuff (28.1 Ma). A single  $^{40}\text{Ar}/^{39}\text{Ar}$  plateau age determined for the Shelly Peak Tuff is  $28.52 \pm 0.08$  Ma; this anomalously old age probably reflects contamination of the sanidine-poor Shelly Peak Tuff by older lithic or xenocrystic feldspar (McIntosh, dissertation, Chapter B).

Bloodgood Canyon Tuff and related units - 28.1 Ma: The  $15,000 \text{ km}^2$ ,  $1000 \text{ km}^3$  Bloodgood Canyon Tuff is the most widely exposed ignimbrite in the southern part of the volcanic field (Ratté et al., 1984). Paleomagnetic data from throughout the extent of this high-silica rhyolitic outflow sheet show distinctive shallow-inclination, southeasterly RM directions. Similarly,  $^{40}\text{Ar}/^{39}\text{Ar}$  plateau ages from 7 widely separated samples are nearly identical, ranging from 27.99 to 28.11 Ma and averaging  $28.05 \pm 0.04$  Ma.

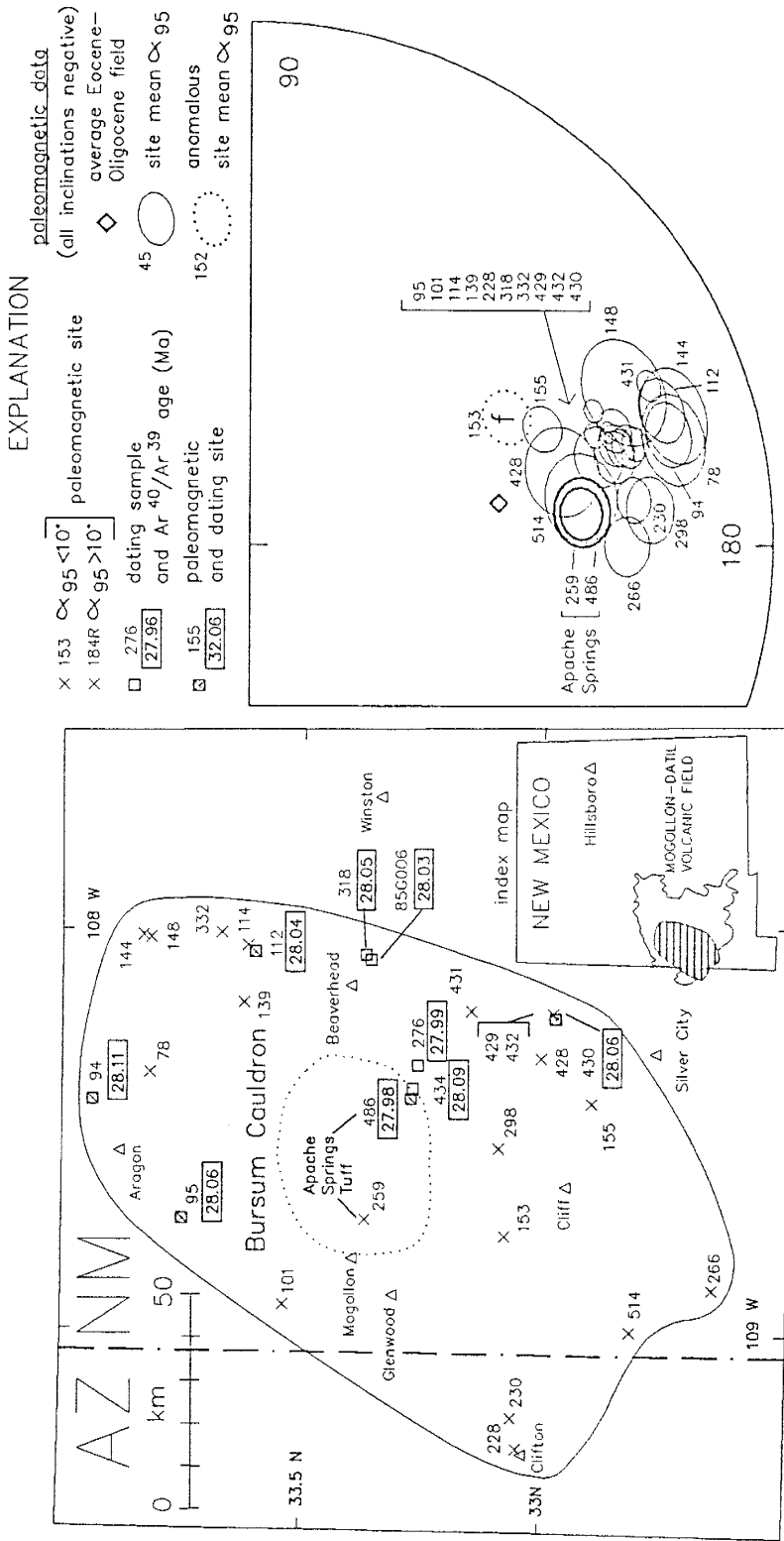


Fig. 28. Bloodgood Canyon Tuff: site locations, extent, <sup>40</sup>Ar/<sup>39</sup>Ar plateau ages, and site-mean paleomagnetic data. Paleomagnetic and <sup>40</sup>Ar/<sup>39</sup>Ar data support interpretation of this unit as the most widespread ignimbrite in the Mogollon-Datil volcanic field. Letters classifying anomalous sites are explained in Figure 9.

These data strongly support the conclusion that the Bloodgood Canyon Tuff is a single large outflow sheet (Ratté et al., 1984) and oppose the interpretation that exposures north of the Bursum cauldron represent a different eruptive unit, termed the Railroad Canyon Tuff (Elston et al., 1973; Rhodes and Smith, 1976; Elston, 1984). Furthermore, the RM direction of the Bloodgood Canyon Tuff is sufficiently distinctive to reliably distinguish this unit from 4 other lithologically similar ignimbrites in the northern part of the field (Fig. 29).

$^{40}\text{Ar}/^{39}\text{Ar}$  and paleomagnetic data are also consistent with the interpretation that the  $1200 \text{ km}^3$  Apache Springs Tuff represents the intracauldron facies equivalent of the Bloodgood Canyon Tuff (Ratté et al., 1984). The single  $^{40}\text{Ar}/^{39}\text{Ar}$  plateau age (27.98 Ma) is statistically indistinguishable from the mean of seven Bloodgood Canyon Tuff samples, and site-mean RM direction from two Apache Springs sites are within  $10^\circ$  of the unit-mean direction of the Bloodgood Canyon Tuff (Fig. 28).

In addition to Bloodgood Canyon and Apache Springs tuffs, two less voluminous associated units were also investigated. The tuff of Diablo Range is the precursor ignimbrite for an extensive sequence of rhyolitic lavas that is stratigraphically between the Shelly Peak and Bloodgood Canyon tuffs (Fig. 6). Two sites from this unit (475 and 436, Fig. 25) yield reversed polarity and a 28.1 Ma age

identical to that of the overlying Bloodgood Canyon Tuff (Table 1).

North of the Bursum cauldron, the Bloodgood Canyon Tuff is overlain by the poorly welded but lithologically similar tuff of Triangle C Ranch (Fig. 6, Fig. 30). The one  $^{40}\text{Ar}/^{39}\text{Ar}$  plateau age from this unit (28.05 Ma, Table 1) is also identical to the mean Bloodgood Canyon age, but the 6 site-mean RM directions are well-grouped in a normal polarity direction. Apparently, the tuff of Triangle C Ranch was erupted soon after a polarity reversal that itself occurred soon after eruption of the Bloodgood Canyon Tuff. This well constrained 28.0 Ma normal-to-reversed polarity transition is tentatively identified as the reversal between chrons 10R and 10 (Fig. 5). The Bloodgood Canyon Tuff and tuff of Triangle C Ranch provide a good example of a situation in which the combination of  $^{40}\text{Ar}/^{39}\text{Ar}$  dating and paleomagnetic correlation provides higher resolution than  $^{40}\text{Ar}/^{39}\text{Ar}$  dating alone.

Lemitar and Caronita tuffs - 28.0 Ma: The Lemitar Tuff is a well-mapped 28.0 Ma regional ignimbrite in the Socorro. Although no source cauldron has been identified for this unit, thickness and distribution (Fig. 32) point to a source in the west-central Magdalena Mountains. Two  $^{40}\text{Ar}/^{39}\text{Ar}$  age determinations and normal magnetic polarity suggest that this unit was erupted during chron 10 (Fig. 5). About half of the sites in this unit show tightly grouped site-mean RM directions, but the remainder are somewhat scattered (Fig.

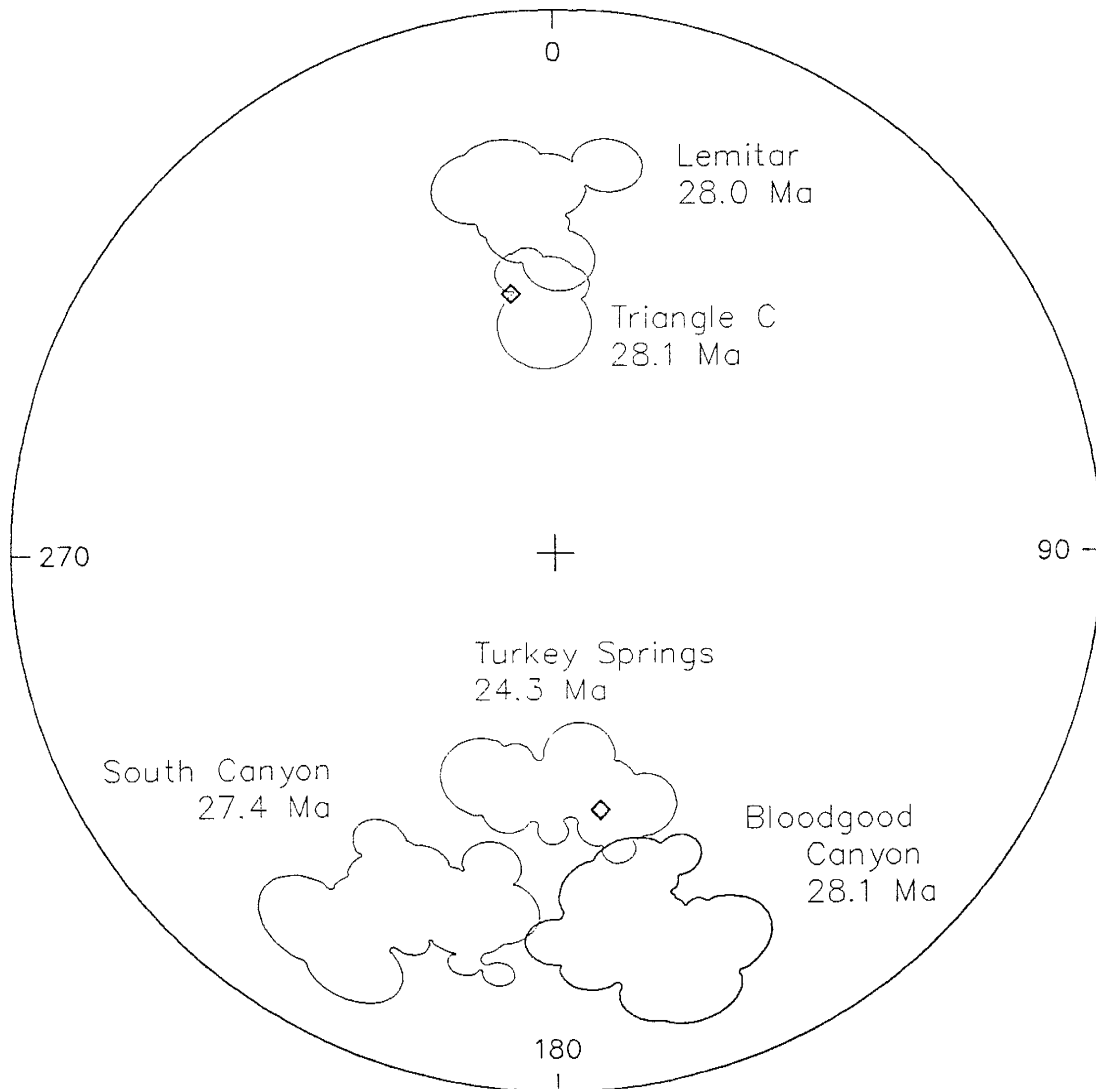
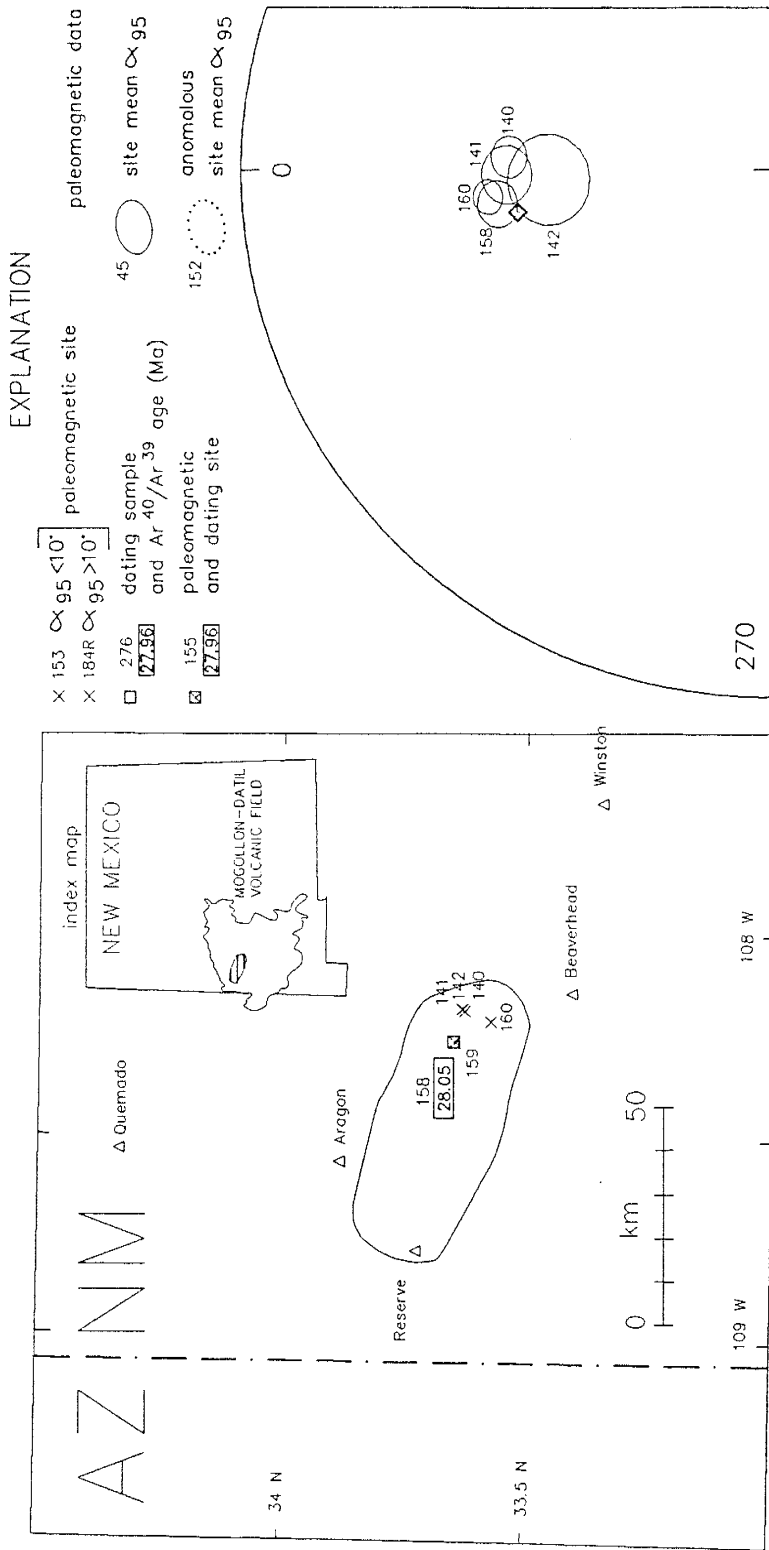


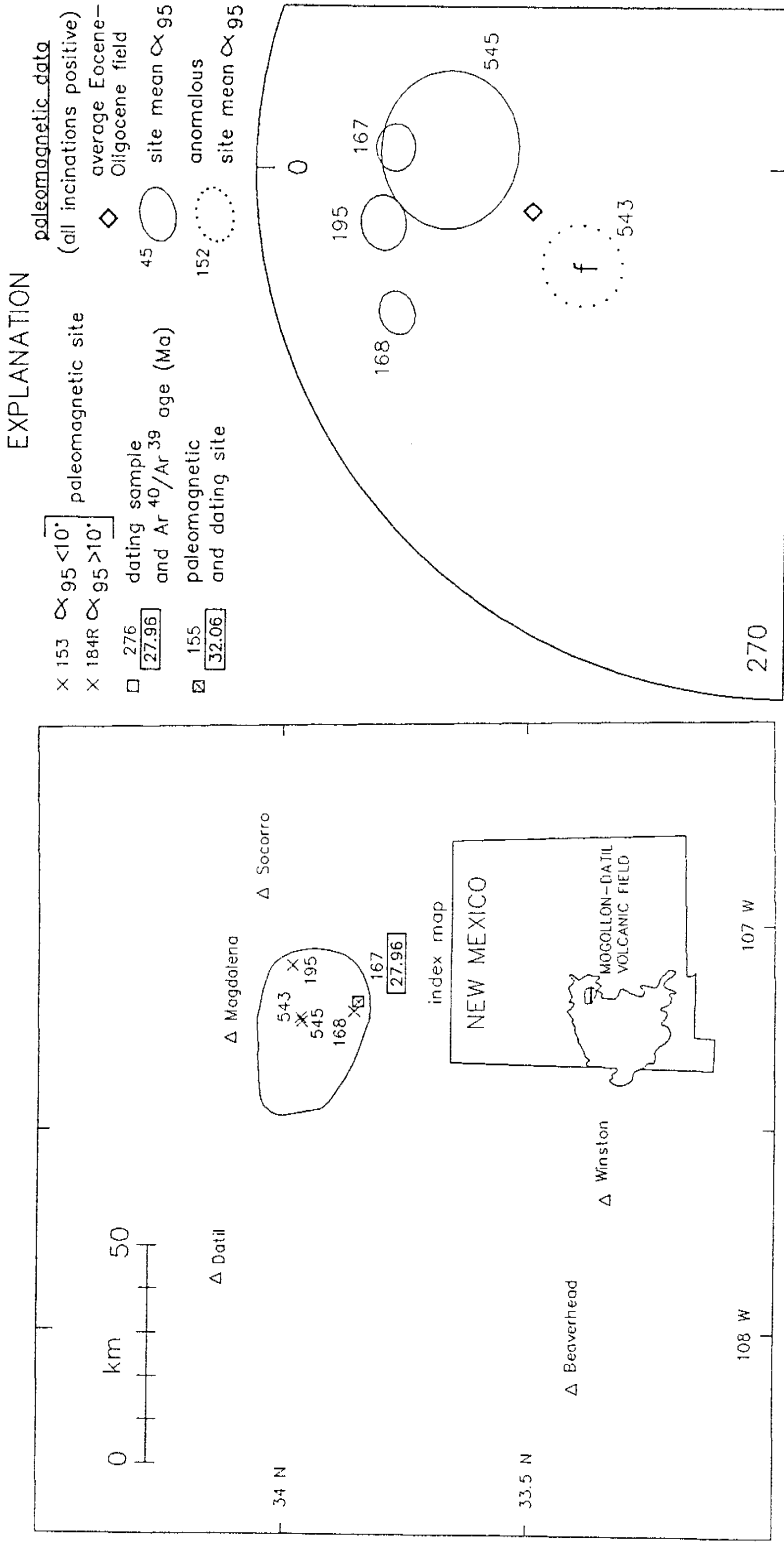
Figure 29. Little overlap is shown by site-mean data from 4 young (28.1-24.3 Ma), lithologically similar ignimbrites from the northern Mogollon-Datil volcanic field. Irregular outlines enclose site-mean ellipses for each unit and diamonds denote time-averaged Eocene-Oligocene normal and reversed field directions. The distinctive unit-mean directions allow these units to be paleomagnetically identified.



tuff of Triangle C Ranch 28.1 Ma

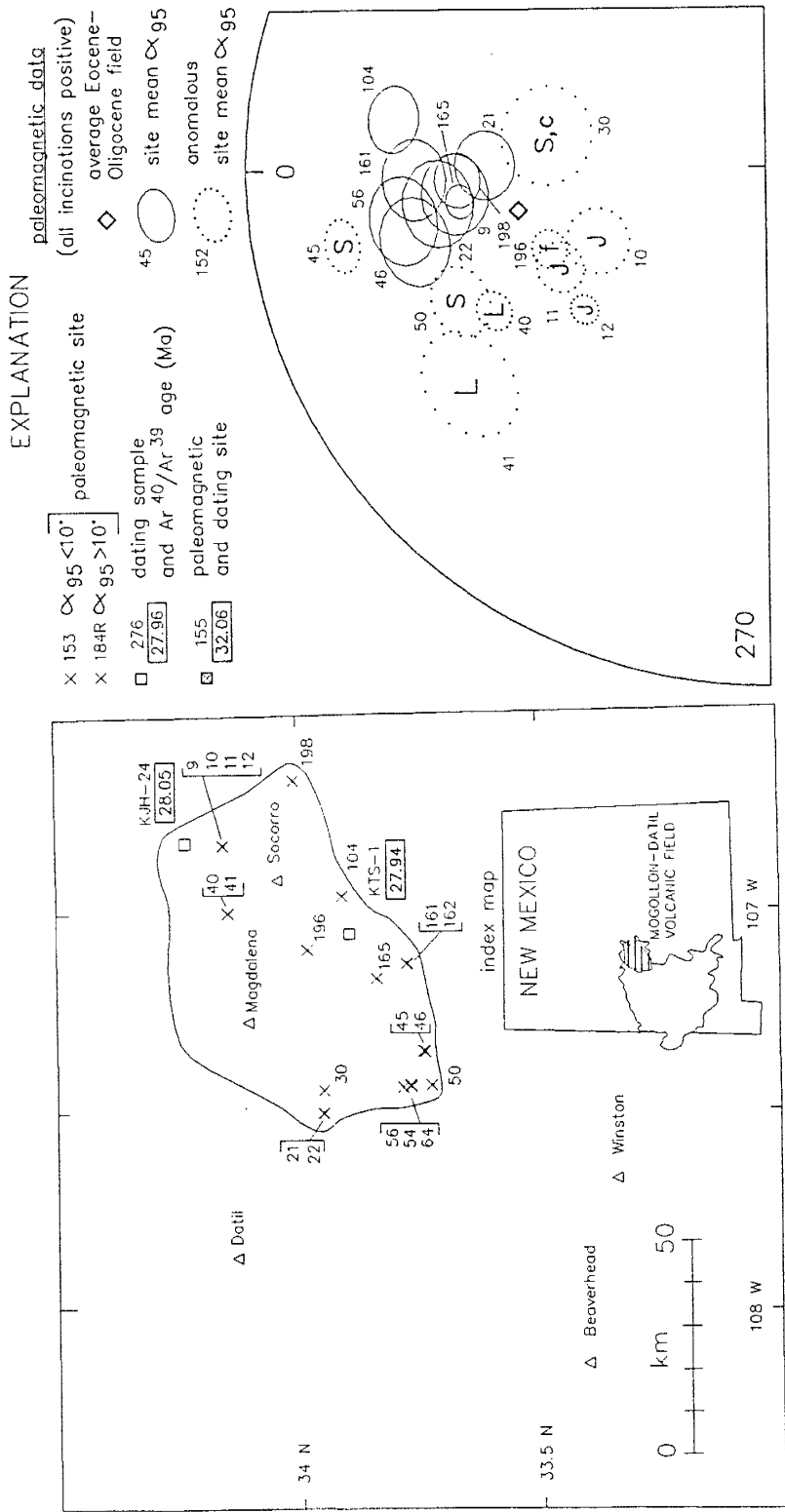
Fig. 30. Tuff of Triangle C Ranch: site locations, extent, <sup>40</sup>Ar/<sup>39</sup>Ar plateau ages, and site-mean paleomagnetic data.





tuff of Caronita Canyon 28.0 Ma

Fig. 31. Caronita Canyon Tuff: site locations, extent, <sup>40</sup>Ar/<sup>39</sup>Ar plateau ages, and site-mean paleomagnetic data. Letters classifying anomalous sites are explained in Figure 9.



Lemitar Tuff 28.0 Ma

Fig. 32. Lemitar Tuff: site locations, extent, <sup>40</sup>Ar/<sup>39</sup>Ar plateau ages, and site-mean paleomagnetic data. Letters classifying anomalous sites are explained in Figure 9.

32). For the most part these anomalous site-mean directions are related to block rotations in the highly extended Lemitar Mountains and Joyita Hills.

The Lemitar Tuff is underlain by the strongly zoned Caronita Canyon Tuff, formerly interpreted a part of the moat-fill sequence emplaced after eruption of the 28.9 Ma La Jencia Tuff (Osburn and Chapin, 1983a). Normal polarity and an  $^{40}\text{Ar}/^{39}\text{Ar}$  age of 28.0 Ma (Table 1, Fig. 31), suggest instead that the Caronita Canyon Tuff was a precursor unit erupted slightly before the Lemitar Tuff.

South Canyon Tuff - 27.4 Ma: The 27.4 Ma South Canyon Tuff is the youngest major, widespread ignimbrite in the northeastern Mogollon-Datil volcanic field. This well-mapped high-silica rhyolite was erupted from the Mt. Withington cauldron, a "trapdoor" cauldron hinged along its southern edge (Fig. 33). Both outflow and intracauldron facies are well exposed and were extensively sampled (total of 43 sites).  $^{40}\text{Ar}/^{39}\text{Ar}$  plateau ages from samples of both facies range from 27.28 to 27.40 Ma. Site-mean paleomagnetic data from outflow and thinner (<500 m) southern intracaldera facies are well-grouped in an unusual shallow, southwesterly direction that is distinct from all other Mogollon-Datil ignimbrites (Figs. 4, 29). This distinctive RM direction, together with  $^{40}\text{Ar}/^{39}\text{Ar}$  data, has been used to identify the 1.5-m-thick unwelded distal fringe of the South Canyon Tuff outflow sheet in the central Black Range (site 258 in Fig. 33).

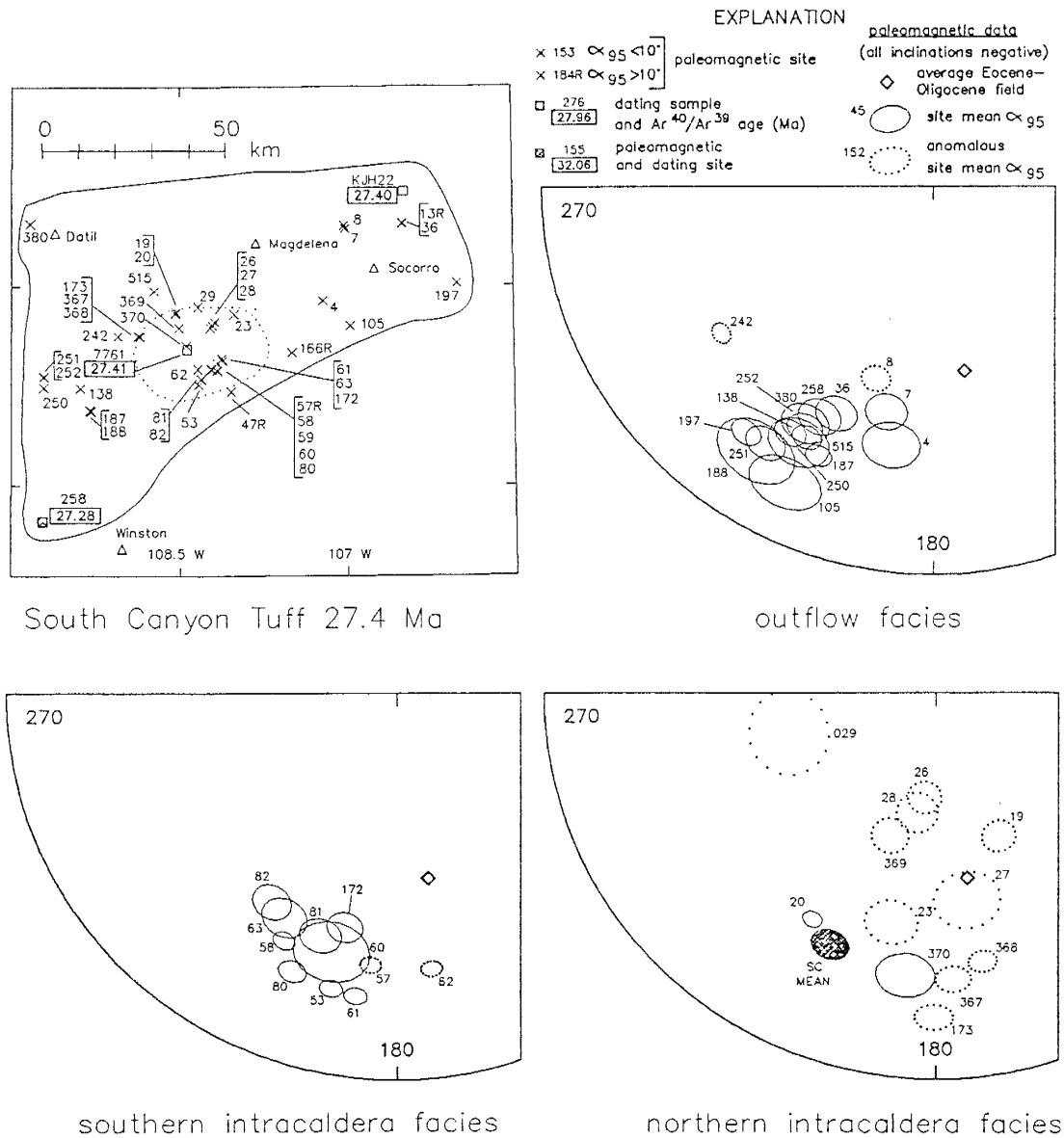


Fig. 33. South Canyon Tuff: site locations, extent, <sup>40</sup>Ar/<sup>39</sup>Ar plateau ages, and site-mean paleomagnetic data. Site-mean RM directions in the outflow and shallow intracaldera facies are well-grouped. Thicker (>500 m) intracaldera-facies sites show scattered site-mean directions probably reflecting secular variation during protracted cooling.

Site-mean RM directions from thicker (500-1500 m) northern intracauldron facies sections show large between-site scatter ( $\alpha_{95}=12.7^\circ$ ), and a mean direction (D=187, I=-46) which is offset toward the expected time-averaged field direction (D=170.5, I=-50), relative to the mean direction of the outflow facies (Fig. 33, Table 1). The preferred explanation for the non-uniform magnetization of the thick intracaldera facies is that it reflects paleosecular variation which occurred during protracted cooling (Reynolds et al., 1986; Wells and Hillhouse, 1989). Alternatively, the scattered site-mean directions might reflect non-horizontality of pumice foliations during initial cooling, or sub-blocking-temperature welding, flowage, or compaction (Rosenbaum, 1986). These possibilities are all discussed in detail in McIntosh, dissertation, Chapter A. In any case, these results support the conclusion that the use of paleomagnetism as a correlation criterion is less effective in thick intracauldron facies than in outflow sheets.

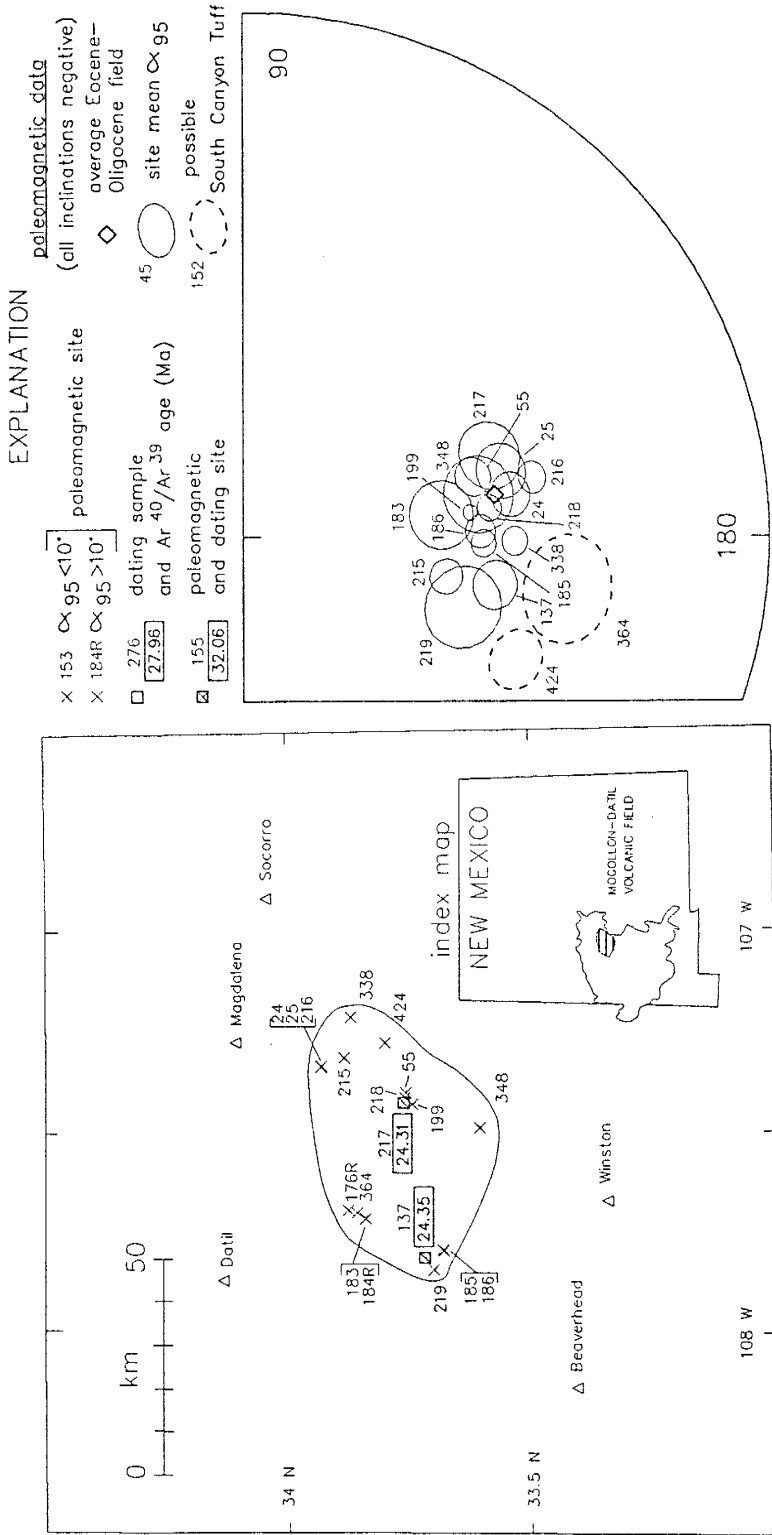
Slash Ranch/Jordan Canyon Tuff - 26 Ma?: The correlative tuffs of Slash Ranch and Jordan Canyon represent a poorly welded, zeolitized, but prominently exposed multi-cooling-unit ignimbrite which lies at or near the top of the Tertiary volcanic section near the center of the volcanic field (Fig. 25). A dome-derived origin is probable, although no vent has been identified.

A single  $^{40}\text{Ar}/^{39}\text{Ar}$  age of 26.1 Ma has been determined and two sites show a highly unusual south and downward RM direction (Table 1, Fig. 25). These data may not be reliable, because of zeolitization and abundant non-volcanic (?) cross-twinned feldspar crystals. Because of this uncertainty and the limited extent (22 km) of the unit, the tuff of Slash Ranch was not used to define the end of eruptive episode 3.

#### Episode 4 - 24.3 Ma

tuff of Turkey Springs - 24.3 Ma: Episode 4 (24.3 Ma): After a 2.9 m.y. hiatus, Mogollon-Datil ignimbrite activity concluded at 24.3 Ma with the eruption of a single, high-silica rhyolitic ignimbrite, the tuff of Turkey Springs (Ferguson, 1986). Prior to paleomagnetic analysis, this moderately extensive outflow sheet (Fig. 34) was not recognized as a stratigraphically distinct unit, but was instead incorrectly mapped as either South Canyon Tuff (Donze, 1980) or Railroad Canyon Tuff (Fodor, 1976).

Paleomagnetically identified tuff of Turkey Springs (Fig. 34) extends over a 50 x 70 km area centered on the northern San Mateo Mountains. All but two of the site-mean directions from this unit cluster tightly about the unit-mean RM direction ( $D=176$ ,  $I=-52$ ). Although the unit-mean RM direction is only  $4^\circ$  from the time-averaged Oligocene field, it is distinctly different from the 4 other lithologically similar ignimbrites with which the tuff of Turkey Springs has been, or might be, confused (Fig. 29). Two of the sites



tuff of Turkey Springs 24.3 Ma

Fig. 34. Tuff of Turkey Springs: site locations, extent, <sup>40</sup>Ar/<sup>39</sup>Ar plateau ages, and site-mean paleomagnetic data. Letters classifying anomalous sites are explained in Figure 9.

thought to be tuff of Turkey Springs (424 and 364 in Figure 33) fall almost equidistant from the unit-means RM directions of tuff of Turkey Springs and South Canyon Tuff. These anomalous site-mean directions probably reflect errors in assessment of the paleohorizontal (McIntosh, dissertation, Chapter A) and serve to emphasize the need to support paleomagnetic correlations with all other available criteria.

Two  $^{40}\text{Ar}/^{39}\text{Ar}$  plateau ages for the tuff of Turkey Springs average 24.33 Ma (Fig. 34, Table 1), 2.9 m.y. younger than any associated underlying ignimbrites. No source has yet been identified for the tuff of Turkey Springs, but the gross distribution of the outflow sheet and an underlying pumice-fall deposit suggest a vent area, perhaps a small cauldron, in the east-central San Mateo Mountains, an area not yet mapped in detail.

#### DISCUSSION

##### Utility of $^{40}\text{Ar}/^{39}\text{Ar}$ and paleomagnetism as correlation criteria

Paleomagnetism has been used as an ignimbrite correlation criterion for more than two decades (e.g. Dalrymple et al., 1965), and the  $^{40}\text{Ar}/^{39}\text{Ar}$  method is rapidly becoming established as a highly precise means of dating mid-Tertiary volcanic rocks (e.g. Lanphere, 1988; Dalrymple and Duffield, 1988). Results of this and other studies (Deino and Best, 1988; Deino, 1980) show that the



combination of these two techniques offers much higher resolution and reliability than either technique used alone.

$^{40}\text{Ar}/^{39}\text{Ar}$  and paleomagnetic correlation criteria are complementary. Where unaltered sanidine is available,  $^{40}\text{Ar}/^{39}\text{Ar}$  data serve to resolve age differences between units in which unit-mean directions are similar (e.g. Fig. 12) or site-mean direction have been disturbed by tectonic rotations (e.g. Fig 32). In cases where correlations can be independently established using  $^{40}\text{Ar}/^{39}\text{Ar}$  and/or lithologic and stratigraphic position data, tectonic rotations can be precisely assessed using paleomagnetic data from individual well-studied regional ignimbrites (e.g. Hagstrum and Gans, 1989; Hillhouse and Wells, 1989; Geissman and Harlan, in press). Paleomagnetic data from stratigraphic sequences of multiple well-studied ignimbrites offer even higher quality constraints on fault block rotations (McIntosh et al., 1986; McIntosh, dissertation, Chapter A).

On the other hand, paleomagnetic analysis, besides being relatively quick and inexpensive, can help identify units that cannot be distinguished using  $^{40}\text{Ar}/^{39}\text{Ar}$  dating. Examples include units that lack sanidine, are too close in age to be resolved by  $^{40}\text{Ar}/^{39}\text{Ar}$  method, or are altered. Tadpole Ridge and Cooney tuffs (Figs. 15, 20) are two examples of sanidine poor units for which paleomagnetic data provide evidence of significant time breaks between eruption of different members. Bloodgood Canyon Tuff and tuff of Triangle C Ranch are good examples of units which contain

abundant fresh sanidine but show ages (both 28.05 Ma) which are too similar to be resolved by the  $^{40}\text{Ar}/^{39}\text{Ar}$  method. The fact that they show opposite magnetic polarity allows them to be readily identified by paleomagnetic analysis and further demonstrates an age difference of at least thousands of years (the duration of a geomagnetic polarity reversal).

Paleomagnetic remanence directions in Mogollon-Datil ignimbrites are generally more resistant to alteration than are sanidine phenocrysts. In most cases, some portion of the remanence is carried by high-temperature deuteric hematite, which is stable in oxidizing environments associated with hydrothermal alteration or K-metasomatism; alteration of these ignimbrites typically destroys magnetite and reduces the intensity of remanence without significantly altering the RM direction (McIntosh, 1983; McIntosh et al., 1986; McIntosh, dissertation, Chapter A).

Long-range ignimbrite correlations reach the highest level of reliability where  $^{40}\text{Ar}/^{39}\text{Ar}$  ages and paleomagnetism are used in concert with lithologic, geochemical, and stratigraphic position data. In the case of the Shelly Peak Tuff, lithology is a more reliable correlation criterion than either  $^{40}\text{Ar}/^{39}\text{Ar}$  or paleomagnetic data. The unit is rich in plagioclase and biotite, quartz-free, almost devoid of sanidine, and contains significant amounts of distinctive green pyroxene. The RM direction of this unit is non-distinctive and the single  $^{40}\text{Ar}/^{39}\text{Ar}$  age shows evidence of contamination by older K-feldspar (McIntosh, dissertation,

Chapter). The distinctive mineralogy allows the Shelly Peak Tuff (which underlies 28.1 Ma Bloodgood Canyon Tuff) to be distinguished from the slightly younger, superficially similar Apache Springs Tuff (Ratté et al., 1984), and furthermore has helped to establish that distal Shelly Peak Tuff overlies the 28.1 Ma Garcia Camp Tuff. Because the Shelly Peak Tuff is sandwiched between two precisely dated 28.1 Ma units, its age is constrained as precisely as if it were itself well-dated.

Lastly, it should be noted that  $^{40}\text{Ar}/^{39}\text{Ar}$  and paleomagnetic work have not yet realized their full potential in the Mogollon-Datil volcanic field. For many of the ignimbrites (Table 1), only one or two paleomagnetic sites and a single sanidine sample have been analyzed. Further work would increase the precision and resolution of both methods. An additional characteristic which needs to be investigated in detail is mineral chemistry. K/Ca ratios in sanidines, routinely determined in the course of  $^{40}\text{Ar}/^{39}\text{Ar}$  dating show significant differences between many of the ignimbrites (McIntosh, dissertation, Chapter B). However, a microprobe study of the Bloodgood Canyon Tuff (Seaman, 1987) has also demonstrated large within-unit sectoral and vertical differences in sanidine composition.

#### **Mogollon-Datil time-stratigraphic framework**

$^{40}\text{Ar}/^{39}\text{Ar}$  plateau ages and paleomagnetic data from Mogollon-Datil ignimbrites have been used to help accurately correlate several units over distances of 40 to 200 km, thus

providing reliable ties between previously established subregional stratigraphic sequences. Regional ignimbrites now shown to be more extensive than previously believed include Kneeling Nun Tuff (34.9 Ma), Box Canyon Tuff (33.5 Ma), Caballo Blanco Tuff (31.7 Ma), Vicks Peak Tuff (28.6 Ma), and Bloodgood Canyon Tuff (28.1 Ma).

Subregional stratigraphic sequences have been assembled to yield an integrated time-stratigraphic framework for the entire volcanic field (Fig. 6). The potential applications of this framework are many fold.

First, it helps constrain the timing and distribution of Mogollon-Datil ignimbrite activity. For example, the Bell Top tuffs (Figs. 3 and 6) were previously interpreted to be locally derived units (Clemons, 1976). This interpretation led to the conclusion that the basin in which the tuffs accumulated was a volcanotectonic depression produced by repeated episodes of local magma withdrawal (Seager, 1976).  $^{40}\text{Ar}/^{39}\text{Ar}$  and paleomagnetic data demonstrate that all but the lowest two Bell Top tuffs are actually distal facies of ignimbrites erupted elsewhere, clearly showing that magma dynamics were not responsible for basin subsidence.

Second, the ignimbrite-based stratigraphic framework provides significant age constraints for sequences of mafic and silicic lavas and sedimentary rocks for which precise ages have not been, or cannot be, measured. For example, the stratigraphic position of the Poverty Creek basaltic

andesite lavas beneath the 29.0 Ma tuff of Little Mineral Creek (Table 1) clearly demonstrates that these lavas are somewhat older than their published K-Ar ages (Elston et al., 1973). Also, in the same area, extensive rhyolitic lavas interlayered with the dated ignimbrites can be shown to have been erupted in two brief, discrete pulses, the first ranging from 29.0 to 28.7 Ma and the second, the Taylor Creek Rhyolites, ranging over an even shorter interval near 28.1 Ma.

Third, within the context of this stratigraphic framework, Mogollon-Datil igneous units provide an inherently discontinuous but precise record of late Eocene-Oligocene geomagnetic polarity. Paleomagnetic data and  $^{40}\text{Ar}/^{39}\text{Ar}$  plateau ages precisely constrain 7 geomagnetic polarity reversals which occurred during Mogollon-Datil activity (Fig. 5). This polarity record has several applications both within and outside the Mogollon-Datil field. Within the field, the 34.9 Ma normal-to-reversed polarity transition (Fig. 5) was recognized, even before it was dated, to be a feature which could be correlated throughout much of the field (McIntosh et al., 1986). Subsequently, the 28.0 Ma reversed-to-normal polarity transition has also been recognized as a regional feature (Figs. 5,6).

This Mogollon-Datil polarity record can be confidently correlated with the polarity record of  $^{40}\text{Ar}/^{39}\text{Ar}$ -dated ignimbrites in the San Juan volcanic field in Colorado (Fig.

5). In both volcanic fields, the initiation of the largest pulse of cauldron-forming activity was virtually coincident with the 29.0 Ma normal-to-reversed polarity transition. The nearly simultaneous eruptive behavior in volcanic fields separated by more than 300 km suggests that the eruptive intervals were triggered by a regional change in crustal stress regime.

Finally, this polarity record has potential to aid in radiometric calibration of the worldwide Magnetic Polarity Time Scale determined from marine magnetic anomalies. As presented in McIntosh, dissertation, Chapter D, Mogollon-Datil normal intervals C and J (Fig. 5) have been tentatively correlated with polarity chrons 10 and 16. This correlation indicates an age of about 33.6 Ma for the Eocene-Oligocene boundary (Fig. 5), significantly younger than most other published Magnetic Polarity Time Scale calibration schemes (e.g. Berggren, 1985).

#### **Summary of Mogollon-Datil ignimbrite activity**

Mogollon-Datil ignimbrite activity ranged from 36.2 to 24.3 Ma and was highly episodic, being confined to 4 brief (<2.6 m.y.) eruptive intervals separated by 1.5 to 3 m.y. long hiatuses. Cauldron-forming activity originated in the 36.1-35.4 Organ/Doña cauldron area and subsequently migrated north and west. Rhyolitic activity was most intense between 29 and 27.3 Ma; this interval is characterized by alternating ignimbrite eruptions from the Mogollon and Socorro cauldron complexes, punctuated by 2 brief intervals

(29.0-28.7 Ma and 28.1 Ma) of extensive rhyolitic dome and flow eruptions in the central Black Range area between the two complexes.

## REFERENCES

- Alexander, E.C., Mickelson, G.M., and Lanphere, M.A., 1978, MMHb-1: a new  $^{40}\text{Ar}/^{39}\text{Ar}$  dating standard: U.S. Geological Survey Open-File Report 78-701, p.6-8.
- Beck, M.E., Sheriff, S.D., Diehl, J.F., and Hailwood, E.A., 1977, Further paleomagnetic results for the San Juan volcanic field of southern Colorado: Earth and Planetary Science Letters, v. 37, p. 124-130.
- Berggren, W.A., Kent, D.V., and Flynn, J.J., 1985, Jurassic to Paleogene: Part 2, Paleogene geochronology and chronostratigraphy, in Snelling, N.J. (ed.), The Chronology of the Geological Record: Geological Society of London Memoir 10, p. 141-195.
- Best, M.G., Shuey, R.T., Caskey, C.R., and Grant, S.K., 1973, Stratigraphic relations of members of the Needles Range Formation at type localities in southwestern Utah: Geological Society of America Bulletin, v. 84, p. 3269-3278.
- Bornhorst, T.J., 1980, Major- and trace-element geochemistry and mineralogy of Upper Eocene to Quaternary volcanic rocks of the Mogollon-Datil volcanic field, southwestern New Mexico: Unpublished Ph.D. dissertation, Albuquerque, Univ. New Mexico, 1104 p.
- Bogue, S.W., and Coe, R.S., 1981, Paleomagnetic correlation of Columbia River basalt flows using secular variation: Journal of Geophysical Research, v. 86, p. 11883-11897.
- Bowring, S.A., 1980, The geology of the west-central Magdalena Mountains, Socorro County, New Mexico: New Mexico Bureau of Mines and Mineral Resources Open-file 120, 135 p.
- Cather, S.M., McIntosh, W.C., and Chapin, C.E., 1987, Stratigraphy, age, and rates of deposition of the Datil Group (Upper Eocene-Lower Oligocene), west-central New Mexico: New Mexico Geology, v. 9, 50-54.
- Chamberlin, R.M., 1983, Cenozoic domino-style crustal extension in the Lemitar Mountains, New Mexico: A summary: New Mexico Geological Society Guidebook 34, p. 111-118.
- Chapin, C.E., and Lindley, J.I., 1986, Potassium metasomatism of igneous and sedimentary rocks in detachment terranes and other sedimentary basins: Economic implications: Arizona Geological Society Digest, v. 16, p. 118-126.



- Chapin, C.E., and Seager, W.R., 1975, Evolution of the Rio Grande Rift in the Socorro and Las Cruces areas: New Mexico Geological Society Guidebook 26, p. 297-322.
- Chapin, C.E., Siemers, W.T., and Osburn, G.R., 1975, Summary of radiometric ages of New Mexico rocks: New Mexico Bureau of Mines and Mineral Resources Open-File Report 60.
- Clemons, R.E., 1976, Geology of the East Half Corralitos Ranch Quadrangle, New Mexico: New Mexico Bureau of Mines and Mineral Resources Geologic Map 36.
- Clemons, R.E., 1976, Sierra del las Uvas ash-flow field, south central New Mexico: New Mexico Geological Society Guidebook 34, p. 111-118.
- Cross, T.A., and Pilger, R.H., 1982, Controls of subduction geometry, location of magmatic arcs, and tectonics of arc and back-arc regions: Geological Society of America Bulletin, v. 93, p. 545-562.
- Dalrymple, G.B., Alexander, E.C., Jr., Lanphere, M.A., and others, 1981, Irradiation of samples for  $^{40}\text{Ar}/^{39}\text{Ar}$  dating using the Geological Survey TRIGA reactor: U. S. Geological Survey Professional Paper 1176, 55 p.
- Dalrymple, G.B., and Duffield, W.A., 1988, High-Precision  $^{40}\text{Ar}/^{39}\text{Ar}$  dating of Oligocene rhyolites from the Mogollon-Datil volcanic field using a continuous laser system: Geophysical Research Letters, v. 15, p. 463-466.
- Deino, A.L., and Best, M.G., 1988, Use of high-precision single-crystal  $^{40}\text{Ar}/^{39}\text{Ar}$  ages and TRM data in correlation of an ash-flow deposit in the Great Basin: Geological Society of America Abstracts with Programs, v. 20, p. 397.
- Deino, A.L., 1989, Single-crystal  $^{40}\text{Ar}/^{39}\text{Ar}$  dating as an aid in correlation of ash flows: examples from the Chimney Spring/New Pass Tuffs and the Nine Hill/Bates Mountain Tuffs of California and Nevada: Continental Magmatism Abstracts, New Mexico Bureau of Mines Bulletin 131, p. 70.
- Diehl, J.F., Beck, M.E., and Lipman, P.W., 1974, Paleomagnetism and magnetic-polarity zonation in some Oligocene volcanic rocks of the San Juan Mountains, south-western Colorado: Geophysical Journal, v. 37, p. 323-332.

- Diehl, J.F., McClannahan, K.M., and Bornhorst, T.J., 1988, Paleomagnetic results from the Mogollon-Datil volcanic field, southwestern New Mexico, and a refined mid-Tertiary reference pole for North America: *Journal of Geophysical Research*, v. 93, P. 4869-4879.
- Donze, M.A., 1980, Geology of the Squaw Peak area, Magdalena Mountains, Socorro County, New Mexico: M.S. Thesis, New Mexico Bureau of Mines and Mineral Resources, Open-file report 123, 131 p.
- Duffield, W.A., Richter, D.H., and Priest, S.S., 1987, Preliminary geologic map of the Taylor Creek Rhyolite, Catron and Sierra Counties, New Mexico: U.S. Geological Survey Open File Report 87-515, 1:50,000.
- Eggleston, T.L., 1982, Geologic Map of the Taylor Creek tin district, Black Range, New Mexico: New Mexico Bureau of Mines and Mineral Resources, Open-file Report 177.
- Elston, W.E., 1957, Geology and Mineral Resources of Dwyer quadrangle, Grant, Luna, and Sierra Counties, New Mexico: New Mexico Bureau Mines and Mineral Resources Bulletin, v. 37, 88p.
- Elston, W.E., 1976, Tectonic significance of mid-Tertiary volcanism in the Basin and Range province: a critical review with special reference to New Mexico: *New Mexico Geological Society Special Publication* 5, p. 93-102.
- Elston, W.E., 1984, Mid-Tertiary ash flow tuff cauldrons, southwestern New Mexico: *Journal of Geophysical Research*, v. 89, p. 8733-8750.
- Elston, W.E., Damon, P.E., Coney, P.E., Rhodes, R.C., Smith, E.I., and Bikerman, M., 1973, Tertiary volcanic rock, Mogollon-Datil province, and surrounding region: K-Ar dates, patterns of eruption, and periods of mineralization: *Geological Society of America Bulletin*, v. 84, p. 2259-2274.
- Elston, W.E., Seager, W.R., and Clemons, R.E., 1975, Emory cauldron, Black Range, New Mexico: Source of the Kneeling Nun Tuff: *New Mexico Geological Society Guidebook* 26, p. 283-292.
- Ferguson, C.A., 1986, Geology of the east-central San Mateo Mountains, Socorro County, New Mexico: New Mexico Bureau of Mines and Mineral Resources Open File Report 252, 135p.
- Finnell, T.L., 1976, Geologic map of the Twin Sisters quadrangle, Grant County, New Mexico: U.S. Geological Survey, Miscellaneous Field Studies Map MF-779.

- Finnell, T.L., 1982, Geologic map of the Dorsey Ranch quadrangle, Grant County, New Mexico: U.S. Geological Survey, Miscellaneous Field Studies Map MF-1431.
- Finnell, T.L., 1987, Geologic map of the Cliff quadrangle, Grant County, New Mexico: U.S. Geological Survey, Miscellaneous Investigations Series, Map I-1768.
- Fleck, R.J., Sutter, J.F., and Elliot, D.H., 1977, Interpretation of discordant  $^{40}\text{Ar}/^{39}\text{Ar}$  age-spectra of Mesozoic tholeiites from Antarctica: *Geochimica Cosmochimica Acta*, v. 41, p. 15-32.
- Fodor, R.V., 1976, Volcanic geology of the northern Black Range, New Mexico, in *Cenozoic Volcanism: New Mexico Geological Society Special Publication 5*, p. 68-70.
- Geissman, J.W., Van der Voo, R., and Howard, K.L., 1982, A paleomagnetic study of the structural deformation in the Yerington district, Nevada, I. Tertiary units and their tectonism: *American Journal of Science*, v. 282, p. 1042-1079.
- Grommé, C.S., McKee, E.H., and Blake, M.C., 1972, Paleomagnetic correlations and potassium-argon dating of middle Tertiary ash-flow sheets in eastern Great Basin, Nevada and Utah: *Geological Society of America Bulletin*, v. 83, p. 1619-1638.
- Hagstrum, J.T., and Gans, P.B., 1989, Paleomagnetism of the Oligocene Kalamazoo Tuff: Implications for Middle Tertiary extension in east central Nevada: *Journal of Geophysical Research*, v. 94, p. 1827-1842.
- Hedlund, D.C., 1978, Geologic map of the C-Bar ranch quadrangle, Grant County, New Mexico: U.S. Geological Survey, Miscellaneous Field Studies Map MF-1039.
- Hildreth, W. and Mahood, G., 1985, Correlation of ash-flow tuffs: *Geological Society of America Bulletin*, v. 96, p. 968-974.
- Holcomb, R., Champion, D., and McWilliams, M., 1986, Dating recent Hawaiian lava flows using paleomagnetic secular variation: *Geological Society of America Bulletin*, v. 97, p. 829-839.
- Hoblitt, R.P., Reynolds, R.R., and Larson, E.E., 1985, Suitability of non-welded pyroclastic-flow deposits for studies of magnetic secular variation. A test based on deposits emplaced on Mount St. Helens, Washington, in 1980: *Geology*, v. 13, p. 242-245.

- Kedzie, L.L., 1984, High-precision  $^{40}\text{Ar}/^{39}\text{Ar}$  dating of major ash-flow tuff sheets, Socorro, New Mexico: unpublished M.S. thesis, New Mexico Institute of Mining and Technology, Socorro, New Mexico, 197 p.
- Krier, D.J., 1981, Geologic Map of the southern part of the Gila Primitive Area, New Mexico: unpublished M.S. thesis, University of New Mexico, Albuquerque, 58 pp.
- Kunk, M.J., Sutter, J.F., and Naeser, C. W., 1985, High-precision  $^{40}\text{Ar}/^{39}\text{Ar}$  ages of sanidine, biotite, hornblende, and plagioclase from the Fish Canyon Tuff, San Juan volcanic field, south-central Colorado: EOS, Transactions AGU, v. 17, p. 636.
- Lanphere, M.A., 1988, High-resolution  $^{40}\text{Ar}/^{39}\text{Ar}$  geochronology of Oligocene volcanic rocks, San Juan Mountains, Colorado: Geochimica Cosmochimica Acta, v. 52, p. 1425-1434.
- Lipman, P.W., Doe, B.R., Hedge, C.E., and Steven, T.A., 1978, Petrologic evolution of the San Juan volcanic field, southwestern Colorado: Pb and Sr isotopic evidence: Geological Society of America Bulletin, v. 89, p. 59-82.
- Lipman, P.W., Protstka, H.J., and Christianson, R.L., 1972, Cenozoic volcanism and plate-tectonic evolution of the Western United States. I. Early and middle Cenozoic: Royal Society of London Philosophical Transactions, Series A., v. 272, p. 217-248.
- Marvin, R.F., Naeser, C.W., Bikerman, M., Mehnert, H.H., and Ratté, J.C., 1987, Isotopic ages post-Paleocene igneous rocks within and bordering the Clifton  $1^{\circ} \times 2^{\circ}$  quadrangle, Arizona-New Mexico: New Mexico Bureau of Mines and Mineral Resources Bulletin 118, 63 p.
- McDowell, F.W., 1983, K-Ar dating: incomplete extraction of radiogenic argon from alkali feldspar: Isotope Geoscience, v. 1, p. 119-126.
- McIntosh, W.C., 1983, Preliminary results from a paleo- and rock-magnetic study of Oligocene ash-flow tuffs in Socorro County, New Mexico: New Mexico Geological Society Guidebook 34, p. 205-210.
- McIntosh, W.C., 1988, Progress toward calibration of the Mid-Tertiary geomagnetic polarity time scale using high-precision  $^{40}\text{Ar}/^{39}\text{Ar}$  dated ignimbrites in southwestern New Mexico: Geological Society of America Abstracts with Programs, v. 20, p. A65-66.

- McIntosh, W.C., Sutter, J.F., Chapin, C.E., Osburn, G.R., and Ratté, J.C., 1986, A stratigraphic framework for the Mogollon-Datil volcanic field based on paleomagnetism and high-precision  $^{40}\text{Ar}/^{39}\text{Ar}$  dating of ignimbrites - a progress report: New Mexico Geological Society Guidebook 37, p. 183-195.
- Mutschler, F.E., Larson, E.E., and Bruce, R.M., 1987, Laramide and younger magmatism in Colorado - new petrologic and tectonic variations on old themes: Colorado School of Mines Quarterly, v. 82, p. 1-47.
- Osburn, G.R., and Chapin, C.E., 1983a, Nomenclature for Cenozoic rocks of the northeast Mogollon-Datil volcanic field, New Mexico: New Mexico Bureau of Mines and Mineral Resources Stratigraphic Chart 1.
- Osburn, G.R., and Chapin, C.E., 1983b, Ash-flow tuffs and cauldrons in the northeast Mogollon-Datil volcanic field: a summary: New Mexico Geological Society Guidebook 34, p. 197-204.
- Ratté, J.C., Gaskill, D.L., 1975, Reconnaissance geologic map of the Gila Wilderness study area, southwestern New Mexico: U.S. Geological Survey Miscellaneous Investigations Map I-886.
- Ratté, J.C., Marvin, R.F., and Naeser, C.W., 1984, Calderas and ash-flow tuffs of the Mogollon Mountains: Journal of Geophysical Research, v. 89, p. 8713-8732.
- Ratté, J.C., McIntosh, W.C., and Houser, B.B., 1989, Geologic map of the Horse Springs West Quadrangle, Catron County, New Mexico: U.S. Geological Survey Open File Report 89-210.
- Reynolds, R.L., 1977, Paleomagnetism of welded tuffs of the Yellowstone Group: Journal of Geophysical Research, v. 82, p. 3677-3693.
- Reynolds, R.R., Hudson, M.R., and Hon, K., 1986, Paleomagnetic evidence for the timing of collapse and resurgence of the Lake City Caldera, San Juan Mountains, Colorado: Journal of Geophysical Research, v. 91, p. 9599-9613.
- Rhodes, R.C., and Smith, E.I., 1976, Stratigraphy and structure of the northwestern part of the Mogollon Plateau volcanic province: New Mexico Geological Society Special Publication 5, p. 57-62.
- Richter, D.H., 1978, Geologic map of the Spring Canyon quadrangle, Catron County, New Mexico: U.S. Geological Survey, Miscellaneous Field Studies Map MF-966.

- Roddick, J.C., 1983, High precision intercalibration of  $^{40}\text{Ar}/^{39}\text{Ar}$  standards: *Geochimica Cosmochimica Acta*, v. 47, p. 887-898.
- Rosenbaum, J.G., 1986, Paleomagnetic directional dispersion produced by plastic deformation on a thick Miocene welded tuff, southern Nevada: Implications for welding temperatures: *Journal of Geophysical Research*, v. 91, p. 12817-12834.
- Seager, W.R., 1981, Geology of the Organ Mountains and southern San Andes Mountains, New Mexico: New Mexico Bureau of Mines and Mineral Resources, Memoir 36, 97 p.
- Seager, W.R., Clemons, R.E., Hawley, J.W., and Kelley, R.E., 1982, Geology of the northwest part of Las Cruces 1° x 2° sheet, New Mexico: New Mexico Bureau of Mines and Mineral Resources Geological Map 53, scale 1:125,000.
- Seager, W.R., Kottowski, F.E., and Hawley, J.W., 1976, Geology of the Doña Ana Mountains, New Mexico: New Mexico Bureau of Mines and Mineral Resources Circular 147, 35 p.
- Seager, W.R., and McCurry, M., 1988, The cogenetic Organ cauldron and batholith, south central New Mexico: Evolution of a large-volume ash flow cauldron and its source magma chamber: *Journal of Geophysical Research*, v. 93, p. 4421-4433.
- Seager, W.R., and Mayer, A.B., 1988, Uplift, erosion, and burial of Laramide fault blocks, Salado Mountains, Sierra County, New Mexico: *New Mexico Geology*, v. 10, p. 49-53.
- Seaman, S., 1988, Geology and petrogenesis of ash-flow-tuffs and rhyolitic lavas associated with the Gila Cliff Dwelling-Bursum Caldera complex: unpublished Ph.D. dissertation, University of New Mexico, Albuquerque, 170 p.
- Steven, T.A., and Lipman, P.W., 1976, Calderas of the San Juan volcanic field, southwestern Colorado: U.S. Geological Survey Professional Paper 958, 35 pp.
- Strangway, D.E., Simpson, J., and York, D., 1976, Paleomagnetic studies of volcanic rocks from the Mogollon Plateau area of Arizona and New Mexico: New Mexico Geological Society Special Publication 5, p. 119-124.
- Turner, G., 1968, The distribution of potassium and argon in chondrites, in Ahrens, L.H. (ed.), *Origin and Distribution of the Elements*: Pergamon, London, p. 387-398.

- Wahl, D.E., Jr., 1980, Mid-Tertiary volcanic geology in parts of Greenlee County, Arizona, Grant and Hidalgo Counties, New Mexico: unpublished Ph.D. dissertation, Arizona State University, Tempe, 149 pp.
- Walker, G.P.L., Heming, R.F., and Wilson, C.J.N., 1980, Low-aspect ratio ignimbrites: *Nature*, v. 283, p. 286-287.
- Weiss, S.J., Noble, D.C., and McKee, E.H., 1989, Paleomagnetic and cooling constraints on the duration of the Pahute Mesa - Trail Ridge eruptive event and associated magmatic evolution, Black Mountain volcanic center, southwestern Nevada: *Journal of Geophysical Research*, v. 94, p. 6075-6084.
- Wells, R.E., and Hillhouse, J.W., 1989, Paleomagnetism and tectonic rotation of the lower Miocene Peach Springs Tuff: Colorado Plateau, Arizona, to Barstow, California: *Geological Society of America Bulletin*, v. 101, p. 846-863.
- Woodward, T.W., 1982, Geology of the Lookout Mountain area, Black Range, Sierra County, New Mexico: unpublished M.S. thesis, Univ. New Mexico, Albuquerque, 95 p.
- Zeitler, P.K., 1987, Argon diffusion in partially outgassed alkali feldspars: Insights from  $^{40}\text{Ar}/^{39}\text{Ar}$  analysis: *Chemical Geology*, v. 65, p. 167-181.

Calibration of the latest Eocene-Oligocene Magnetic  
Polarity Time Scale using  $^{40}\text{Ar}/^{39}\text{Ar}$  dated ignimbrites  
McIntosh, William C., N.M. Bureau of Mines and Mineral  
Resources and Department of Geosciences, N.M.  
Institute of Mining and Technology, Socorro, NM 87801

#### ABSTRACT

A discontinuous record of Late Eocene-Oligocene geomagnetic polarity has been determined using high-precision ( $\pm 0.15$  Ma)  $^{40}\text{Ar}/^{39}\text{Ar}$  sanidine dating of a sequence of 36.2 to 24.3 Ma ignimbrites in southwest New Mexico. This polarity record includes 7 polarity reversals and tightly constrains the age and length of four polarity intervals: 27.4-28.0 Ma normal, 28.0-28.9 Ma reversed, 34.6-34.9 Ma reversed, and 34.9-35.9 Ma normal.

The Mogollon-Datil polarity records best fits the marine magnetic anomaly record if these 4 polarity intervals are correlated with marine anomalies 10, 10r, 15r, and 16. This calibration indicates an Eocene-Oligocene boundary age near 33.6 Ma, in agreement with radiometric data from Barbados microtektites and Gubbio biotites.

#### INTRODUCTION

Radiometric calibration of the mid-Tertiary Magnetic Polarity Time Scale (MPTS) has been the focus of much work during the last two decades. The number and relative lengths of Tertiary geomagnetic polarity chrons have been



well-established (Mankinen and Dalrymple, 1979; Ness et al., 1980, Berggren et al., 1985) and these chrons have been reliably correlated with marine biostratigraphy (Lowrie et al., 1982, Berggren et al., 1985). Precise radiometrically dated calibration points for the MPTS, however, have proven elusive. For example, published estimates of the age of the Eocene-Oligocene boundary range from 32 to 38 Ma (Fig. 1; Berggren et al., 1985).

Direct calibration of the MPTS by radiometric dating of sea-floor basalts is severely limited by problems of alteration and excess argon retention (Berggren et al., 1985). Instead, terrestrial and marine stratigraphic sequences have been used to provide radiometric calibration points.

K-Ar ages and polarity determinations from terrestrial lavas have been used to calibrate the late Neogene MPTS to 10 Ma (Cox and Dalrymple, 1967; McDougall et al., 1976; Harrison et al., 1979). However, it has proven impossible to extend this purely volcanic-based calibration method beyond 10-15 Ma, because errors in conventional K-Ar determinations become large relative to the lengths of individual polarity intervals (Berggren et al., 1985).

Most published Tertiary MPTS calibration schemes (Fig. 1) have used interpolation between the Neogene lava data and various older calibration points, including K-Ar constraints on biostratigraphic boundaries (LaBrecque et al., 1977; Ness et al., 1980; Lowrie and Alvarez, 1981) and K-Ar dated

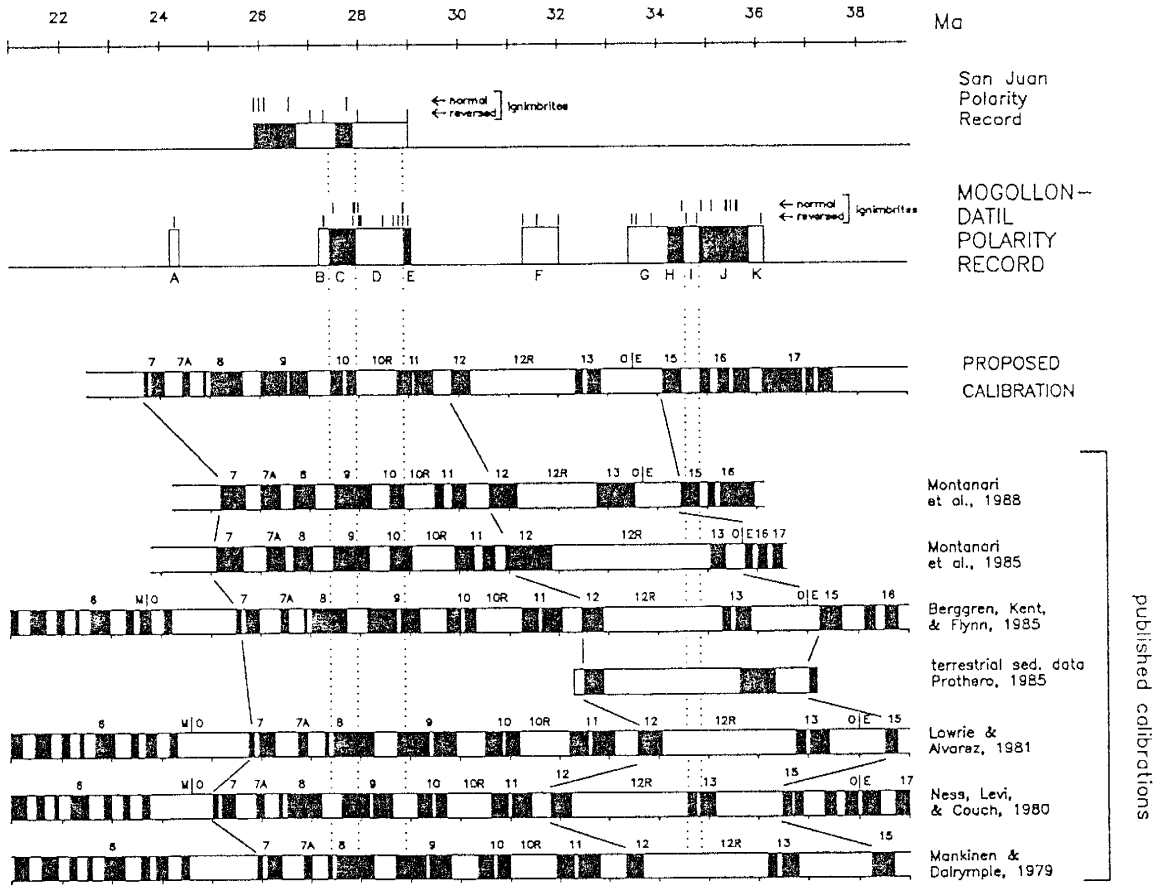


Fig. 1. Polarity record of Mogollon-Datil ignimbrites, its proposed correlation with the MPTS, and comparisons with other published MPTS schemes. Black denotes normal and white reversed polarity. Mogollon-Datil polarity intervals are lettered A-K and reversals are numbered 1-7. Marine anomalies are conventionally numbered (Mankinen and Dalrymple, 1979). M|O and O|E respectively denote inferred ages of the Miocene-Oligocene and Oligocene-Eocene boundaries. Also shown for comparison is the polarity record of  $^{40}\text{Ar}/^{39}\text{Ar}$  dated ignimbrites from the San Juan volcanic field, after paleomagnetic data of Diehl et al. (1974) and Beck et al. (1977) and radiometric data of Lanphere (1988) and Lipman (1987).

volcanic units within magnetostratigraphically studied terrestrial sedimentary sequences (Berggren et al., 1985; Prothero, 1985; Prothero and Armentrout, 1985). These terrestrial-based MPTS schemes show good agreement, suggesting ages of 36 to 38 Ma for the Eocene-Oligocene boundary (Fig. 1).

Younger Eocene-Oligocene boundary ages have been inferred from radiometrically dated materials from marine sedimentary sequences.  $^{40}\text{Ar}/^{39}\text{Ar}$  ages of microtektites in Late Eocene marine deposits in Barbados imply an Eocene-Oligocene boundary age of  $34.4 \pm 0.6$  Ma (Glass et al., 1986). Glauconite K-Ar ages suggest a boundary near 32 Ma (Curry and Odin, 1982), but are considered unreliable (Montanari et al., 1985; Berggren et al., 1985). K-Ar and Rb-Sr ages of biotites from bentonites within Italian carbonate sections were originally interpreted to indicate an age of  $35.7 \pm 0.4$  Ma for the Eocene-Oligocene boundary (Fig. 1; Montanari et al., 1985), but have been re-interpreted as supporting a boundary age of  $33.7 \pm 0.4$  Ma (Montanari et al., 1988).

The 20% variation in published estimates for the Eocene-Oligocene boundary highlights the present uncertainty in radiometric calibration of the mid-Tertiary MPTS. A new approach to this problem lies in high-precision  $^{40}\text{Ar}/^{39}\text{Ar}$  dating and paleomagnetic polarity studies of mid-Tertiary silicic volcanic fields.

This study has focussed on the late Eocene-Oligocene silicic Mogollon-Datil volcanic field of southwestern New

Mexico (Fig. 2), which includes at least 30 widespread (>1000 km<sup>2</sup>), voluminous (100-1300 km<sup>3</sup>) ignimbrites (ash-flow tuffs). High-precision <sup>40</sup>Ar/<sup>39</sup>Ar dating and paleomagnetic analysis have facilitated correlation of the ignimbrites between isolated fault block mountain ranges, allowing development of an integrated time-stratigraphic framework for the volcanic field (McIntosh et al., 1986).

#### METHODS

Oriented samples were drilled from 402 sites in ignimbrites and 66 sites in mafic and silicic lavas. Samples were analyzed using standard paleo- and rock-magnetic techniques, including progressive alternating field and thermal demagnetization, thermomagnetic analysis, isothermal and anhysteretic remanent magnetization acquisition/demagnetization experiments, and reflected light microscopy.

<sup>40</sup>Ar/<sup>39</sup>Ar plateau ages (Fleck et al., 1977) were obtained from 87 samples of ultra-pure (>>99%) sanidine separates. Samples were irradiated in the US Geological Survey TRIGA reactor and neutron fluxes were monitored using MMhb1 (520.4 Ma, Sampson and Alexander, 1987) and FCT-3 (Fish Canyon Tuff sanidine, 27.83 Ma, recalculated from Kunk et al., 1985, using the above age for MMhb1). Each sample was analyzed in 3-7 incremental heating steps using the U.S. Geological Survey VG-Micromass 1200B spectrometer at Reston, Va. (analytical precision of Ar isotopic ratios typically ±0.1%).

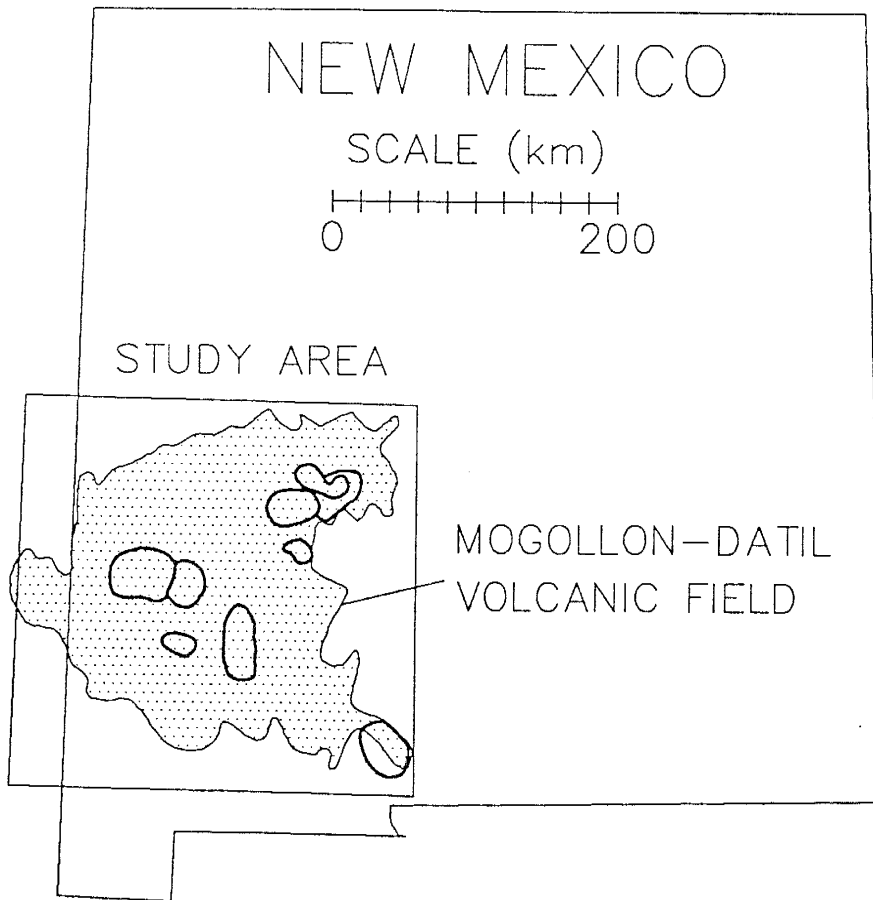


Fig. 2. Map showing location of the study area in the Mogollon-Datil volcanic field (stippled). Heavy lines depict inferred calderas.

## MOGOLLON-DATIL POLARITY RECORD

Paleo- and rock-magnetic analyses show that Mogollon-Datil ignimbrites, with few exceptions, carry thermoremanent magnetizations (TRMs) carried primarily by ultrafine magnetite and acquired during rapid post-emplacement cooling. TRM data have been used to distinguish between lithologically identical ignimbrites, and to trace units to their thin, unwelded, distal fringes, demonstrating overlap relationships between different eruptive centers (McIntosh et al., 1986).

$^{40}\text{Ar}/^{39}\text{Ar}$  sanidine plateau ages from Mogollon-Datil ignimbrites provide a tremendous increase in precision over conventional K-Ar and fission-track dating techniques (Table 1; cf. Lanphere, 1988). The 1 analytical precision of individual plateau ages is  $\pm 0.07$ - $0.14$  Ma, and multiple plateau ages from separate samples of individual units show 1 errors of  $\pm 0.04$  to  $0.13$  Ma (Table 1, Fig. 3; McIntosh et al., 1986; Kedzie et al., 1985). These results stand in sharp contrast to 1 errors of at least  $\pm 1.3$ - $2.3$  Ma for multiple conventional K-Ar and fission-track ages on the same units (Table 1; Marvin et al., 1987). The high precision of these  $^{40}\text{Ar}/^{39}\text{Ar}$  ages is further shown by their close agreement with independently established stratigraphic order (Fig. 3). The units range in age from 36.2 to 24.3 Ma and group into 4 strongly episodic eruptive intervals (Fig. 3).

A composite stratigraphic sequence of Mogollon-Datil

# MOGOLLON-DATIL POLARITY RECORD

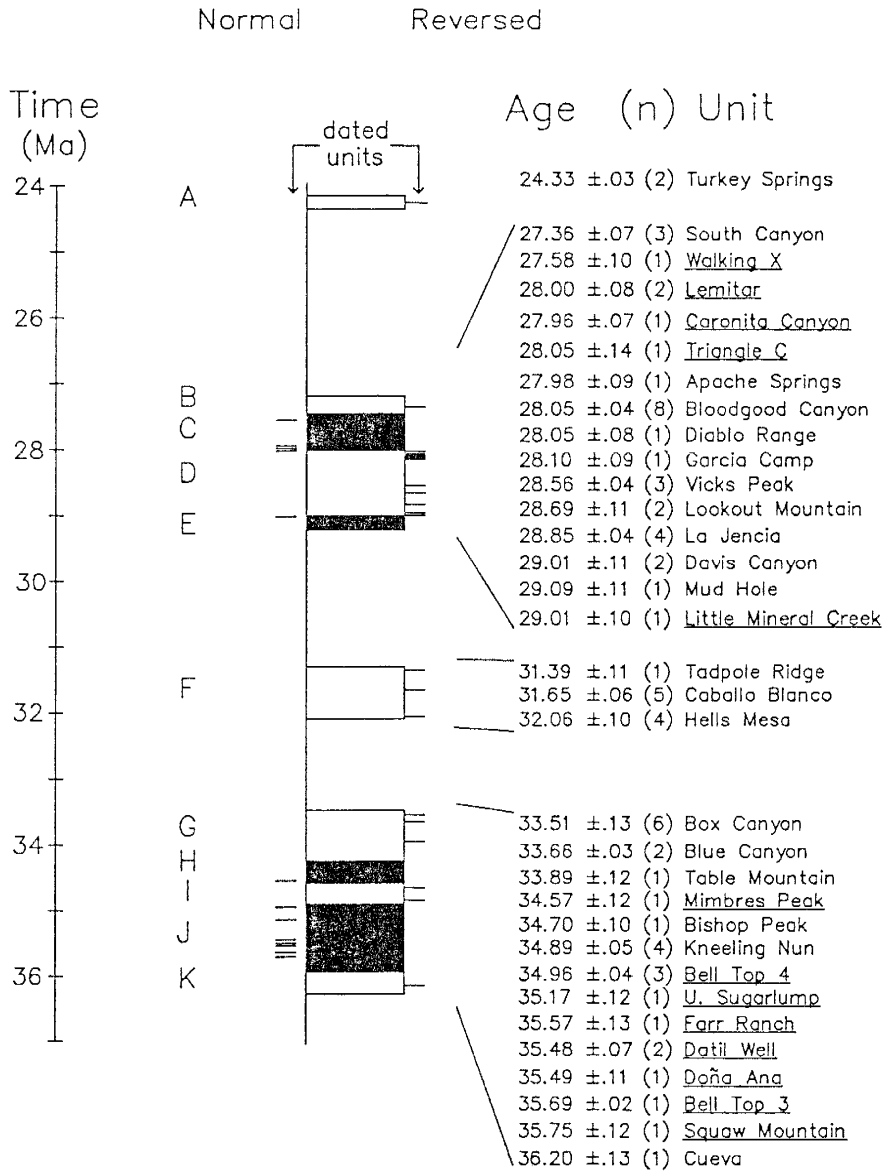


Fig. 3. Composite stratigraphic section and magnetic polarity record of well-dated Mogollon-Datil ignimbrites, showing episodic nature of volcanism. Polarity intervals are lettered (black=normal, white=reversed), and adjacent horizontal lines depict dated ignimbrites. Right column shows mean  $^{40}\text{Ar}/^{39}\text{Ar}$  plateau ages, unit names, polarity (normal units underlined), and number of age determinations (in parentheses). The majority of the stratigraphic relationships can be unequivocally demonstrated, independently of age data, using field relations and paleomagnetic correlation.

Table 1. A comparison of  $^{40}\text{Ar}/^{39}\text{Ar}$ , K/Ar, and fission-track age determinations for the Bloodgood Canyon Tuff. K/Ar and fission-track data from Marvin et al., 1987.

method	mineral	n	mean age (Ma)	standard deviation ( $1\sigma$ )
$^{40}\text{Ar}/^{39}\text{Ar}$	sanidine	8	28.05	$\pm 0.04$
K/Ar	sanidine	27	26.9	$\pm 1.3$
K/Ar	biotite	8	28.8	$\pm 1.4$
Fission track	zircon	11	28.2	$\pm 2.1$
Fission track	sphene	4	28.1	$\pm 2.2$



ignimbrites (Fig. 3) has been developed by augmenting existing detailed mapping with correlations based on  $^{40}\text{Ar}/^{39}\text{Ar}$  and paleomagnetic data. Although this sequence is nowhere present in its entirety, the majority of the individual stratigraphic relationships are unequivocal.

The combination of  $^{40}\text{Ar}/^{39}\text{Ar}$ , paleomagnetic, and stratigraphic data from the Mogollon volcanic field yields a precise but discontinuous record of mid-Tertiary geomagnetic polarity history which includes 11 distinct polarity intervals (informally labelled A to K in Figures 1 and 3). Although some polarity intervals (A,B,H,K) are each represented by a single dated ignimbrite, their existence is further supported by polarity data from other stratigraphically constrained but undated tuffs and lavas. Seven polarity reversals are represented in the Mogollon-Datil polarity record; 5 of these (1,2,3,5,6 in Figure 3) are tightly constrained by ignimbrites differing in age by 0.2 Ma or less. For reversals 2 and 3, established stratigraphic order allows unambiguous determination of the reversal pattern, although the mean ages of some units disagree with this established order by as much as 0.1 m.y. (Fig. 3).

The Mogollon-Datil polarity record shows good agreement with the polarities of  $^{40}\text{Ar}/^{39}\text{Ar}$  dated units from the San Juan volcanic field (Fig. 1).

#### CORRELATION WITH THE MARINE ANOMALY RECORD

Two features in the Mogollon-Datil polarity record are

particularly significant for correlation with marine magnetic anomalies: the 0.9 m.y. reversed interval D, and the 0.7-1.2 m.y. normal interval J (Fig. 1). No published MPTS schemes correlate well with these two features (Fig. 1). The best fit with the marine anomaly record requires the correlation of polarity intervals D and J respectively with marine anomalies 10r and 15. Anomaly 10r, with a calculated duration of 0.9 Ma (Berggren et al., 1985), represents the only single reversed interval of suitable age long enough to correspond to zone D. Similarly, normal interval J is too long to correlate with marine anomalies 13 or 15.

A calibration scheme for the mid-Tertiary MPTS based on the above correlation is given in Figure 1. Anomaly ages have been calculated using Mogollon-Datil reversals 2 (28.00 Ma) and 6 (34.90 Ma) and interpolating the ages of other anomalies under the assumption of constant spreading rates from 36 to 24 Ma. This calibration indicates an Eocene-Oligocene boundary near 33.6 Ma, based on a boundary located at the midpoint of anomaly 13r (Berggren et al., 1985). This boundary age closely agrees with radiometric data from Gubbio biotites (Montanari et al., 1988) and Caribbean microtektites (Glass et al., 1986), but is considerably younger than the age indicated by most terrestrial-based MPTS calibration schemes (Figs. 1,4).

#### DISCUSSION

The proposed Mogollon-Datil calibration of the mid-

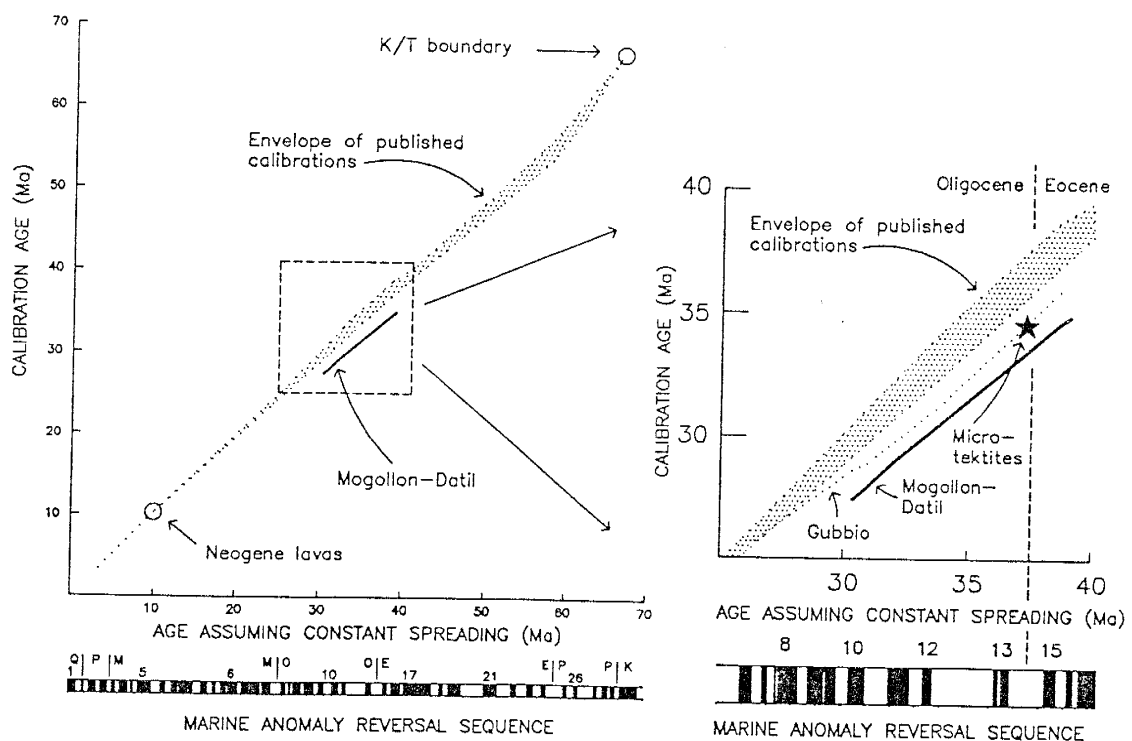


Fig. 4. A comparison of the Mogollon-Datil ignimbrite-based MPTS calibration (solid line), with the Montanari et al (1988) calibration (dotted line), microtektite ages (star, after Glass et al., 1986), and other published calibration schemes (shaded region envelopes Berggren et al., 1985; Lowrie and Alvarez, 1981; Ness et al., 1980; and Mankinen and Dalrymple, 1979). Circles depict widely accepted calibration points at 10.3 and 66.4 Ma.

Tertiary MPTS is analogous to the successful use of lava sequences to calibrate the late Neogene geomagnetic polarity record (McDougall et al., 1976; Harrison et al., 1979).

This type of approach was formerly limited to the Neogene by inherent errors in whole-rock K-Ar dating of basalts, but extension of this technique into mid-Tertiary time is now permitted by high-precision  $^{40}\text{Ar}/^{39}\text{Ar}$  dating of sanidine-bearing ignimbrites. The development of an accurate stratigraphic framework for the Mogollon-Datil volcanic field was essential to this approach, because the placement of each volcanic unit in stratigraphic context allows substantial increases in resolution and reliability over random dating of unrelated units (Cox, 1982; Harrison et al., 1979).

Sanidine-bearing ignimbrites in North American silicic volcanic fields offer the most precisely datable record of mid-Tertiary polarity history. Although this polarity record is inherently discontinuous compared to the record of sedimentary sequences, ignimbrites can be dated to a much higher precision than the mafic lavas or biotite-bearing ashes used in other calibration schemes (Montanari, 1988, Prothero, 1985; Prothero and Armentrout, 1985).

Furthermore, because ignimbrites carry TRMs, the geomagnetic polarity at the time of emplacement can be determined with absolute certainty. Unambiguous TRMs of this nature are far superior to the post-depositional chemical remanence components carried by many sedimentary units (e.g. Walker et

al., 1981).

The implications of the MPTS radiometric calibration supported by the Mogollon-Datil magnetic polarity record are far-reaching. An Eocene-Oligocene boundary near 33.6 Ma requires re-evaluation of present correlations between mid-Tertiary marine and terrestrial biostratigraphic records. Furthermore, the indicated ages of anomalies 10 to 16 are significantly younger than ages predicted from models based on constant spreading rates (Fig. 4). If other calibration points based on Neogene lavas (Harrison et al., 1979) and the age of the K-T boundary (Berggren et al., 1985) are correct, the Mogollon-Datil calibration points indicate a world-wide early Tertiary acceleration of sea-floor spreading rates, followed by late Tertiary deceleration (Fig. 4). Calibration of the MPTS using mid-Tertiary silicic volcanic fields will eventually allow "fine-tuning" of sea floor spreading rate determinations and provide constraints on accelerations inferred from other forms of data (e.g. Pollitz, 1988).

## REFERENCES

- Beck, M.E., Sheriff, S.D., Diehl, J.F., and Hailwood, E.A., 1977, Further paleomagnetic results for the San Juan volcanic field of southern Colorado: Earth and Planetary Science Letters, v. 37, p. 124-130.
- Berggren, W.A., Kent, D.V., and Flynn, J.J., 1985, Jurassic to Paleogene: Part 2, Paleogene geochronology and chronostratigraphy, In: N.J. Snelling (ed.), The Chronology of the Geological Record: Geological Society of London Memoir 10, p. 141-195.
- Cox, A.V., 1982, Magnetic reversal time-scale, in Harland et al., A Geological Time Scale: Cambridge University Press, Cambridge, 128 p.
- Cox, A.V., and Dalrymple, G.B., 1967, Statistical analysis of geomagnetic reversal data and the precision of potassium-argon dating: Journal of Geophysical Research, v. 72, p. 2603-2614.
- Curry, D., and Odin, G.S., 1982, Dating of the Paleogene, in Odin, G.S. (ed.), Numerical Dating in Stratigraphy: John Wiley, New York, p. 607-30.
- Diehl, J.F., Beck, M.E., and Lipman, P.W., 1974, Paleomagnetism and magnetic-polarity zonation in some Oligocene volcanic rocks of the San Juan Mountains, south-western Colorado: Geophysical Journal, v. 37, p. 323-332.
- Fleck, R.J., Sutter, J.F., and Elliot, D.H., 1977, Interpretation of discordant  $^{40}\text{Ar}/^{39}\text{Ar}$  age-spectra of Mesozoic tholeiites from Antarctica: Geochimica Cosmochimica Acta, v. 41, p. 15-32.
- Glass, B.P., Hall, C.M., and York, D., 1986,  $^{40}\text{Ar}/^{39}\text{Ar}$  dating of North American tektite fragments from Barbados and the age of the Eocene-Oligocene boundary: Chemical Geology, v. 59, p. 181-186.
- Harrison, C.G.A., McDougall, I., and Watkins, N.D., 1979, A geomagnetic field reversal time-scale back to 13.0 million years before present: Earth and Planetary Science Letters, v. 42, p. 143-152.
- Kedzie, L.L., Sutter, J.F., and Chapin, C.E., 1985, High-precision  $^{40}\text{Ar}/^{39}\text{Ar}$  ages of widespread Oligocene ash-flow tuff sheets near Socorro, New Mexico [abs.]: EOS (American Geophysical Union Transactions), v. 17, p. 625.

- Kunk, M.J., Sutter, J.F., and Naeser, C. W., 1985, High-precision  $^{40}\text{Ar}/^{39}\text{Ar}$  ages of sanidine, biotite, hornblende, and plagioclase from the Fish Canyon Tuff, San Juan volcanic field, south-central Colorado [abs.]: EOS (American Geophysical Union Transactions), v. 17, p. 636.
- LaBrecque, J.L., Kent, D.V., and Cande, S.C., 1977, Revised magnetic polarity time-scale from Late Cretaceous and Cenozoic time: *Geology*, v. 5, p. 330-335.
- Lanphere, M.A., 1988, High-resolution  $^{40}\text{Ar}/^{39}\text{Ar}$  chronology of Oligocene volcanic rocks, San Juan Mountains, Colorado: *Geochimica Cosmochimica Acta*, v. 52, p. 1425-1434.
- Lipman, P.W., 1987, Oligocene central San Juan caldera cluster, Colorado: Geological Society of America Abstracts with Programs, v. 19, p. 315.
- Lowrie, W., and Alvarez, W., 1981, One hundred million years of geomagnetic polarity history: *Geology*, v. 9, p. 329-397.
- Lowrie, W., Napoleone, G., Perch-Nielson, K., Premoli Silva, I., and Toumarkine, M., 1982, Paleogene magnetic stratigraphy in Umbrian pelagic carbonate rocks: The Contessa sections, Gubbio: Geological Society of America Bulletin, v. 93, p. 414-432.
- Mankinen, E.A., and Dalrymple, G.B., 1979, Revised geomagnetic polarity time scale for the interval 0-5 m.y. B.P.: *Journal of Geophysical Research*, v. 84, p. 615-626.
- Marvin, R.F., Naeser, C.W., Bikerman, M., Mehnert, H.H., and Ratté, J.C., 1987, Isotopic ages post-Paleocene igneous rocks within and bordering the Clifton  $1^\circ \times 2^\circ$  quadrangle, Arizona-New Mexico: New Mexico Bureau of Mines and Mineral Resources Bulletin 118, 63 p.
- McDougall, I., Watkins, N.D., Walker, G.P.L., and Kristjansson, L., 1976, Potassium-Argon and paleomagnetic analysis of Icelandic lava flows: Limits on the age of Anomaly 5: *Journal of Geophysical Research*, v. 81, p. 1505-1521.
- McIntosh, W.C., Sutter, J.F., Chapin, C.E., Osburn, G.R., and Ratté, J.C., 1986, A stratigraphic framework for the Mogollon-Datil volcanic field based on paleomagnetism and high-precision  $^{40}\text{Ar}/^{39}\text{Ar}$  dating of ignimbrites - a progress report: New Mexico Geological Society Guidebook 37, p. 183-195.

- Montanari, A., Drake, R., Bice, D.M., Alvarez, W., Curtis, G.H., Turrin, B.D., DePaolo, D.J., 1985, Radiometric time scale for the upper Eocene and Oligocene based on K-Ar and Rb-Sr dating of volcanic biotites from the pelagic sequence of Gubbio, Italy: *Geology*, v. 13, p. 596-599.
- Montanari, A., DePaolo, D.J., Drake, R., Alvarez, W., Deino, A., Curtis, G.H., Odin, G.S., Turrin, B.D., DePaolo, D.J., Bice, D.M., 1988, Radio-isotopic calibration of the Upper Eocene and Oligocene magnetic polarity and foraminiferal time scales in the northern Apennines of Italy: *Geological Society of America Abstracts with Programs*, v. 20, p. 178.
- Ness, G., Levi, S., and Couch, R., 1980, Marine magnetic anomaly timescales for the Cenozoic and Late Cretaceous. A precis, critique, and synthesis: *Reviews of Geophysics and Space Physics*, v. 18, p. 753-770.
- Pollitz, F.F., 1988, Episodic North America and Pacific plate motions: *Tectonics*, v. 7, p. 711-726.
- Prothero, D.R., 1985, Chadronian (Early Oligocene) magnetostratigraphy of eastern Wyoming: implications for the age of the Eocene-Oligocene boundary: *Journal of Geology*, v. 93, p. 555-565.
- Prothero, D.R., and Armentrout, J.M., 1985, Magnetostratigraphic correlation of the Lincoln Creek Formation, Washington: implications for the age of the Eocene/Oligocene boundary: *Geology*, v. 13, p. 208-211.
- Samson, S.D., and Alexander, E.C.Jr., 1987, Calibration of the interlaboratory  $^{40}\text{Ar}/^{39}\text{Ar}$  dating standard, MMhb-1: *Chemical Geology*, v. 66, p. 27-34.
- Walker, T.R., Larson, E.E., and Hoblitt, R.P., 1981, The Nature and origin of hematite in the Moenkopi Formation (Triassic), Colorado Plateau: A contribution to the origin of magnetism in red beds: *Journal of Geophysical Research*, v. 86, p. 317-333.



Appendix 1. Complete site-level paleomagnetic data from Mogollon-Datil ignimbrites.

site loc.	lat(N)	long(W)	dip	str	NRM					AF demag					type			
					inc	dec	int	k	$\alpha_{95}$	n/t	dm	inc	dec	int		k	$\alpha_{95}$	n/t
tuff of Turkey Springs (24.3 Ma)																		
024 rt107	33.931	107.334	22	332	-47.3	172.0	2.2E+01	478	2.8	7/8	30	-51.8	175.9	112	3.6	15/2/2		
025 rt107	33.930	107.333	22	332	-48.6	164.0	1.5E-01	261	4.2	6/8	40	-47.4	171.0	1.0E-01	345	3.3	7/8	1
055 park	33.761	107.425	32	120	-48.6	154.1	7.9E-01	4	34.4	8/8	30	-52.8	165.4	1.7E-01	369	2.9	8/8	2
137 paddy	33.719	107.812	0	0	-55.6	212.3	5.5E-01	3	60.0	5/8	30	-49.7	190.9	2.3E-01	449	3.6	5/8	2
183 frnch	33.840	107.715	6	200	40.7	173.0	4.7E+00	1	180.0	2/8	40	-58.9	173.8	6.7E-02	139	5.1	7/8	2
185 stone	33.681	107.795	4	180	-52.4	180.9	4.0E-01	680	2.1	8/8	30	-52.3	181.6	3.0E-01	747	2.0	8/8	1
186 stone	33.682	107.791	4	180	-53.1	178.0	2.3E-01	510	2.5	8/8	30	-52.8	178.7	7.5E-02	521	2.4	8/8	1
199 allen	33.744	107.429	10	330	-51.3	172.4	2.0E-01	1335	1.5	8/8	30	-54.3	174.0	8.4E-02	2250	1.2	8/8	1
215 cochl	33.929	107.333	30	3	-61.9	189.5	2.4E-01	56	7.5	8/8	30	-57.7	191.1	2.3E-01	442	2.6	8/8	1
216 rt107	33.883	107.312	22	334	-44.0	168.0	1.9E-01	542	2.4	8/8	30	-43.3	168.4	1.9E-01	569	2.3	8/8	1
217 parkE	33.757	107.399	10	259	-46.3	156.2	2.5E-01	12	15.8	9/9	30	-49.2	161.8	1.1E-01	107	5.0	9/9	2
218 parkE	33.759	107.412	25	316	-51.1	171.9	1.9E-01	669	2.1	8/8	30	-51.1	173.3	9.5E-02	802	2.0	8/8	1
219 paddy	33.701	107.842	0	0	-50.0	237.6	8.6E-01	3	45.9	6/8	40	-53.8	197.9	1.0E-01	119	6.2	6/8	2
338 porto	33.869	107.211	20	35	-49.0	176.8	7.2E-02	33	9.8	8/8	30	-47.2	180.9	4.6E-02	677	2.1	8/8	1
348 holdC	33.605	107.487	12	130	-54.9	144.6	6.6E-01	9	21.7	7/8	30	-52.5	169.8	1.7E-01	114	5.7	7/8	2
364 kelog	33.857	107.700	6	145	-16.2	200.0	1.8E+00	1	82.6	6/8	40	-37.4	189.3	7.4E-02	77	7.7	6/8	2 Aag
424 tmile	33.799	107.275	8	0	-36.6	141.2	6.5E-01	2	48.2	8/8	40	-42.5	204.4	2.6E-01	231	4.4	6/8	2 Aag
176 kelog	33.875	107.693	15	165	-36.3	138.9	1.0E-01	2	75.5	8/8	80	-41.1	171.7	3.0E-03	43	19.0	3/8	4 R
184 frnch	33.840	107.713	6	200	76.7	54.5	3.1E+00	1	67.9	8/8	40	-72.1	301.2	2.9E-01	1	180.0	8/8	4 R
tuff of Slash Ranch (26.1 Ma)																		
115 rrcan	33.481	108.129	0	0	61.2	178.9	3.9E-02	92	6.3	7/8	20	57.6	166.9		371	13.0	2/0/1	E
471 vxtL	33.472	108.119	0	0	43.3	65.3	5.4E-02	5	24.3	9/8	20	58.9	161.8	8.7E-03	39	8.9	8/8	2 E
473 rict	33.270	108.145	0	0	35.3	352.6	1.8E-02	5	28.2	8/8	100	40.1	60.4	1.7E-03	9	43.6	3/8	4 R
South Canyon Tuff - outflow facies (27.4 Ma)																		
mean outflow and thin intracaldera facies South Canyon												-30.2	204.3		66	4.7	15/3/2	
												-30.7	202.1		70	3.5	24/5/4	
004 molin	33.963	107.068	40	330	-27.5	185.8	2.3E-01	34	9.6	8/8	20	-32.9	189.3	5.9E-02	106	5.4	8/8	1
007 cork	34.144	107.002	35	150	-50.8	208.4	2.9E-02	5	27.7	8/8	20	-38.3	191.5	2.1E-02	195	4.3	7/8	2
036 joyit	34.156	106.828	43	185	-38.1	205.3	2.8E-01	203	3.9	8/8	30	-36.5	202.9	1.3E-01	237	3.9	7/8	1
105 nogal	33.898	106.986	30	302	-16.1	206.9	2.8E-01	64	7.0	8/8	20	-15.9	206.4	1.5E-01	76	6.4	8/8	1
138 paddy	33.743	107.793	0	0	-28.6	206.5	2.1E-01	619	2.7	6/8	30	-29.1	207.6	1.1E-01	471	3.1	6/8	1
187 stone	33.687	107.768	4	180	-27.6	202.3	1.5E-01	683	2.6	6/8	40	-25.7	202.9	3.2E-02	782	2.4	6/8	1
188 stone	33.686	107.763	4	180	-16.3	213.5	2.1E-01	73	6.5	8/8	30	-19.2	213.6	3.5E-02	59	7.3	8/8	1
250 luera	33.745	107.903	0	0	-18.3	208.2	1.8E-01	7	23.3	8/8	30	-27.7	209.9	1.2E-01	343	3.0	8/8	2
251 luera	33.772	107.903	0	0	1.1	216.1	4.4E-01	2	54.7	8/8	40	-22.3	212.9	3.1E-02	218	3.8	8/8	2
252 luera	33.773	107.902	0	0	-29.2	207.6	2.0E-01	260	3.4	8/8	30	-30.3	207.7	1.7E-01	274	3.4	8/8	1
258 scale	33.410	107.904	8	180	-38.3	204.9	3.2E-01	38	8.5	9/9	30	-34.2	206.0	5.4E-02	162	4.0	9/9	1
380 s.lmp	34.158	107.942	0	0	-38.6	180.0	2.9E-01	6	25.9	8/8	40	-31.3	208.1	4.6E-02	152	4.5	8/8	2
515 monic	33.987	107.574	0	0	-25.5	202.4	4.3E-02	14	14.5	9/9	30	-26.5	207.5	1.1E-02	141	5.7	6/9	2
197 jorna	34.006	106.664	42	180	-22.9	218.8	5.4E-01	193	4.0	8/8	30	-21.8	217.0	1.2E-01	379	2.9	8/8	1
008 cork	34.152	107.004	35	150	-32.2	200.9	1.8E-01	6	26.2	7/8	20	-44.6	195.5	1.6E-01	298	3.5	7/8	2 Ad
242 kelog	33.874	107.682	15	145	-9.5	235.9	6.7E-01	778	2.0	8/8	30	-9.0	236.7	1.5E-01	515	2.4	8/8	1 Ac
013 joyit	34.156	106.826	33	195	-15.4	197.4	2.3E+00	18	13.4	8/8	30	-14.2	197.9	2.5E-01	18	13.5	8/8	2 R
166 porto	33.833	107.162	25	358	-27.8	156.3	2.2E+00	1	79.7	8/8	80	-38.0	202.3	2.4E-02	37	11.2	6/8	2 R
South Canyon Tuff - southern intracaldera facies																		
053 park	33.765	107.435	13	36	-24.9	201.0	3.3E-01	19	13.2	8/8	40	-31.3	198.4		87	5.6	9/2/2	
058 oakS	33.791	107.406	22	5	-29.4	205.5	6.8E-01	547	2.4	8/8	40	-23.0	192.8	3.2E-01	718	2.1	8/8	2
060 rattl	33.789	107.388	9	355	-11.8	237.8	1.1E+01	1	52.9	8/8	30	-30.5	204.7	1.7E-01	706	2.1	8/8	1
061 rosed	33.806	107.387	17	4	-21.2	169.0	1.6E+00	4	36.6	7/8	40	-31.6	194.4	3.8E-01	61	7.1	8/8	2
063 rosed	33.810	107.370	22	21							40	-22.2	188.0	5.9E-01	852	2.1	7/8	2 ?
080 oakS	33.791	107.407	27	5	-24.4	200.8	5.1E-01	223	2.6	15/15	30	-37.2	211.1		244	3.9	7/8	2
081 park	33.766	107.436	17	78	-34.7	197.7	2.8E-01	232	4.0	7/8	40	-27.6	199.7	2.1E-01	188	2.8	15/15	1
082 allen	33.751	107.443	19	60	-34.1	208.5	1.0E-01	78	6.3	8/8	40	-34.6	197.1	2.5E-01	175	4.6	7/8	1
127 rosed	33.817	107.373	33	5	-40.4	191.5	4.9E-01	83	6.1	8/8	40	-35.4	206.8	1.0E-01	157	4.4	8/8	1
057 oakS	33.790	107.402	14	196	-30.3	185.7	4.7E-01	823	1.9	8/8	30	-38.0	192.7	1.7E-01	258	3.5	8/8	1
062 rosed	33.791	107.446	12	350	-44.4	126.5	4.9E-01	3	56.6	5/8	30	-28.1	182.6	1.7E-01	491	2.5	8/8	1 Af
047 e.red	33.733	107.346	9	329	-28.1	192.8	3.8E-02	4	34.5	8/8	30	-29.2	172.9	1.1E-01	1612	1.9	5/8	2 Af
059 rattl	33.786	107.387	16	48	-35.0	226.1	1.1E-02	5	28.9	8/8	40	-19.0	188.1	1.9E-02	5	29.2	8/8	4 R
South Canyon Tuff - northern intracaldera facies																		
019 monic	33.930	107.513	13	233	-60.1	151.0	5.4E+00	3	39.6	8/8	30	-42.8	174.0	7.6E-01	8	20.5	8/8	4 R
												-46.2	186.7		13	12.7	12	
												-56.9	156.5	7.9E-01	318	3.4	7/8	2 Af

E2

Appendix 1. (continued) Complete site-level paleomagnetic data from Mogollon-Datil ignimbrites.

site loc.	lat(°N)	long(°W)	dip	str	NRM						AF demag						type	
					inc	dec	int	k	α95	n/t	dm	inc	dec	int	k	α95		n/t
020 monic	33.934	107.511	11	260	-34.1	208.3	1.3E+00	920	1.8	8/8	30	-35.1	210.7	2.5E-01	378	2.9	8/8	1 Af
023 rt107	33.929	107.337	22	345	-39.5	191.0	5.1E-01	122	5.0	8/8	40	-42.5	189.2	2.4E-01	156	5.4	6/8	1
026 bigro	33.910	107.395	55	0	-63.3	189.2	9.3E-01	72	7.2	7/8	40	-67.8	186.2	8.1E-01	309	3.4	7/8	1 Af
027 bigro	33.896	107.408	35	342	-40.7	169.8	3.1E-01	49	8.0	8/8	30	-45.0	171.5	2.3E-01	90	6.4	7/8	1 Af
028 bigro	33.900	107.401	27	349	-60.9	188.8	5.0E-01	183	5.0	6/8	30	-64.4	189.0	3.2E-01	256	4.2	6/8	1 Af
029 e.mon	33.947	107.445	10	75	-64.2	247.8	3.9E+00	7	25.6	7/8	40	-58.0	254.6	5.5E-01	63	8.5	6/8	2 Af
173 sargC	33.873	107.615	32	237	-16.5	181.2	2.9E+00	311	3.4	7/8	30	-17.3	180.4	8.0E-01	342	3.3	7/8	1 Af
367 sargC	33.874	107.620	20	210	-24.3	175.0	7.4E+00	75	6.4	8/8	30	-26.9	176.6	2.0E+00	310	3.1	8/8	1 Af
368 sargC	33.875	107.621	20	210	-16.2	158.3	1.2E+00	3	41.7	8/8	40	-30.4	170.2	1.9E-01	468	2.6	8/8	2 Af
369 withi	33.894	107.502	20	290	-55.8	213.3	4.4E+00	17	13.7	8/8	30	-58.2	197.9	8.5E-01	220	3.7	8/8	2 Af
370 grass	33.850	107.480	18	350	-18.8	168.0	6.0E-01	7	24.2	7/8	30	-27.5	186.2	4.4E-02	128	5.4	7/8	2
tuff of Walking X Ranch (27.6 Ma)																		
510 burro3	2.4758	108.442	25	315	65.7	9.5	1.9E-01	307	3.5	7/8	40	64.0	5.7	5.9E-02	334	3.3	7/8	1
Lemitar Tuff (28.0 Ma)																		
009 joyit	34.156	106.823	45	180	38.5	353.1	1.1E-01	88	5.9	8/8	30	36.6	356.9		128	4.3	10/8/3	
021 monic	33.950	107.502	22	85	39.9	354.2	1.1E+00	52	7.8	8/8	30	45.1	0.9	3.7E-01	181	5.0	6/8	1
022 monic	33.953	107.501	12	120	46.6	351.8	5.1E-01	22	12.1	8/8	30	36.7	354.0	9.0E-02	120	6.2	6/8	2
046 e.red	33.737	107.349	16	336	21.8	224.3	2.3E+00	2	65.0	8/8	40	31.7	348.4	9.3E-02	81	6.2	8/8	2
054 park	33.768	107.432	0	0	64.5	329.9	2.3E+00	3	40.6	8/8	40	42.2	2.2	2.1E-01	33	9.7	8/8	3
056 exter	33.784	107.438	17	349	19.0	6.8	2.1E+00	2	54.2	8/8	PCA	30.3	352.0	9.0E-02	85	6.0	8/8	3
104 nogal	33.908	106.955	30	317	38.7	29.2	4.4E+00	2	46.2	8/8	30	28.8	7.8	6.4E-01	149	4.5	8/8	2
161 porto	33.774	107.127	5	333	24.9	22.0	1.0E+00	3	35.7	8/8	40	32.9	358.4	7.8E-02	98	5.6	8/8	2
165 porto	33.836	107.165	30	346	40.6	354.0	1.3E+00	781	2.4	6/8	30	37.3	353.0	4.4E-01	164	4.3	8/8	1
198 jorna	34.007	106.663	42	180	42.7	333.3	9.0E-02	21	12.5	8/8	30	40.4	358.0	6.3E-02	199	3.9	8/8	2
010 joyit	34.156	106.823	45	180	62.8	338.4	2.3E-01	136	4.8	8/8	30	61.1	336.6	1.8E-01	180	5.0	6/8	1 Ad
011 joyit	34.156	106.824	45	180	53.7	334.4	1.4E+00	162	3.8	10/10	30	53.8	337.9	5.6E-01	98	6.0	8/10	1 Ad
012 joyit	34.156	106.825	67	180	52.4	323.7	7.8E-01	538	2.2	9/8	40	53.4	322.2	4.5E-01	639	2.2	8/8	1 Ad
030 e.mon	33.950	107.444	45	32	50.4	40.4	5.5E-01	6	35.3	5/8	40	54.9	8.7	3.5E-01	109	7.4	5/8	2 Ad
040 corkC	34.147	106.995	55	185	40.6	332.5	7.5E-02	551	2.9	6/8	30	40.0	333.2	4.4E-02	412	3.3	6/8	1 Ade
041 corkC	34.148	106.996	55	185	31.2	332.2	7.2E-01	119	4.0	12/12	30	29.9	324.2	3.1E-01	31	7.6	13/12	3 Ade
045 e.red	33.741	107.348	16	328	28.4	351.6	1.7E+00	98	5.6	8/8	40	18.4	349.9	5.4E-01	269	3.4	8/8	1 Ade
196 6mile	33.983	107.090	22	357	53.3	339.6	5.8E-02	541	2.9	6/8	30	55.3	341.1	3.1E-02	347	3.6	6/8	1 Ac
050 hiddS	33.724	107.434	8	298	36.1	336.6	8.3E-01	149	5.0	7/8	40	26.4	352.4	4.5E-01	32	10.9	7/8	3 R
064 park	33.812	107.372	8	355	34.8	352.6	5.7E-01	2	81.2	7/8	PCA	42.4	341.5	1.2E-01	67	11.3	4/8	3 R
162 porto	33.774	107.127	5	333	65.7	297.6	2.4E+01	1	81.9	8/8	40	40.4	332.1	1.5E+00	4	34.3	8/8	2 R
tuff of Caronita Canyon (28.0 Ma)																		
167 porto	33.847	107.184	24	2	42.7	2.9	2.0E-01	365	2.9	8/8	30	40.6	3.1	1.4E-01	429	2.7	8/8	1
168 porto	33.856	107.207	38	336	37.8	340.3	6.7E-01	726	2.2	7/8	30	37.5	339.6	5.9E-01	609	2.5	7/8	1
195 6mile	33.982	107.091	22	357	38.6	353.8	6.7E-02	388	3.4	6/8	30	38.6	352.3	5.6E-02	472	3.1	6/8	1
545 sbald	33.960	107.250	22	350	48.4	1.4	1.8E-01	32	10.8	7/7	30	47.7	3.3	9.3E-02	45	9.1	7/7	2
543 sbald	33.950	107.290	28	5	68.9	346.0	3.2E-02	6	29.3	6/6	30	62.2	334.5	2.0E-02	190	4.9	6/6	2 Aac
tuff of Triangle C Ranch (28.1 Ma)																		
140 coyoC	33.625	108.181	0	0	32.0	30.1	3.3E-01	2	48.1	8/8	40	49.1	2.9	2.0E-02	340	3.0	8/8	2
141 coyoC	33.631	108.174	0	0	48.2	356.8	4.5E-02	179	4.2	8/8	30	48.7	359.0	1.4E-02	175	4.2	8/8	1
142 coyoC	33.629	108.174	0	0	59.2	336.1	9.4E-01	37	20.4	3/8	80	55.5	357.5	2.9E-02	101	6.7	6/8	2
158 coyoP	33.645	108.254	0	0	42.1	357.3	8.8E-02	4	30.7	8/8	40	46.9	352.9	2.8E-02	268	3.4	8/8	2
160 obaro	33.571	108.205	0	0	39.9	354.9	1.9E-01	45	8.4	8/8	35	45.4	354.6	1.8E-01	500	2.5	8/8	1
159 coyoP	33.645	108.259	0	0	50.8	71.3	2.9E-01	1	45.5	8/8	40	52.3	354.6	6.9E-03	42	11.9	5/8	2 R
Bloodgood Canyon Tuff (28.1 Ma)																		
078 rael	33.818	108.355	5	130	-18.7	162.2	2.1E-01	86	6.0	8/8	40	-17.7	166.0	6.2E-02	90	5.9	8/8	1
094 divid	33.935	108.425	0	0	-21.7	169.0	2.5E-01	53	8.4	7/8	40	-18.4	165.2	2.2E-01	208	4.2	7/8	1
095 resrv	33.747	108.722	16	220	-28.6	158.2	2.6E-01	121	5.1	8/8	40	-31.3	162.4	2.0E-01	999	1.8	8/8	1
101 brush	33.540	108.935	13	190	-28.2	168.7	2.3E-01	252	3.8	7/8	40	-29.0	166.5	1.7E-01	268	3.6	7/8	1
112 rrcan	33.601	108.056	5	170	-15.5	180.0	2.8E-01	3	47.8	7/8	30	-18.4	161.9	3.8E-02	208	4.2	7/8	2
114 rrcan	33.616	108.039	2	112	-26.3	179.6	2.4E-01	11	18.8	7/8	30	-24.9	165.3	4.5E-02	711	2.3	7/8	2
139 coyoC	33.625	108.181	0	0	-28.8	162.2	6.3E-01	988	1.3	14/14	40	-28.9	162.6	6.1E-01	1395	1.5	8/14	1
144 farrR	33.833	108.013	0	0	29.1	191.0	7.5E-02	3	41.8	8/8	30	-16.4	163.0	4.2E-02	83	6.1	8/8	2
148 farrR	33.817	108.019	0	0	28.6	149.5	1.1E+00	1	180.0	6/8	80	-23.7	157.8	6.1E-02	160	7.2	4/8	2



## E4

Appendix 1. (continued) Complete site-level paleomagnetic data from Mogollon-Datil ignimbrites.

site loc.	lat(*N)	long(*W)	dip	str	NRM						AF demag						type	
					inc	dec	int	k	$\alpha_{95}$	n/t	dm	inc	dec	int	k	$\alpha_{95}$		n/t
414 apach	32.891	107.224	10	0	-34.0	170.9	1.1E-01	177	4.2	8/8	40	-35.2	170.7	5.2E-02	331	3.0	8/8	1
502 tulaN	33.771	108.687	11	222	-32.5	188.7	1.3E-01	663	2.1	8/8	30	-33.5	187.7	2.9E-02	720	2.1	8/8	1
006 corkC	34.146	106.993	75	174	-22.8	151.2	1.8E-01	238	5.0	5/8	20	-24.6	150.5	1.2E-01	122	7.0	5/8	1 Ad
048 e.red	33.737	107.364	9	329	-48.0	142.3	6.8E-02	269	3.4	8/8	30	-46.6	146.0	1.8E-02	300	3.2	8/8	2 Ac
133 blkbu	34.409	106.681	10	212	10.2	135.3	1.4E+00	1	82.7	8/8	40	-42.3	163.4	1.1E-01	51	7.8	8/8	2 Ad
175 kelog	33.880	107.685	24	135	-43.3	180.3	2.5E-01	382	2.8	8/8	40	-44.3	180.9	6.8E-02	559	2.4	8/8	1 Ac
344 devil	33.790	107.164	40	330	-14.5	168.7	3.8E-01	9	19.8	8/8	40	-17.1	168.5	1.3E-01	206	3.9	8/8	2 A
351 samtC	33.552	107.503	20	132	-32.8	154.5	4.7E-01	110	5.3	8/8	30	-32.8	153.3	2.3E-01	227	3.7	8/8	1 Aac
389 stime	33.571	107.396	15	0	-41.1	165.7	7.2E-03	15	16.3	7/8	30	-46.3	173.7	4.5E-03	47	8.9	7/8	2 A
394 vickP	33.536	107.431	15	0	-34.4	80.6	1.8E-01	1	87.7	8/8	80	-34.1	181.6	3.5E-03	54	12.6	4/8	2 R
tuff of Lookout Mountain (28.7 Ma)																		
441 lookM	33.354	107.823	10	180	-61.0	153.1	3.3E-01	34	9.7	8/8	40	-53.4	160.8	8.6E-02	1383	1.5	8/8	1
La Jencia Tuff (28.9 Ma)																		
016 joyit	34.157	106.818	28	180	-38.3	146.7	1.1E-01	2	58.5	8/8	40	-45.6	167.0	1.6E-02	358	3.2	7/8	2
018 joyit	34.155	106.819	28	180	-71.7	281.7	7.5E+00	2	66.1	7/8	100	-58.4	167.7	8.4E-02	122	6.0	6/8	2
034 joyit	34.156	106.821	35	180	-56.7	162.1	7.1E-01	62	7.1	8/8	30	-57.6	163.4	4.4E-01	74	7.1	7/8	1
049 e.red	33.738	107.372	7	353	-56.9	155.2	1.6E-01	565	2.3	8/8	30	-57.1	161.2	1.3E-01	1132	1.6	8/8	1
067 jorna	33.983	106.677	60	160	-48.4	173.1	1.2E+00	46	8.3	8/8	30	-48.3	167.4	7.8E-01	319	3.1	8/8	1
074 wahoo	33.641	107.722	5	300	-43.8	163.4	3.3E-01	267	3.4	8/8	30	-41.3	165.5	1.1E-01	261	3.4	8/8	1
111 scale	33.412	107.888	14	197	-46.1	173.1	2.3E+00	4	34.1	8/8	40	-45.3	168.6	5.9E-01	80	6.2	8/8	2
120 chupa	33.870	106.935	33	2	-43.3	173.3	4.0E-01	179	4.2	8/8	30	-45.7	176.0	3.1E-01	471	2.5	8/8	1
146 farrR	33.817	108.021	0	0	-23.5	159.0	5.3E+00	8	20.9	8/8	40	-39.1	161.9	1.8E+00	268	3.4	8/8	2
191 akeR	33.874	107.749	2	235	-59.2	211.4	2.9E+00	5	28.5	8/8	40	-54.4	168.5	7.4E-01	139	4.7	8/8	2
193 alamt	34.352	107.312	5	110	-55.8	167.9	2.3E-01	299	3.0	9/8	40	-55.8	167.2	1.5E-01	479	2.5	8/8	1
194 alamt	34.351	107.311	5	110	-56.3	162.3	4.3E-01	364	3.2	7/8	30	-56.5	163.0	1.0E-01	500	2.7	7/8	1
346 puert	33.787	107.170	40	330	-48.9	182.0	2.2E-01	34	9.6	8/8	30	-46.6	181.7	1.1E-01	157	4.4	8/8	1
352 shipC	33.543	107.459	36	325	-37.8	180.4	5.6E-02	23	14.4	6/8	30	-41.0	172.9	3.1E-02	160	5.3	6/8	2
372 shawC	33.795	108.056	0	0	-50.0	156.2	2.4E+00	35	9.5	8/8	30	-44.4	167.6	1.2E+00	1647	1.4	8/8	1
135 blkbu	34.408	106.681	10	212	-33.2	155.4	3.3E-01	5	27.5	8/8	40	-45.7	146.5	7.5E-02	585	2.3	8/8	2 Ad
005 cork	34.145	106.992	99	158	-71.1	150.8	3.6E-02	110	6.4	6/8	40	-60.2	133.8	2.5E-02	460	11.7	2/8	1 R
017 joyit	34.156	106.818	28	180	-35.4	154.4	7.0E-02	11	28.9	4/8	80	-40.4	155.6	3.0E-02	121	11.2	3/8	2 R
032 loren	34.244	106.998	40	172	-62.3	145.7	3.5E-02	4	26.2	10/10	50	-70.0	142.0	9.6E-03	144	10.3	3/10	1 R
033 loren	34.244	106.999	25	167	-50.4	143.8	1.0E-01	3	36.1	8/8	50	-51.3	122.6	4.1E-02	6	31.5	6/8	3 R
076 wahoo	33.640	107.722	5	270	78.9	108.6	6.0E-03	1	180.0	5/8	40	-14.2	167.7	2.7E-03	5	36.9	5/8	4 R
164 puert	33.782	107.124	16	112	-7.1	188.4	1.5E+01	1	57.1	8/8	100	-68.2	195.0	1.7E-01	3	37.3	8/8	2 R
247 kelIN	33.893	107.628	16	70	-45.5	263.1	3.4E+01	2	53.6	8/8	40	-50.5	212.9	2.1E+00	5	26.2	8/8	2 R
467 bears	34.227	107.253	0	0	-12.4	181.9	2.5E+00	2	52.5	12/12	40	-40.9	161.4	3.0E-01	6	18.7	12/12	2 R
Davis Canyon Tuff (29.0 Ma)																		
096 tulaS	33.738	108.699	20	211	-53.6	162.9	1.2E-01	139	7.8	4/8	30	-53.2	157.7	2.7E-02	217	3.8	8/8	1
261 fluro	33.079	108.498	5	310	-45.6	136.8	2.8E-01	10	18.8	8/8	40	-51.3	137.9	2.7E-01	192	4.0	8/8	2
267 canoP	32.654	108.891	17	300	-53.9	166.2	1.8E-01	104	5.5	8/8	30	-56.0	169.0	6.1E-02	90	5.9	8/8	1
493 johns	33.696	108.976	10	200	-48.4	158.9	8.4E-01	1316	1.5	8/8	50	-48.0	161.0	5.0E-01	964	1.8	8/8	1
494 saliz	33.620	108.891	6	290	-48.2	171.3	1.3E-01	132	4.8	8/8	40	-49.9	174.4	2.4E-02	177	4.2	8/8	1
503 tulaN	33.772	108.686	11	222	-50.0	165.2	2.5E-02	9	19.6	8/8	10	-61.4	156.9	2.5E-02	289	3.3	8/8	2
302 shelfP	33.188	108.572	8	310	-16.4	187.6	4.8E-01	9	21.1	7/8	40	-18.3	184.8	3.4E-01	8	23.3	7/8	4 R
tuff of Mudhole (29.1 Ma)																		
157 mudho	33.461	107.850	10	180	-55.8	124.3	4.4E-02	171	4.3	8/8	30	-55.9	124.5	2.8E-02	173	4.2	8/8	1
Stiver Canyon Tuff (approx. 29 Ma)																		
257 monuC	33.345	107.844	5	220	-49.4	179.8	1.6E-01	100	5.6	8/8	40	-52.7	172.6	4.1E-02	421	2.7	8/8	1
tuff of Little Mineral Creek (29.0 Ma)																		
421 wingr	33.255	107.624	14	40	58.8	2.1	6.4E-01	525	2.4	8/8	40	58.0	3.1	9.3E-02	459	2.6	8/8	1
tuff of Monument Creek (approx. 29 Ma)																		
480 terry	33.082	108.009	10	270	35.3	352.4	2.1E-01	85	8.4	5/8	30	35.2	344.0	8.8E-02	363	4.0	5/8	1
tuff #4 of Pueblo Creek (<33.5 Ma)																		
235 luna	33.859	108.927	9	264	54.4	325.6	5.5E+00	8	23.6	7/8	30	51.8	336.9	2.1E+00	148	5.0	7/8	2





Appendix 1. (continued) Complete site-level paleomagnetic data from Mogollon-Datil ignimbrites.

site loc.	lat(°N)	long(°W)	dip	str	NAM						AF demag						type					
					inc	dec	int	k	$\alpha_{95}$	n/t	dm	inc	dec	int	k	$\alpha_{95}$		n/t				
412	wingr	33.271	107.629	8	194	72.9	54.4	1.1E+00	2	56.0	4 / 8	40	66.5	29.3	8.9E-03	11	29.0	4 / 8	4 R			
413	wingr	33.271	107.629	8	194	-18.1	292.6	2.5E-01	2	44.6	4 / 8	40	-10.6	107.7	8.8E-04	2	36.3	4 / 8	2 R			
tuff of Stone House Ranch (approx 35.0 Ma)												43.5	323.9		46	18.3	3/0/0					
177	dryC	33.382	107.712	10	130	50.2	322.4	2.9E-02	334	3.0	8 / 8	30	52.2	325.1	1.59E-02	349	3.0	8 / 8	1			
212	wingr	33.281	107.633	8	240	37.3	318.1	1.3E-01	85	8.0	8 / 8	30	30.1	321.3	7.58E-02	64	7.0	8 / 8	1			
213	wingr	33.284	107.635	8	240	48.3	325.7	3.9E-01	112	5.7	7 / 8	30	48.1	326.2	3.74E-01	116	5.6	7 / 8	1			
411	wingr	33.271	107.629	8	194	36.4	123.2	9.4E-02	1	180.0	4 / 8	40	45.3	53.6	2.82E-02	12	28.1	4 / 8	2 R			
Bell Top 4 Tuff (35.0 Ma)												56.1	2.7		457	3.6	5/0/0					
125	goods	32.508	107.145	8	285	54.0	5.5	4.9E+00	656	2.2	8 / 8	40	54.4	5.9	1.98E+00	636	2.2	8 / 8	1			
206	uvas	32.532	107.106	3	280	67.4	84.9	7.6E+00	1	84.3	8 / 8	100	58.9	5.3	3.90E-01	125	6.8	5 / 8	2			
209	uvas	32.555	107.077	7	225	60.3	359.2	1.6E+00	844	1.9	8 / 8	30	60.1	0.1	1.09E+00	970	1.8	8 / 8	1			
211	wingr	33.280	107.633	8	240	36.7	126.8	2.3E-02	4	28.6	9 / 9	PCA	55.4	1.8	2.08E-02	401	3.0	7 / 9	3			
317	ramos	33.366	107.524	30	330	45.4	346.8	4.3E-01	25	11.4	8 / 8	30	51.5	0.5	1.73E-01	618	2.2	8 / 8	2			
tuff of Farr Ranch (35.6 Ma)												50.4	345.5		123	4.7	9/2/2					
065	jorna	33.767	107.436	15	162	38.5	17.2	2.6E+00	4	35.9	6 / 8	30	50.0	347.7	5.4E-01	331	3.7	6 / 8	2			
066	jorna	33.983	106.675	15	162	63.7	9.5	9.4E-01	14	16.9	7 / 8	40	51.5	348.9	7.2E-01	482	2.8	7 / 8	2			
071	jorna	33.998	106.654	43	175	44.3	345.7	9.8E-01	48	8.1	8 / 8	40	52.8	354.0	4.5E-01	965	1.8	8 / 8	1			
091	horsS	33.916	108.196	3	122	62.5	19.7	6.5E-01	5	26.7	8 / 8	40	57.7	345.7	3.0E-01	423	2.7	8 / 8	2			
308	lunap	33.499	107.418	19	293	43.8	340.7	2.7E-01	180	4.1	8 / 8	30	43.7	337.9	1.38E-01	310	3.1	8 / 8	1			
316	ramos	33.365	107.524	30	330	43.5	338.9	6.0E-01	300	3.2	8 / 8	30	43.5	339.3	5.66E-01	302	3.2	8 / 8	1			
368	lunaP	33.492	107.409	10	0	61.4	344.5	2.0E-01	152	4.5	8 / 8	30	60.7	347.6	9.17E-02	206	3.9	8 / 8	1			
390	lunaP	33.498	107.419	16	0	50.6	347.2	3.6E-01	158	4.4	8 / 8	30	51.6	347.1	3.49E-01	410	2.7	8 / 8	1			
437	horsN	33.974	108.213	0	0	1.0	324.5	5.5E+00	3	45.3	7 / 8	40	41.1	344.7	5.8E-01	109	5.8	7 / 8	2			
238	horsM	33.989	108.068	5	195	44.7	353.1	6.8E+00	1	180.0	8 / 8	100	33.3	2.7	6.3E-02	39	8.9	8 / 8	2 Ae			
313	cuchi	33.335	107.533	26	347	25.7	350.5	3.2E+00	110	5.8	7 / 8	40	27.1	351.0	1.06E+00	157	4.8	7 / 8	1 Aag			
178	dryC	33.383	107.711	9	5	31.4	344.1	4.1E-02	4	32.7	8 / 8	PCA	22.2	43.4	1.42E-02	28	12.8	6 / 8	3 R			
365	horsN	33.995	108.173	0	0	41.8	284.9	1.0E+01	2	73.8	8 / 8	100	52.8	14.1	1.4E-01	11	24.3	5 / 8	2 R			
Datil Well Tuff (35.5 Ma)												53.3	19.9		144	5/0/0						
085	datil	34.160	107.845	7	152	0.7	224.6	1.0E+00	2	77.1	7 / 8	40	49.4	15.5	8.3E-02	156	4.8	7 / 8	2			
090	horsS	33.916	108.196	3	122	67.9	130.5	4.8E-01	2	47.0	8 / 8	40	56.3	20.8	2.3E-01	647	2.2	8 / 8	2			
237	horsM	33.989	108.067	5	195	9.9	66.6	1.7E+00	1	84.2	7 / 8	35	45.6	15.1	8.9E-02	65	7.5	7 / 8	2			
466	alleg	34.162	108.126	2	135	5.2	128.7	5.1E-01	2	82.0	5 / 8	40	55.0	19.8	1.3E-01	488	3.5	5 / 8	2			
481	e.cab	33.307	107.021	9	272	0.0	230.3	1.1E+01	2	72.9	6 / 8	100	59.6	31.3	6.9E-02	70	6.6	8 / 8	2			
Sugarlump tuffs (approx. 35 Ma)																						
455	hills	32.836	107.597	15	340	39.9	352.1	1.4E+00	135	4.8	8 / 8	30	41.4	346.0	3.5E-01	338	3.0	8 / 8	1			
462	faywd	32.607	107.896	8	125	40.3	286.8	1.3E+00	3	38.0	8 / 8	30	49.2	271.1	2.2E-01	250	3.5	8 / 8	2 E			
461	hurly	32.721	108.122	6	47	41.5	345.6	5.4E+00	47	8.2	8 / 8	30	46.6	348.7	9.1E-01	1032	1.7	8 / 8	1			
460	hurly	32.714	108.120	7	32	44.1	358.8	7.2E-01	2	58.3	6 / 8	40	63.7	340.4	3.8E-02	166	5.2	6 / 8	2			
509	burro	32.482	108.464	28	315	58.8	337.1	2.5E-01	523	2.6	7 / 8	30	60.9	335.2	1.2E-01	487	2.7	7 / 8	1			
Rubio Peak tuffs (approx. 35 Ma)																						
347	sullC	33.755	107.684	30	270	-30.6	172.7	6.3E+00	57	7.4	8 / 8	30	-34.4	175.1	5.3E+00	150	4.5	8 / 8	1			
458	faywd	32.617	107.881	7	165	-34.1	154.7	1.2E-01	42	8.6	8 / 8	10	-40.1	166.5	6.9E-02	129	4.9	8 / 8	1			
463	faywd	32.607	107.892	7	110	-50.5	152.1	7.0E-02	18	14.6	7 / 8	20	-63.8	152.6	2.2E-02	154	5.4	6 / 8	2			
older Steeple Rock tuffs (approx. 35 Ma)																						
512	stepl3	2.7766	108.942	33	298	62.7	23.0	2.8E-02	2	49.2	8 / 8	40	-60.8	158.7	9.9E-03	81	6.2	8 / 8	2			
513	stepl3	2.7826	108.937	27	296	-77.2	125.5	1.4E-02	22	12.1	8 / 8	50	50.8	26.7	7.9E-03	141	4.7	8 / 8	2			
Bell Top 3 Tuff (35.7 Ma)												69.9	329.9		9000	1.6	2/0/0					
122	goods	32.489	107.131	5	250	59.4	271.5	1.8E+00	2	53.1	8 / 8	30	70.2	329.2	5.0E-02	123	5.0	8 / 8	2			
205	uvas	32.530	107.105	3	280	69.4	321.5	8.9E-01	26	11.0	8 / 8	30	69.5	329.7	9.5E-02	302	3.2	8 / 8	2			
Bell Top Tuff 2 (>35.7 Ma)												39.7	350		210	17.3	2/0/0					
121	goods	32.486	107.131	5	250	45.9	346.7	1.1E+00	23	14.2	6 / 8	30	42.5	346.4	2.3E-01	61	8.6	6 / 8	2			
204	uvas	32.529	107.105	3	280	39.9	352.1	1.0E-01	87	6.0	8 / 8	30	36.7	353.4	7.0E-02	70	6.7	8 / 8	1			

Appendix 1. Complete site-level paleomagnetic data from Mogollon-Datil ignimbrites.

site loc.	lat(°N)	long(°W)	dip	str	NRM						AF demag						type	
					inc	dec	int	k	α <sub>95</sub>	n/t	dm	inc	dec	int	k	α <sub>95</sub>		n/t
Organ Mountain Intracaldera Sequence (36.2-35.5 Ma)																		
Dona Ana Tuff (35.5 Ma)																		
130 dona	32.450	106.788	15	260	68.2	345.9	4.4E-02	340	4.2	5 / 8	30	54.4	155.3		29	48.5	2/0/0	
203 dona	32.437	106.838	19	165	48.2	329.5	3.7E+00	117	5.1	8 / 8	30	44.4	329.7	1.2E+00	109	5.3	8 / 8	1
Squaw Mountain Tuff, Organ Mts. (35.8 Ma)																		
417 organ	32.289	106.598	46	158	31.3	355.1	2.2E-01	4	36.5	7 / 8	30	58.8	178		34	44.5	2/0/0	
529 organ3	2.2949	106.607	44	162	42.2	343.7	3.2E-01	3	37.4	9 / 9	30	66.9	10.5	1.4E-02	43	9.3	7 / 8	2
Achenback Park Tuff, Organ Mts. (approx. 36 Ma)																		
418 organ	32.284	106.594	44	170	3.1	223.8	2.7E-01	1	35.3	9 / 9	30	50	177		13	35.6	3/0/0	
419 organ	32.285	106.584	43	162	53.8	358.3	8.7E-02	43	7.9	9 / 9	30	47.0	321.6	7.2E-03	63	6.7	7 / 9	1
484 pena	32.235	106.602	26	215	44.1	10.2	1.5E-01	4	34.6	8 / 8	40	51.3	0.1	6.7E-02	150	4.2	9 / 9	1
Cueva Tuff, Organ Mts. (36.2 Ma)																		
482 pena	32.223	106.604	26	215	-44.3	197.2	5.5E-02	19	14.3	7 / 8	30	-53.4	220.3		4	67.8	2/0/1	
485 pena	32.223	106.600	26	215	-62.9	168.5	1.2E-01	141	4.7	8 / 8	30	-67.1	208.4	6.1E-03	121	5.5	7 / 8	2
483 pena	32.223	106.603	26	215	19.4	290.8	5.6E-01	1	81.8	8 / 8	40	-65.4	167.4	1.1E-02	99	5.6	8 / 8	1
483 pena	32.223	106.603	26	215	19.4	290.8	5.6E-01	1	81.8	8 / 8	40	-12.2	245.2	2.9E-03	3	38.8	8 / 8	4 R
local dome-related ignimbrites (35 - 28 Ma)																		
150 grnwd	32.894	108.475	15	330	-23.1	273.3	5.0E-01	1	180.0	8 / 8	40	-43.1	134.8	1.5E-02	1	75.7	8 / 8	4 R
151 grnwd	32.896	108.473	15	330	-72.1	88.5	5.1E-01	2	62.6	8 / 8	30	-62.8	152.4	1.3E-01	538	2.4	8 / 8	2
152 grnwd	32.898	108.471	15	330	54.7	210.1	1.5E+00	1	86.5	8 / 8	30	-37.2	158.3	1.9E-01	148	4.8	8 / 8	2
174 p'orx	33.947	107.675	14	197	-41.6	266.8	7.1E-01	1	87.8	9 / 9	40	28.2	320.8	3.2E-03	84	7.4	6 / 9	2
214 wingr	33.274	107.673	14	155	60.4	299.7	4.9E-03	2	75.1	8 / 6	30	-1.5	245.8	3.1E-03	1	76.9	8 / 8	4 R
220 adobe	33.593	107.813	0	0	-57.0	273.5	5.1E-01	2	68.3	8 / 8	30	-55.4	146.6	1.2E-01	471	2.6	8 / 8	2
221 adobe	33.590	107.845	0	0	9.4	246.7	4.1E-01	4	34.0	8 / 8	30	-49.5	207.0	4.7E-02	1004	1.8	8 / 8	2
222 adobe	33.571	107.838	15	182	-60.8	82.7	2.1E-01	47	8.1	8 / 8	30	-62.7	120.9	6.3E-02	417	2.7	8 / 8	1
223 adobe	33.578	107.853	10	167	-53.9	183.3	1.9E-01	172	4.2	8 / 8	30	-52.5	184.0	9.2E-02	200	3.9	8 / 8	1
224 adobe	33.583	107.858	10	187	-57.1	192.7	1.4E-01	205	4.7	6 / 8	30	-56.2	197.0	4.3E-02	238	4.3	6 / 8	1
225 adobe	33.547	107.857	15	207	-45.0	177.9	6.0E-01	645	2.2	8 / 8	30	-44.8	177.5	6.0E-01	590	2.3	8 / 8	1
264 canoP	32.651	108.893	18	320	-52.3	205.5	1.6E-01	6	25.1	8 / 8	40	-30.7	193.7	3.5E-02	221	3.7	8 / 8	2
265 canoP	32.650	108.893	18	320	58.5	26.6	3.0E-02	73	7.9	6 / 8	2	60.3	26.9	2.8E-02	52	9.4	6 / 8	1
307 dorys	32.903	108.442	18	307	-69.6	144.6	5.3E-02	22	12.0	8 / 8	40	-67.9	155.3	9.8E-03	48	8.8	7 / 8	2
309 garcC	33.514	107.459	20	208	70.9	138.6	1.7E-03	2	180.0	2 / 4	30	33.8	20.5	2.4E-04	23	54.3	2 / 4	4 R
320 rkspC	33.525	107.422	18	305	-53.9	169.4	6.6E-01	8	26.2	6 / 8	40	-44.3	159.5	4.6E-01	70	8.1	6 / 8	2
323 rkspC	33.525	107.422	24	295	-23.1	242.8	1.9E-02	2	47.5	8 / 8	30	-30.8	160.3	7.7E-03	69	6.7	8 / 8	2
327 lbRan	33.903	108.228	2	90	-8.1	174.7	2.2E+00	12	16.6	8 / 8	40	-37.5	181.4	5.6E-01	334	3.0	8 / 8	2
330 mangC	33.989	108.244	3	157	-68.2	50.1	8.0E-02	2	47.9	8 / 8	nd	nd	nd	nd	nd	nd	/8	4 R
340 peurt	33.869	107.202	43	342	nd	nd	nd	nd	nd	nd	35	-38.0	168.5	8.3E-03	121	8.5	4 / 4	2
341 peurt	33.867	107.202	43	342	nd	nd	nd	nd	nd	nd	100	-53.2	52.6	1.9E-03	1	180.0	4 / 4	4 R
342 peurt	33.866	107.202	43	342	nd	nd	nd	nd	nd	nd	60	-47.1	182.4	4.1E-04	8	35.4	4 / 4	4 R
360 8002P	33.556	107.406	0	0	-13.1	153.6	2.4E+00	2	63.1	8 / 8	40	-39.8	157.3	1.6E-02	17	13.7	8 / 8	4 R
362 millP	33.550	107.386	16	42	-21.3	90.2	2.1E+01	2	76.5	8 / 8	40	-34.9	153.1	1.9E+00	32	9.9	8 / 8	2
365 p'orx	33.942	107.644	18	260	nd	nd	nd	nd	nd	nd	35	-21.8	192.7	1.7E-03	7	27.3	6 / 4	4 R
378 rt12	34.119	107.880	5	82	-0.3	72.5	1.6E-01	3	46.1	7 / 8	40	-47.9	182.3	1.5E+02	11	19.1	7 / 8	4 R
382 andrM	34.125	107.926	4	40	-41.9	205.1	6.1E-02	2	67.6	7 / 8	40	-59.1	192.2	1.3E-02	23	55.4	2 / 8	4 R
396 hunt	33.510	107.435	41	310	-61.3	71.2	4.1E-02	3	75.3	4 / 4	30	-59.5	69.6	2.1E-02	3	61.7	4 / 4	4 R
398 hunt	33.509	107.436	41	310	56.7	327.8	4.7E-01	389	3.4	6 / 8	40	56.7	328.2	4.7E-01	379	3.5	6 / 8	1
425 bigro	33.859	107.305	13	42	-52.1	204.4	8.0E-02	2	62.6	4 / 4	30	19.0	200.6	1.3E-03	4	56.2	4 / 4	4 R
427 bigro	33.853	107.297	13	42	-6.0	120.7	2.9E-01	21	20.6	4 / 4	2	-8.7	117.9	2.4E-01	15	24.8	4 / 4	4 R
445 nogal	33.903	106.971	8	0	-19.7	261.6	1.4E-01	2	85.2	4 / 4	40	-4.5	302.1	1.1E-02	2	57.4	4 / 4	4 R
448 nogal	33.908	106.958	0	0	-40.1	179.4	1.3E-01	5	43.8	4 / 4	40	-37.2	182.8	5.1E-02	8	34.5	4 / 4	4 R
454 hills	32.841	107.629	18	340	60.3	354.6	1.5E+00	1173	2.7	4 / 4	30	58.7	353.0	4.4E-01	1078	2.8	4 / 4	1
457 schwz	32.673	107.840	5	343	19.2	219.5	1.2E-01	2	51.3	8 / 8	30	40.6	67.8	2.9E-03	2	46.7	8 / 8	4 R
475 tur	33.142	108.439	24	276	-25.3	200.9	1.8E+00	42	14.3	4 / 4	50	-24.8	200.3	2.8E-01	494	4.1	4 / 4	2

Explanation: Site mean paleomagnetic data AF demagnetization level (dm); PCA=principal component analysis used to identify TRM; inc and dec are site-mean inclination and declination; k is Fishers (1953) precision parameter; n - for sites: denotes number of samples used in mean/total, for unit-means: denotes number of sites used in mean/number of sites rejected because of anomalous directions (> 15° from unit mean)/number of sites rejected because α<sub>95</sub>>10°; type denotes demagnetization behavior: 1=TRM, 2=TRM+IRM, 3=TRM+CRM, 4=TRM+lithic hosted components; R=rejected site (α<sub>95</sub>>10°); A=anomalous site, differs from unit-mean by >15°, following letter gives probable reason: Aa=poor attitude control, Ab=basal site in area of pre-eruptive topographic relief, Ac=local structural complexity, Ad=tectonically extended area, Ae=unremoved CRM or IRM components, AF=secular variation recorded in thick intracaldera facies, Ag=possible incorrect unit ID, E=excluded from pole calculations because of anomalous VGP.





Appendix 2. Complete site-level paleomagnetic data from Mogollon-Datil lavas.

sit	lat(N)	long(W)	dip	stk	NRM						AF demag						type	fm	local		
					inc	dec	int	n/t	k	$\alpha_{95}$	dm	inc	dec	int	n/t	k $\alpha_{95}$					
397	33.510	107.436	41	310	29	308	2.2E+00	3 /4	10	41	40	30	333	1.2E-01	3 /4	38	20	2	R	Rhomb P.	LP/hunt
391	33.497	107.420	16	0	50	113	2.4E+01	4 /4	1	180	30	74	184	4.4E+00	4 /4	1	180	3	R		LPI/u
392	33.498	107.420	15	0	58	263	2.2E+01	4 /4	3	67	40	74	307	2.2E+00	4 /4	5	45	3	R		LPI/u
087	34.155	107.847	7	152	47	318	3.8E-01	4 /4	2	82	40	71	313	7.4E-02	4 /4	4	50	2	R		DW-
399	33.493	107.451	34	332	42	114	7.7E-01	4 /4	3	75	30	42	20	6.4E-02	4 /4	13	26	2	R		redrR

Explanation: Site mean paleomagnetic data at NRM and at AF demagnetization level (dm); inc, dec, and int are site-mean inclination, declination, and intensity (A/m); k is Fishers (1953) precision parameter;  $\alpha_{95}$  is alpha 95, n/t is number of samples used in mean/total; type denotes demagnetization behavior: 1=TRM, 2=TRM+IRM, 3=TRM+CRM; R=site data rejected because  $\alpha_{95} > 10^\circ$ ; formation names shown named lavas; final column shows how lava is stratigraphically constrained by overlying (+) or underlying ignimbrites (-), abbreviated as in text.

Appendix 3.  $^{40}\text{Ar}/^{39}\text{Ar}$  data from Mogollon-Datil ignimbrites.

temp(°C)	$^{40}\text{Ar}/^{39}\text{Ar}$	$^{37}\text{Ar}/^{39}\text{Ar}$	$^{36}\text{Ar}/^{39}\text{Ar}$	% $^{39}\text{Ar}$	%rad	$^{39}\text{Ar}$ (moles)	K/Ca	age(Ma)	$\pm 1\sigma$
nm137	Turkey Spr, sanidine	J= 0.004995		RD-56	weight=	0.1971		disc=296.5	
850	2.831	1.628E-02	6.861E-04	5.1	92.8	1.139E-12	31.9	23.54	$\pm 1.02$
1125	2.752	1.560E-02	1.236E-04	26.6	98.7	5.962E-12	33.3	24.31	$\pm 0.10$
1250	2.780	1.542E-02	2.061E-04	45.1	97.8	1.010E-11	33.7	24.35	$\pm 0.07$
1400	2.802	1.494E-02	2.374E-04	21.5	97.5	4.815E-12	34.8	24.45	$\pm 0.18$
1550	2.927	1.521E-02	5.416E-04	1.6	94.5	3.656E-13	34.2	24.76	$\pm 1.21$
total gas							33.8	24.33	
plateau	850- 1050			100.0				24.35	$\pm 0.09$
nm217	Turkey Spr, sanidine	J= 0.005007		RD-56	weight=	0.1983		disc=296.5	
850	2.924	1.823E-02	6.276E-04	4.2	93.7	9.464E-13	28.5	24.56	$\pm 0.83$
1125	2.734	1.635E-02	1.176E-04	22.6	98.7	5.051E-12	31.8	24.22	$\pm 0.16$
1210	2.745	1.597E-02	1.394E-04	22.9	98.5	5.118E-12	32.6	24.26	$\pm 0.10$
1375	2.756	1.566E-02	1.357E-04	47.5	98.5	1.061E-11	33.2	24.36	$\pm 0.09$
1550	2.820	1.494E-02	2.776E-05	2.7	99.7	5.943E-13	34.8	25.29	$\pm 1.14$
total gas							32.6	24.34	
plateau	850- 1550			100.0				24.31	$\pm 0.09$
nm472	Jordan Can, sanidine	J= 0.005023		RD-56	weight=	0.2036		disc=296.5	
750	6.911	6.905E-02	1.012E-02	3.8	56.7	7.893E-13	7.5	35.18	$\pm 0.97$
1100	2.937	1.464E-02	1.440E-04	38.8	98.6	8.048E-12	35.5	26.04	$\pm 0.15$
1225	2.957	1.178E-02	1.488E-04	30.6	98.5	6.334E-12	44.1	26.20	$\pm 0.19$
1350	2.986	1.097E-02	1.272E-04	25.6	98.7	5.294E-12	47.4	26.53	$\pm 0.17$
1550	3.340	1.887E-02	6.584E-04	1.2	94.2	2.506E-13	27.6	28.27	$\pm 2.15$
total gas							40.0	26.59	
plateau	1100- 1225			69.4				26.10	$\pm 0.12$
kjh22	South Canyon, sanidine	J= 0.006917		RD-22	weight=	0.1405		disc=296.5	
650	4.226	2.061E-02	6.537E-03	4.2	54.2	9.62E-13	25.2	28.35	$\pm 0.09$
950	2.849	1.775E-02	2.078E-03	8.1	78.3	1.86E-12	29.3	27.62	$\pm 0.07$
1150	2.346	1.841E-02	4.421E-04	29.4	94.2	6.74E-12	28.2	27.37	$\pm 0.07$
1250	2.361	1.381E-02	4.892E-04	26.7	93.7	6.13E-12	37.7	27.39	$\pm 0.07$
1350	2.411	1.547E-02	6.401E-04	17.9	92.0	4.11E-12	33.6	27.45	$\pm 0.07$
1450	2.667	1.735E-02	1.274E-03	10.6	85.7	2.43E-12	30.0	28.29	$\pm 0.07$
1550	3.314	1.409E-02	3.551E-03	3.1	68.2	7.03E-13	36.9	27.98	$\pm 0.09$
total gas							31.6	27.57	
plateau	1150- 1350			74.0				27.40	$\pm 0.07$
78-6-1	South Canyon, sanidine	J= 0.004562		RD32	weight=	0.1584		disc=296.5	
900	3.662	2.762E-02	1.025E-03	28.2	91.6	1.39E-13	18.8	27.40	$\pm 0.08$
1050	3.496	2.755E-02	4.488E-04	29.2	96.1	1.44E-13	18.9	27.43	$\pm 0.07$
1125	3.579	2.718E-02	7.304E-04	20.2	93.9	9.97E-14	19.1	27.43	$\pm 0.07$
1200	3.868	2.704E-02	1.736E-03	11.1	86.6	5.45E-14	19.2	27.37	$\pm 0.07$
1275	4.274	2.644E-02	3.006E-03	5.5	79.1	2.72E-14	19.7	27.61	$\pm 0.08$
1400	4.820	2.698E-02	4.832E-03	4.0	70.3	1.98E-14	19.3	27.67	$\pm 0.08$
1550	8.107	2.707E-02	1.597E-02	1.7	41.8	8.35E-15	19.2	27.64	$\pm 0.08$
total gas							19.0	27.44	
plateau	900- 1200			88.7				27.41	$\pm 0.07$

## E12

Appendix 3 (continued).  $^{40}\text{Ar}/^{39}\text{Ar}$  data from Mogollon-Datil ignimbrites.

temp(°C)	$^{40}\text{Ar}/^{39}\text{Ar}$	$^{37}\text{Ar}/^{39}\text{Ar}$	$^{36}\text{Ar}/^{39}\text{Ar}$	% $^{39}\text{Ar}$	%rad	$^{39}\text{Ar}$ (moles)	K/Ca	age(Ma)	$\pm 1\sigma$
nm258	South Canyon, sanidine		J= 0.003777		RD54	weight=	0.1972	disc=299.3	
700	5.774	2.456E-02	5.898E-03	2.5	69.7	4.86E-13	21.2	27.23 ± 0.12	
1025	4.132	1.375E-02	3.247E-04	32.1	97.6	6.28E-12	37.8	27.26 ± 0.08	
1150	4.115	1.297E-02	2.558E-04	33.6	98.0	6.56E-12	40.1	27.29 ± 0.08	
1300	4.175	1.269E-02	3.366E-04	29.1	97.5	5.68E-12	41.0	27.52 ± 0.08	
1550	5.374	1.277E-02	4.189E-03	2.7	76.9	5.30E-13	40.7	27.93 ± 0.11	
total gas							38.7	27.36	
plateau	1025- 1150			65.7				27.28 ± 0.08	
nm510	Walking X, Big Burros		J= 0.005028		RD-56	weight=	0.1994	disc=296.5	
1025	3.316	1.680E-02	8.543E-04	12.2	92.4	2.533E-12	31.0	27.57 ± 0.11	
1150	3.110	1.629E-02	1.890E-04	16.4	98.2	3.405E-12	31.9	27.49 ± 0.22	
1300	3.119	1.637E-02	2.017E-04	51.3	98.1	1.061E-11	31.8	27.54 ± 0.11	
1400	3.109	1.596E-02	1.139E-04	17.5	98.9	3.622E-12	32.6	27.70 ± 0.15	
1550	3.177	1.494E-02	6.223E-04	2.6	94.2	5.303E-13	34.8	28.42 ± 1.48	
total gas							31.4	27.82	
plateau	1025- 1550			100.0				27.58 ± 0.10	
kts1	Lemitar, sanidine		J= 0.005499		RD20	weight=	0.1016	disc=296.5	
900	3.896	2.283E-02	3.582E-03	11.40	72.7	1.58E-13	22.8	27.89 ± 0.08	
1000	3.178	2.168E-02	1.133E-03	17.20	89.3	2.39E-13	24.0	27.94 ± 0.09	
1050	3.190	2.125E-02	1.137E-03	14.20	89.3	1.96E-13	24.5	28.04 ± 0.07	
1100	3.138	2.100E-02	1.025E-03	13.70	90.2	1.90E-13	24.8	27.86 ± 0.06	
1150	3.190	2.068E-02	1.111E-03	13.10	89.6	1.82E-13	25.1	28.12 ± 0.08	
1200	3.295	2.079E-02	1.473E-03	11.00	86.7	1.53E-13	25.0	28.10 ± 0.10	
1300	3.519	2.055E-02	2.296E-03	8.70	80.6	1.20E-13	25.3	27.91 ± 0.06	
1450	3.688	2.088E-02	2.830E-03	10.70	77.2	1.48E-13	24.9	28.02 ± 0.06	
total gas							24.5	27.98	
plateau	900- 1100			56.5				27.94 ± 0.10	
kjh24	Lemitar, sanidine		J= 0.006917		RD22	weight=	0.2128	disc=296.5	
650	3.719	1.876E-02	4.847E-03	6.9	61.4	2.65E-12	27.7	28.26 ± 0.07	
900	2.463	2.021E-02	6.822E-04	12.4	91.6	4.75E-12	25.7	27.95 ± 0.07	
1000	2.338	1.670E-02	2.442E-04	22.2	96.7	8.54E-12	31.1	28.00 ± 0.07	
1050	2.381	1.745E-02	3.760E-04	9.5	95.1	3.65E-12	29.8	28.05 ± 0.07	
1125	2.350	1.535E-02	2.897E-04	11.8	96.2	4.55E-12	33.9	27.97 ± 0.07	
1200	2.343	1.590E-02	2.188E-04	13.4	97.0	5.16E-12	32.7	28.15 ± 0.07	
1300	2.365	1.581E-02	3.105E-04	11.4	95.9	4.38E-12	32.9	28.08 ± 0.07	
1550	2.394	1.588E-02	3.681E-04	12.4	95.3	4.76E-12	32.7	28.23 ± 0.07	
total gas							30.8	28.07	
plateau	950- 1350			68.3				28.05 ± 0.07	
nm167	Caronita Can, sanidine		J= 0.004569		RD32	weight=	0.1282	disc=296.5	
650	4.610	2.035E-02	4.308E-03	7.9	72.3	3.85E-14	25.6	27.26 ± 0.08	
950	3.784	2.160E-02	1.281E-03	18.9	89.9	9.21E-14	24.1	27.81 ± 0.09	
1050	3.766	2.162E-02	1.159E-03	14.0	90.8	6.82E-14	24.1	27.96 ± 0.07	
1125	3.706	2.161E-02	1.002E-03	16.8	91.9	8.21E-14	24.1	27.85 ± 0.08	
1200	3.747	2.150E-02	1.067E-03	14.5	91.5	7.05E-14	24.2	28.03 ± 0.08	
1275	3.854	2.137E-02	1.475E-03	10.9	88.6	5.31E-14	24.3	27.92 ± 0.09	
1400	3.898	2.141E-02	1.580E-03	11.7	87.9	5.72E-14	24.3	28.02 ± 0.08	
1550	4.601	2.107E-02	3.715E-03	5.3	76.0	2.61E-14	24.7	28.60 ± 0.08	
total gas							24.3	27.91	
plateau	1050- 1400			67.9				27.96 ± 0.07	

Appendix 3 (continued).  $^{40}\text{Ar}/^{39}\text{Ar}$  data from Mogollon-Datil ignimbrites.

temp(°C)	$^{40}\text{Ar}/^{39}\text{Ar}$	$^{37}\text{Ar}/^{39}\text{Ar}$	$^{36}\text{Ar}/^{39}\text{Ar}$	% $^{39}\text{Ar}$	%rad	$^{39}\text{Ar}$ (moles)	K/Ca	age(Ma)	$\pm 1\sigma$
nm158a	Triangle C, sanidine		J= 0.004591		RD32	weight=	0.1518		disc=296.5
650	5.268	1.868E-02	6.085E-03	3.8	65.8	2.39E-14	27.8	28.47 ± 0.08	
950	3.639	1.503E-02	7.455E-04	11.2	93.8	7.03E-14	34.6	28.05 ± 0.07	
1050	3.632	1.158E-02	7.923E-04	10.3	93.4	6.42E-14	44.9	27.88 ± 0.07	
1125	3.661	1.072E-02	8.718E-04	14.6	92.8	9.14E-14	48.5	27.92 ± 0.08	
1200	3.621	1.032E-02	7.543E-04	16.3	93.7	1.02E-13	50.4	27.88 ± 0.08	
1275	3.641	1.018E-02	7.687E-04	18.1	93.6	1.13E-13	51.1	28.00 ± 0.08	
1400	3.707	1.017E-02	9.615E-04	19.2	92.2	1.20E-13	51.1	28.08 ± 0.09	
1550	4.285	9.963E-03	2.848E-03	6.5	80.2	4.04E-14	52.2	28.25 ± 0.08	
total gas							46.2	28.01	
plateau	950- 1275			70.5				27.95 ± 0.08	
nm158b	Triangle C, sanidine		J= 0.004591		RD32	weight=	0.1518		disc=296.5
1000	4.197	1.520E-02	2.656E-03	19.7	81.2	7.64E-14	34.2	27.99 ± 0.08	
1150	3.720	1.070E-02	1.012E-03	21.4	91.8	8.29E-14	48.6	28.06 ± 0.07	
1250	3.697	1.027E-02	8.976E-04	31.6	92.7	1.23E-13	50.6	28.15 ± 0.07	
1400	3.800	9.983E-03	1.243E-03	21.7	90.2	8.41E-14	52.1	28.16 ± 0.08	
1550	5.139	9.947E-03	5.755E-03	5.5	66.8	2.13E-14	52.3	28.21 ± 0.08	
total gas							46.2	28.11	
plateau	1150- 1550			80.2				28.15 ± 0.07	
nm487	Apache Spr, sanidine		J= 0.003799		RD54	weight=	0.2053		disc=299.2
700	5.581	2.491E-02	4.848E-03	4.3	74.3	7.15E-13	20.9	28.18 ± 0.13	
1075	4.247	1.832E-02	4.555E-04	26.4	96.7	4.39E-12	28.4	27.93 ± 0.08	
1250	4.209	1.647E-02	3.162E-04	37.5	97.7	6.23E-12	31.6	27.95 ± 0.10	
1450	4.299	1.581E-02	5.707E-04	26.9	96.0	4.47E-12	32.9	28.05 ± 0.09	
1550	4.857	1.559E-02	2.444E-03	5.0	85.0	8.23E-13	33.4	28.08 ± 0.11	
total gas							30.4	27.99	
plateau	1075- 1450			90.7				27.98 ± 0.09	
nm94	Bloodgood C, sanidine		J= 0.004990		RD-56	weight=	0.1999		disc=296.5
850	4.736	1.292E-02	5.172E-03	4.4	67.7	9.429E-13	40.3	28.66 ± 0.78	
1140	3.308	1.201E-02	5.649E-03	24.1	49.5	5.164E-12	43.3	28.05 ± 0.15	
1250	3.221	1.203E-02	2.602E-04	34.0	97.6	7.286E-12	43.2	28.08 ± 0.09	
1350	3.195	1.148E-02	1.526E-04	33.6	98.6	7.203E-12	45.3	28.13 ± 0.09	
1550	3.249	1.240E-02	2.101E-04	4.0	98.1	8.639E-13	41.9	28.45 ± 0.51	
total gas							43.8	28.13	
plateau	850- 1550			100.0				28.11 ± 0.10	
nm95	Bloodgood Can, sanidine		J= 0.004990		RD-56	weight=	0.2018		disc=296.5
750	6.366	2.073E-02	1.007E-02	2.1	53.2	4.342E-13	25.1	30.27 ± 0.94	
1100	3.373	1.305E-02	8.212E-04	19.2	92.8	3.949E-12	39.8	27.95 ± 0.25	
1225	3.189	1.267E-02	1.941E-04	25.6	98.2	5.265E-12	41.1	27.98 ± 0.15	
1350	3.195	1.236E-02	1.693E-04	50.6	98.4	1.040E-11	42.1	28.08 ± 0.09	
1550	3.283	1.287E-02	5.674E-03	2.4	48.9	4.944E-13	40.4	27.79 ± 0.84	
total gas							40.9	28.22	
plateau	1100- 1550			97.7				28.06 ± 0.10	
nm112	Bloodgood Can, sanidine		J= 0.004992		RD-56	weight=	0.1997		disc=296.5
800	3.987	1.951E-02	3.059E-03	3.4	77.3	6.960E-13	26.7	28.62 ± 0.57	
1050	3.259	1.448E-02	4.712E-04	14.3	95.7	2.882E-12	35.9	27.87 ± 0.14	
1175	3.166	1.412E-02	1.323E-04	17.3	98.8	3.493E-12	36.8	27.94 ± 0.23	
1350	3.204	1.400E-02	2.161E-04	61.0	98.0	1.231E-11	37.2	28.06 ± 0.08	
1550	3.259	1.324E-02	2.677E-04	4.0	97.6	8.012E-13	39.3	28.43 ± 1.12	
total gas							36.0	28.25	
plateau	800- 1550			100.0				29.04 ± 0.10	

## E14

Appendix 3 (continued).  $^{40}\text{Ar}/^{39}\text{Ar}$  data from Mogollon-Datil ignimbrites.

temp(°C)	$^{40}\text{Ar}/^{39}\text{Ar}$	$^{37}\text{Ar}/^{39}\text{Ar}$	$^{36}\text{Ar}/^{39}\text{Ar}$	% $^{39}\text{Ar}$	%rad	$^{39}\text{Ar}$ (moles)	K/Ca	age(Ma)	$\pm 1\sigma$
nm276	Bloodgood C, sanidine		J= 0.003808		RD54	weight=	0.2123	disc=299.2	
700	3.002	2.107E-02	1.214E-02	1.6	55.1	2.42E-13	24.7	30.05 ± 0.28	
900	4.354	1.029E-02	8.640E-04	12.9	94.0	2.01E-12	50.5	27.90 ± 0.09	
1000	4.234	1.030E-02	4.606E-04	14.7	96.7	2.28E-12	50.5	27.90 ± 0.09	
1100	4.539	1.067E-02	1.412E-03	20.3	90.7	3.17E-12	48.8	28.06 ± 0.09	
1200	4.350	1.030E-02	7.672E-04	36.5	94.7	5.69E-12	50.5	28.07 ± 0.08	
1300	4.630	1.065E-02	1.549E-03	12.1	90.0	1.88E-12	48.8	28.40 ± 0.09	
1400	6.254	1.631E-02	6.847E-03	1.2	67.6	1.91E-13	31.9	28.81 ± 0.37	
1550	9.827	1.106E-02	1.911E-02	0.8	42.5	1.20E-13	47.0	28.45 ± 0.55	
total gas							48.8	28.10	
plateau	900- 1200			84.4				27.99 ± 0.12	
nm318	Bloodgood Can, sanidine		J= 0.003803		RD54	weight=	0.1977	disc=299.2	
750	5.862	1.536E-02	5.571E-03	3.3	71.8	5.64E-13	33.8	28.67 ± 0.17	
1025	4.264	1.284E-02	5.610E-04	25.5	96.0	4.30E-12	40.5	27.86 ± 0.08	
1150	4.239	1.264E-02	4.177E-04	34.1	97.0	5.75E-12	41.1	27.98 ± 0.07	
1300	4.251	1.232E-02	3.933E-04	33.3	97.1	5.62E-12	42.2	28.11 ± 0.07	
1550	5.384	1.458E-02	3.980E-03	3.8	78.1	6.38E-13	35.7	28.61 ± 0.10	
total gas							40.8	28.04	
plateau	1150- 1300			67.4				28.05 ± 0.07	
nm430	Bloodgood Can, sanidine		J= 0.003797		RD54	weight=	0.199	disc=299.2	
750	4.418	1.300E-02	1.005E-03	25.3	93.2	4.49E-12	40.0	27.98 ± 0.08	
1050	4.233	1.254E-02	3.584E-04	45.9	97.4	8.15E-12	41.5	28.01 ± 0.07	
1150	4.265	1.214E-02	4.205E-04	25.5	97.0	4.52E-12	42.8	28.11 ± 0.08	
1300	4.842	1.290E-02	2.367E-03	1.9	85.5	3.37E-13	40.3	28.12 ± 0.25	
1550	7.192	1.297E-02	1.014E-02	1.4	58.3	2.52E-13	40.1	28.47 ± 0.20	
total gas							41.4	28.04	
plateau	1050- 1150			71.4				28.06 ± 0.08	
nm434	Bloodgood Can, sanidine		J= 0.003811		RD54	weight=	0.2044	disc=299.2	
700	5.175	1.106E-02	3.410E-03	5.5	80.4	9.09E-13	47.0	28.39 ± 0.12	
1075	4.310	1.045E-02	6.685E-04	28.2	95.3	4.63E-12	49.8	28.02 ± 0.08	
1250	4.231	1.043E-02	3.890E-04	33.7	97.2	5.52E-12	49.9	28.04 ± 0.09	
1450	4.318	1.050E-02	6.413E-04	28.7	95.5	4.70E-12	49.5	28.13 ± 0.08	
1550	5.465	1.123E-02	4.399E-03	3.9	76.1	6.32E-13	46.3	28.37 ± 0.16	
total gas							49.4	28.09	
plateau	1075- 1450			90.6				28.07 ± 0.09	
nm434hfb	Bloodgood Can, sanidine		J= 0.004966		RD-56	weight=	0.1995	disc=296.5	
750	7.224	3.633E-02	1.111E-02	1.2	54.5	2.410E-13	14.3	34.90 ± 1.95	
1025	3.215	1.096E-02	1.251E-04	19.2	98.9	3.826E-12	47.4	28.19 ± 0.15	
1150	3.175	1.032E-02	3.885E-05	25.6	99.6	5.096E-12	50.4	28.07 ± 0.17	
1300	3.185	1.050E-02	5.877E-05	43.7	99.5	8.704E-12	49.5	28.10 ± 0.12	
1550	3.272	1.048E-02	3.387E-04	8.8	96.9	1.754E-12	49.6	28.14 ± 0.40	
1750	3.386	1.094E-02	1.100E-03	1.4	90.4	2.849E-13	47.5	27.18 ± 2.57	
total gas							48.9	28.18	
plateau	1025-1750			98.8				28.12 ± 0.10	
85G006	Bloodgood Can, sanidine		J= 0.003801		RD54	weight=	0.203	disc=299.2	
750	5.691	3.035E-02	5.057E-03	4.3	73.7	6.33E-13	17.1	28.52 ± 0.13	
1050	4.258	2.526E-02	5.000E-04	24.5	96.4	3.58E-12	20.6	27.94 ± 0.08	
1150	4.195	2.348E-02	2.001E-04	39.4	98.5	5.76E-12	22.1	28.11 ± 0.08	
1550	4.679	2.017E-02	1.744E-03	31.8	88.9	4.64E-12	25.8	28.29 ± 0.07	
total gas							22.4	28.14	
plateau	1050- 1150			63.9				28.03 ± 0.08	

Appendix 3 (continued).  $^{40}\text{Ar}/^{39}\text{Ar}$  data from Mogollon-Datil ignimbrites.

temp(°C)	$^{40}\text{Ar}/^{39}\text{Ar}$	$^{37}\text{Ar}/^{39}\text{Ar}$	$^{36}\text{Ar}/^{39}\text{Ar}$	% $^{39}\text{Ar}$	%rad	$^{39}\text{Ar}$ (moles)	K/Ca	age(Ma)	$\pm 1\sigma$
nm435	Diablo Range, sanidine		J= 0.003808		RD54	weight=	0.2057	disc=299.2	
700	6.623	1.553E-02	8.243E-03	3.1	63.2	5.28E-13	33.5	28.50 ± 0.15	
1075	4.345	1.546E-02	7.756E-04	19.8	94.6	3.38E-12	33.6	28.02 ± 0.08	
1250	4.210	1.521E-02	3.133E-04	28.2	97.7	4.81E-12	34.2	28.03 ± 0.08	
1450	4.215	1.521E-02	3.056E-04	42.6	97.7	7.28E-12	34.2	28.08 ± 0.07	
1550	4.606	1.541E-02	1.543E-02	6.3	90.0	1.08E-12	33.7	28.25 ± 0.09	
total gas							34.0	28.08	
plateau	1075- 1450			90.6				28.05 ± 0.08	
nm149a	Shelley Pk, sanidine		J= 0.004595		RD32	weight=	0.1419	disc=296.5	
650	7.386	2.219E-02	1.469E-02	2.7	41.2	1.49E-14	23.4	25.04 ± 0.09	
950	4.521	2.193E-02	3.568E-03	8.7	76.6	4.85E-14	23.7	28.47 ± 0.08	
1050	4.147	2.076E-02	2.286E-03	9.8	83.6	5.47E-14	25.0	28.51 ± 0.08	
1125	4.074	2.087E-02	2.097E-03	12.8	84.7	7.13E-14	24.9	28.37 ± 0.09	
1200	4.042	2.018E-02	1.876E-03	15.8	86.2	8.76E-14	25.8	28.64 ± 0.09	
1275	4.026	1.969E-02	1.805E-03	17.4	86.6	9.66E-14	26.4	28.68 ± 0.10	
1400	3.853	1.973E-02	1.222E-03	27.0	90.5	1.50E-13	26.4	28.67 ± 0.09	
1550	5.794	1.910E-02	7.489E-03	5.8	61.7	3.24E-14	27.2	29.40 ± 0.09	
total gas							25.7	28.54	
plateau	1200- 1400			60.2				28.67 ± 0.08	
nm149b	Shelley Pk, sanidine		J= 0.004595		RD32	weight=	0.1419	disc=296.5	
1125	4.227	2.101E-02	2.521E-03	40.2	82.3	7.92E-14	24.8	28.60 ± 0.09	
1400	3.927	1.975E-02	1.581E-03	50.8	88.0	1.00E-13	26.3	28.42 ± 0.08	
1550	7.017	2.069E-02	1.198E-02	9.0	49.5	1.77E-14	25.1	28.55 ± 0.08	
total gas							25.6	28.50	
plateau	1125- 1550			100.0				28.52 ± 0.09	
nm319	Garcia Camp, sanidine		J= 0.003771		RD54	weight=	0.2126	disc=299.2	
750	6.319	2.248E-02	6.888E-03	3.2	67.7	6.08E-13	23.1	28.89 ± 0.20	
1025	4.343	2.088E-02	5.928E-04	20.5	95.9	3.93E-12	24.9	28.10 ± 0.07	
1150	4.235	2.060E-02	2.647E-04	30.9	98.1	5.92E-12	25.2	28.03 ± 0.08	
1300	4.245	2.027E-02	2.354E-04	40.6	98.3	7.78E-12	25.7	28.15 ± 0.07	
1550	4.767	1.881E-02	2.010E-03	4.7	87.4	9.06E-13	27.7	28.13 ± 0.11	
total gas							25.4	28.13	
plateau	1025- 1300			92.1				28.10 ± 0.09	
nm116	Taylor Cr Rhy, sanidine		J= 0.003668		RD42	weight=	0.1139	disc=297.5	
900	7.032	1.632E-02	8.727E-03	4.3	63.3	2.74E-14	31.9	29.21 ± 0.16	
1100	4.640	1.806E-02	1.317E-03	10.9	91.5	6.90E-14	28.8	27.88 ± 0.08	
1200	4.570	1.789E-02	9.577E-04	14.6	93.7	9.24E-14	29.1	28.11 ± 0.07	
1300	4.600	1.785E-02	9.774E-04	18.8	93.6	1.19E-13	29.1	28.27 ± 0.08	
1450	4.680	1.794E-02	1.250E-03	35.5	92.0	2.24E-13	29.0	28.26 ± 0.08	
1550	5.475	1.784E-02	3.962E-03	15.8	78.5	9.95E-14	29.1	28.23 ± 0.10	
total gas							29.1	28.24	
plateau	1220- 1550			84.7				28.23 ± 0.10	
85G003	Taylor Cr Rhy, sanidine		J= 0.003807		RD54	weight=	0.2109	disc=299.2	
700	5.611	2.752E-02	4.882E-03	2.7	74.2	4.58E-13	18.9	28.38 ± 0.10	
1075	4.210	2.386E-02	3.773E-04	23.7	97.3	3.99E-12	21.8	27.90 ± 0.09	
1250	4.182	2.232E-02	2.527E-04	43.5	98.1	7.33E-12	23.3	27.96 ± 0.08	
1450	4.260	2.157E-02	4.705E-04	24.5	96.6	4.13E-12	24.1	28.05 ± 0.08	
1550	4.819	2.074E-02	2.130E-03	5.6	86.8	9.39E-13	25.1	28.51 ± 0.11	
total gas							23.1	28.01	
plateau	1075- 1450			91.7				27.97 ± 0.10	

Appendix 3 (continued).  $^{40}\text{Ar}/^{39}\text{Ar}$  data from Mogollon-Datil ignimbrites.

temp(°C)	$^{40}\text{Ar}/^{39}\text{Ar}$	$^{37}\text{Ar}/^{39}\text{Ar}$	$^{36}\text{Ar}/^{39}\text{Ar}$	% $^{39}\text{Ar}$	%rad	$^{39}\text{Ar}$ (moles)	K/Ca	age(Ma)	$\pm 1\sigma$
kjh10	Vicks Peak, sanidine		J= 0.006917	RD-22	weight=	0.0925	disc=296.5		
650	6.015	4.845E-02	1.253E-02	3.5	38.4	3.81E-13	10.7	28.58	$\pm 0.10$
900	3.088	7.601E-03	2.597E-03	6.9	75.0	7.56E-13	68.4	28.66	$\pm 0.09$
1000	2.788	1.511E-02	1.387E-03	6.0	85.1	6.65E-13	34.4	29.37	$\pm 0.08$
1100	2.617	9.280E-03	1.090E-03	10.2	87.5	1.12E-12	56.0	28.35	$\pm 0.08$
1200	2.504	5.580E-03	6.524E-04	14.7	92.1	1.63E-12	93.2	28.55	$\pm 0.07$
1300	2.555	1.250E-02	8.523E-04	15.2	89.9	1.68E-12	41.6	28.45	$\pm 0.07$
1550	2.425	1.211E-02	3.883E-04	43.5	95.1	4.80E-12	42.9	28.54	$\pm 0.08$
total gas							43.2	28.57	
plateau	950- 1350			73.4				28.51	$\pm 0.08$
nm143	Vicks Peak, sanidine		J= 0.004595	RD32	weight=	0.1395	disc=296.5		
650	5.771	1.295E-02	7.582E-03	5.6	61.1	2.26E-14	40.2	28.99	$\pm 0.08$
950	4.450	1.104E-02	3.348E-03	15.4	77.7	6.26E-14	47.1	28.42	$\pm 0.08$
1050	4.279	1.031E-02	2.665E-03	10.8	81.5	4.41E-14	50.5	28.67	$\pm 0.09$
1125	3.979	1.212E-02	1.713E-03	19.5	87.2	7.92E-14	42.9	28.52	$\pm 0.07$
1200	4.032	1.135E-02	1.848E-03	18.5	86.3	7.52E-14	45.8	28.62	$\pm 0.08$
1275	4.288	1.085E-02	2.685E-03	14.3	81.4	5.80E-14	47.9	28.69	$\pm 0.08$
1400	4.138	1.093E-02	2.147E-03	10.2	84.5	4.16E-14	47.6	28.76	$\pm 0.07$
1550	4.792	1.080E-02	4.336E-03	5.7	73.2	2.33E-14	48.1	28.82	$\pm 0.07$
total gas							46.1	28.63	
plateau	1050- 1275			63.1				28.62	$\pm 0.08$
nm414	Vicks Peak, sanidine		J= 0.003771	RD54	weight=	0.1947	disc=299.2		
750	7.845	9.396E-03	1.183E-02	3.2	55.4	4.58E-13	55.3	29.33	$\pm 0.24$
1025	4.545	5.884E-03	1.065E-03	18.9	98.0	2.74E-12	88.4	28.51	$\pm 0.08$
1150	4.432	6.504E-03	6.336E-04	41.9	95.7	6.07E-12	79.9	28.61	$\pm 0.08$
1300	4.651	6.298E-03	7.584E-04	30.1	95.1	4.35E-12	82.6	29.84	$\pm 0.10$
1550	5.782	7.564E-03	4.693E-03	5.9	75.9	8.55E-13	68.7	29.62	$\pm 0.12$
total gas							80.3	29.05	
plateau	1025- 1150			60.8				28.56	$\pm 0.08$
nm502	Vicks Peak, sanidine		J= 0.005030	RD-56	weight=	0.1982	disc=296.5		
850	4.397	1.125E-02	4.014E-03	5.5	73.0	1.036E-12	46.2	28.89	$\pm 0.57$
1075	3.480	8.976E-03	8.789E-04	13.8	92.5	2.577E-12	57.9	28.99	$\pm 0.37$
1200	3.539	9.379E-03	4.300E-04	24.7	96.4	4.609E-12	55.4	30.68	$\pm 0.14$
1350	3.522	1.046E-02	3.776E-04	51.4	96.8	9.610E-12	49.7	30.69	$\pm 0.09$
1550	3.615	1.074E-02	5.258E-04	4.5	95.7	8.472E-13	48.4	31.12	$\pm 0.90$
total gas							52.8	30.37	
plateau	1200- 1550			80.7				30.69	$\pm 0.11$
nm433	Lookout Mtn, sanidine		J= 0.003812	RD54	weight=	0.2064	disc=299.2		
700	9.423	2.333E-02	1.755E-02	1.3	44.9	2.13E-13	22.3	28.89	$\pm 0.52$
1050	4.438	1.579E-02	7.695E-04	46.4	94.8	7.44E-12	32.9	28.70	$\pm 0.10$
1150	4.267	1.638E-02	2.566E-04	25.3	98.1	4.06E-12	31.7	28.56	$\pm 0.08$
1300	4.496	1.617E-02	9.460E-04	26.0	93.7	4.17E-12	32.2	28.74	$\pm 0.09$
1550	8.111	1.842E-02	1.273E-02	0.9	53.5	1.43E-13	28.2	29.63	$\pm 0.56$
total gas							32.2	28.69	
plateau	1050- 1300			97.8				28.67	$\pm 0.12$



Appendix 3 (continued).  $^{40}\text{Ar}/^{39}\text{Ar}$  data from Mogollon-Datil ignimbrites.

temp(°C)	$^{40}\text{Ar}/^{39}\text{Ar}$	$^{37}\text{Ar}/^{39}\text{Ar}$	$^{36}\text{Ar}/^{39}\text{Ar}$	% $^{39}\text{Ar}$	%rad	$^{39}\text{Ar}$ (moles)	K/Ca	age(Ma)	$\pm 1\sigma$
nm441	Lookout Mtn, sanidine	J= 0.003809			RD54	weight=	0.2121		disc=299.2
750	6.940	1.378E-02	8.647E-03	4.4	63.1	7.47E-13	37.7	29.86	$\pm 0.18$
1050	4.394	1.374E-02	6.225E-04	36.5	95.7	6.21E-12	37.8	28.67	$\pm 0.09$
1150	4.299	1.449E-02	2.907E-04	31.0	97.9	5.27E-12	35.9	28.69	$\pm 0.08$
1300	4.396	1.455E-02	5.549E-04	24.1	96.2	4.11E-12	35.7	28.82	$\pm 0.08$
1550	5.743	1.443E-02	4.862E-03	4.0	74.9	6.79E-13	36.0	29.33	$\pm 0.16$
total gas							36.6	28.79	
plateau	1050- 1300			91.6				28.72	$\pm 0.11$
kjh4	La Jencia, sanidine	J= 0.005499			RD20	weight=	0.1001		disc=296.5
900	3.601	1.862E-02	2.160E-03	16.7	82.2	1.93E-13	27.9	29.11	$\pm 0.08$
1000	3.078	1.830E-02	4.860E-04	19.2	95.2	2.22E-13	28.4	28.84	$\pm 0.06$
1050	3.073	1.810E-02	4.706E-04	16.1	95.3	1.87E-13	28.7	28.83	$\pm 0.07$
1100	3.143	1.791E-02	7.003E-04	14.1	93.3	1.63E-13	29.0	28.86	$\pm 0.07$
1150	3.240	1.766E-02	1.052E-03	12.1	90.3	1.40E-13	29.4	28.79	$\pm 0.09$
1200	3.323	1.767E-02	1.320E-03	9.5	88.1	1.10E-13	29.4	28.82	$\pm 0.07$
1300	3.524	1.743E-02	1.823E-03	7.1	84.6	8.17E-14	29.8	29.33	$\pm 0.09$
1450	4.104	1.788E-02	3.995E-03	5.3	71.1	6.13E-14	29.1	28.73	$\pm 0.08$
total gas							28.8	28.91	
plateau	1000- 1200			71.0				28.82	$\pm 0.07$
kjh5	La Jencia, sanidine	J= 0.005499			RD-20	weight=	0.0931		disc=296.5
900	3.769	1.956E-02	2.693E-03	11.20	78.8	1.17E-13	26.6	29.22	$\pm 0.07$
1000	3.150	1.917E-02	8.814E-04	12.80	91.6	1.34E-13	27.1	28.39	$\pm 0.06$
1050	3.088	1.894E-02	5.431E-04	19.00	94.7	1.99E-13	27.5	28.77	$\pm 0.08$
1100	3.119	1.859E-02	6.262E-04	15.80	93.9	1.65E-13	28.0	28.84	$\pm 0.07$
1150	3.374	1.823E-02	1.516E-03	13.40	86.6	1.40E-13	28.5	28.75	$\pm 0.07$
1200	3.244	1.837E-02	1.022E-03	11.60	90.6	1.22E-13	28.3	28.91	$\pm 0.08$
1300	3.391	1.826E-02	1.649E-03	9.10	85.5	9.57E-14	28.5	28.53	$\pm 0.06$
1450	4.034	1.864E-02	3.709E-03	6.90	72.7	7.27E-14	27.9	28.87	$\pm 0.09$
total gas							27.8	28.78	
plateau	1050- 1200			59.8				28.81	$\pm 0.09$
nm146a	La Jencia, sanidine	J= 0.004590			RD32	weight=	0.1513		disc=296.5
650	10.927	1.841E-02	2.635E-02	1.7	28.7	7.95E-15	28.2	25.77	$\pm 0.10$
950	5.183	2.184E-02	5.870E-03	7.0	66.5	3.22E-14	23.8	28.29	$\pm 0.07$
1050	4.580	2.196E-02	3.488E-03	9.1	77.4	4.22E-14	23.7	29.11	$\pm 0.07$
1125	4.225	2.162E-02	2.346E-03	14.9	83.5	6.88E-14	24.1	28.97	$\pm 0.07$
1200	4.155	2.156E-02	2.137E-03	14.4	84.7	6.66E-14	24.1	28.90	$\pm 0.08$
1275	4.140	2.142E-02	2.026E-03	15.5	85.4	7.17E-14	24.3	29.05	$\pm 0.09$
1400	4.003	2.150E-02	1.576E-03	23.2	88.3	1.07E-13	24.2	29.01	$\pm 0.08$
1550	4.398	2.116E-02	2.925E-03	14.3	80.2	6.60E-14	0.0	28.98	$\pm 0.08$
total gas							24.2	29.11	
plateau	1125- 1550			82.3				28.98	$\pm 0.08$
nm146b	La Jencia, sanidine	J= 0.004590			RD32	weight=	0.1513		disc
1000	5.604	2.196E-02	1.046E-02	15.1	53.1	2.16E-14	23.7	28.82	$\pm$
1400	4.110	2.133E-02	1.989E-03	70.2	85.6	1.00E-13	24.4	28.89	$\pm 0.07$
1550	5.742	2.164E-02	1.096E-02	14.7	51.9	2.10E-14	24.0	28.74	$\pm 0.07$
total gas							24.2	28.86	
plateau	1000- 1550			100.0				28.82	$\pm 0.08$

Appendix 3 (continued).  $^{40}\text{Ar}/^{39}\text{Ar}$  data from Mogollon-Datil ignimbrites.

temp(°C)	$^{40}\text{Ar}/^{39}\text{Ar}$	$^{37}\text{Ar}/^{39}\text{Ar}$	$^{36}\text{Ar}/^{39}\text{Ar}$	% $^{39}\text{Ar}$	%rad	$^{39}\text{Ar}$ (moles)	K/Ca	age(Ma)	$\pm 1\sigma$
nm111	La Jencia, sanidine	J= 0.003692		RD42	weight=	0.113		disc=297.5	
900	5.465	2.564E-02	3.722E-03	9.3	79.8	7.28E-14	20.3	28.82 ± 0.09	
1100	4.554	2.474E-02	6.571E-04	21.2	95.6	1.66E-13	21.0	28.78 ± 0.07	
1200	4.496	2.319E-02	4.095E-04	20.2	97.2	1.58E-13	22.4	28.89 ± 0.08	
1300	4.484	2.293E-02	3.579E-04	24.2	97.5	1.90E-13	22.7	28.90 ± 0.08	
1450	4.542	2.221E-02	6.642E-04	19.0	95.6	1.49E-13	23.4	28.69 ± 0.08	
1550	4.929	2.106E-02	1.807E-03	6.0	89.1	4.69E-14	24.7	29.01 ± 0.09	
total gas							22.2	28.83	
plateau	900- 1300			74.9				28.86 ± 0.09	
nm157	Mud Hole, sanidine	J= 0.038124		RD54	weight=	0.1895		disc=299.2	
750	7.750	2.529E-02	1.155E-02	3.5	55.9	5.61E-13	20.6	29.56 ± 0.17	
1025	4.606	2.110E-02	1.307E-03	27.0	91.5	4.30E-12	24.6	28.77 ± 0.09	
1150	4.435	2.039E-02	5.751E-04	36.4	96.1	5.79E-12	25.5	29.07 ± 0.13	
1300	4.470	1.868E-02	5.965E-04	29.0	96.0	4.61E-12	27.8	29.26 ± 0.08	
1550	5.588	1.995E-02	4.081E-03	4.0	78.3	6.33E-13	26.1	29.86 ± 0.09	
total gas							25.7	29.09	
plateau	1150- 1300			65.4				29.16 ± 0.11	
nm96	Davis Canyon, sanidine	J= 0.004569		RD32	weight=	0.0963		disc=296.5	
1000	4.054	1.771E-02	1.680E-03	24.9	87.6	7.80E-14	29.4	29.04 ± 0.08	
1400	3.730	1.717E-02	5.628E-04	67.0	95.4	2.10E-13	30.3	29.10 ± 0.08	
1550	4.537	1.708E-02	3.277E-03	8.1	78.6	2.55E-14	30.5	29.14 ± 0.08	
total gas							30.1	29.09	
plateau	1000- 1550			100.0				29.09 ± 0.08	
nm494	Davis Canyon, sanidine	J= 0.004995		RD-56(mult)	weight=	0.0535		disc=296.5	
1150	3.350	1.209E-02	4.748E-04	40.2	95.8	4.210E-13	43.0	28.70 ± 0.08	
1250	3.344	1.221E-02	3.505E-04	27.6	96.9	2.893E-13	42.6	28.97 ± 0.08	
1350	3.313	1.171E-02	2.867E-04	32.1	97.4	3.365E-13	44.4	28.86 ± 0.08	
total gas							43.3	28.83	
plateau	1250- 1350			59.8				28.93 ± 0.10	
nm491	L. Mineral Cr, sanidine	J= 0.005030		RD-56	weight=	0.1677		disc=296.5	
850	3.385	4.191E-02	6.216E-04	6.2	94.6	1.196E-12	12.4	28.83 ± 0.49	
1125	3.266	3.311E-02	1.862E-04	20.5	98.3	3.932E-12	15.7	28.90 ± 0.19	
1225	3.305	2.702E-02	2.988E-04	25.9	97.3	4.974E-12	19.2	28.96 ± 0.15	
1350	3.316	2.324E-02	3.137E-04	33.5	97.2	6.436E-12	22.4	29.02 ± 0.10	
1550	3.335	2.417E-02	2.992E-04	13.9	97.3	2.671E-12	21.5	29.22 ± 0.18	
total gas							19.5	28.99	
plateau	850- 1550			100.0				29.01 ± 0.10	
nm496	Tadpole Ridge, sanidine	J= 0.005031		RD-56(mult)	weight=	0.0491		disc=296.5	
1135	3.646	6.316E-02	5.450E-04	29.8	95.6	2.738E-13	8.2	31.34 ± 0.09	
1210	3.649	5.221E-02	5.047E-04	29.6	95.9	2.724E-13	10.0	31.48 ± 0.11	
1250	3.726	4.634E-02	8.102E-04	20.6	93.6	1.891E-13	11.2	31.36 ± 0.12	
1270	3.763	4.606E-02	8.936E-04	14.8	93.0	1.360E-13	11.3	31.48 ± 0.15	
1325	3.816	4.179E-02	1.330E-03	5.2	89.7	4.758E-14	12.4	30.79 ± 0.16	
total gas							10.0	31.38	
plateau	1135- 1270			94.8				31.39 ± 0.11	

Appendix 3 (continued).  $^{40}\text{Ar}/^{39}\text{Ar}$  data from Mogollon-Datil ignimbrites.

temp(°C)	$^{40}\text{Ar}/^{39}\text{Ar}$	$^{37}\text{Ar}/^{39}\text{Ar}$	$^{36}\text{Ar}/^{39}\text{Ar}$	% $^{39}\text{Ar}$	%rad	$^{39}\text{Ar}$ (moles)	K/Ca	age(Ma)	$\pm 1\sigma$
nm200	Caballo Blanco, san		J= 0.003684		RD42	weight=	0.1196		disc=297.5
900	5.475	9.299E-03	2.198E-03	8.6	88.0	1.19E-13	55.9	31.75 ± 0.08	
1100	4.974	8.338E-03	5.825E-04	19.5	96.4	2.69E-13	62.4	31.60 ± 0.08	
1200	4.959	8.415E-03	5.383E-04	20.7	96.7	2.85E-13	61.8	31.59 ± 0.08	
1300	4.973	8.127E-03	5.367E-04	24.3	96.7	3.35E-13	64.0	31.68 ± 0.11	
1450	5.059	8.320E-03	8.134E-04	22.1	95.1	3.05E-13	62.5	31.71 ± 0.09	
1550	6.661	8.670E-03	6.044E-03	4.7	73.1	6.53E-14	60.0	32.08 ± 0.09	
total gas							61.9	31.68	
plateau	900- 1450			95.3				31.66 ± 0.11	
nm236	Caballo Blanco, san		J= 0.005010		RD-56	weight=	0.1541		disc=296.5
850	5.011	1.148E-02	5.048E-03	2.6	70.2	5.592E-13	45.3	31.52 ± 0.65	
1150	3.671	8.485E-03	4.630E-04	27.9	96.3	6.067E-12	61.3	31.66 ± 0.13	
1250	3.640	8.316E-03	3.862E-04	38.5	96.9	8.385E-12	62.5	31.58 ± 0.09	
1350	3.600	8.015E-03	1.902E-04	30.5	98.4	6.644E-12	64.9	31.75 ± 0.11	
1550	4.000	8.601E-03	8.447E-04	0.5	93.8	1.172E-13	60.5	33.60 ± 3.61	
total gas							62.4	31.66	
plateau	850- 1550			100.0				31.64 ± 0.11	
nm268	Caballo Blanco, san		J= 0.003809		RD54	weight=	0.1954		disc=299.2
700	6.197	1.168E-02	5.087E-03	3.1	75.7	6.26E-13	44.5	31.93 ± 0.11	
1075	4.784	8.288E-03	4.529E-04	23.4	97.1	4.78E-12	62.7	31.64 ± 0.10	
1250	4.767	7.922E-03	3.688E-04	42.6	97.6	8.71E-12	65.6	31.69 ± 0.08	
1450	4.816	8.012E-03	4.757E-04	26.7	97.7	5.46E-12	64.9	31.81 ± 0.08	
1550	5.715	9.046E-03	3.411E-03	4.2	82.3	8.61E-13	57.5	32.03 ± 0.13	
total gas							63.4	31.73	
plateau	1075- 1450			92.7				31.71 ± 0.12	
nm478	Caballo Blanco, san		J= 0.003810		RD54	weight=	0.2063		disc=299.2
700	5.972	1.122E-02	4.185E-03	3.0	79.2	6.28E-13	46.4	32.23 ± 0.12	
1075	4.834	9.249E-03	7.121E-04	13.6	95.5	2.86E-12	56.2	31.47 ± 0.09	
1250	4.736	8.670E-03	3.476E-04	25.9	97.7	5.45E-12	60.0	31.54 ± 0.09	
1450	4.754	8.530E-03	3.462E-04	48.8	97.7	1.03E-11	61.0	31.66 ± 0.09	
1550	4.911	8.718E-03	8.033E-04	8.8	95.1	1.86E-12	59.6	31.81 ± 0.10	
total gas							59.4	31.63	
plateau	1075- 1450			88.2				31.56 ± 0.12	
nm525	Caballo Blanco, san		J= 0.005028		RD-56	weight=	0.2005		disc=296.5
850	3.740	9.891E-03	8.697E-04	3.4	93.1	9.376E-13	52.6	31.32 ± 0.79	
1140	3.557	8.230E-03	1.655E-04	14.7	98.6	4.079E-12	63.2	31.54 ± 0.17	
1240	3.601	7.735E-03	3.089E-04	28.2	97.5	7.822E-12	67.2	31.56 ± 0.10	
1375	3.578	7.569E-03	1.665E-04	50.7	98.6	1.407E-11	68.7	31.73 ± 0.09	
1550	3.669	7.458E-03	2.414E-04	3.0	98.1	8.201E-13	69.7	32.36 ± 1.19	
total gas							66.9	31.66	
plateau	850- 1550			100.0				31.67 ± 0.11	

Appendix 3 (continued).  $^{40}\text{Ar}/^{39}\text{Ar}$  data from Mogollon-Datil ignimbrites.

temp(°C)	$^{40}\text{Ar}/^{39}\text{Ar}$	$^{37}\text{Ar}/^{39}\text{Ar}$	$^{36}\text{Ar}/^{39}\text{Ar}$	% $^{39}\text{Ar}$	%rad	$^{39}\text{Ar}$ (moles)	K/Ca	age(Ma)	$\pm 1\sigma$
khj26 Hells Mesa, sanidine J= 0.005499 RD20 weight= 0.0967 disc=296.5									
900	3.720	9.052E-03	1.474E-03	13.2	86.1	2.24E-13	57.4	32.23	$\pm 0.10$
1000	3.384	8.629E-03	3.432E-04	13.0	96.8	2.18E-13	60.3	32.22	$\pm 0.09$
1050	3.418	8.274E-03	4.310E-04	15.3	96.1	2.57E-13	62.8	32.30	$\pm 0.07$
1100	3.389	8.099E-03	3.722E-04	12.6	96.6	2.12E-13	64.2	32.19	$\pm 0.08$
1150	3.429	8.136E-03	5.044E-04	11.6	95.5	1.96E-13	63.9	32.19	$\pm 0.08$
1200	3.469	8.029E-03	5.861E-04	11.8	94.9	1.99E-13	64.8	32.34	$\pm 0.07$
1250	3.577	8.117E-03	9.865E-04	8.7	91.7	1.46E-13	64.1	32.25	$\pm 0.08$
1450	3.725	8.066E-03	1.492E-03	13.8	88.0	2.32E-13	64.5	32.23	$\pm 0.10$
total gas							62.5	32.24	
plateau	900- 1450			100.0				32.25	$\pm 0.08$
kjh26 Hells Mesa, sanidine J= 0.006917 RD22 weight= 0.1373 disc=296.5									
650	4.234	3.491E-03	5.468E-03	3.6	61.7	1.03E-12	149.0	32.32	$\pm 0.09$
950	2.767	7.239E-03	5.851E-04	12.8	93.6	3.71E-12	71.8	32.02	$\pm 0.08$
1050	2.699	5.805E-03	3.420E-04	18.4	96.1	5.35E-12	89.6	32.06	$\pm 0.08$
1150	2.656	5.001E-03	1.896E-04	21.7	97.7	6.29E-12	104.0	32.08	$\pm 0.09$
1250	2.687	5.089E-03	2.840E-04	19.6	96.7	5.69E-12	102.2	32.13	$\pm 0.08$
1350	2.728	7.616E-03	4.083E-04	15.1	95.4	4.39E-12	68.3	32.18	$\pm 0.11$
1450	3.014	3.442E-03	1.345E-03	8.0	86.6	2.33E-12	151.1	32.29	$\pm 0.09$
1650	7.312	3.382E-02	1.568E-02	0.7	36.6	2.00E-13	15.4	33.09	$\pm 0.22$
total gas							88.6	32.13	
plateau	950- 1350			87.6				32.10	$\pm 0.11$
								w. plat	32.10 $\pm 0.11$
kjh26 Hells Mesa, sanidine J= 0.003808 RD54 weight= 0.2023 disc=299.2									
700	6.080	1.393E-02	4.495E-03	3.0	78.1	6.70E-13	37.3	32.32	$\pm 0.12$
1075	4.798	9.163E-03	3.594E-04	23.0	97.7	5.14E-12	56.7	31.91	$\pm 0.08$
1250	4.816	8.395E-03	3.856E-04	47.0	97.5	1.05E-11	61.9	31.98	$\pm 0.08$
1450	4.881	8.388E-03	5.590E-04	22.1	96.5	4.94E-12	62.0	32.08	$\pm 0.08$
1550	6.063	1.053E-02	4.613E-03	4.9	77.4	1.10E-12	49.4	31.97	$\pm 0.11$
total gas							55.4	32.00	
plateau	1075- 1450			92.1				31.99	$\pm 0.11$
kjh26 Hells Mesa, sanidine J= 0.004998 RD-56 weight= 0.2013 disc=296.5									
850	3.707	1.158E-02	5.064E-04	3.6	96.0	9.775E-13	44.9	31.82	$\pm 0.24$
1150	3.615	8.764E-03	1.388E-04	32.2	98.9	8.814E-12	59.3	31.93	$\pm 0.11$
1250	3.682	8.344E-03	3.367E-04	38.0	97.3	1.041E-11	62.3	32.01	$\pm 0.09$
1325	3.679	8.248E-03	2.651E-04	24.9	97.9	6.809E-12	63.0	32.17	$\pm 0.10$
1550	3.830	7.714E-03	1.420E-03	1.3	89.0	3.486E-13	67.4	32.59	$\pm 2.05$
total gas							61.0	32.03	
plateau	850- 1250			73.8				31.99	$\pm 0.11$
kjh26-hfa Hells Mesa, sanidine J= 0.005002 RD-56 weight= 0.2010 disc=296.5									
850	3.730	1.095E-02	4.258E-04	3.7	96.6	1.085E-12	47.5	32.22	$\pm 0.55$
1140	3.590	8.834E-03	8.092E-05	38.6	99.3	1.132E-11	58.9	31.88	$\pm 0.10$
1240	3.596	8.151E-03	7.205E-05	30.5	99.4	8.924E-12	63.8	31.97	$\pm 0.10$
1375	3.622	8.140E-03	9.348E-05	26.9	99.2	7.898E-12	63.9	32.14	$\pm 0.12$
1550	4.401	9.800E-03	3.120E-03	0.3	79.1	7.932E-14	53.1	31.27	$\pm 7.25$
total gas							61.3	31.99	
plateau	850- 1240			72.8				32.03	$\pm 0.11$

## E21

Appendix 3 (continued).  $^{40}\text{Ar}/^{39}\text{Ar}$  data from Mogollon-Datil ignimbrites.

temp(°C)	$^{40}\text{Ar}/^{39}\text{Ar}$	$^{37}\text{Ar}/^{39}\text{Ar}$	$^{36}\text{Ar}/^{39}\text{Ar}$	% $^{39}\text{Ar}$	%rad	$^{39}\text{Ar}$ (moles)	K/Ca	age(Ma)	$\pm 1\sigma$
kjh26-hfb Hells Mesa, sanidine J= 0.005004 RD-56 weight= 0.2018 disc=296.5									
850	3.731	1.068E-02	4.518E-04	3.1	96.4	8.765E-13	48.7	32.18	$\pm 0.45$
1150	3.585	8.687E-03	4.626E-05	38.3	99.6	1.070E-11	59.9	31.94	$\pm 0.10$
1250	3.596	8.070E-03	6.717E-05	31.7	99.4	8.843E-12	64.4	32.00	$\pm 0.09$
1325	3.614	7.841E-03	6.550E-05	26.2	99.5	7.305E-12	66.3	32.16	$\pm 0.12$
1550	3.724	9.112E-03	7.967E-04	0.7	93.7	2.071E-13	57.1	31.19	$\pm 2.08$
total gas plateau	850- 1550			100.0			62.6	32.02	$\pm 0.11$
kd1 Hells Mesa, sanidine J= 0.005499 RD20 weight= 0.0576 disc=296.5									
900	3.843	9.032E-03	1.853E-03	14.9	85.6	1.51E-13	57.6	32.34	$\pm 0.08$
1050	3.372	8.441E-03	3.608E-04	27.1	96.7	2.75E-13	61.6	32.05	$\pm 0.06$
1150	3.347	8.022E-03	2.324E-04	27.1	97.8	2.75E-13	64.8	32.17	$\pm 0.08$
1250	3.460	7.943E-03	5.724E-04	19.6	95.0	1.99E-13	65.5	32.30	$\pm 0.09$
1350	3.810	8.183E-03	1.837E-03	8.5	85.6	8.66E-14	63.5	32.07	$\pm 0.08$
1450	5.516	1.114E-02	7.469E-03	2.7	59.9	2.77E-14	46.7	32.48	$\pm 0.09$
total gas plateau	1050- 1150			54.2			62.1	32.19	$\pm 0.10$
kbn3 Hells Mesa, sanidine J= 0.006917 RD22 weight= 0.1986 disc=296.5									
650	5.454	2.159E-02	9.135E-03	3.5	50.4	1.08E-12	24.1	34.00	$\pm 0.14$
950	2.795	3.299E-02	5.391E-04	14.0	94.2	4.25E-12	15.8	32.55	$\pm 0.06$
1050	2.658	7.585E-03	1.925E-04	23.1	97.7	7.02E-12	68.6	32.10	$\pm 0.06$
1150	2.714	8.116E-03	3.839E-04	26.4	95.6	8.04E-12	64.1	32.10	$\pm 0.06$
1250	2.691	5.228E-03	2.680E-04	28.3	96.9	8.63E-12	99.5	32.24	$\pm 0.06$
1450	3.242	7.616E-03	2.078E-03	3.9	80.9	1.18E-12	68.3	32.43	$\pm 0.09$
1550	6.039	4.000E-02	1.151E-02	0.9	43.6	2.66E-13	13.0	32.58	$\pm 0.13$
total gas plateau	1050- 1250			77.8			45.7	32.28	$\pm 0.11$
SU-4-77 Hells Mesa, sanidine J= 0.004476 RD16 weight= 0.1329 disc=296.5									
750	7.228	4.985E-02	1.030E-02	1.1	57.8	2.07E-14	10.4	33.44	$\pm 0.20$
900	4.449	2.285E-02	1.341E-03	5.3	91.0	9.57E-14	22.8	32.40	$\pm 0.09$
1000	4.329	1.490E-02	1.116E-03	18.1	92.3	3.29E-13	34.9	31.97	$\pm 0.10$
1050	4.512	1.112E-02	1.726E-03	19.2	88.6	3.48E-13	46.8	31.98	$\pm 0.09$
1100	4.897	1.025E-02	3.065E-03	14.0	81.4	2.53E-13	50.7	31.89	$\pm 0.09$
1150	4.987	9.851E-03	3.345E-03	27.2	80.1	4.94E-13	52.8	31.96	$\pm 0.09$
1200	8.495	1.024E-02	1.528E-02	15.0	46.8	2.72E-13	50.8	31.81	$\pm 0.11$
total gas plateau	1000- 1200			93.5			53.8	31.97	$\pm 0.11$
nm201 Box Canyon, sanidine J= 0.003686 RD42 weight= 0.1126 disc=297.5									
900	5.499	1.095E-02	1.572E-03	8.6	91.5	1.09E-13	47.5	33.14	$\pm 0.09$
1100	5.269	1.008E-02	6.530E-04	17.2	96.2	2.17E-13	51.6	33.40	$\pm 0.09$
1200	5.306	9.839E-03	7.149E-04	16.3	95.9	2.06E-13	52.9	33.52	$\pm 0.09$
1300	5.340	9.606E-03	8.420E-04	16.2	95.2	2.04E-13	54.1	33.50	$\pm 0.10$
1450	5.313	9.722E-03	6.949E-04	26.7	96.0	3.37E-13	53.5	33.61	$\pm 0.09$
1550	5.678	9.570E-03	1.877E-03	14.9	90.1	1.88E-13	54.3	33.71	$\pm 0.09$
total gas plateau	1100- 1450			76.4			52.7	33.52	$\pm 0.12$

Appendix 3 (continued).  $^{40}\text{Ar}/^{39}\text{Ar}$  data from Mogollon-Datil ignimbrites.

temp(°C)	$^{40}\text{Ar}/^{39}\text{Ar}$	$^{37}\text{Ar}/^{39}\text{Ar}$	$^{38}\text{Ar}/^{39}\text{Ar}$	% $^{39}\text{Ar}$	%rad	$^{39}\text{Ar}$ (moles)	K/Ca	age(Ma)	$\pm 1\sigma$
nm207	Box Canyon, sanidine		J= 0.003808		RD54	weight=	0.1005		disc=299.2
700	7.193	1.687E-02	7.487E-03	4.0	69.2	4.45E-13	30.8	33.87	$\pm 0.15$
1075	5.275	1.096E-02	1.152E-03	20.6	93.4	2.30E-12	47.4	33.55	$\pm 0.10$
1250	5.503	1.038E-02	1.923E-03	34.4	89.6	3.85E-12	50.1	33.55	$\pm 0.09$
1450	5.408	9.844E-03	1.576E-03	32.0	91.3	3.58E-12	52.8	33.60	$\pm 0.11$
1550	6.404	9.725E-03	4.765E-03	8.9	77.9	9.94E-13	53.5	33.97	$\pm 0.14$
total gas							49.4	33.61	
plateau	1075- 1450			87.1				33.57	$\pm 0.09$
nm232	Box Canyon?, sanidine		J= 0.003812		RD54	weight=	0.208		disc=299.2
700	6.109	1.498E-02	4.153E-03	2.0	79.8	4.65E-13	34.7	33.23	$\pm 0.12$
1075	5.015	1.030E-02	4.895E-04	20.4	97.0	4.72E-12	50.5	33.15	$\pm 0.10$
1250	5.063	9.621E-03	5.506E-04	23.2	96.7	5.35E-12	54.1	33.35	$\pm 0.09$
1450	5.043	9.272E-03	4.829E-04	35.0	97.1	8.08E-12	56.1	33.35	$\pm 0.09$
1550	5.259	9.306E-03	1.095E-03	19.4	93.7	4.47E-12	55.9	33.59	$\pm 0.10$
total gas							53.7	33.36	
plateau	1075- 1450			78.6				33.29	$\pm 0.14$
nm234	Box Canyon?, sanidine		J= 0.003812		RD54	weight=	0.1996		disc=299.2
700	6.158	1.327E-02	4.156E-03	1.9	80.0	4.48E-13	39.2	33.55	$\pm 0.17$
1075	4.991	9.788E-03	3.544E-04	19.1	97.8	4.44E-12	53.1	33.26	$\pm 0.09$
1250	5.016	9.365E-03	2.679E-04	29.6	98.3	6.86E-12	55.5	33.60	$\pm 0.10$
1450	5.054	9.235E-03	3.733E-04	43.5	97.7	1.01E-11	56.3	33.64	$\pm 0.10$
1550	5.488	9.604E-03	1.864E-03	5.9	89.9	1.37E-12	54.1	33.60	$\pm 0.10$
total gas							54.9	33.55	
plateau	1250- 1450			73.0				33.62	$\pm 0.10$
nm297	Box Canyon, sanidine		J= 0.003808		RD54	weight=	0.1842		disc=299.2
700	6.945	1.126E-02	6.748E-03	6.9	71.2	1.09E-12	46.2	33.66	$\pm 0.11$
1075	5.103	9.559E-03	7.050E-04	30.7	95.8	4.87E-12	54.4	33.28	$\pm 0.09$
1250	5.039	9.540E-03	4.095E-04	50.8	97.5	8.05E-12	54.5	33.44	$\pm 0.10$
1450	6.214	1.084E-02	4.179E-03	7.6	80.0	1.21E-12	48.0	33.86	$\pm 0.13$
1550	6.197	1.168E-02	5.087E-03	4.0	75.7	6.26E-13	44.5	31.92	$\pm 0.11$
total gas							52.8	33.38	
plateau	1075- 1250			81.5				33.36	$\pm 0.10$
nm505	Box Canyon, sanidine		J= 0.005028		RD-56	weight=	0.1981		disc=296.5
850	3.840	2.477E-02	3.798E-04	5.7	97.1	1.086E-12	21.0	33.51	$\pm 0.43$
1150	3.765	2.434E-02	9.714E-05	31.3	99.2	5.945E-12	21.4	33.59	$\pm 0.10$
1250	3.821	2.265E-02	2.521E-04	34.1	98.1	6.486E-12	23.0	33.65	$\pm 0.10$
1310	3.861	2.171E-02	3.593E-04	25.5	97.3	4.846E-12	24.0	33.74	$\pm 0.11$
1550	3.972	2.176E-02	5.539E-04	3.4	95.9	6.554E-13	23.9	34.24	$\pm 0.38$
total gas							22.6	33.67	
plateau	1150-1310			90.8				33.65	$\pm 0.12$
nm508	Box Canyon, sanidine		J= 0.005031		RD-56	weight=	0.2017		disc=296.5
850	4.424	1.078E-02	2.262E-03	3.6	84.9	1.001E-12	48.2	33.77	$\pm 0.54$
1150	3.829	9.783E-03	3.552E-04	21.5	97.3	6.025E-12	53.2	33.49	$\pm 0.12$
1240	3.768	9.816E-03	2.795E-04	9.7	97.8	2.723E-12	53.0	33.14	$\pm 0.18$
1325	3.771	9.449E-03	1.295E-04	63.0	99.0	1.761E-11	55.0	33.55	$\pm 0.10$
1550	3.852	9.326E-03	4.671E-04	2.1	96.4	6.005E-13	55.8	33.43	$\pm 0.54$
total gas							54.2	33.50	
plateau	1325-1550			65.1				33.55	$\pm 0.12$

Appendix 3 (continued).  $^{40}\text{Ar}/^{39}\text{Ar}$  data from Mogollon-Datil ignimbrites.

temp(°C)	$^{40}\text{Ar}/^{39}\text{Ar}$	$^{37}\text{Ar}/^{39}\text{Ar}$	$^{36}\text{Ar}/^{39}\text{Ar}$	% $^{39}\text{Ar}$	%rad	$^{39}\text{Ar}$ (moles)	K/Ca	age(Ma)	$\pm 1\sigma$
nm240	Blue Canyon, sanidine	J= 0.003656			RD42	weight=	0.13	disc=297.5	
900	5.654	1.883E-02	1.656E-03	10.1	91.3	1.36E-13	27.6	33.72 ± 0.09	
1100	5.259	1.765E-02	3.888E-04	21.1	97.7	2.83E-13	29.5	33.58 ± 0.09	
1200	5.264	1.753E-02	4.009E-04	20.4	97.7	2.73E-13	29.7	33.59 ± 0.09	
1300	5.287	1.744E-02	4.144E-04	28.2	97.6	3.77E-13	29.8	33.71 ± 0.10	
1450	5.402	1.736E-02	6.808E-04	17.4	96.2	2.32E-13	30.0	33.95 ± 0.09	
1550	6.270	2.056E-02	3.333E-03	2.8	84.2	3.76E-14	25.3	34.50 ± 0.13	
total gas							29.3	33.72	
plateau	900- 1300			79.8				33.64 ± 0.11	
nm328	Blue Canyon, sanidine	J= 0.005020			RD-56(mult)	weight=	0.1001	disc=296.5	
1125	3.847	1.777E-02	2.878E-04	23.1	97.8	2.162E-13	29.3	33.74 ± 0.10	
1180	3.785	1.762E-02	1.501E-04	23.5	98.8	2.199E-13	29.5	33.56 ± 0.09	
1205	3.810	1.728E-02	2.315E-04	18.9	98.2	1.769E-13	30.1	33.57 ± 0.10	
1235	3.832	1.754E-02	2.689E-04	10.1	97.9	9.488E-14	29.7	33.67 ± 0.09	
1260	3.829	1.723E-02	2.138E-04	11.7	98.3	1.096E-13	30.2	33.76 ± 0.09	
1290	3.838	1.729E-02	2.452E-04	10.5	98.1	9.858E-14	30.1	33.78 ± 0.09	
1325	3.880	1.856E-02	4.416E-04	2.3	96.6	2.157E-14	28.0	33.63 ± 0.11	
total gas							29.7	33.66	
plateau	1125-1325			100.0				33.68 ± 0.12	
80-12-6a	Blue Canyon, sanidine	J= 0.004595			RD32	weight=	0.1568	disc=296.5	
650	5.747	1.917E-02	5.327E-03	3.3	72.5	2.16E-14	27.1	34.22 ± 0.09	
950	4.447	1.920E-02	1.034E-03	10.1	93.0	6.63E-14	27.1	33.97 ± 0.09	
1050	4.372	1.891E-02	7.735E-04	9.7	94.7	6.35E-14	27.5	33.98 ± 0.10	
1125	4.316	1.898E-02	6.181E-04	15.0	95.7	9.83E-14	27.4	33.90 ± 0.09	
1200	4.319	1.882E-02	6.056E-04	14.7	95.8	9.65E-14	27.6	33.95 ± 0.09	
1275	4.314	1.883E-02	5.354E-04	12.3	96.2	8.04E-14	27.6	34.08 ± 0.09	
1400	4.297	1.868E-02	4.589E-04	22.4	96.7	1.47E-13	27.8	34.13 ± 0.12	
1550	4.464	1.865E-02	9.779E-04	12.6	93.4	8.29E-14	27.9	34.24 ± 0.09	
total gas							27.6	34.05	
plateau	950- 1400			84.2				34.00 ± 0.09	
80-12-6b	Blue Canyon, sanidine	J= 0.004595			RD32	weight=	0.1568	disc=296.5	
1000	4.615	1.926E-02	1.585E-03	15.5	89.8	5.93E-14	27.0	34.01 ± 0.09	
1150	4.306	1.920E-02	5.888E-04	24.5	95.9	9.38E-14	27.4	33.89 ± 0.09	
1275	4.257	1.875E-02	3.799E-04	38.0	97.3	1.46E-13	27.7	33.99 ± 0.10	
1400	4.410	1.871E-02	8.270E-04	18.0	94.4	6.88E-14	27.8	34.16 ± 0.09	
1550	5.819	1.855E-02	5.527E-03	4.0	71.9	1.54E-14	28.0	34.33 ± 0.09	
total gas							27.6	34.01	
plateau	1000- 1275			78.0				33.96 ± 0.08	
nm468	Rockhouse Can, sanidine	J= 0.005020			RD-56	weight=	0.1491	disc=296.5	
850	4.232	2.045E-02	1.371E-03	4.8	90.4	8.206E-13	25.4	34.34 ± 0.34	
1150	3.898	1.763E-02	2.356E-04	34.0	98.2	5.836E-12	29.5	34.34 ± 0.13	
1250	3.949	1.646E-02	3.938E-04	36.0	97.1	6.184E-12	31.6	34.38 ± 0.11	
1325	3.961	1.614E-02	3.668E-04	23.8	97.3	4.087E-12	32.2	34.56 ± 0.12	
1550	4.102	1.621E-02	1.463E-03	1.4	89.5	2.482E-13	32.1	32.94 ± 1.71	
total gas							30.7	34.39	
plateau	1150-1325			93.8				34.42 ± 0.12	

## E24

Appendix 3 (continued).  $^{40}\text{Ar}/^{39}\text{Ar}$  data from Mogollon-Datil ignimbrites.

temp(°C)	$^{40}\text{Ar}/^{39}\text{Ar}$	$^{37}\text{Ar}/^{39}\text{Ar}$	$^{36}\text{Ar}/^{39}\text{Ar}$	% $^{39}\text{Ar}$	%rad	$^{39}\text{Ar}$ (moles)	K/Ca	age(Ma)	$\pm 1\sigma$
nm239	Rockhouse Can, sanidine		J= 0.003711	RD42	weight=	0.1034	disc=297.5		
900	6.395	1.813E-02	3.744E-03	10.0	82.6	9.45E-14	28.7	35.04	$\pm 0.09$
1100	5.536	1.586E-02	9.111E-04	19.2	95.1	1.80E-13	32.8	34.89	$\pm 0.10$
1200	5.473	1.564E-02	7.481E-04	21.7	95.9	2.04E-13	33.3	34.79	$\pm 0.09$
1300	5.532	1.564E-02	8.642E-04	17.0	95.3	1.60E-13	33.2	34.96	$\pm 0.09$
1450	5.672	1.521E-02	1.377E-03	22.5	92.7	2.12E-13	34.2	34.88	$\pm 0.10$
1550	5.846	1.518E-02	1.832E-03	9.6	90.7	9.05E-14	34.3	35.14	$\pm 0.09$
	total gas						32.9	34.92	
	plateau	1100- 1450		80.3				34.88	$\pm 0.11$
nm296	Table Mtn, sanidine		J= 0.004917	RD-56	weight=	0.1498	disc=296.5		
850	4.292	1.823E-02	1.916E-03	4.1	86.8	7.411E-13	28.5	32.74	$\pm 0.56$
1160	3.978	1.656E-02	3.996E-04	30.2	97.0	5.520E-12	31.4	33.92	$\pm 0.12$
1250	3.835	1.479E-02	6.872E-04	40.5	94.7	7.399E-12	35.2	34.06	$\pm 0.15$
1350	4.036	1.516E-02	4.542E-04	24.6	96.7	4.502E-12	34.3	34.27	$\pm 0.12$
1550	4.422	1.822E-02	9.421E-04	0.7	93.7	1.226E-13	28.5	36.30	$\pm 2.93$
	total gas						32.6	34.03	
	plateau	1160-1250		70.7				33.96	$\pm 0.12$
nm454	Mimbres Pk, sanidine		J= 0.004992	RD-56	weight=	0.1338	disc=296.5		
850	4.753	2.832E-02	2.951E-03	4.3	81.7	5.670E-13	18.4	34.62	$\pm 1.07$
1125	3.997	2.259E-02	4.689E-04	20.6	96.5	2.747E-12	23.0	34.40	$\pm 0.45$
1225	3.940	1.973E-02	2.921E-04	25.6	97.8	3.414E-12	26.4	34.39	$\pm 0.29$
1350	3.963	1.856E-02	2.910E-04	42.4	97.8	5.657E-12	28.0	34.59	$\pm 0.12$
1550	4.137	2.072E-02	8.109E-04	7.1	94.2	9.471E-13	25.1	34.76	$\pm 0.45$
	total gas						25.9	34.51	
	plateau	850-1550		100.0				34.57	$\pm 0.12$
nm231	Bishop Peak, sanidine		J= 0.003812	RD54	weight=	0.1539	disc=299.2		
700	6.641	5.182E-02	5.101E-03	10.0	77.3	1.16E-12	10.0	34.95	$\pm 0.12$
1075	5.459	4.996E-02	1.241E-03	33.3	93.2	3.86E-12	10.4	34.67	$\pm 0.10$
1250	5.467	4.633E-02	1.237E-03	30.7	93.3	3.55E-12	11.2	34.74	$\pm 0.10$
1450	5.576	4.508E-02	1.503E-03	20.1	92.0	2.33E-12	11.5	34.94	$\pm 0.09$
1550	6.688	4.597E-02	5.244E-03	5.8	76.8	6.76E-13	11.3	34.98	$\pm 0.18$
	total gas						10.9	34.79	
	plateau	1075- 1250		64.0				34.70	$\pm 0.10$
nm92	Kneeling Nun, sanidine		J= 0.004999	RD-56	weight=	0.2028	disc=296.5		
850	4.533	8.582E-03	1.937E-03	3.4	87.4	9.547E-13	60.6	35.37	$\pm 0.72$
1160	4.031	8.426E-03	4.384E-04	26.3	96.8	7.376E-12	61.7	34.84	$\pm 0.11$
1260	4.055	8.244E-03	4.841E-04	43.4	96.5	1.219E-11	63.1	34.94	$\pm 0.10$
1350	3.959	8.122E-03	2.192E-04	26.5	98.4	7.437E-12	64.0	35.14	$\pm 0.11$
1550	4.564	5.665E-03	2.585E-03	0.5	83.3	1.404E-13	91.8	34.00	$\pm 6.30$
	total gas						63.0	34.97	
	plateau	850-1260		73.0				34.90	$\pm 0.12$
nm202	Kneeling Nun, sanidine		J= 0.005013	RD-56	weight=	0.2000	disc=296.5		
850	4.068	1.347E-02	2.968E-04	3.0	97.8	8.322E-13	38.6	35.64	$\pm 0.94$
1150	3.921	1.059E-02	1.188E-04	26.0	99.1	7.124E-12	49.1	34.80	$\pm 0.13$
1250	3.933	1.043E-02	1.441E-04	26.7	98.9	7.320E-12	49.8	34.84	$\pm 0.11$
1350	3.934	1.015E-02	1.069E-04	43.3	99.2	1.186E-11	51.2	34.95	$\pm 0.10$
1550	4.040	1.153E-02	1.044E-03	1.0	92.4	2.688E-13	45.1	33.52	$\pm 2.57$
	total gas						49.9	34.89	
	plateau	850-1550		100.0				34.89	$\pm 0.12$



Appendix 3 (continued).  $^{40}\text{Ar}/^{39}\text{Ar}$  data from Mogollon-Datil ignimbrites.

temp(°C)	$^{40}\text{Ar}/^{39}\text{Ar}$	$^{37}\text{Ar}/^{39}\text{Ar}$	$^{36}\text{Ar}/^{39}\text{Ar}$	% $^{39}\text{Ar}$	%rad	$^{39}\text{Ar}$ (moles)	K/Ca	age(Ma)	$\pm 1\sigma$
nm208	Kneeling Nun, sanidine		J= 0.003794		RD54	weight=	0.1984	disc=299.2	
750	6.062	1.120E-02	3.025E-03	6.2	85.2	1.32E-12	46.4	35.00 ± 0.11	
1050	5.249	8.672E-03	4.148E-04	20.9	97.6	1.44E-12	60.0	34.72 ± 0.09	
1250	5.271	8.224E-03	4.450E-04	32.9	97.4	6.97E-12	63.2	34.81 ± 0.11	
1450	5.298	7.694E-03	4.624E-04	33.0	97.3	7.00E-12	67.6	34.96 ± 0.10	
1550	5.712	9.070E-03	1.825E-03	7.0	90.5	1.48E-12	57.3	35.03 ± 0.12	
total gas							62.0	34.87	
plateau	1050- 1450			86.8				34.83 ± 0.15	
nm294	Kneeling Nun, sanidine		J= 0.005025		RD-56	weight=	0.1144	disc=296.5	
850	4.089	7.594E-03	7.651E-04	3.8	94.5	6.254E-13	68.5	34.70 ± 0.69	
1150	3.909	7.907E-03	7.825E-05	26.9	99.4	4.428E-12	65.8	34.89 ± 0.22	
1250	3.931	8.822E-03	2.399E-05	29.3	99.8	4.815E-12	58.9	35.08 ± 0.26	
1350	3.931	8.372E-03	1.228E-04	38.5	99.1	6.334E-12	62.1	34.96 ± 0.15	
1550	4.096	1.298E-02	8.952E-04	1.5	93.5	2.396E-13	40.1	34.43 ± 1.86	
total gas							62.1	34.96	
plateau	850-1550			100.0				34.96 ± 0.13	
nm498	Kneeling Nun, sanidine		J= 0.005029		RD-56	weight=	0.2001	disc=296.5	
850	3.985	9.114E-03	2.569E-04	6.3	98.1	1.670E-12	57.1	35.13 ± 0.30	
1160	3.931	8.375E-03	7.686E-05	32.6	99.4	8.673E-12	62.1	35.11 ± 0.10	
1240	3.973	8.475E-03	1.925E-04	30.9	98.6	8.225E-12	61.4	35.18 ± 0.16	
1340	3.967	8.184E-03	1.433E-04	28.6	98.9	7.616E-12	63.5	35.25 ± 0.10	
1550	4.049	8.520E-03	2.441E-04	1.5	98.2	4.055E-13	61.0	35.73 ± 1.47	
total gas							61.9	35.18	
plateau	850-1550			100.0				35.17 ± 0.12	
nm110	Kneeling Nun, sanidine		J= 0.004595		RD32	weight=	0.1137	disc=296.5	
650	8.066	9.238E-03	1.231E-02	4.0	54.8	1.94E-14	56.3	36.29 ± 0.10	
950	5.124	8.870E-03	2.780E-03	8.6	83.9	4.21E-14	58.6	35.27 ± 0.09	
1050	4.885	8.549E-03	1.991E-03	8.1	87.8	3.96E-14	60.8	35.22 ± 0.09	
1125	4.655	8.544E-03	1.231E-03	12.3	92.1	6.02E-14	60.9	35.18 ± 0.09	
1200	4.679	8.578E-03	1.267E-03	16.3	91.9	7.99E-14	60.6	35.29 ± 0.09	
1275	4.628	8.515E-03	1.021E-03	14.1	93.4	6.89E-14	61.1	35.46 ± 0.09	
1400	4.591	8.483E-03	9.387E-04	18.2	93.8	8.92E-14	61.3	35.36 ± 0.09	
1550	4.727	8.411E-03	1.426E-03	18.5	91.0	9.05E-14	61.8	35.30 ± 0.09	
total gas							60.7	35.34	
plateau	1200- 1550			67.1				35.35 ± 0.12	
nm465	Kneeling Nun, sanidine		J= 0.005021		RD-56	weight=	0.1988	disc=296.5	
850	3.927	9.790E-03	4.354E-04	3.1	96.7	6.822E-13	53.1	34.11 ± 0.74	
1160	4.426	8.033E-03	7.687E-05	27.2	99.5	6.010E-12	64.7	39.45 ± 0.12	
1240	4.892	7.499E-03	8.280E-05	33.3	99.5	7.373E-12	69.3	43.56 ± 0.20	
1550	5.980	7.239E-03	9.871E-05	33.9	99.5	7.505E-12	71.8	53.11 ± 0.17	
1550	6.699	7.578E-03	2.947E-05	2.5	99.9	5.599E-13	68.6	59.63 ± 1.44	
total gas							68.4	45.81	
no plateau									
nm206	Bell Top #4, sanidine		J= 0.003801		RD54	weight=	0.2105	disc=299.2	
850	6.277	5.011E-02	3.652E-03	12.0	82.8	1.63E-12	10.4	35.29 ± 0.10	
1000	5.557	4.939E-02	1.381E-03	15.6	92.6	2.12E-12	10.5	34.96 ± 0.11	
1250	5.340	4.735E-02	6.457E-04	39.8	96.4	5.41E-12	11.0	34.96 ± 0.10	
1450	5.420	4.646E-02	8.295E-04	27.4	95.4	3.73E-12	11.2	35.13 ± 0.10	
1550	6.487	4.708E-02	4.383E-03	5.3	80.0	7.20E-13	11.0	35.24 ± 0.20	
total gas							10.9	35.06	
plateau	1000- 1450			82.7				35.01 ± 0.13	

Appendix 3 (continued).  $^{40}\text{Ar}/^{39}\text{Ar}$  data from Mogollon-Datil ignimbrites.

temp(°C)	$^{40}\text{Ar}/^{39}\text{Ar}$	$^{37}\text{Ar}/^{39}\text{Ar}$	$^{36}\text{Ar}/^{39}\text{Ar}$	% $^{39}\text{Ar}$	%rad	$^{39}\text{Ar}$ (moles)	K/Ca	age(Ma)	$\pm 1\sigma$
nm209	Bell Top #4, sanidine		J= 0.005007		RD-56	weight=	0.1977		disc=296.5
850	4.604	5.390E-02	2.533E-03	6.0	83.7	9.932E-13	9.6	34.50 ± 0.90	
1150	4.059	5.026E-02	5.604E-04	26.4	95.9	4.395E-12	10.3	34.83 ± 0.21	
1250	4.204	4.681E-02	1.012E-03	39.3	92.9	6.529E-12	11.1	34.93 ± 0.13	
1350	4.057	4.360E-02	4.887E-04	20.4	96.4	3.397E-12	11.9	35.00 ± 0.16	
1550	4.183	4.357E-02	8.313E-04	7.9	94.1	1.316E-12	11.9	35.22 ± 0.40	
	total gas						11.1	34.91	
	plateau 850-1550			100.0				34.94 ± 0.12	
nm501	Bell Top #4, sanidine		J= 0.005031		RD-56	weight=	0.2006		disc=296.5
850	4.900	4.617E-02	3.457E-03	5.9	79.2	1.203E-12	11.3	34.86 ± 0.35	
1150	4.108	4.623E-02	7.497E-04	24.6	94.6	5.005E-12	11.2	34.94 ± 0.13	
1250	4.244	4.141E-02	1.217E-03	39.1	91.5	7.955E-12	12.6	34.92 ± 0.14	
1300	4.258	4.082E-02	1.081E-03	27.2	92.5	5.519E-12	12.7	35.39 ± 0.11	
1550	4.516	4.289E-02	1.811E-03	3.2	88.1	6.432E-13	12.1	35.77 ± 0.63	
	total gas						12.2	35.08	
	plateau 1150-1250			63.8				34.93 ± 0.12	
nm460	Sugarlump 2, sanidine		J= 0.005022		RD-56	weight=	0.2003		disc=296.5
850	4.376	3.155E-02	1.590E-03	3.9	89.3	7.768E-13	16.5	35.05 ± 0.37	
1150	4.001	2.227E-02	3.389E-04	24.4	97.5	4.904E-12	23.4	35.00 ± 0.13	
1250	4.109	2.176E-02	6.184E-04	34.5	95.6	6.945E-12	23.9	35.23 ± 0.10	
1550	4.052	2.122E-02	3.730E-04	34.8	97.3	7.002E-12	24.5	35.36 ± 0.10	
1550	4.195	2.234E-02	6.149E-04	2.4	95.7	4.830E-13	23.3	36.01 ± 0.49	
	total gas						23.7	35.23	
	plateau 1150-1250			58.9				35.17 ± 0.12	
nm238	Farr Ranch, sanidine		J= 0.003656		RD42	weight=	0.1129		disc=297.5
900	6.150	4.185E-02	2.257E-03	10.7	89.1	9.66E-14	12.4	35.79 ± 0.09	
1100	5.588	4.236E-02	4.885E-04	20.2	97.4	1.82E-13	12.3	35.54 ± 0.09	
1200	5.588	4.145E-02	5.632E-04	14.4	97.0	1.30E-13	12.5	35.39 ± 0.09	
1300	5.620	4.005E-02	5.693E-04	15.7	97.0	1.42E-13	13.0	35.58 ± 0.10	
1450	5.680	3.974E-02	7.463E-02	23.3	96.1	2.10E-13	13.1	35.64 ± 0.10	
1550	5.870	3.901E-03	1.388E-03	15.7	93.0	1.41E-13	13.3	35.64 ± 0.09	
	total gas						12.8	35.59	
	plateau 1100- 1550			89.3				35.57 ± 0.13	
nm85a	Datil Well, sanidine		J= 0.004590		RD32	weight=	0.144		disc=296.5
900	5.184	4.222E-02	2.898E-03	20.2	83.4	9.09E-14	12.3	35.45 ± 0.11	
1050	4.767	4.192E-02	1.440E-03	25.9	91.0	1.17E-13	12.4	35.57 ± 0.10	
1125	4.780	4.155E-02	1.511E-03	23.1	90.6	1.04E-13	12.5	35.50 ± 0.09	
1200	5.212	4.161E-02	2.902E-03	12.3	83.5	5.55E-14	12.5	35.68 ± 0.09	
1275	5.650	4.105E-02	4.337E-03	6.5	77.3	2.95E-14	12.7	35.79 ± 0.10	
1400	5.490	4.151E-02	3.815E-03	8.1	79.4	3.66E-14	12.5	35.74 ± 0.10	
1550	6.768	4.194E-02	8.105E-03	3.9	64.6	1.75E-14	12.4	35.82 ± 0.10	
	total gas						12.4	35.58	
	plateau 900- 1200			81.5				35.55 ± 0.10	
nm85b	Datil Well, sanidine		J= 0.004590		RD32	weight=	0.0983		disc=296.5
900	6.249	4.182E-02	6.450E-03	12.8	69.5	3.81E-14	12.4	35.58 ± 0.12	
1050	4.910	4.249E-02	1.983E-03	17.3	88.0	5.16E-14	12.2	35.42 ± 0.10	
1125	4.867	4.173E-02	1.841E-03	19.0	88.8	5.67E-14	12.5	35.42 ± 0.09	
1400	4.812	4.137E-02	1.574E-03	42.3	90.3	1.26E-13	12.6	35.61 ± 0.13	
1550	5.996	4.092E-02	5.472E-03	8.6	73.0	2.56E-14	12.7	35.87 ± 0.10	
	total gas						12.4	35.56	
	plateau 900- 1400			91.4				35.51 ± 0.1	

## E27

Appendix 3 (continued).  $^{40}\text{Ar}/^{39}\text{Ar}$  data from Mogollon-Datil ignimbrites.


temp(°C)	$^{40}\text{Ar}/^{39}\text{Ar}$	$^{37}\text{Ar}/^{39}\text{Ar}$	$^{36}\text{Ar}/^{39}\text{Ar}$	% $^{39}\text{Ar}$	%rad	$^{39}\text{Ar}$ (moles)	K/Ca	age(Ma)	$\pm 1\sigma$
nm237	Datil Well, sanidine		J= 0.003655		RD42	weight=	0.1129	disc=297.5	
900	6.245	3.795E-02	2.720E-03	21.1	87.1	1.81E-13	13.7	35.51 $\pm$ 0.10	
1100	5.615	3.731E-02	6.525E-04	27.6	96.5	2.37E-13	13.9	35.38 $\pm$ 0.10	
1200	5.668	3.684E-02	8.576E-04	25.1	95.5	2.16E-13	14.1	35.33 $\pm$ 0.09	
1300	5.735	3.597E-02	9.698E-04	18.9	94.9	1.62E-13	14.5	35.55 $\pm$ 0.11	
1450	6.181	3.497E-02	2.689E-03	5.3	87.1	4.56E-14	14.9	35.15 $\pm$ 0.10	
1550	7.261	3.048E-02	5.867E-03	2.0	76.1	1.70E-14	17.1	36.06 $\pm$ 0.29	
	total gas						14.1	35.43	
	plateau 900- 1300			92.7				35.43 $\pm$ 0.13	
nm90b	Datil Well, sanidine		J= 0.004581		RD32	weight=	0.0935	disc=296.1	
1000	4.789	5.966E-02	1.645E-03	32.6	89.8	9.55E-14	8.7	35.20 $\pm$ 0.12	
1150	4.578	4.549E-02	7.752E-04	31.1	94.9	9.11E-14	11.4	35.57 $\pm$ 0.10	
1250	4.862	4.475E-02	1.207E-03	23.4	92.6	6.87E-14	11.6	36.83 $\pm$ 0.09	
1400	5.630	4.466E-02	2.404E-03	11.2	87.3	3.29E-14	11.6	40.19 $\pm$ 0.13	
1550	10.398	4.978E-02	1.644E-02	1.7	53.3	5.11E-15	10.4	45.20 $\pm$ 0.10	
	total gas						10.4	36.43	
	no plateau								
nm203	Dona Ana, sanidine		J= 0.005007		RD-56	weight=	0.1983	disc=296.5	
850	4.204	9.148E-03	8.538E-04	7.2	94.0	1.361E-12	56.8	35.35 $\pm$ 0.20	
1125	4.004	8.271E-03	1.270E-04	35.2	99.1	6.691E-12	62.9	35.48 $\pm$ 0.11	
1210	4.114	8.327E-03	4.930E-04	22.8	96.5	4.327E-12	62.4	35.49 $\pm$ 0.13	
1350	4.280	8.074E-03	9.705E-04	33.1	93.3	6.281E-12	64.4	35.71 $\pm$ 0.18	
1550	4.583	8.681E-03	2.002E-03	1.8	87.1	3.419E-13	59.9	35.70 $\pm$ 1.49	
	total gas						62.8	35.55	
	plateau 850-1550			100.0				35.49 $\pm$ 0.11	
nm205	Bell Top #3, sanidine		J= 0.003738		RD42	weight=	0.1194	disc=297.5	
900	5.961	7.156E-03	1.953E-03	13.6	90.2	1.33E-13	72.7	35.92 $\pm$ 0.09	
1100	5.450	7.099E-03	3.602E-04	27.7	97.9	2.71E-13	73.2	35.65 $\pm$ 0.11	
1200	5.457	7.130E-03	3.532E-04	31.8	98.0	3.11E-13	72.9	35.70 $\pm$ 0.10	
1300	5.538	6.999E-03	5.643E-04	16.6	96.9	1.63E-13	74.3	35.83 $\pm$ 0.10	
1450	5.724	7.661E-03	1.266E-03	6.9	93.4	6.76E-14	67.9	35.69 $\pm$ 0.10	
1550	6.305	1.169E-02	3.126E-03	3.3	85.3	3.25E-14	44.5	35.90 $\pm$ 0.17	
	total gas						71.3	35.74	
	plateau 1100- 1450			83.0				35.68 $\pm$ 0.12	
nm205	Bell Top #3, sanidine		J= 0.003799		RD54	weight=	0.1973	disc=299.2	
900	5.909	7.675E-03	2.163E-03	8.4	89.1	1.38E-12	67.7	35.73 $\pm$ 0.10	
1150	5.521	6.958E-03	9.002E-04	35.3	95.1	5.77E-12	74.7	35.63 $\pm$ 0.11	
1300	5.533	6.983E-03	9.215E-04	36.3	95.0	5.93E-12	74.5	35.66 $\pm$ 0.11	
1450	5.736	7.087E-03	1.525E-03	16.5	92.0	2.69E-12	73.4	35.83 $\pm$ 0.11	
1550	7.314	8.527E-03	6.617E-03	3.5	73.2	5.67E-13	61.0	36.32 $\pm$ 0.17	
	total gas						73.2	35.71	
	plateau 1150- 1450			88.1				35.75 $\pm$ 0.14	
nm529	Squaw Mtn, sanidine		J= 0.005013		RD-56	weight=	0.1984	disc=296.5	
850	4.201	2.974E-02	7.790E-04	5.9	94.5	9.489E-13	17.5	35.55 $\pm$ 0.45	
1150	4.041	2.933E-02	1.997E-04	34.0	98.5	5.452E-12	17.7	35.66 $\pm$ 0.12	
1225	4.226	2.799E-02	7.445E-04	32.4	94.8	5.194E-12	18.6	35.87 $\pm$ 0.13	
1375	4.899	2.748E-02	2.837E-03	20.1	82.9	3.225E-12	18.9	36.36 $\pm$ 0.23	
1550	5.481	2.799E-02	4.596E-03	7.6	75.2	1.226E-12	18.6	36.91 $\pm$ 0.48	
	total gas						18.7	35.96	
	plateau 850-1225			72.3				30.69 $\pm$ 0.11	

Appendix 3 (continued).  $^{40}\text{Ar}/^{39}\text{Ar}$  data from Mogollon-Datil ignimbrites.

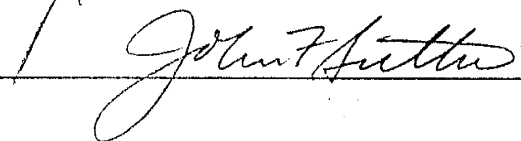
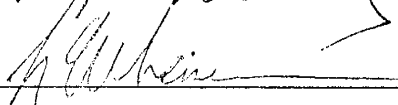
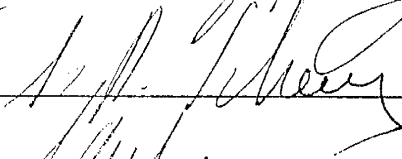
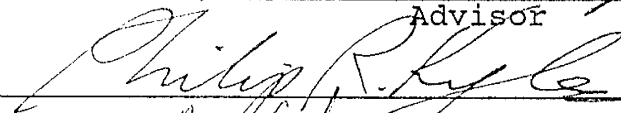
temp(°C)	$^{40}\text{Ar}/^{39}\text{Ar}$	$^{37}\text{Ar}/^{39}\text{Ar}$	$^{36}\text{Ar}/^{39}\text{Ar}$	% $^{39}\text{Ar}$	%rad	$^{39}\text{Ar}$ (moles)	K/Ca	age(Ma)	$\pm 1\sigma$
nm483	Cueva, sanidine		J= 0.005030		RD-56	weight=	0.2021		disc=296.5
850	4.667	3.552E-03	2.245E-03	8.1	85.8	1.539E-12	146.4	35.97	$\pm 0.51$
1150	4.278	3.128E-03	8.778E-04	46.9	93.9	8.945E-12	166.2	36.10	$\pm 0.11$
1225	4.278	3.277E-03	8.006E-04	28.6	94.5	5.456E-12	158.7	36.30	$\pm 0.11$
1350	4.332	3.170E-03	1.098E-03	11.3	92.5	2.147E-12	164.0	35.99	$\pm 0.20$
1550	4.687	3.695E-03	1.916E-03	5.1	87.9	9.722E-13	140.7	37.01	$\pm 0.23$
total gas							160.9	36.18	
plateau	850-1350			94.9				36.20	$\pm 0.13$
nm482	Cueva, sanidine		J= 0.005017		RD-56	weight=	0.1985		disc=296.5
850	4.178	4.180E-03	5.429E-04	7.9	96.2	1.397E-12	124.4	36.01	$\pm 0.24$
1125	4.113	4.767E-03	3.455E-04	23.8	97.5	4.177E-12	109.1	35.94	$\pm 0.14$
1235	4.057	5.762E-03	5.099E-04	42.8	96.3	7.517E-12	90.3	35.01	$\pm 0.10$
1375	4.197	4.714E-03	5.127E-04	23.6	96.4	4.143E-12	110.3	36.24	$\pm 0.15$
1550	4.371	4.634E-03	1.686E-03	1.9	88.6	3.425E-13	112.2	34.68	$\pm 1.83$
total gas							102.6	35.60	
no plateau									

Explanation: Each data set is preceded by sample number, unit name, irradiation parameter (J), irradiation batch number, sample weight, and measured discrimination of atmospheric argon. Columns in data sets give temperature of incremental heating steps, ratios of Ar isotopes ( $^{40}\text{Ar}$ =initial and radiogenic,  $^{39}\text{Ar}$ =potassium-derived,  $^{37}\text{Ar}$ =Calcium derived,  $^{36}\text{Ar}$ =initial), % of total  $^{39}\text{Ar}$  in heating step, radiogenic yield of  $^{40}\text{Ar}$ , moles of potassium derived  $^{39}\text{Ar}$ , K/Ca ratio calculated from  $^{37}\text{Ar}/^{39}\text{Ar}$  ratio, age, and  $1\sigma$  error. Lines following each data step show total gas K/Ca and age, and plateau temperature range,  $^{39}\text{Ar}$  percent, age, and error (method of Fleck et al., 1981).

This dissertation is accepted on behalf of the faculty  
of the Institute by the following committee:



Advisor



Date